UNIVERSITY OF STRATHCLYDE

DOCTORAL THESIS

Applications of High-Brightness 280 nm Light Emitting Diodes in Biomedical Optical Imaging

---

Author:
Mollie MCFARLANE

Supervisor:
Prof. Gail MCCONNELL

A thesis submitted in fulfillment of the requirements
for the degree of Doctor of Philosophy

in the

Department of Physics

March 30, 2023

Declaration of Authorship

I, Mollie MCFARLANE, declare that this thesis titled, Applications of High-Brightness 280 nm Light Emitting Diodes in Biomedical Optical Imagingand the work presented in it are my own. I confirm that:

- This work was done wholly while in candidature for a research degree at this University.
- Where any part of this thesis has previously been submitted for a degree or any other qualification at this University or any other institution, this has been clearly stated.
- Where I have reproduced content from published papers of which I am an author, permission has been sought from the publishers and this is clearly stated at the forefront of the chapter.
- Where I have quoted from the work of others, the source is always given. With the exception of such quotations, this thesis is entirely my own work.
- The work done within this thesis is entirely my own work, except from contributions from others which will be listed here. All packaging and heat sinking of LEDs was carried out with the help of CoolLED using their LED packaging facilities. Optical modelling of lenses in order to create collector optics in figure 3.5 was done by Alex Gramann at CoolLED. The USB2000+UV-Vis spectrometer and the Ealing reflective objective were loaned to me by Paul Edwards of the SSD group at the University of Strathclyde. The code for analysing quantum dots in chapter 4 was written by Nicholas Hall. The code for analysing standing wave images used in chapter 5 was written by Ross Scrimgeour.

Signed:

_____

Date:

_____

Let's go, girls.

- Shania Twain

Acknowledgements

If you are reading this, it means that my thesis writing has finally come to an end and I am very glad to be done with this chapter of my PhD journey.

I would like to start off by saying thank you to my supervisor Gail for everything she has done for me and everyone else in the group. No matter the circumstance, Gail has always made time for me to answer my questions, give advice on my research, listen to my complaining, offer words of encouragement and many more matters above and beyond being *just* a supervisor. Getting through a PhD is no mean feat and to do this without the constant support of Gail is unimaginable to me.

Thank you to everyone at CoolLED who have supported me from the start of my PhD. Special thanks to the R&D team, Gerry, Alex and Luther who have always engaged with my project and been there to answer my questions and help me to solve problems. Thank you to my funders Medical Research Scotland for providing me with the opportunity to undertake this project.

I would like to thank each and every member, past and present, of the Centre for Biophotonics. To Jordan, Shannan and Eliana Pan di Stelle who have been there with me from the start - you are my rocks and I could not imagine having to go through this process with anyone else. Without you three, I wouldn't have gotten through this PhD. To Katrina, thank you for being my trapeze partner, cinema date and for always bumping into me when we're walking. To Lisa, thank you for being there for me during our writing and for always making me laugh. To Peter, thank you for believing in me from the beginning. To Liam - congratulations on your many published papers. A special mention to my lovely biologists, Ryan, Tanith and the Hollies - thank you for being amazing officemates and putting up with all of our loud (and often inappropriate) conversations. Still to this day I find myself asking - which plague of Egypt *would* I be? Thank you all for all the laughs we have shared on a daily basis. I have no doubt that we will be friends for life.

Abstract

Light-emitting diodes (LEDs) have long been proven as excellent illumination sources for optical microscopy for reasons including their versatile spectral emission, reliability and fast switching times. Deep-ultraviolet (deep-UV) microscopy using LEDs has, however, historically been limited due to low optical power and poor transmission through glass. Recently, new developments in deep-UV LED technology have allowed high-brightness LEDs emitting at 280 nm with powers in the 100 mW range. In this thesis, I explore the applications of these 280 nm LEDs in biomedical optical imaging.

I first characterise the optical properties of the LED important in microscopy, including electroluminescence spectrum and optical stability. Within this chapter, I also present the development of a novel technique for characterisation of the emission pattern of deep-UV LEDs without the need for UV-enhanced detectors. I next discuss the issue of transmission of this wavelength of light through glass and present a systematic comparison of existing methods to overcome this issue, including quartz objective lenses, reflective objective lenses and transmission fluorescence. I compare these methods based on properties such as transmission of 280 nm light, illumination homogeneity and image quality, and use this information to identify the most appropriate illumination method for applying this LED to image biological specimens.

After choosing an illumination method, I then use this to excite quantum dot-labelled cells with 280 nm light and present the benefits of using this wavelength compared to the longer, more traditionally used wavelength of 365 nm, determining an up to 3.59-fold increase in fluorescence intensity associated with using 280 nn excitation.

Finally, I develop a new method of generating a standing wave using 280 nm light and use this to carry out 280 nm standing wave microscopy of fluorescent lens specimens and fixed mammalian cells. I characterise the standing wave both in air and in a biologically-equivalent environment and quantify an achieved axial resolution of 48.9 nm - a near two-fold improvement on previous standing wave work with visible wavelengths.

Contents

List of Figures

List of Tables

List of Abbreviations

UV	Ultraviolet
FWHM	Full width half maximum
FLIM	Fluorescence lifetime imaging microscopy
Fiji	Fiji is just Imagej
NA	Numerical aperture
LED	Light-emitting diode
ROI	Regions of interest
QD	Quantum dots
BSA	Bovine serum albumin
PI	Propidium iodide
CPD	Cyclobutane pyrimidine dimers
DMEM	Dulbecco's modified eagle medium
AlGaN	Aluminium gallium nitride
PBS	Phosphate buffered saline
PSF	Point spread function
CCD	Charge coupled device
CMOS	Complimentary metal-oxide semiconductor
FOV	Field of view
LP	Long pass

Research Output

Published Papers

Mollie McFarlane and Gail McConnell "Characterisation of a deep-ultraviolet light-emitting diode emission pattern via fluorescence", *Measurement Science and Technology*, 2020, 31, 077001

Mollie McFarlane, Nicholas Hall and Gail McConnell "Enhanced fluorescence from semiconductor quantum dot-labelled cells excited at 280 nm", *Methods Applications in Fluorescence*, 2022, 10, 025004

Oral Presentations

Department of Physics Postgraduate Conference, Ross Priory, 2019 "Applications of High Brightness 280nm LEDs in Biomedical Optical Imaging"

Frontiers in Bioimaging, Birmingham, 2022. "Enhanced fluorescence from semiconductor quantum dot-labelled cells excited at 280 nm"

Poster Presentations

Photonex, Glasgow, 2019. "Applications of High Brightness 280nm LEDs in Biomedical Optical Imaging"

SUPA Annual Gathering 2019. "Applications of High Brightness 280nm LEDs in Biomedical Optical Imaging"

Department of Physics Postgraduate Conference, Online, 2020 "Characterisation of a deep-ultraviolet light-emitting diode emission pattern via fluorescence"

Photonics Online Meetup, Online, 2020. "Characterisation of a deep-ultraviolet light-emitting diode emission pattern via fluorescence"

Frontiers in Bioimaging, Birmingham, 2022. "Enhanced fluorescence from semiconductor quantum dot-labelled cells excited at 280 nm" (Poster prize winner)

Covid Impact Statement

During my PhD funding period of October 2018 to September 2022, the Covid-19 pandemic hit the UK which interrupted my studies considerably for a number of months. From March 2020 to September 2020, during the nationwide lockdowns, I was unable to obtain access to the lab or any equipment within, meaning that no experimental work could be carried out. In the months that followed, the University reopened for essential medical research with social distancing rules put in place within the University, meaning that access to equipment was limited. Overall, I would estimate a minimum of 6 months of disruption to my research which was not compensated for by an extension to my funding period.

Chapter 1

Introduction

It is the aim of this chapter to give the reader an overview into the main concepts explored within this thesis. These include optical microscopy for biomedical imaging, including standard brightfield and fluorescence microscopy as well as deep-ultraviolet microscopy and its applications. This chapter will then review the principles of light-emitting diodes and their advantages as light sources in microscopy. Finally, the chapter will discuss the optical properties of semiconductor quantum dots, their biofunctionalisation and their applications in biomedical optical imaging.

1.1 Optical Microscopy

1.1.1 History of light microscopy and resolution

Optical microscopy is the name given to the field which typically uses visible light and a system of lenses to form images of small objects for their study. Although other types of microscopy such as electron microscopy now exist, historically, optical microscopy has been of interest due to its ability to image biological specimens on a cellular level without significantly damaging the specimen.

The invention of the optical microscope can be dated back to Dutch spectacle makers Hans and Zacharias Janssen in around 1590 [1, 2]. This design used two convex lenses, separated at a distance, to form a magnified image on the retina [1, 2]. Shortly, after this in 1609, it is thought that a similar instrument was invented by Galileo and this was the first to be described as a microscope [2]. Although no observations from these microscopes were published, it was these designs which paved the way for future, more sophisticated microscope designs. Optical microscopy was brought into

popular use by Robert Hooke's 1665 book *Micrographia*, considered to be the first important work using microscopy [3]. This publication was popular not only in the scientific community, but also with the public as this contained large, finely-detailed illustrations and descriptions of some specimens Hooke viewed under the microscope including insects, fungi and plants. Hooke was the first person to use the word cell to describe the compartments he visualised inside specimens.

Almost ten years later came the discovery of bacteria and microorganisms by Antoni van Leeuwenhoek, often considered to be the father of microbiology [4, 5]. van Leeuwenhoek used microscopy to visualise the first living cell and, together with Hooke, laid the groundwork for better understanding of biological processes, informing the diagnosis and treatment of infectious diseases.

After these developments in the 1600s, it was around 200 years later that Ernst Abbe demonstrated how the diffraction of light by the specimen and by the objective lens determined image resolution [6, 7]. Abbe defined the lateral resolution of a microscope using equation 1.1 [6]:

$$d_{min} = \frac{\lambda}{2nsin\theta} \tag{1.1}$$

where d_{min} is the lateral resolution, λ is the wavelength of light, n is the refractive index of the medium the lens is immersed in and θ is the maximum half-angle of light that can enter the lens. Abbe was the first person to use the term numerical aperture (NA) to describe $nsin\theta$ and to use this as a measurement of the resolving power of the lens. From this equation, it is clear that the spatial resolution in a light microscope is dependent on wavelength and NA. Based on this, Abbe predicted that the lateral resolution of the optical microscope was limited to around 200 nm.

A complimentary method of determining the limits of resolution for diffraction through circular apertures uses the Airy disk. When light from a point object passes through a circular aperture such as a lens, the resulting diffraction pattern is a bright circle in the center, surrounded by a series of concentric rings of decreasing intensity. The central ring is known as the Airy disk and the radius of this disk is an important factor in determining the resolution of the optical system. The radius of the Airy disk, r_{Airy}, is given by [6]:

$$r_{Airy} = \frac{0.61\lambda}{NA} \tag{1.2}$$

In an optical microscope, the Airy disk occurs in three dimensions and is known as the point spread function (PSF). When considering two point sources separated by a small distance within the specimen plane, the resolving power of the microscope is then determined by the minimum distance between which two separate Airy disks can be distinguished from each other.

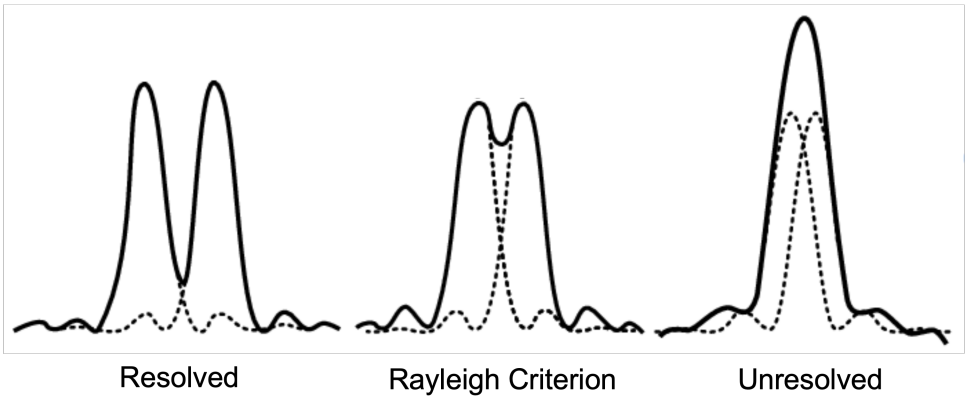

FIGURE 1.1: The Rayleigh resolution limit in optical microscopy. Left - two Airy disks sufficiently seperated such that they are resolvable from each other. Center - two Airy disks at their minimum resolvable distance. Right - two Airy disks which are no longer resolvable because they are too close together.

This is typically described by the Rayleigh resolution limit [6], which states that the diffraction patterns of two spatially close together objects are resolved at the point which the central maximum of the Airy pattern of one object overlaps with the first minimum of the Airy pattern of the second object. This generally means that the images of two point sources are said to be resolved if the distance between them is equal to, or larger than, the radius of the Airy disk [6]. This is illustrated in figure 1.1 which shows two Airy disks separated by distances more than, equal to and less than the resolution limit set by the Rayleigh criterion.

The axial resolution is defined by [6]

$$z_{min} = \frac{2\lambda n}{NA^2} \tag{1.3}$$

where z_{min} is the minimum axial resolvable distance. Notably, from equations 1.2

and 1.3, the PSF does not have a uniform intensity distribution across three dimensions and the axial resolution is elongated along the optical axis of the microscope. This results in axial resolution in optical microscopy always being significantly poorer than the lateral resolution [6].

Although equations 1.2 and 1.3 give the theoretical resolution of an optical microscope, typically, in experimental microscopy scenarios, a measurement of the PSF of the optical system in use is performed to measure the actual lateral and axial resolution of the system. Typically, the full-width-half-maximum (FWHM) of a sub-resolution point emitter is used to measure the PSF of a microscope, and this can be done using a single emitter such as a bead. Measurement of the PSF of the microscope is necessary as the measured PSF can be different from the theoretical value due to aberrations in optical microscopy. These aberrations can affect both the lateral and axial PSF, impacting the resolution of the microscope.

A common aberration in microscopy is chromatic aberration, occurring due to the difference in refraction angle with different wavelengths [8]. This results in different wavelengths passing through a lens being focused at different distances along the optical axis. Another common type of aberration is spherical aberration, in which light passing through the center of a lens is focussed to a different distance along the optical axis than light passing through the edge of the lens [8]. This can worsen as the diameter of the lens increases or when the specimen has a different refractive index from the surrounding imaging medium. Although these are two of the most common aberrations experienced in optical microscopy, more do exist such as coma aberration and astigmatism. To combat the effects of these in microscopy, modern objective lenses are corrected to reduce or remove the effects of aberrations in the PSF of the microscope, such as chromatic and spherical aberrations, and improve imaging quality.

1.1.2 Brightfield microscopy

Brightfield microscopy is often considered the simplest of all optical microscopy techniques. Brightfield microscopy is a technique in which white light is transmitted through a specimen and collected by the objective lens. In this technique, contrast is generated through the absorption of light by the specimen.

A schematic of a typical brightfield microscope is shown in figure 1.2. In the brightfield microscope, light from a light source travels through a series of lenses and apertures to reach the specimen. Typically, to illuminate the sample as evenly as possible, a set of three convex lenses and two apertures are used [9]. The collector lens collimates the rays of light from a divergent source e.g. arc lamp. This is followed by a field aperture at the front focal plane of the collector lens. Both the field aperture and the condenser aperture are placed at the front and back focal planes of the field lens. The field lens is used to focus an image of the LED chip onto the condenser aperture. Finally, the condenser lens collimates the light onto the specimen. This is known as Köhler illumination. This light passes through the sample and is collected by the objective lens and focussed onto a camera (placed at the intermediate image plane) using the tube lens.

As shown in figure 1.2, the microscope contains two groups of optical planes responsible for controlling illumination and image formation - these are called illumination planes and imaging planes respectively. Illumination planes occur at the focal points of the illumination rays (green) shown in figure 1.2, and imaging planes at the focal points of the imaging rays (red). The illumination planes are located at the LED, the condenser aperture and the back focal plane of the objective. Similarly, the imaging planes are located at the field aperture, the specimen plane and the intermediate image plane.

An alternative method of sample illumination is critical illumination (shown in figure 1.3, which uses only the collector lens, condenser aperture and condenser lens to illuminate the specimen. In this method, an image of the light source is projected

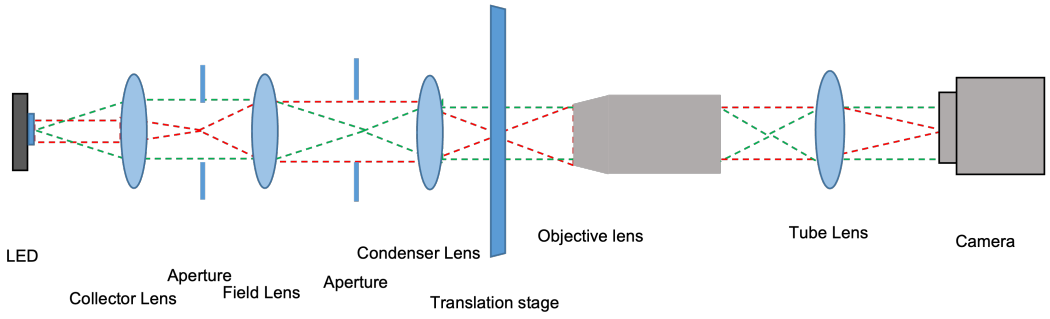

FIGURE 1.2: Schematic of a brightfield microscope set up for Köhler illumination. Illumination rays are shown in green and imaging rays in red.

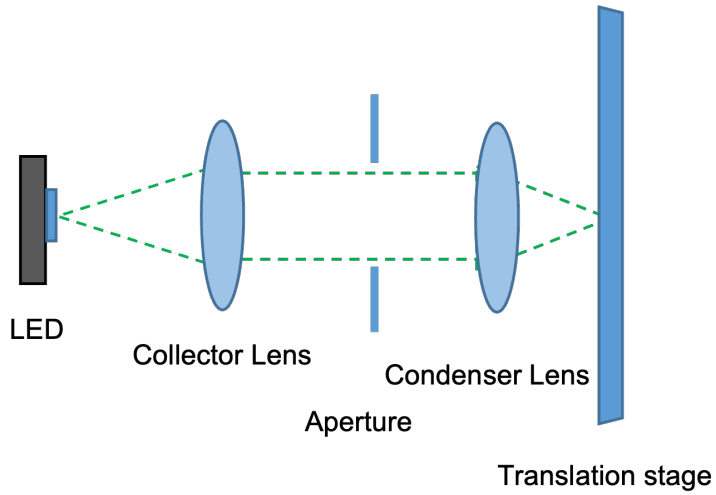

FIGURE 1.3: Schematic of the illumination optics involved in critical illumination.

onto the specimen. This often results in inhomogeneous sample illumination as many sources such as LEDs have patterned emissive areas.

In brightfield microscopy, image contrast is generated by absorption/attenuation of light by the specimen. This gives the appearance of a dark specimen on a light background. However, imaging biological specimen can be problematic as cellular features and structures which are often translucent can be difficult to distinguish from the background. This can be improved by using absorptive dyes such as haemotoxylin and eosin (H&E) to stain tissue. These are often used in tissue pathology to improve contrast [10].

Brightfield microscopy is a widefield technique, i.e. the whole field of view is illuminated and detected at once. This allows for high speed acquisition, which, although contrast is still a limiting factor, makes brightfield a common technique for studying fast cellular dynamics.

1.1.3 Fluorescence microscopy

Fluorescence is a phenomenon occurring when a substance absorbs a photon of a particular energy and re-emits a photon of a lower energy. The first person to report the phenomenon of fluorescence is considered to be George Stokes who, in his 1852 paper, observed the emission of visible light from substances under UV excitation [11].

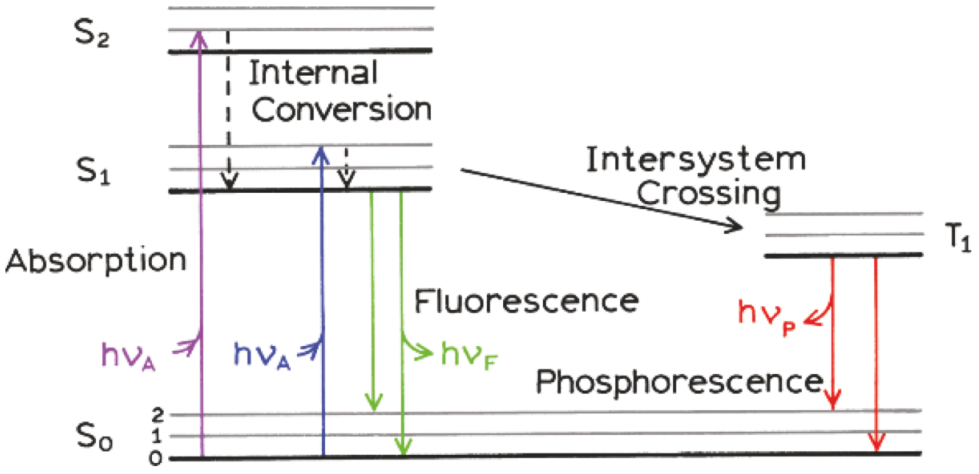

FIGURE 1.4: Jablonski diagram illustrating the process of fluorescence. The absorption of a photon causes excitation of an electron in the ground singlet state to an excited singlet state. It then undergoes non-radiative decay to the lowest excited singlet state, where it remains for a short amount of time (nanoseconds) before decaying back to the ground state while emitting a photon. Reprinted from reference [12] with permission from Springer Publishing.

The term fluorescence was coined by Stokes from the mineral fluorspar from which he observed the emission of light.

The luminescent phenomena of fluorescence and phosphorescence are most commonly described using a Jablonski diagram 1.4 which details the transitions of electrons between ground and excited states. The singlet electronic ground and first states are denoted as S_0 and S_1, respectively and the first excited triplet state T_1. Each of these energy levels has a set of vibrational states denoted 0,1,2 etc. When a fluorescent molecule absorbs a photon with equal energy gap, it is excited into a vibrational energy level of S_1. From here, the electron undergoes internal conversion into the lowest excited singlet state, losing some energy non-radiatively in the process. The electron stays here for a period of time typically in the nanosecond regime. This time is known as the fluorescence lifetime [12]. The system can relax from this state by emission of a photon, returning the molecule to its ground state [13]. Due to loss of energy via internal conversion, the energy of the photon emitted is less than the energy required to excite the fluorophore hence the emission wavelength is longer than the excitation wavelength. This is a phenomenon known as the Stokes shift as discovered by George Stokes in 1852 [13] [11].

Similarly, phosphorescence occurs when a material absorbs a certain wavelength of light and is promoted to the first excited triplet state via inter-system crossing. This is a "forbidden state" and as a result it takes significantly longer for excited molecules in the excited triplet state to decay back to the ground state. The mechanism by which photons are emitted via the triplet state is phosphorescence. Phosphorescence can be distinguished from fluorescence by its significantly longer lifetime and larger Stokes shift.

Fluorescence exhibits a number of general characteristics. The first is in the excitation and emission spectra of the fluorescence molecule. Fluorescence excitation spectra describes the range of wavelengths (or energies) over which a molecule can become promoted to S_1 as a function of probability. Similarly, the emission spectra of a fluorescent molecule describes the wavelengths over which the molecule is likely to emit photons. A general property of a molecule's fluorescence spectra is that emission spectra are typically independent of excitation wavelength - this is known as Kasha's rule [13]. Due to this process of internal conversion, the emission wavelength of a fluorophore is always longer than its excitation wavelength [13] (except in the case of two-photon excitation). A further important property in fluorescence is the fluorescence quantum yield. This is the ratio of absorbed photons to emitted photons and is often used to describe the brightness of a particular fluorophore. Another property used to describe fluorescent molecules are their fluorescence lifetimes. One advantage to using the fluorescence lifetime of a molecule to describe its fluorescence properties is that this is an absolute value, whereas fluorescence intensity is dependent on several properties such as excitation intensity and detector sensitivity [12].

A particularly important property of a fluorophore used in microscopy is its photostability. When continuously illuminated with light, a fluorophore will go through a finite number of excitation and emission cycles before the number of ground state molecules is diminished due to irreversible photochemical damage [14]. After this time, the fluorophore can no longer participate in the excitation-emission cycle and the fluorophore is "bleached". This can be a problematic property of fluorophores, particularly in long-term fluorescence measurements and quantitative measurements of fluorescence intensity.

In situations where excitation of an intrinsic fluorophore, such as tryptophan or

tyrosine [15], is not possible, fluorescence microscopy techniques are dependent on suitable extrinsic fluorophores which can be used to tag bio-molecules. Fluorescent labels can be split broadly into three categories - fluorescent molecules, fluorescent proteins and fluorescent nanoparticles. Fluorescent molecules, often referred to as fluorophores, are typically 1-2 nm in size and are available with a range of different excitation and emission wavelengths. These are one of the most popular choices for fixed cell imaging. These can include the families of fluorescein, rhodamine and cyanine [16]. Fluorescence can be applied to microscopy by labelling cellular components with dyes using e.g. antibody labelling (which will be described in more detail in section 1.3) to identify and distinguish sub-cellular components such as the cell membrane, nucleus and cytoskeleton to name just a few. Labelling of specific cellular components with fluorescent dyes has allowed the study of cellular processes over time and means that morphological changes can be observed, such as mitosis [17]. Other dyes are inherently sensitive to the cell environment. This includes dyes such as propidium iodide (PI), a DNA/chromosomal stain, and DiI, a lipophilic stain, which are specific to a particular cellular region - in this case, nucleus and membrane respectively - and thus can be used without pre-conjugation to antibodies and in both live and fixed cell imaging.

Fluorescent probe technology was further improved by the discovery of the green fluorescent protein (GFP) by Osamu Shimomura in the jellyfish *Aequorea victoria* in 1962 [18]. Using samples from this jellyfish, Shimomura was able to isolate fluorescent proteins from the jellyfish's fluorescent organs. Later, Douglas Prasher was able to study the gene within the jellyfish responsible for encoding GFP and reported its sequence, allowing the expression of GFP in other organisms [19]. Since this time, much research has been conducted in the field of fluorescent proteins, allowing the creation of a rainbow of photoproteins allowing excitation and emission spanning across the visible spectrum and beyond [20]. Fluorescent proteins have a particular advantage in fluorescence microscopy as they are expressed by the cell - meaning that, following genetic modification, no further labelling of cells has to take place. Fluorescent proteins have transformed live cell imaging where fluorescent probes have been historically limited due to the lack of fluorophores able to penetrate and label live cells.

Finally, fluorescent nanoparticles such as semiconductor quantum dots (QDs) offer

a highly stable solution for fluorescence imaging - these will be discussed in detail in section 1.3.

The discovery of fluorescent biomarkers dramatically improved the field of optical microscopy. Fluorescence is a useful property in microscopy as it can be more sensitive and specific than absorption and reflection. The application of fluorophores has also made it possible to identify sub-cellular components with a high degree of specificity. These advantages have lead to fluorescence microscopy becoming one of the most widely used techniques for imaging biological specimens.

The two most common modes of fluorescence microscopy are widefield fluorescence microscopy, in which the whole field of view is illuminated and detected simultaneously, and confocal microscopy, in which a single point or line of the specimen is imaged and then the specimen is scanned.

The basic principle of a widefield epifluorescence microscope is shown in figure 1.5 and can be described as follows: light of a wavelength specific to the excitation wavelength of the fluorophore is emitted from a light source and passes through various optics to reach the specimen plane in Köhler illumination. The excitation light is reflected by a dichroic mirror into the objective lens where it is collimated onto the sample plane. Subsequent fluorescence emission from the specimen is collected by the objective lens, transmitted by the dichroic mirror and focused onto a camera at the intermediate image plane by a tube lens. A longpass filter is placed before the camera (or in a filter cube alongside the dichroic) to ensure that only fluorescence is detected [21].

This technique, where both the excitation and emission light pass through the same objective lens, is known as epifluorescence and can be applied to both widefield and confocal methods [22]. In contrast to epifluorescence, transmission fluorescence is a technique in which excitation light is transmitted through the sample to be collected by the objective lens, and fluorescence emission is carefully separated from excitation light by a series of excitation and emission filters. However, this configuration can often lead to lower image contrast, as there is a direct light path from excitation source to detector.

In widefield microscopy, the whole field of view is bathed in excitation light and as a result the whole field of view is illuminated and detected simultaneously. In thick

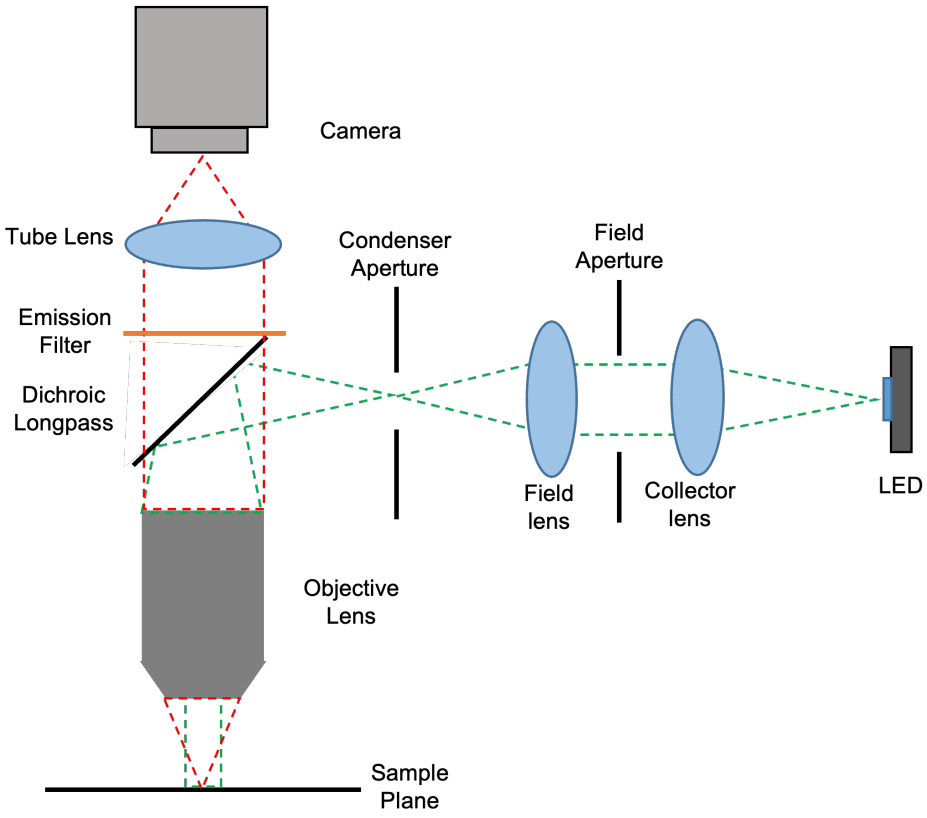

FIGURE 1.5: Schematic of an epifluorescence microscope set up. Excitation light is shown in green and fluorescence emission in red.

samples, this means that out-of-focus fluorescence from parts of the specimen outside of the focal plane are present, making the specimen appear less sharp and obscuring the resolution of features within the focal plane. It is difficult to tell how deep in a sample the fluorescence originated from, hence widefield microscopy is best applied to thin specimens. Widefield fluorescence microscopy is excellent for producing 2D images of specimens with high temporal resolution as the entire field can be captured at once. In practice, the resolution of a widefield microscope with high-NA objective lenses is approximately 230 nm laterally and 800 nm axially, which is not enough to resolve many biological structures [23].

To counteract some of these issues, the confocal microscope was invented by Marvin Minsky in 1957 [6]. Minsky recognised that in order to obtain a three-dimensional visualisation of a biological specimen, each image plane must be thin enough to remove the out-of-focus blur inherent in widefield imaging. His solution to this problem was to use a pinhole in front of the detector to block all out-of-focus light. Since its invention, many improvements to the confocal microscope have been put in place to

develop it into the commercial laser scanning confocal microscope in use today, such as a laser source and the use of scanning mirrors to move the laser across the specimen [24].

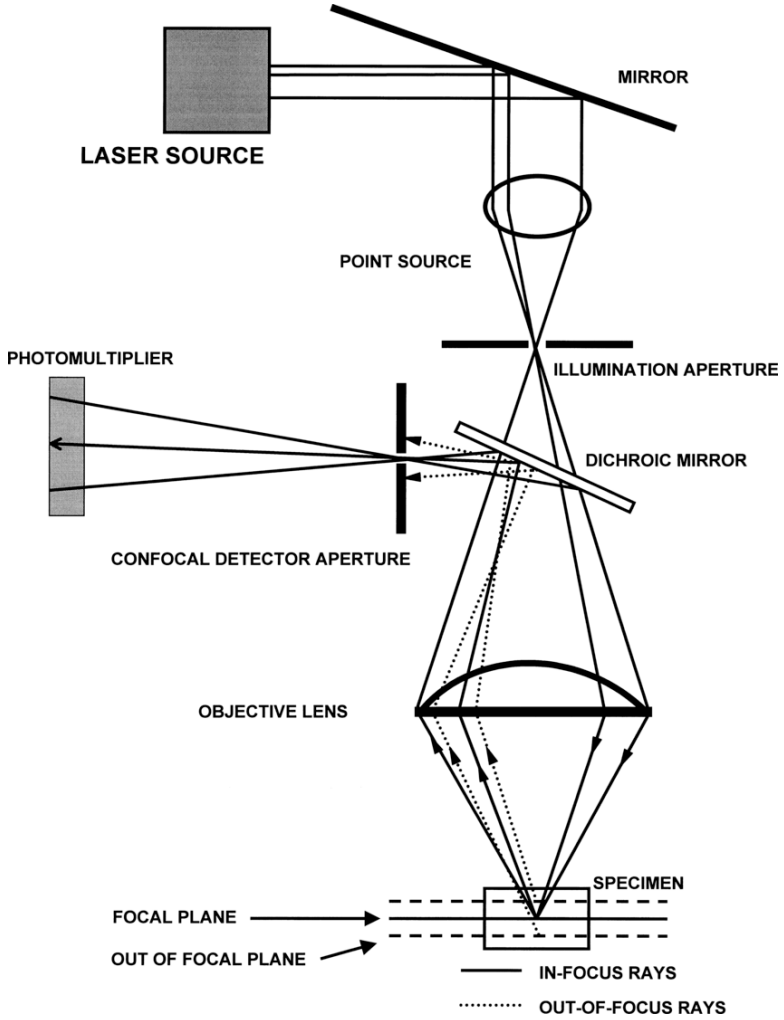

FIGURE 1.6: Schematic of a confocal microscope. Reproduced with permission from Springer Nature [25].

A schematic of a confocal laser scanning microscope is shown in figure 1.6. The principle of confocal laser scanning microscopy is as follows: excitation light from a laser source is reflected through a series of mirrors and is focussed onto the specimen plane at a point by the objective lens. Although not shown in this diagram, confocal microscopes typically make use of galvanometer scanning mirrors and these are placed between the dichroic mirror and objective lens to direct light to the specimen. Typically, two mirrors are used which each control the position of the laser on the specimen in the x and y directions and these mirrors work together to scan the laser point across the specimen in a pattern known as a raster scan to generate an image point by

point. As the laser is scanned across the specimen by the galvo scanner, fluorescence emitted from points of the specimen in the same focal plane are focused at the detector pinhole aperture. The fluorescence emission that occurs at points above and below the focal plane of the objective is minimised by the pinhole, which mainly transmits fluorescence originating from the focal plane in the specimen. The images produced by scanning across a particular lateral plane of the specimen are called optical sections and allow thin axial sections of the specimen to be acquired without physically slicing it [6]. Optical sectioning can be done across successive focal planes in the sample by moving the stage or objective lens axially to produce z-stacks from which 3D images can be made. Advantages of the confocal microscope include reduced blurring of the image due to the rejection of out-of-focus fluorescence, better contrast when imaging thick specimens [26], improved signal-to-noise ratio over widefield techniques [27], possibility of xy-scan over wide areas for imaging of larger specimens and inclusion of optical sectioning which can give details about internal structure [6]. In theory, the use of a pinhole in the confocal microscope increases lateral resolution by a factor of 1.4 [24], however this resolution improvement is rarely realised in practice as when the size of the pinhole is reduced, there is a trade off between resolution and signal strength as the number of photons reaching the detector is reduced [28]. The main disadvantage of the confocal laser scanning microscope is the scanning speed, taking for example several minutes to hours to image the entire volume of a specimen, depending on its size [28]. This makes confocal microscopy generally unsuitable for studying fast cellular dynamics in comparison to widefield techniques. The thickness of specimens suitable for imaging with confocal microscopy is typically limited to a few tens of microns, however this has been overcome by techniques such as use of the Mesolens which can image specimens up to 3 mm in thickness [29]. Another potential disadvantage of the confocal microscope is phototoxicity due to the highly localised laser spot, however this can be reduced by increasing the scanning speed or decreasing the laser power [28].

Another type of confocal microscope uses a spinning Nipkow disk, which is an opaque wheel perforated by a spiral of rectangular holes. This disk was invented by Paul Nipkow in 1884 for television cameras before being applied to confocal microscopy in 1968 [30]. These holes generate a raster scanning pattern where excitation light is

projected onto the disk, with only light passing through the hole reaching the specimen, and subsequent fluorescence passing through the same holes to reach the detector. Because of the multiple laser beam spots and short time a sample is exposed to them, spinning disk confocal microscopy can reduce photobleaching compared to laser scanning. Whilst the multiple beams used in this technique overcame the speed disadvantage of single beam scanning confocal microscopy, with an acquisition rate of 10 frames per second or more [31], disadvantages include requirement of high precision pinhole placement, problems with scattered excitation light inside the detection system [32] and cross-talk between pinholes.

1.1.4 Ultraviolet microscopy

After Abbe's theory of the resolution limit in light microscopy was published in 1873 [7], it became clear to scientists that a higher image resolution could be achieved by using a shorter wavelength of light. Whilst Abbe and Carl Zeiss pursued the improvement of spatial resolution by using high NA lenses, it was August Köhler who pursued the use of ultraviolet (UV) wavelengths in microscopy [33]. In 1904, Köhler published his first work describing a UV microscope constructed completely from quartz and calcium fluoride lens elements to allow UV transmission [33, 34]. Emission of UV light was obtained using an electric spark of cadmium and magnesium with peak wavelengths of 275 nm and 280 nm respectively. Shortly after its development, this microscope was used by researchers Ernst and Wolbach of Harvard Medical School to image bacteria [35]. Here, the authors were able to observe structures within the cell with only UV light without the need for staining. The observation of bacteria and other biological specimen using UV microscopy remained popular throughout the first half of the 20th century and in the 1930s, the wavelengths used in UV microscopy were reduced down to 250-270 nm to coincide with the absorption of nucleic acids at these wavelengths [33]. Using the absorptive properties of nucleic acids, researchers were able to measure the distributions of nucleic acids throughout cellular specimens [33]. It was also during his development of the UV microscope that Köhler first noticed the emission of fluorescence from specimens irradiated with UV light, which would go on to become the first use of fluorescence microscopy [33]. Many molecules within biological samples fluoresce at these wavelengths, such as the aromatic amino acids

tryptophan and tyrosine which have strong absorption peaks at 280 nm and emission peaking below 400 nm [13]. This has been demonstrated previously by studies using 280 nm to excite fluorescence from tryptophan protein crystals [36, 37].

Deep-UV microscopy made a further resurgence at the beginning of the 21st century owing to new developments in UV optics and light sources [33]. Most notably was the work done by Benjamin Zeskind in his 2007 publication [38, 39]. In this work, Zeskind developed a deep-UV microscope using quartz optical elements and a weakly emitting 1 mW light-emitting diode (LED) to provide 280 nm illumination. Zeskind identified the ability of this wavelength of light to provide quantitative information about the cell - based on the Beer-Lambert law of absorption, in a deep-UV transmission image, the intensity of a particular pixel and the intensity of the same pixel in a blank field of view together determine the optical density of the specimen. Using this theory together with the already established technique of using 260 nm/280 nm to measure nucleotide absorption [33, 40], the authors were able to determine the mass of protein and nucleic acid contained within each pixel of cell images. The authors showed that by using brightfield microscopy at a wavelength of 280 nm, images of cells provided sufficient image contrast, thanks to absorptive elements at this wavelength, to distinctly identify cell nuclei, cytoplasm and membranes without the need for stains. The authors also investigated autofluorescence imaging of tryptophan within cells at this wavelength. By using these images and the mass of the known proteins within the cell, they calculated the quantum yield of the fluorescent protein within each pixel.

Further work by Frederick Jamme sought to implement deep-UV microscopy using a synchotron radiation source allowing wavelengths down to 180 nm [41]. Jamme *et. al.* developed a deep-UV microscope coupled to a synchotron excitation source, allowing tunable excitation from 180-600 nm [41]. This was an inverted epifluorescence design using a Zeiss Ultrafluar objective lens for UV transmission. Using this design, the authors were able to acquire transmission and autofluorescence images of living cells with a wavelength of 275 nm. A second paper by Jamme *et. al.* built upon this work by using the synchotron source combined with deep-UV multispectral imaging to observe the distribution of fluorescent molecules spatially across the living HeLa cells and distinguish between sources of fluorescence within the cell [42]. The group

then went on to identify several autofluorescent compounds occuring within cells, including tryptophan,tyrosine, pyridoxine, collagen, elastin and NADH. The area of a live cell was then investigated to determine the distributions of tryptophan and tyrosine throughout the cell. The latest work by this group use the synchotron deep-UV microscope to detect calcium oxylate in kidney biopsies to aid in the diagnosis of renal oxalosis, a cause of kidney failure [43].

In addition to standard microscopy techniques, there have also been examples of time-resolved imaging including fluorescence lifetime imaging microscopy (FLIM) with deep-UV excitation. In general, time-resolved techniques are of interest due to their decreased sensitivity to factors such as photobleaching and fluorophore concentration when compared to steady-state techniques [44]. Advantages in using deep-UV wavelengths for FLIM include the ability to excite intrinsic fluorophores tryptophan and tyrosine [44], the former of which is inherently sensitive to its solvent and its local environment and can therefore be used as a probe [45]. FLIM also affords the opportunity to better separate scattered excitation light from fluorescence using time gating [45]. Implementations of UV-FLIM include confocal imaging using a frequency-tripled Ti:Sapphire laser [45] or a 266 nm emitting laser [44], although these techniques both required use of a quartz objective lens to deliver light to the specimen plane. Further work by de Jong et. al. showed that it was possible to adapt a commercial FLIM microscope for UV excitation by using a UV LED emitting at 270 nm as an excitation source in transmission fluorescence mode [37], negating the need for further quartz optics.

In more recent years, several papers on deep-UV microscopy have been published using Microscopy with Ultraviolet Surface Excitation (MUSE). MUSE was developed in 2017 by Farzad Fereidouni and is a technique which uses UV light to excite fluorescence from the surface of tissue [10]. MUSE uses oblique illumination to excite fluorescence from the sample, removing the need to replace existing microscope optics with quartz or implement a quartz objective lens to transmit light to the specimen (figure 1.7). In this work, the optical system comprises of one or more UV LEDs and a quartz sample stage which allows transmission of the UV light to the specimen. Oblique UV illumination excites the specimen, bypassing the objective lens, which, because it cannot transmit deep-UV light, also acts as an emission filter. The use of

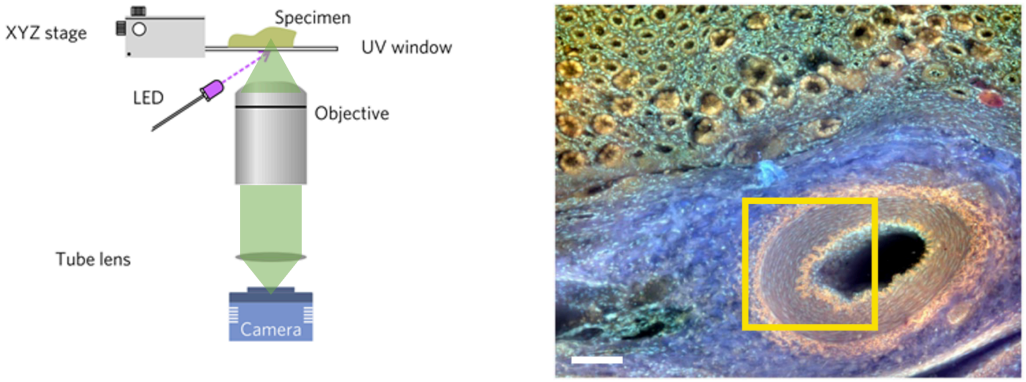

FIGURE 1.7: Left: Schematic diagram of MUSE microscope. Right: Example MUSE image of thick kidney tissue labelling using rhodamine and Hoechst and excited at 280 nm. Adapted with permission from Springer Nature License: [10].

oblique illumination also reports the advantage of creating a shadowing effect on the tissue, improving the visualisation of surface topography. MUSE also reports a unique advantage of imaging with light of wavelengths below 300 nm, which is surface limited excitation due to the short penetration depth of UV light (a few μm in depth). This results in images with significantly improved contrast due to the reduction of out of focus fluorescence from within the tissue.

In addition to this, MUSE also uses a wide range of conventional fluorescent dyes, namely DAPI, rhodamine, Hoechst, PI and eosin, which are compatible with 280 nm excitation as this allows the dye molecule to be excited to S_2, followed by non-radiative relaxation to the first excited state before emission of a photon. In this original work, the authors use these dyes to stain tissue sections and compare MUSE imaging with fluorescent dyes to more traditional H&E staining. Since then, MUSE has been applied to several studies: In 2018, MUSE was used in dermatopathology to provide a fast non-destructive method to produce diagnostic quality images of skin biopsies [46], with MUSE acquisition taking only a few minutes compared to the overnight processing of H&E slides. MUSE has also been evaluated in breast cancer applications using water immersion to identify tumour margins [47]. In this work, the authors showed that MUSE can provide image quality that matches that of typical H&E sections but its applications in clinic use are currently limited by the ability of clinicians to analyse MUSE images.

As a technique for deep-UV imaging, MUSE has certain limitations. The use of

oblique illumination requires that there is substantial distance between the objective lens and sample in order for the illumination light to reach the sample. This restricts the objectives to long working distance, low magnification, low NA lenses, and hence the resolution is poor. The limited penetration depth of the UV light also restricts samples to those that are either thin and transparent, or thick tissues in which only the surface is of interest [10].

A more recent development in MUSE has come from the group of David Mayerich [48]. Whilst MUSE has previously been limited to the surface of tissue due to the limited penetration depth, this is overcome by using Microscopy by milling with ultraviolet excitation (MUVE). Three-dimensional MUVE has applications in the study of many chronic conditions such as cancer and neurodegenerative diseases which are difficult to explore using traditional 2D histology. In this work, the authors use the oblique UV excitation detailed in previous MUSE papers, but with the addition of a microtome to shave off the top layer of tissue after acquisition. This allows 3D reconstructions of tissue samples. Using this technique, the authors were able to create 3D reconstructions of mouse brain such as thalamus and the cerebral cortex with comparable speed to widefield imaging. However, as this technique uses a microtome to shave away layers of tissue during image acquisition, this results in destruction of the specimen and as a result is more disruptive than other 3D methods such as optical sectioning.

MUSE has also been extended from using traditional histological stains to using immunofluorescence. The use of antibodies against tissue targets allows for specific labelling of proteins within the tissue and allows multiplexing with multiple targets and dye wavelengths. This has been demonstrated in a 2020 paper which uses quantum dot-conjugated antibodies to label tissue [49]. Further work has been done using off-axis illumination in deep-UV imaging. As MUSE removes the need for expensive quartz optics, this makes the technique much more accessible. Further work using oblique illumination has shown the possibility to develop an ultraviolet microscope using off-the-shelf optical components, allowing applications in point-of-care diagnostics [50].

Alongside the use of UV-excitable dyes in MUSE, label free deep-UV imaging has also become popular in recent years. In particular, label free imaging is advantageous

in haematological analysis as it provides fast, quantitative information of blood cells. In 2020, Ojaghi *et. al.* developed a brightfield system with a broadband UV light source which could differentiate between white blood cells, characterise red blood cells and identify platelets, all with subcellular resolution [51]. This methodology was significantly faster than standard white blood cell analysis which currently requires expensive and laborous methods. Notably, this technique was assessed by a panel of haematologists who near-concurrently diagnosed blood conditions using this technique compared to gold-standard methods. This was quickly followed by a second study in which the authors use UV absorption based mass mapping to quantify haemoglobin within red blood cells [52]. This used 4 wavelengths, 220, 260, 280 and 300 nm to create images using molecules within red blood cells which absorb at different wavelengths. The authors compared this technique to commonly used techniques for haemoglobin quantification and found good correlation, confirming the accuracy of deep-UV microscopy to quantify red blood cells. Both of these studies enable high-resolution label-free imaging of blood cells, enabling fast and cost-effective clinical use.

1.1.5 Live cell imaging of mammalian cells

Whilst imaging fixed cell specimens allows a detailed view of the complex internal structure of a cell, this provides only a snapshot in time and the ability to observe dynamic processes within cells is vital to the understanding of cell function. However, imaging mammalian cells under a light microscope whilst ensuring their normal functions are not affected adds an extra layer of optimisation onto imaging apparatus and techniques [53]. It is first critical to consider the environmental conditions surrounding the cell whilst it is being imaged. In cell culture conditions, the cell environment is carefully controlled to a specific temperature, humidity and CO_2 content. To transfer this to a microscope stage can be difficult and most commonly uses an enclosure which encompasses the entire microscope. Within this enclosure, temperature, humidity and CO_2 can be controlled to preserve cell viability over long term imaging experiments [53]. Other options are stage-top incubators, which work in the same way but within a smaller design which sits on top of the microscope stage. Simpler

apparatus includes heated stage plates which work to keep the cells at 37°C but do not have active humidity or CO_2 control.

Secondly, the chamber that the cell is imaged within is an important consideration. To achieve the best viability, cells should be imaged within culture media containing the sufficient nutrients to allow them to behave as normal. To allow this, live cell imaging is typically carried out on an inverted microscope rather than upright. This way, cells can be grown onto the bottom surface of a live cell imaging chamber, such as a dish, filled with cell media [54]. Cells are then imaged from below using the objective lens, where the bottom surface of the dish acts as a coverslip.

One of the most important considerations when using live cell imaging is phototoxicity to the specimen caused by illumination light. Phototoxicity in cells under fluorescence excitation is generally thought to be due to the release of reactive oxygen species (ROS) [55] as a fluorophore photobleaches. ROS react with a large number of easily oxidisable components within the cell such as proteins, nucleic acids and lipids, leading to cell death [56]. As a result, the only way to preserve cell health whilst imaging is to reduce the light dose that the cell receives as much as possible. However, doing so directly impairs image quality because of reduced fluorescence signal - in fact, fluorescence microscopy of live cells is often a trade off between acquiring images with sufficient signal to background ratio and damaging the specimen with light [53, 56]. Another method to decrease photobleaching and phototoxicity is to starve the specimen of oxygen such that molecules entering the triplet state cannot interact with them to produce ROS [54, 57]. However, this is not ideal for living biological specimens that require oxygen to survive.

For this reason, there have been many studies recommending the appropriate control of light exposure in live cell imaging. One such study in 2007 recommended the use of controlled light exposure microscopy (CLEM) [56]. In this technique, the authors use a confocal laser scanning system and illuminate the specimen inhomogenously - using more light only in areas of the specimen which require it. Here, the excitation light dose is reduced in bright areas of the specimen and increased in dim areas, controlled by a feedback system between the illuminator and detector. Using this system, the authors were able to greatly reduce photobleaching and the formation of ROS by eight-fold in HeLa cells.

It has been suggested that pulsing the excitation light, as opposed to continuous exposure, results in a dramatic reduction in phototoxicity [57]. In their 2016 paper, Boudreau *et. al.* [57] used continuous and pulsed confocal laser light on the nanosecond and microsecond timescales to investigate the effect of limiting the light dose to the specimen, using cell protrusion rates and mitochondrial morphology as a marker for phototoxicity. Using this approach, they were able to show that by using rapid line scanning confocal, cells protruded at double the rate of that of slow scan settings. This work was shortly followed by a report by Laissue *et. al.* [58] which outlined suggested assays to assess phototoxicity in live samples and pointed out that phototoxicity markers are entirely species-dependent. Further to this, a study by Mubaid *et. al.* [59] concluded that a combination of low excitation light intensity and long camera exposure times resulted in significantly reduced photobleaching to GFP. This reduces phototoxicity in cells but does not compromise image quality seeing as the overall light dose to the specimen remains the same. However, upon further investigations in 2020, the group realised that much of the phototoxicity associated with short exposure times and high LED power was actually due to the issue of illumination overhead (IO) [55]. IO occurs due to a lag in either USB control or mechanical shuttering, meaning that cell specimens are being exposed to considerably more light than intended. TTL triggering is the only form of acquisition control which does not significantly increase the time specimens are exposed to light and as a result, this method should be used to control image acquisition to best prolong cell health. When using USB control, longer exposure times with lower excitation power should be used as with longer exposures, the percentage contribution of IO is decreased [55].

Although visible wavelength light has been used successfully in live cell imaging with little significant effect on viability, it is well documented that UV irradiation can be a contributing factor to cell death. The effects of UV irradiation on cells is a much studied topic due to its implications in skin cancer and other diseases [60, 61]. UV light is typically separated into three classes based on wavelength range and level of damage to the human cell. UVA (315 - 400 nm), UVB (280 - 315 nm) and UVC (200 - 280 nm). UVC, although shielded by the earth's atmosphere [62], is by far the most toxic to biological specimens [60]. The main target of deep-UV irradiation in live cells is DNA [60, 63], primarily due to the peak absorption of DNA occurring at 260 nm. One of

the most cytotoxic DNA lesions formed by deep-UV light are cyclobutane pyrimidine dimers (CPDs) which cause two adjacent DNA bases (typically thymine and cytosine) to covalently bond, destroying normal base pairing [60, 61, 63]. This type of DNA lesion is expected to cause around 75% of UV-induced photodamage products, with the other 25% caused by 6-4 photoproducts [60, 61]. 6-4 photoproducts are mutations causing DNA damage via hydrogen bonding of two adjacent bases within a single DNA strand, but cause more distortion to the DNA structure [64]. As well as this, photoproducts such as reactive oxygen species and free radicals are formed, which can induce damage to cell structure and components as well as causing oxidative stress [62].

Ultimately, DNA damage is significantly increased when irradiated with wavelengths around the absorption peak of DNA (∼260 nm), which was studied in detail by Masuma *et. al.* in 2013 [60]. In this study, the authors compared DNA damage and CPD formation of cells irradiated with 4 wavelengths of light: 250, 270, 290 and 310 nm. To determine the toxicity of these wavelengths, the authors quantified the number of viable cells, and the number of CPDs formed after irradiation with an equal dose of each wavelength of UV light. They also investigated the median lethal dose (the dose required for killing 50% of cells) and the DNA-repair ability of cells irradiated with each wavelength of light. The authors found that cell viability was significantly reduced following exposure to 250, 270 and 290 nm light, with 260 nm light causing the highest reduction in cell viability at high doses. The formation of CPDs was highest at 250 and 290 nm, with 270 nm irradiation causing less CPDs to be formed. Perhaps most interestingly, cells irradiated with 250, 270 and 290 nm light actually show a high recovery rate compared to cells irradiated with 310 nm light, which did not recover at all. This study concluded that, whilst wavelengths closer to the peak wavelength of DNA do cause a decrease in cell viability, cells are able to recover more from this than irradiation at longer UV wavelengths.

Despite the obstacle of DNA damage, there have been successful attempts at imaging live cells using 280 nm light. Early work on UV imaging necessitated long exposure times. In 1950, Walker and Davies attempted live cell UV imaging with wavelengths ranging from 248 to 312 nm, necessitating 2.4 second exposures every 12 seconds [65]. This level of exposure resulted in major changes in the nucleus, with only

8 images being acquired before the onset of cell damage. Since then, there have been advances in light sources that have dramatically reduced the exposure time needed to acquire images. In work by Benjamin Zeskind [38], low intensity 280 nm light and 100 ms exposures at 1 minute intervals were used to image dynamic cellular processes including mitosis and motility. With this light dose, they are able to image over a period of 6 hours without visible damage to cells or any visible changes in cell dynamics or structure. However, when tagging cells with a marker for DNA damage and irradiating with the same light dose, they found evidence of DNA damage after 45 minutes. This study confirms that, although damaging to cells, 280 nm light can be used for short-term imaging of cells as long as exposure conditions are carefully controlled.

1.2 Light-Emitting Diodes

1.2.1 LED principle

A light-emitting diode (LED) is a semiconductor device which emits light when a current passes through it. The path to the development of LEDs began with Henry Round's discovery in 1907 [66], in which he observed the emission of light after the application of a current to the semiconductor silicon carbide (SiC) [67], a phenomenon now known as electroluminescence.

An LED is formed using a p-n junction, a semiconductor configuration with a p-type (positively charged) and n-type (negatively charged) region in contact with each other (figure 1.8) [68]. In the p-type region, the majority of charge carriers are positive (holes), and similarly in the n-type region the majority of carriers are negative (electrons). The area where the p-type and n-type regions meet is known as the p-n junction. The p-type and n-type materials in the p-n junctions are realised by the process of doping - a technique in semiconductor physics in which an impurity is added to the semiconductor material to alter the number of charge carriers present in the material, creating either a positive or negative overall charge [68]. This creates two energy bands - the conduction band, with an excess of electrons and the valence band, with an excess of holes.

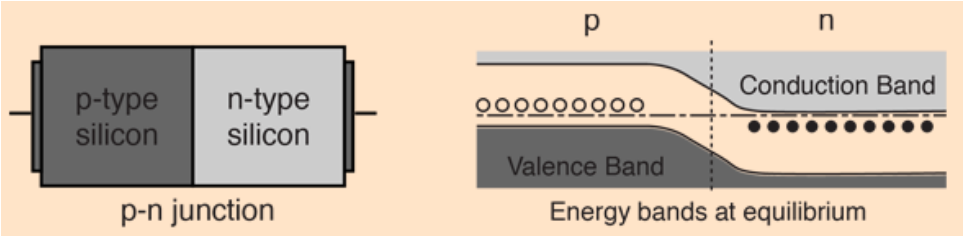

FIGURE 1.8: Principle of LED p-n junction. The semiconductor material is doped with impurities to create an n-type region and a p-type region, with excess charge carriers of holes and electrons, respectively. Reproduced with permission from [68].

Within the p-n junction, some of the free electrons in the n-type region diffuse across the junction and combine with holes in the p-type region, leaving behind positive ions in the n-type region. Similarly, holes in the p-type region diffuse across the junction and recombine with electrons in the n-type region, leaving behind negative ions in the p-type region. A charge builds up between these ions, creating what is

known as the depletion region. Coulomb force inhibits any further electron transfer unless assisted by applying a bias to the system.

LEDs have very strict biasing conditions. A reverse bias is applied to the LED from positive to negative. Here, the energy of the p-type region increases, making it more difficult for electrons to cross the depletion region and recombine with holes. Under this condition, no recombination events occur to allow the emission of photons.

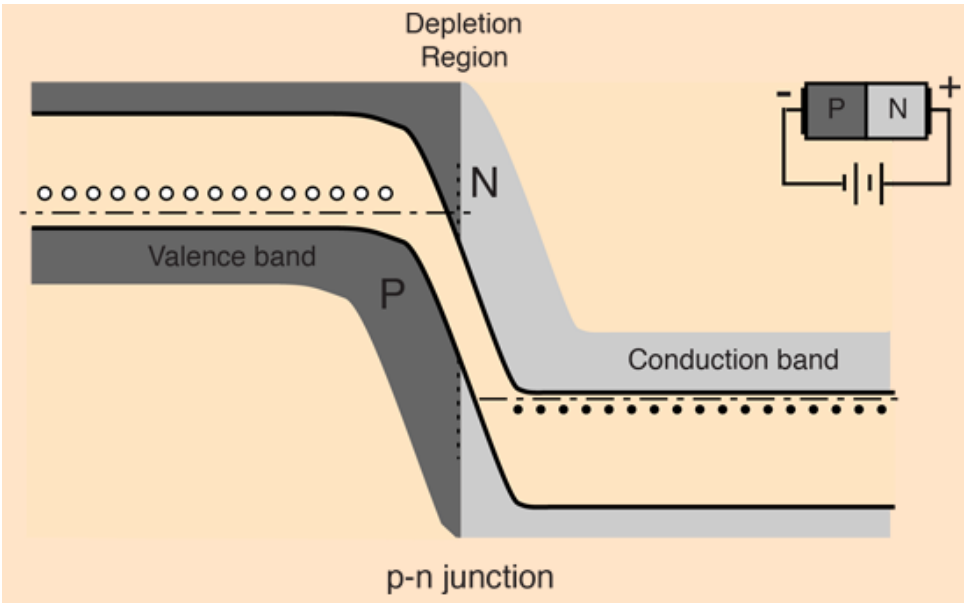

FIGURE 1.9: P-n junction in reverse bias. Reproduced with permission from [68].

Forward biasing is when a current is applied to the LED from negative to positive. In this condition, the energy of the p-type region decreases. Electrons in the n-type region of the material then find themselves at a higher energy than holes in the p-type region and are able to cross the p-n junction to recombine with holes. This creates a continuous forward current through the p-n junction.

Recombination of electrons and holes under forward bias causes emission of a photon by the mechanism of spontaneous emission. The wavelength at which light is emitted from the LED depends on the bandgap of the active region (i.e. the average energy between the conduction and valence bands) and hence the semiconductor material it is constructed from. The optical properties of LEDs will be described in further detail in the following chapter.

Nowadays, LEDs are used in a huge variety of applications across science and day to day life. Whilst a full review of these would be too in-depth for this thesis, a number

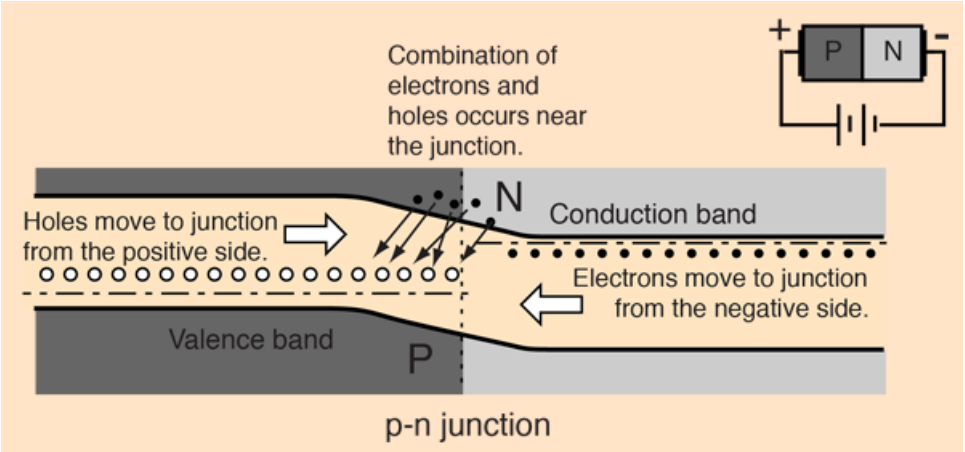

FIGURE 1.10: P-n junction in forward bias. Reproduced with permission from [68].

of these include lighting, electronic displays and communication [67].

1.2.2 Ultraviolet LEDs

LEDs emitting at wavelengths below 360 nm typically have AlGaN active regions [69, 70]. By alloying GaN with AlN, and controlling the aluminium content, the emission of AlGaN LEDs can be tuned to create photons emitting at wavelengths covering almost the entire UV spectrum (210 - 400 nm) [70]. A typical emission spectrum of an AlGaN LED with varying drive current is shown in figure 1.11 with a peak emission wavelength of 289 nm [69].

A known issue in AlGaN LEDs is additional emission at visible wavelengths. This is thought to be due to reasons such as electron overflow in the LED chip [71, 72, 73]. Electron overflow is when electrons from the active region of the LED chip escape from the active region into neighbouring layers, where they recombine with holes. The bandgap of these layers are often different to that of the active region, so radiative recombination yields photons of different wavelength. Electron-blocking layers are often added to overcome this problem but are hindered by the difficulty in doping AlGaN [70].

Alongside this so called "parasitic emission", other issues in AlGaN LEDs have been reported. When aluminium was first used as a semiconductor material in the 1960s [67], it was quickly realised that this was a "luminescence killer" because of its

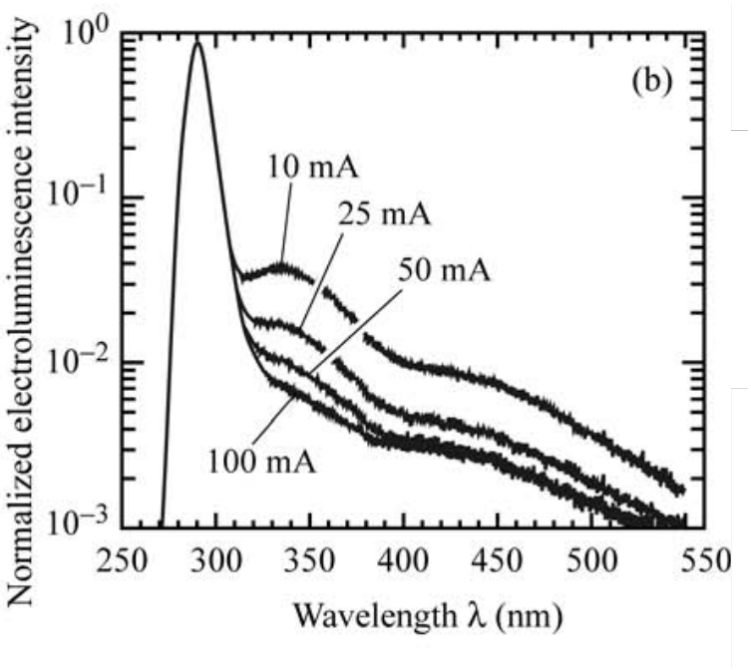

FIGURE 1.11: Typical AlGaN LED electroluminescence spectrum shown at varying drive current on a log scale. Reproduced with permission from [69]

high affinity to oxygen. This makes the incorporation of oxygen into AlGaN increasingly likely as the aluminium content increases in order to achieve lower wavelengths. This leads to a reduction in emissive efficiency, although this is often countered by sealing the chip in a nitrogen filled chamber. High power devices also produce higher levels of heat which must be removed to avoid excessively high junction temperature. More detail on how LED temperatures affects their optical properties will be covered in chapter 2.

A common way to measure the performance of an LED is via its external quantum efficiency (EQE). This is defined as [74]:

$$EQE = \frac{\text{number of photons emitted into free space per second}}{\text{number of electrons injected into the active region per second}} \tag{1.4}$$

and is typically given as a percentage. EQEs can be limited, for example, by light leaving the active region being reabsorbed by neighbouring layers of the LED in the case that the materials in these layers absorb at this wavelength [74]. In addition, total internal reflection can occur at the surface of the LED preventing photons from escaping the LED chip.

The EQEs of deep-UV devices are generally very low - the drop in the EQEs of LEDs emitting below 365 nm, marking the transition between InGaN and AlGaN materials, is noticable [69]. The first 280 nm LED was reported as recently as 2004 [71] and exhibited a radiant power of 0.85 mW at 20 mA and an EQE of just 1%. This is significantly lower than that of visible wavelength LEDs, or even that of near-UV emitting LEDs which display EQEs of up to 76% [70]. However, recent developments have shown vast improvements in the efficiencies of deep-UV LEDs, summarised in a recent review paper by Kneissl *et. al.* [70]. In recent years, LEDs emitting at a wavelength of 280 nm can reach EQEs of up to 20% and radiant powers in the 100 mW range [70] - the highest efficiencies in the family of AlGaN emitters [70]. Although these still have a long way to go before they reach the standard of their visible-spectrum counterparts, these LEDs now have properties which make them viable for use in fluorescence microscopy.

Deep-UV LEDs have already demonstrated a wide range of applications. A current interest in deep-UV LEDs (<300 nm) stems from sterilisation. Since deep-UV light is deeply absorbed by the earth's atmosphere, most biological organisms have not developed a defence mechanism to these wavelengths and as a result can be significantly damaged by exposure to deep-UV light (as covered in section 1.1.5) [70]. Deep-UV LEDs have previously been used for water disinfection [75], where it was shown that both 269 and 282 nm LEDs were capable of inactivating the bacterial spores *B. subtilis*. In this application, deep-UV LEDs offered a great alternative to traditionally used mercury lamps as they are easier to dispose of, are compact, have fast start-up times and are more durable [75]. In addition to sterilisation, deep-UV LEDs are advantageous in gas sensing applications. For example, 285 nm LEDs have been used to detect acetone in the breath [76] as this can be an indicator of metabolic conditions. In this work, the authors found that by using an LED source emitting at 285 nm and detecting the absorption of this wavelength through the breath, the acetone content could be detected with a precision of 0.4 parts per million volume.

With new, state-of-the-art 280 nm LEDs emitting with optical powers of 100 mW [70], it is hoped that the issue of limited optical power at the specimen plane in the application of fluorescence microscopy will be overcome. In fact, a prediction by Roland Haitz deemed "Haitz' Law" states that the amount of light generated by an LED would

increase by a factor of 20 every 10 years - this has proven to be a reliable forecast as LEDs have doubled in brightness every 2 years and performance is predicted to increase by 20% annually [77].

1.2.3 LEDs as excitation sources in microscopy

One of the key components of any optical microscope is a light source. Traditional light sources include broad-spectrum halogen lamps - still to this day, nearly all microscopes are equipped with a lamp for brightfield transmission imaging e.g. for locating samples before imaging [78]. Light sources for fluorescence microscopy, however, have some specific requirements. The light source must first have emission which overlaps in wavelength with the excitation spectrum of the fluorophore for imaging [77]. The light source must secondly have sufficient radiant power such that it is able to excite enough fluorescence from the fluorophore to produce an image. Thirdly, the light source must be sufficiently narrow in spectral emission such that it does not overlap in wavelength with the emission of the fluorophore and cause bleedthrough to the detector, reducing image contrast. The light source must also have an appropriate spatial profile such that can illuminate the specimen as homogeneously as possible, either by direct illumination or by the methods of critical or Köhler illumination as described previously.

Historically, mercury-vapour high-pressure arc lamps (HBO lamps) have been the most popular choice for fluorescence microscopy [77]. In fact, a system grew around the use of these lamps in which fluorophores for fluorescence microscopy were chosen specifically to match the excitation peaks of these lamps [77]. HBO lamps are characterised by high emission in the UV, blue and green, with very low intensity between these peaks. This makes the choice of fluorophore limited to those with excitation spectra which match closely to the peaks of the HBO lamp [77] whilst the other wavelengths of HBO emission require suppression via excitation filters to avoid noise and low image contrast. HBO lamps have a short life cycle, spanning around 300 h, and use must be carefully recorded to ensure that the lamp is not performing outwith its expected lifetime - mercury explosions can be dangerous and a risk to the surrounding equipment and users. Replacement of these lamps can be time consuming and disposal of mercury sources must be carefully controlled [79]. There is no mechanism

to control the intensity of the lamps outside of using neutral density filters and arc lamps take a significant time to reach full intensity ($\sim$ 30 mins) which means that any use of arc lamps must be pre-planned to allow sufficient time for the lamp to turn on. In addition to this, the lack of electronic control means that to limit the light reaching the specimen, mechanical shutters must be used which are the slowest of all light control mechanisms [55]. Arc lamps are also considered to be inherently unstable due to plasma oscillations and thermal runaway [66].

In comparison, light emitting diodes (LEDs) offer a cheap and stable alternative [77]. LEDs have long lifetimes, in the range of tens of thousands of hours. This means that they require limited maintenance, less time spent in replacing and do not generate as much waste. Compared to arc lamps, LEDs emit in spectral bands of a couple of tens of nm [74] which make them much easier to spectrally separate from fluorescence emission. LEDs are extremely versatile light sources, with emission wavelengths available from the deep-UV to the infrared, meaning that essentially every excitation wavelength for any chosen fluorophore or photoprotein is available. Perhaps one of the most appealing benefits of using an LED source is that its radiant power is directly proportional to drive current, allowing for adjustment of the radiant power (and hence intensity of light reaching the specimen) to be controlled using a variable power supply [80]. This is in stark contrast to arc lamps, in which intensity can be controlled only through the use of neutral density filters. LEDs can also be turned on and off as fast as electronics will allow [59]. This eliminates the need for warm up times, the time taken for shutters to be mechanically operated - allowing for fast switching between excitation wavelengths in multiplexing applications and efficient light control in live-cell time lapse imaging. LEDs are also inherently stable compared to arc lamps. A 2019 study by Mubaid *et. al.* compared the stability of LED sources, a metal halide lamp and a HBO lamp over short (1 min), intermediate (2.5 h) and long-term (300 h) time periods [59]. In all cases, the LEDs were found to be significantly more stable than both lamps.

One of the other advantages of using LEDs in fluorescence microscopy is the ease of introducing LED illumination to an existing microscope. This is typically done by coupling the LED to the epifluorescence port of the microscope using two methods - direct fit or via liquid light guide [66]. Since the use of LEDs in microscopy became

popular in the early 2000s, several informative papers have been published detailing how to implement these effectively in microscopy. For example, Albeanu *et. al.* in 2008 detailed a simple, cost-effective homemade LED illuminator which performed better than a xenon arc lamp [66]. A further 2015 paper by Bosse *et. al.* details a full procedure for installing an LED illuminator for microcopy, from LED unit assembly to aligning the epifluorescence pathway for Köhler illumination to driving the LED electronically [81].

1.3 Quantum Dots

1.3.1 Optical properties and advantages over fluorescent dyes

Quantum dots (QDs) are semiconductor nanoparticles exhibiting fluorescent properties. QDs are made of semiconducting materials such as CdSe or CdS and are typically between 2-10 nm in diameter. When the radius of the QD is smaller than the exciton Bohr radius (i.e. the average distance between the conduction band and the valence band) the energy bands in the QD become quantised according to quantum confinement [82]. The difference in band diagram between bulk semiconductors and semiconductor QDs is shown in figure 1.12b, with the valence bands and conduction bands of semiconductor QDs formed of many intermediate energy levels from which electron-hole recombinations are possible. When a QD absorbs a photon at the energy of (or above) their bandgap, electrons in the valence band are excited to the conduction band, leaving a hole behind. This creates an electron-hole pair, commonly referred to as an exciton [83]. Because of the Coulomb force acting on the exciton, the electron then decays back into the valence band and recombines with the hole, emitting a photon in the process.

The most common configuration of a QD is a core-shell type (figure 1.12a). QD cores are the nanoparticles themselves, with sizes of between 2-10 nm. A common strategy for enhancing the optical properties of QDs is by encapsulating the QD core in a larger energy bandgap material. By doing this, the electron-hole recombinations at the surface of the QD, which lead to non-radiative recombinations, are reduced. This can have the effect of increasing the quantum yield of the QD as more of the recombination events that take place will result in the emission of a photon [84]. In addition to improving optical properties, the addition of a shell can protect both the QD against environmental changes and the cell from being exposed to toxic materials such as cadmium.

QDs have many unique properties which make them advantageous over fluorescent dyes [85]. One of the most interesting properties of QDs is their size-dependent emission. As the size of the QD core increases, the confinement energy of the exciton decreases (figure 1.12b). As recombination events then occur over different energies, this results in both the excitation and emission spectra of QDs being size tunable.

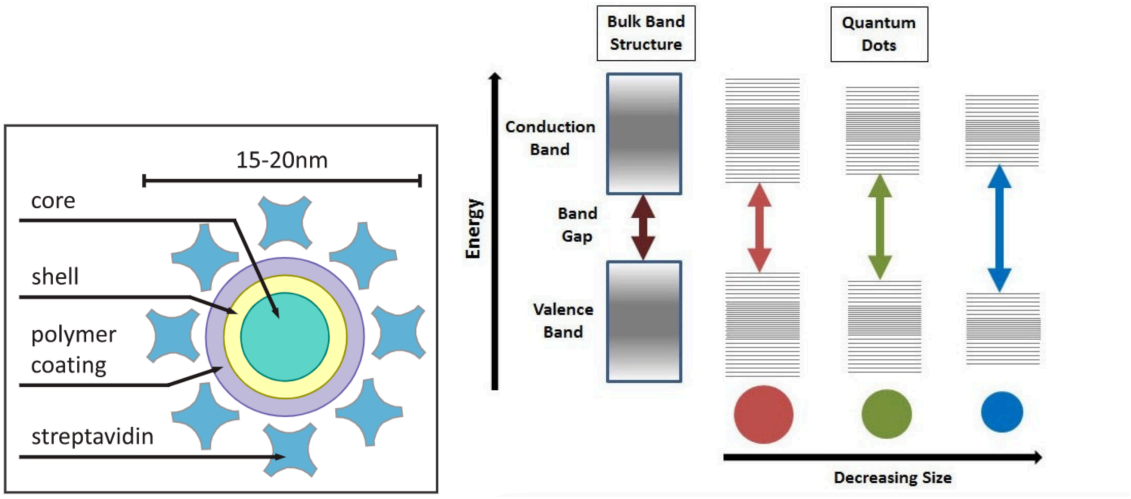

(A) QD composition

(B) QD energy levels

FIGURE 1.12: (a) Composition of streptavidin conjugated semiconductor QDs. Reprinted with permission from [49] The Optical Society. (b) Energy level composition of QDs. Reproduced from Sigma Aldrich with permission.

Another particularly interesting feature of QDs is their spectral characteristics. Because of their quantised energy bands, QDs have the ability to be excited at any wavelength below their semiconductor bandgap. This allows QDs to have a broad, continuous excitation spectrum (figure 1.14), unlike fluorescent dyes which excite in sharp peaks mirrored to their emission spectrum [12]. The emission spectrum of a QD is independent of its excitation wavelength [86]. This means that several sizes (therefore colours) of QD can be excited simultaneously with a single excitation wavelength, making QDs excellent for multiplexing applications.

The emission spectra of QDs also make them ideal for fluorescence imaging. Although QDs have a broad, continuous excitation spectrum due to their quantised energy levels, QDs emit in sharp spectral peaks. QDs emit with a typical FWHM spectral bandwidth of 20-30 nm [86], significantly smaller compared to fluorescent dyes such as DAPI which emit with a FWHM spectral bandwidth of close to 100 nm.

The sharp emission spectra of QDs is advantageous in multiplexing applications as spectral separation between differing sizes of QD is significantly easier. Moreover, the broad excitation spectrum of QDs allows a large effective Stokes shift to be obtained dependent on the desired excitation wavelength, minimising the risk of bleedthrough

of excitation light to the detector.

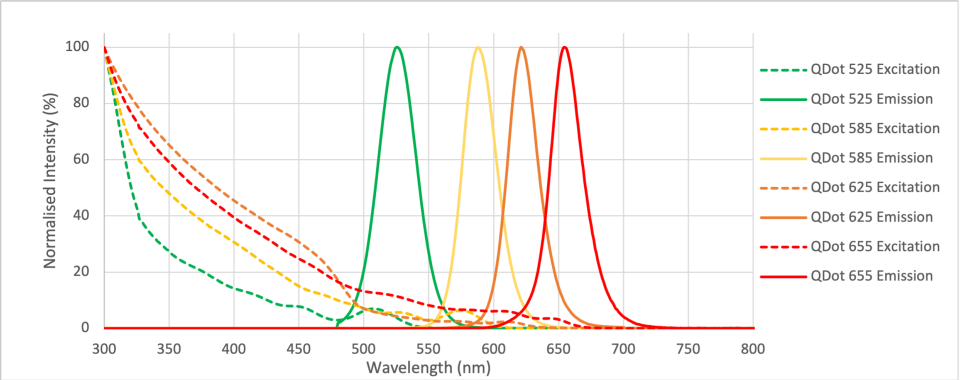

FIGURE 1.13: Excitation (dotted lines) and emission (full lines) spectra of commercial CdSe QDs of different diameters. As QD size increases, the emission wavelength increases.

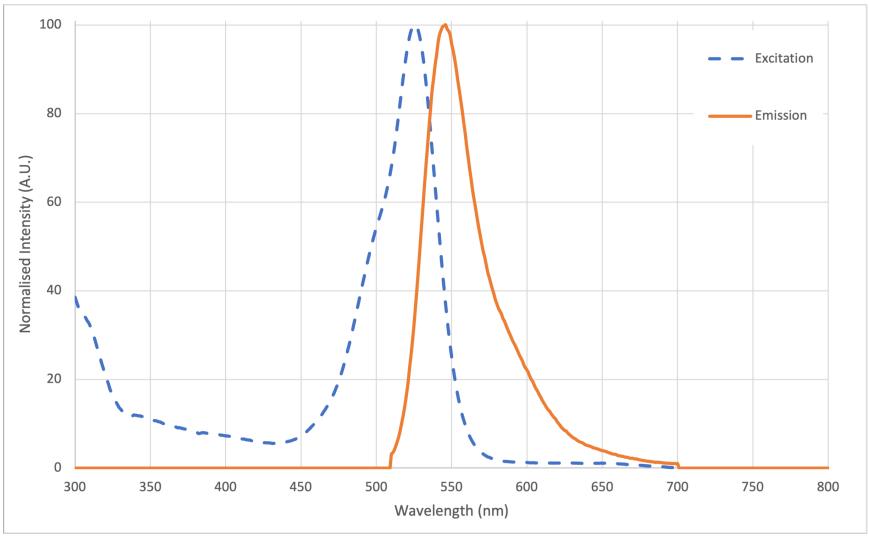

FIGURE 1.14: Excitation (dotted lines) and emission (full lines) spectra of Eosin (a common fluorescent dye) for comparison to QD spectra.

QDs are over 50 times more photostable and resistant to photobleaching than fluorescent dyes [87], owing to their differing electronic structures and inability of QDs to enter a triplet state and photobleach. This is an advantage over fluorescent dyes in microscopy which photobleach quickly under excitation light, making long-term imaging of fluorescent specimens difficult [88]. In comparison to dyes, QDs can be studied over an extended period (∼few hours) using confocal microscopy, total internal reflection microscopy or widefield epifluorescence microscopy with little to no observed decrease in fluorescence intensity [89, 90]. QDs also have a much higher quantum yields than fluorophore dyes, however, as mentioned above, these can be

limited by surface recombination events [91].

There are also some properties of semiconductor QDs that can be disadvantageous in fluorescence microscopy. QDs have a strong tendency to aggregate in solution which can affect labelling homogeneity [92]. One property QDs can exhibit is known as fluorescent blinking, which is the ability of a QD to randomly alternate between an emitting and non-emitting state [88]. This property is again linked to surface states on the QD, and as a result is often minimised by the addition of a QD shell [84, 93]. However, these are most often observed in single QDs [88] so mainly pose a problem only in single molecule detection applications. QDs often contain heavy metal ions in their structure (e.g. cadmium) which can be cytotoxic, limiting their use in live cell studies without further modification. Fluorescent dyes have a lower toxicity in comparison to QDs. Finally, the substantial size of QDs (up to $\sim$ 20 nm) make them unsuitable for labelling small structures such as the cell membrane.

1.3.2 Quantum dot bioconjugates

Synthesis of semiconductor QDs can be conducted in a variety of different ways, the most common of which being the use of chemical methods. These are known as "bottom up" approaches and typically work by first promoting nucleation of nanoparticles using precursor materials such as cadmium and selenium and then their growth into QDs [94, 95, 96, 97, 98].

However, QDs prepared using these methods have no aqueous solubility, and therefore are not biologically compatible [99]. Therefore, before any bioconjugation can take place, the QDs must first be rendered water-soluble. Many methods for this have been devised over the years. The first method involves ligand exchange, where the original hydrophobic coating on the QD is removed and replaced with a water-soluble molecule with one end conjugated to the QD and the other being hydrophilic [99]. The second is coating with a hydrophilic silica shell, which is a popular method as silica is biocompatible and can be easily functionalised. The third is encapsulation of the QD in polymers such as polyethylene glycol (PEG) which have strong interaction with the QD surface [99]. Some water-based synthesis methods have also been developed which yield quantum dots that are intrinsically water soluble [100].

The first bioconjugations of QDs were performed by Bruchez *et. al.* [86] and Chan *et. al.* [82] in 1998, paving the way for the use of QDs as biological sensors. Nowadays, there are a number of commercially available QD conjugates, including carboxyl groups, antibodies and other ligands [99, 101, 102]. Due to the large surface area of a QD, there are many surface attachment groups which can be used together to give a QDs multiple functionalities, e.g. in addition to a recognition molecule, QDs can be given membrane crossing/cell internalisation capability [102]. 2 to 5 protein molecules and 10-100 small molecules such as peptides or nucleotides can be conjugated to a single 4 nm QD [103].

Perhaps the most popular choice for bioconjugation of QDs is (strept)avidin, first described by Goldman *et. al.* in 2002 [104]. Avidin is a glycoprotein which has a high binding affinity for the vitamin biotin. Streptavidin has identical biotin-binding properties, but lacks the glycoprotein portion of the molecule and therefore displays less non-specific binding - in fact, the streptavidin-biotin bond is one of the strongest and most specific non-covalent bonds in existence. By conjugating QDs with (strept)avidin, QD conjugates can be prepared which tightly bind to any biotinylated protein, antibody or DNA [104].

Functionalisation of this type is a particular advantage as antibody labelling (immunolabelling) is a very popular tool in fluorescence microscopy. Antibodies are Y-shaped proteins that bind specifically to a molecule within the cell, often called an antigen. In immunolabelling, specificity stems from the affinity of the antibody for its antigen, i.e. an antibody against actin will theoretically bind only to the actin in a cell. Several methods of antibody labelling are used in practice, including direct and indirect options. Direct antibody labelling is when an antibody against an antigen within the cell (the primary antibody) is directly conjugated to a fluorescent dye. This can be advantageous as the process of labelling is simpler and shorter and avoids cross-talk between secondary antibodies. Indirect antibody labelling involves a primary antibody against the antigen in the cell, raised in a host animal (e.g. mouse). A secondary antibody with a dye conjugate is then chosen to bind to the primary antibody. The secondary antibody must be raised in a different host animal to the primary, e.g. rat (rat-anti-mouse antibody). This technique offers greater sensitivity as more than

one primary antibody can bind to each primary antibody, resulting in a higher fluorescence signal [102]. Thanks to advances in QD functionalisation, labelling with semiconductor QDs can be done using both direct and indirect methods. With the addition of streptavidin conjugated QDs to the family of commercially available QD labels, a single biotinylated antibody against a target can be used with virtually any wavelength of streptavidin conjugated QD, dramatically increasing the versatility of the antibody and reducing costs. However, the culminative volume of these layers can reduce the efficiency when studying precisely the positions of receptors in applications such as super-resolution microscopy.

1.3.3 Quantum dots as cellular probes in microscopy

Since their first use in biological applications in 1998, QDs have been tested in many applications traditionally using fluorophore dyes. QDs can be internalised by cells using a variety of methods and labelling protocols, which bypasses the requirement for bioconjugation - however, these methods are non-specific and provide only generalised labelling of cells. The simplest is to allow the cells to endocytose the QDs. This is a non-specific labelling method which will not highlight any particular cellular structure but may be suitable for applications in which general fluorescence is required in the cell, such as cell migration [92]. Streptavidin conjugated QDs may endocytose and bind to endogenous biotin within the cell. However, when using endocytic uptake with streptavidin-conjugated QDs, it has been shown that the quantum dots tend to aggregate within the cell and do not provide homogenous labelling of the cell [105]. QDs can also be used as whole-cell labels without requiring any functionalisation by internalisation via microinjection[106], electroporation or phagocytosis [89]. In eukaryotic cell studies, QDs were observed to eventually end up in intracellular vesicles that could be identified in some cases as endosomes or lysosomes [102]. Nonspecific labelling of QDs in these ways can give information on cell motility which in turn is useful to study migration of cells of interest e.g. cancer cells [105].

However, a better specificity can be achieved by using functionalised QDs. As described above, QDs can be functionalised using streptavidin and primary/secondary antibodies amongst other methods to offer specificity in cell labelling. Cell components which have previously been labelled with QDs include nuclei, mitochondria,

microtubules, actin, cytokeratin and the plasma membrane [92, 107]. Applications using antibody labelling have included the use of streptavidin QDs to detect Her2 cancer biomarkers on the surface of SKBR3 breast cancer cells [103]. A similar strategy has been used in cultured spinal neurons to detect glycine receptors [108].

QDs have been used both in fixed and live cell studies. The unique optical properties of QDs make them appealing for live cell imaging in particular - the strong resistance to photobleaching ensures that long-term imaging can be carried out with no loss in fluorescence from the cells and their high quantum yields mean that less excitation light is required to achieve sufficient fluorescence intensity [89]. However, QDs are made out of heavy metals such as cadmium and as a result, one of the challenges is in ensuring these do not interfere with normal cell behaviors [89]. Cytotoxicity in QDs has been found in a number of QD studies, found to affect both cell growth and viability [109, 110], however this was found to be dependent on factors including size, capping material, number of QDs and bioconjugation method. A more recent study investigated the cytotoxicity of CdTe quantum dots uptaken in cells via the electroporation method [110]. This study used the MTT test (using metabolic activity as an indicator of cell viability) to determine cytotoxicity of the quantum dots and showed that cadmium ions are released from quantum dots after both incubation and electroporation which is indicative of cytotoxicity. The study also found that larger nanocrystals (3.7 nm) caused a smaller decrease in cell viability than smaller quantum dots (2 nm) after electroporation. This paper confirms earlier reports of cadmium ions being released from the quantum dot surface leading to cell death [111]. Importantly, cytotoxicity in QDs was found to be reduced by using an appropriate cap over the QD core to prevent the escape of cadmium ions from the QD core into the cell [109]. This is a notable finding as most QD bioconjugates which are commercially available are core-shell type.

Despite some of QD toxicity, live cell imaging has been carried out extensively by the group of Sanford Simon. In their 2003 publication, the authors label live HeLa cells with DHLA (dihydrolipoic acid) capped QDs and study these in cell culture conditions for over a week, observing no change in their growth rate [89]. The authors also labelled *D. discoideum* cells with QDs, imaging once per minute over a period of 14 h, and found that QD-labelled cells developed normally compared to a control sample

of unlabelled cells. No toxicity was reported in a further method described by Jaiswal *et. al.* who used DHLA capped quantum dots at a concentration of 100 pmol [92].

1.4 Thesis Outline

The following chapters in this thesis will describe the work carried out to characterise, implement and apply a 280 nm LED in biomedical optical imaging. This thesis will be structured as follows:

Chapter 2 describes the characterisation of the optical properties of the LED used throughout the project which are relevant to biomedical optical imaging. This chapter describes the theory behind the optical properties of the LED, including electroluminescence spectrum, optical power and emission pattern, and why these are important factors to consider when implementing an LED as an illumination source for microscopy. This chapter describes the challenges of characterising deep-UV LEDs, how characterisation of the deep-UV LED in use throughout this thesis was carried out and also outlines a novel characterisation method that was developed in lieu of UV-enhanced detectors.

Chapter 3 is a systematic comparison into methods of delivering 280 nm light to the specimen for fluorescence microscopy. Due to the low transmission of 280 nm light through standard glass optical elements, alternative methods of light delivery were sought out for 280 nm light. This chapter investigates the transmission of this wavelength through a commercial microscope, the use of transmission fluorescence and the use of epifluorescence using specialised objective lenses such as quartz and reflective objectives. In this chapter, I compare properties such as available power at the specimen plane, illumination homogeneity and quality of the resulting images. Based on this, I then conclude by determining an appropriate optical set up to use throughout the rest of the work in this thesis.

After choosing the best illumination method, I then apply this to biological specimen. Chapter 4 specifically focuses on the use of 280 nm excitation of QDs and the benefits of using this wavelength. In the work carried out within this chapter, I investigated semiconductor QDs and their ability to be excited by 280 nm light. In particular, I measured the increase in fluorescence from semiconductor QDs when excited by 280 nm when compared to a longer, more accessible wavelength of 365 nm. I also investigated whether the increase in energy associated with 280 nm light causes increased (if any) photobleaching to QD specimens. Finally, I assessed the suitability of using this

wavelength of excitation with live cell specimens.

Chapter 5 presents standing wave microscopy carried out with 280 nm excitation. In this chapter, I discuss why the standard methods of standing wave microscopy cannot be used with 280 nm light and I present an alternative method of standing wave microscopy capable of generating a standing wave with 280 nm excitation. I then show the characterisation of the generated standing wave and compare its properties to those of the theoretical standing wave. Finally, I show the work done in using this 280 nm standing wave technique to image fixed mammalian cells.

Finally, chapter 6 presents a conclusion of the work carried out in this thesis.

Chapter 2

Characterisation of 280 nm LEDs

A light source is a critical component of any optical microscopy method, but light source optical properties such as wavelength, stability and emission pattern are particularly important when it comes to fluorescence imaging. Whilst the optical properties of visible-wavelength LEDs can easily be measured, detection in the deep-UV with standard components is difficult due to low transmission of optical components or poor sensitivity of detectors at these wavelengths. This chapter will present the development of a novel technique to determine the emission pattern of a deep-UV LED without the requirement of UV-enhanced sensors. This chapter will also explore methods to characterise three properties of the 280 nm LED used throughout this thesis, namely the electroluminescence spectrum, optical power and emission pattern. Parts of this chapter have been adapted, with permission, from the following article published by IOP publishing: Mollie McFarlane and Gail McConnell "Characterisation of a deep-ultraviolet light- emitting diode emission pattern via fluorescence", Measurement Science and Technology, 2020, 31, 077001.

2.1 Introduction

2.1.1 Electroluminescence Spectrum

Electroluminescence is an electrical phenomenon in which a semiconducting material emits light in response to an electric current. The mechanism by which LEDs emit photons is spontaneous recombination of electron-hole pairs within the active region and simultaneous emission of photons.

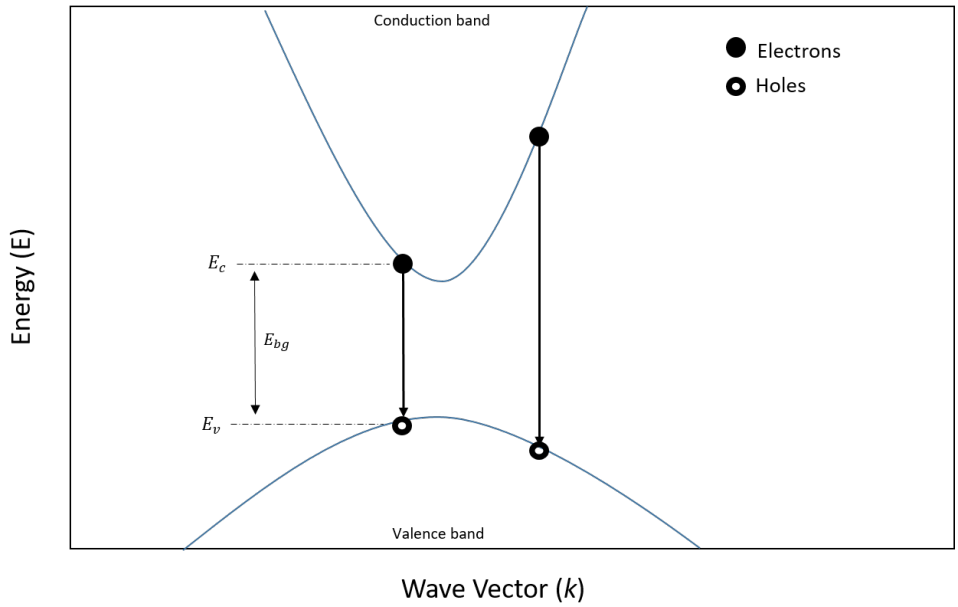

FIGURE 2.1: Parabolic electron and hole distributions within a semiconductor. The energy of a photon emitted via electroluminescence is equal to the difference in energy between the hole in the valence band and the electron in the conduction band.

Electrons within the conduction band and holes within the valence band of the active region are assumed to have parabolic dispersion relations [74], as shown in figure 2.1.

As the electron momentum cannot change significantly during transitions between the conduction band and valence band, transitions must occur within the same wave vector value (k). This means that transitions must occur vertically (figure 2.1), i.e. electrons may only recombine with holes which have the same k value [74]. Energy conservation requires that the energy of the emitted photon is given by the difference between electron energy E_e and the hole energy E_h. The photon energy is then given by:

$$h\upsilon = E_e - E_h \approx E_{bg} \tag{2.1}$$

where the photon energy is approximately equal to the bandgap energy E_{bg} provided that there are negligible heating effects on the semiconductor. As a result, as described in chapter 1, the emission wavelength of an LED can be determined by choosing a semiconductor material with the appropriate bandgap energy.

As the distribution of carriers (electrons and holes) in the bands are governed by the Boltzmann distribution [74], the electroluminescence spectrum of an LED is directly dependent on temperature, with both the position of maximum intensity and the spectral FWHM affected by changes in temperature. The maximum emission energy E and the spectral FWHM ΔE are given by:

$$E = E_{bg} + \frac{1}{2}kT \tag{2.2}$$

and

$$\Delta E = 1.8kT \tag{2.3}$$

respectively, where E_{bg} is the bandgap energy, k is the Boltzmann constant and T is temperature.

Due to the direct dependence of the electroluminescence spectrum on temperature, heating of LED chips can be an issue and this is normally caused by non-radiative recombination events within the semiconductor. Non-radiative recombinations can occur owing to a number of different mechanisms. Defects in the crystal structure are the most common cause, including foreign atoms and dislocations [112]. Such defects can cause energy levels to be formed within the bandgap of the semiconductor, known as deep-level states which promote non-radiative recombination events [112, 113, 114]. Another common mechanism for non-radiative recombination events are via Auger processes. In this type of recombination event, the energy released via electron-hole recombination is used to promote an electron high into the conduction band or a hole deep into the valence band. These carriers will then lose energy via heat until they return to the edge of their respective bands. Thirdly, substantial non-radiative recombination can occur at the surface of the LED, where the periodicity of the semiconductor crystal lattice ends. At this surface, further energy states within the bandgap occur and recombination events here result in heating of the LED surface.

In general, all non-radiative processes combine to result in formation of heat within the semiconductor. Due to the temperature dependence on both spectral linewidth and peak position, the heat generated by non-radiative recombinations can cause both red shifting of the peak spectral position of the electroluminescence spectrum and

cause broadening of the spectral FWHM. As a result, proper steps must be taken to reduce generation of excess heat, such as appropriate heat-sinking or cooling using fans [115].

The electroluminescence spectrum of an LED is an important factor to consider in fluorescence microscopy, for two main reasons. Firstly, the spectrum of an LED describes the wavelengths of light emitted by the LED as a function of intensity. When choosing a fluorophore for fluorescence microscopy, it is advantageous to choose an excitation light source whose wavelength overlaps significantly with the excitation spectrum of the chosen fluorophore [77]. Knowing accurately the peak wavelength and spectral FWHM of an LED will allow the degree of overlap with the fluorophore to be assessed, and therefore the degree of excitation efficiency [54, 77]. The ability of an LED to excite fluorescence from a fluorophore could be affected by any red-shifting due to the thermal effects described above, and as a result it is important to characterise the spectral stability of the LED package over time and with increased drive currents. In addition, image contrast in fluorescence microscopy depends heavily on the adequate separation of excitation light and emission light, which can prove difficult when many fluorophores have small Stokes shifts. Knowing the peak wavelength and spectral FWHM of the electroluminescence spectrum can establish the need for, and specifications of, any excitation filters to assist in the spectral separation of excitation and emission light.

2.1.2 Optical Power and LED Stability

The brightness of an LED can be described in many ways, convoluted by the lack of a standard measurement across industries. Most descriptions of the brightness of an LED can be divided into two categories: radiometric quantities, which describe physical properties of radiation and photometric quantities, which describe the perception of radiation by the human eye [116, 117]. Here, we will focus on radiometric quantities such as radiant power, radiant intensity and irradiance because a wavelength of 280 nm is not detectable by the human eye.

The radiant power P of an LED is defined as the energy dQ of optical radiation emitted by a source per unit time dt.

$$P = \frac{dQ}{dt} \tag{2.4}$$

The unit of radiant power is the watt (W). The total radiant power of an LED source is often measured by an integrating sphere which collects light emitted at all angles from the LED. The radiant power of the LED is the most common value quoted by LED manufacturers to describe the intensity of an LED light source. Most visible wavelength LEDs have high radiant power, of the order of several hundred mW, and are often operated at relatively high drive currents to produce optimum optical powers.

The radiant intensity I of an LED is defined as radiant power dP emitted per unit angle dΦ in a given direction. Radiant intensity is measured in watts per steradian (W/sr):

$$I = \frac{dP}{d\Phi} \tag{2.5}$$

Irradiance E is obtained from the ratio of radiant power dP falling onto a surface dA. Irradiance is measured in watts per square metre:

$$E = \frac{dP}{dA} \tag{2.6}$$

Irradiance is not a property of a source but instead indicates the ratio of the radiant power from the LED source falling on a particular area. The quantities mentioned here are only a few of the many ways to measure the optical properties of an LED source and as a result, it is not practical to consider them all. In this thesis, we will focus on radiant power, from now on referred to simply as optical power, as a measurement for the LED light source.

Although the total optical power of the LED is an important parameter as this indicates the limitations of the LED in terms of its throughput in an optical system such as a microscope, the power of light at the specimen plane is a particularly important factor to consider in fluorescence microscopy. Because the number of photons emitted by a fluorescent material is directly proportional to the number of photons incident on the specimen, any change in the optical power at the specimen plane directly impacts the fluorescence intensity of the specimen [77]. This is particularly important in

quantitative imaging, where any fluctuations in light source optical power can cause misleading results [59].

As discussed above, with each electron passing through by the LED, there is excess energy generated in the form of heat due to non-radiative recombinations and as well as causing spectral shifting and broadening, this can also lead to degradation of the LED lifetime and fluctuations in light intensity [74].

Reproducibility in acquisition has been identified as one of the most important topics across all fields of microscopy [59] and a stable light source is one of the key components for reproducible experiments. In particular, light source stability is an important factor in fluorescence microscopy because, as described above, small changes in excitation power can translate to small changes in fluorescence intensity [77]. This is of particular importance in quantitative imaging, where light source fluctuations can lead to inaccurate data and misleading results [59]. Recently, an in-depth study was performed by Firas Mubaid and coworkers in which they tested the stability of several LED light sources (as well as mercury lamps) over time periods of up to 300 hours [59]. To assess the stability of these sources over time, the authors used a power sensor coupled to an optical power meter. From this study, the authors deduced that LED stability was better than that of arc lamps in both the short term (2.5 h) and long term (300 h). The study concluded that whilst LEDs offer far superior optical stability over arc lamps, not all LEDs behave the same and some can take time to stabilise after switch-on. Therefore, as the 280 nm LED used in this study is a relatively new light source whose stability has not been thouroughly tested in fluorescence microscopy applications, the stability of this LED must be assessed in order to evaluate its potential for long and short term imaging experiments.

2.1.3 Emission Pattern

LEDs have a characteristic emission pattern, or the light intensity as a function of angle and distance from the LED chip. In a planar LED chip, this is generally Lambertian in nature.

Lambertian emission patterns are a result of the difference in refractive index between the semiconductor chip and the surrounding medium (i.e. air). If a point source

emits a ray of light at an angle ϕ to the normal of the LED surface, the light ray is refracted at the semiconductor-air interface. This results in a ray of light escaping the semiconductor with angle Φ with respect to the normal (figure 2.2).

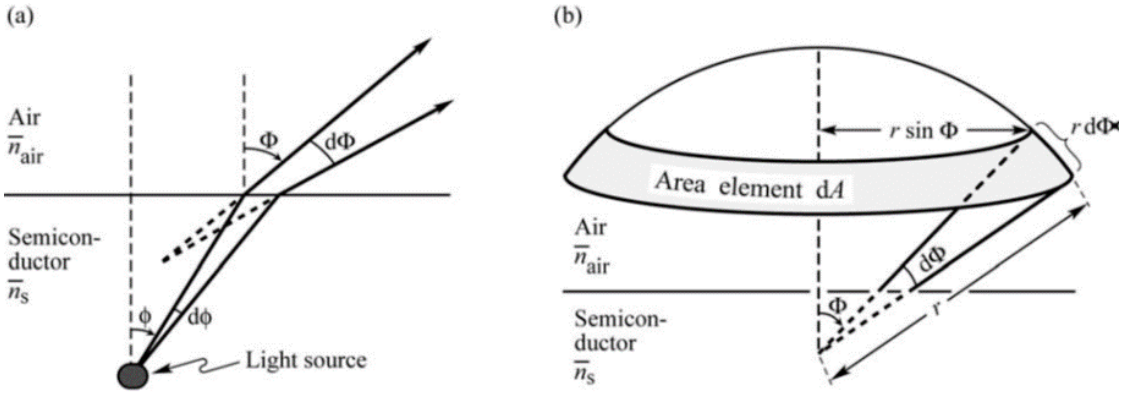

FIGURE 2.2: LED model used to derive the Lambertian emission pattern. Reproduced from [74] with permission.

The light intensity in air (I_{air})is then given by:

$$I_{air} = \frac{P_{source}}{4\pi r^2} \frac{n_{air}^2}{n_s^2} cos\Phi \tag{2.7}$$

where P_{source} is the optical power of the LED, r is the distance from the source to the position of measurement, n_{air} is the refractive index of air and n_s is the refractive index of the semiconductor material. This is known as the Lambertian emission pattern. This has a characteristic cosine dependence on the angle of light emitted from the semiconductor, with maximum intensity measured at the normal of the LED chip. Whilst the Lambertian emission pattern is the standard because of its origins in refractive index differences, LEDs can come in other packaging geometries which can be achieved by either microlenses encompassing the chip or by patterns on the chip surface. These additional geometries can include hemispherical, which exhibit isotropic emission patterns, and parabolic, which have strongly directional emission patterns [74].

LED emission patterns can also be classified into two groups: near-field and far-field. Near-field studies focus on LED-target distances that are within 5 times the dimension of the active region, whilst far-field studies focus on distances over this limit, after which the emission pattern no longer changes with LED-target distance [118]. In optical microscopy, it is the far-field emission pattern which is notable as,

generally, the LED-target distance will be more than a few mm in distance. The far-field emission pattern of an LED is of interest in optical microscopy as it can impact the homogeneity of illumination across the specimen - this is particularly important in quantitative analysis as any areas of higher intensity illumination across the specimen can result in increased fluorescence intensity, causing misleading results.

Some mathematical models have been developed to simulate the emission patterns of packaged LEDs and LED arrays [118, 119, 120]. These can be based on light propagation characteristics, for example following a light rays from the point of emission within the active region of the semiconductor, through the different refractive indices in the LED and through the LED packaging [118]. Other numerical methods can use ray tracing algorithms such as Monte Carlo to predict the emission of the LED [120]. However, as discussed above, packaged LEDs come available in different emission patterns which makes a general model difficult to obtain [118] [120]. In addition to this, LED chips of the same model can vary between individual parts, so it is advantageous to characterise the specific LED used in studies. Experimentally, the emission pattern of a visible spectrum LED can be obtained using a charge-coupled device (CCD) or complementary metal-oxide-semiconductor (CMOS) camera, however this is difficult to apply to deep-UV LEDs as standard cameras are not sensitive at these wavelengths due to glass and poly-silicon elements which absorb in the UV. Back-thinned cameras offer a solution to this, but are expensive. As a result, it is advantageous to develop a low-cost, simple method which can be undertaken without the use of expensive, specialised equipment.

Previous work studying AlGaN in LEDs has been shown to overcome these detection limits by using fluorescence to convert deep-UV radiation into visible light [121], such that it can be detected by a standard camera. In this work, the authors use fluorescence to image the active region of the chip (i.e. the near-field emission pattern) and investigate the electroluminescence distribution on the microscopic scale. In this chapter, this approach was modified in order to investigate the far-field emission pattern of an LED, or how it emits light into air, using a fluorescent material placed in front of the LED and using the intensity distribution across this to indicate the emissive properties of the LED. This is an inexpensive method, using standard microscope optics and cameras already present in the lab. Although this gives information on only

the section of the LED emission pattern that is within the field of view of the objective lens, this can be overcome by rotating the LED to measure the full emission pattern, as demonstrated previously using visible spectrum LEDs [122].

2.2 Methods

2.2.1 Electronic Circuitry

The 280 nm LED used throughout the project was the LG LEUVA66H70HF00 LED. This model of LED has a chip size of 1 mm $\times$ 1 mm, a typical total optical power of 100 mW at a drive current of 350 mA and a typical viewing angle of 110°.

LEDs are most commonly available from manufacturers as bare chips [123]. This is the most cost effective way to purchase an LED, but requires mounting of the LED chip to a printed circuit board (PCB) to create an LED Array Module (LAM) package, and connecting it to a power supply and heat sink. This was carried out at CoolLED ltd. using their LED packaging facilities.

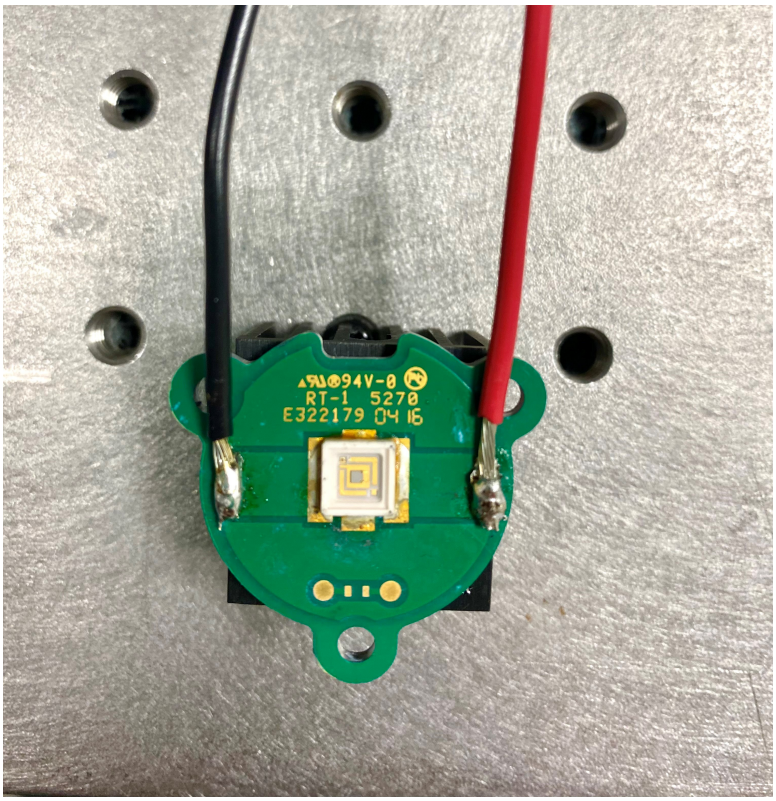

FIGURE 2.3: 280 nm LED Array Module (LAM) design used in early stages of the project. The LED is in white packaging in the center of a PCB. The LAM is mounted to a heat sink using a thermal adhesive to allow heat dissipation.

As mentioned in the introduction to this chapter, high-power LEDs give off excess heat which can affect the performance of the LED. To counter this, and complete the LED unit, the LED was bonded to a 1-inch by 1-inch heat sink (RS 674-4756) using a

thermal adhesive (MG Chemical 8329 TFS) to allow for heat dissipation. This resulted in the packaged LAM shown in figure 2.3.

The positive and negative terminals of the PCB were then connected to a variable power supply (Aim-TTi QL355T Digital) using crocodile clips to allow the LED to be driven in forward bias. The optical power of the LED could then be adjusted by changing the drive current passing through the LED chip using the power supply.

2.2.2 Electroluminescence Spectrum

The electroluminescence spectrum of the LED was investigated using an Ocean Optics USB2000+UV-VIS spectrometer which has a detection range between 200 and 850 nm and a resolution of 1.37 nm. The spectrometer uses an optical fibre (QP600-2-SR) to collect the light and relay it to the detector, the end of which was placed directly above the LED chip at a sufficient distance as not to over-saturate the detector.

The spectrometer was controlled using the Ocean Optics SpectraSuite software and the integration time was set to 100 ms. The spectrum of the LED was measured at different LED drive currents in order to investigate the stability of the electroluminescence spectrum (and infer its thermal stability) at high currents. The drive current was varied from 1 to 500 mA using the variable power supply. This current range was chosen as the manufacturer recommends that the LED be driven at 350 mA, and so currents which "over-drive" the LED (i.e. 350-500 mA) were used to check the stability of the LED at high currents - using high currents is particularly desirable as this leads to increased optical power from the LED, however this can come at the cost of increased heating and shorter LED lifetimes.

The wavelength at which the peak intensity occurs was investigated over time to determine the stability of the electroluminescence spectrum over extended periods of time. To measure this, a spectrum was acquired every 10 minutes for 6 hours at a constant current of 100 mA and the wavelength which corresponded to the highest spectral intensity was recorded.

It was noticed that the chip appears faintly blue to the eye when switched on which is unusual for an LED of centre wavelength 280 nm as emission at this wavelength should not be visible to the human eye. As this was not noticable in the spectrum, a second spectrometer with detection range above 350 nm was used in case the strong

signal at 280 nm was masking any signal from longer wavelengths. This spectrometer, the OceanOptics USB2000, was used to measure the spectrum between 350-1100 nm, as when using the UV-extended spectrometer, the signal at 280 nm was too strong to reveal the presence of any lower intensity light at longer wavelengths. This spectrometer was also used to compare the performance of two bandpass excitation filters chosen to reduce any signal at wavelengths above 280 nm. To do this, a 280/10 nm bandpass filter (Laser 2000 FF01-280/10-25) and a 300/50 nm bandpass filter (Edmund Optics 12-093) were each placed in the optical path between LED chip and detector while acquiring spectra.

2.2.3 Optical Power

The relationship between drive current and LED optical power was determined to ensure that increases in current applied to the LED translated to a linear increase in optical power. To measure the linearity of the relationship between drive current and optical power, a FieldMax-II-To power meter was used alongside a PM10 thermopile sensor. The sensor was placed in front of the LED and the LED drive current was varied from 0 to 500 mA. At each drive current, the optical power was measured using the power meter and its Coherent FieldMax software.

The stability of optical power of the LED was measured using the Coherent PM10 thermopile sensor coupled to the FieldMax-II-To power meter. The LED was placed as close as possible to the sensor, limited to around 5 mm by the offset of the sensor from the packaging. The LED was operated at a drive current of 100mA and the power was measured over a total period of 6 hours (a typical time for a microscopy time-lapse experiment) with a power value taken every minute. Experiments were repeated in triplicate and averaged.

To determine the reproducibility of results between sensors, stability experiments were repeated using a second power sensor, a Thorlabs S120VC photodiode sensor coupled to a PM100A power meter. Again, the LED was placed as close to the active area of the sensor as possible and measurements were obtained every minute for 6 hours at 100 mA. Measurements were again repeated in triplicate and averaged.

2.2.4 Emission Pattern

The experimental set-up to obtain the emission pattern of the 280 nm LED is shown in figure 2.4. This set-up uses a fluorescent specimen to convert 280 nm emission from the LED into visible wavelength light capable of being detected by a standard camera. An image of the fluorescent specimen is focussed onto the detector and the image can then be used to measure the intensity of the LED laterally, based on the distribution of fluorescence intensity across the specimen. This measurement can give an indication of the spatial distribution of light with which the LED would directly illuminate the sample, and hence what optics have to be used to create homogenous illumination of the specimen.

To do this, the LED was mounted in a rotating platform mount (Thorlabs PCM). A 280/10 nm bandpass filter (Edmund Optics, 35-881) was placed in front of the LED to narrow the electroluminescence spectrum to only the peak at 280 nm.

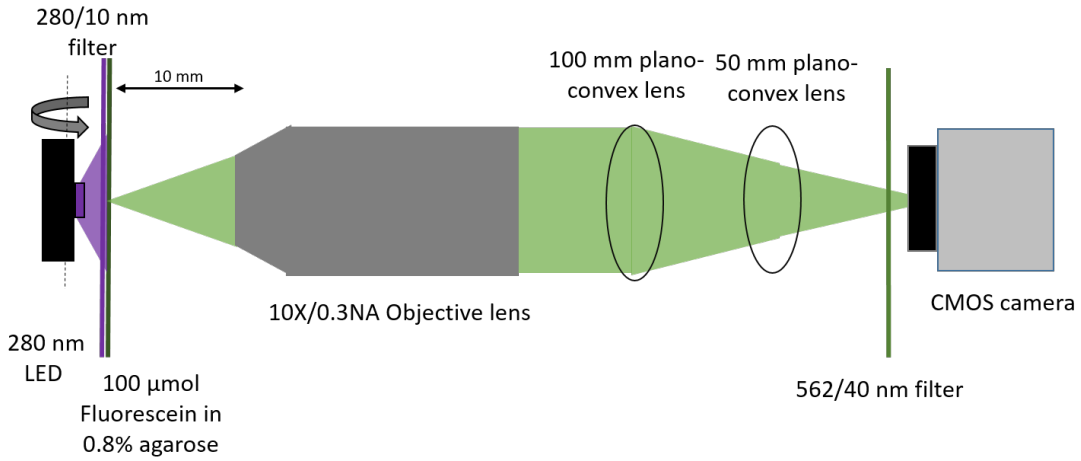

FIGURE 2.4: Experimental set up for imaging the emission pattern of a deep-UV LED. A fluorescent sample is placed in the focal plane of the objective lens and the LED is placed adjacent to the sample, behind a bandpass filter which narrows the electroluminesence spectrum of the LED. Two plano-convex lenses are employed to focus the image onto the camera chip. An emission filter is used to exclude any excitation light. To capture angular measurements, the LED was rotated about the indicated axis.

To create a fluorescent sample capable of excitation of fluorescence at 280 nm, fluorescein was chosen due to its high quantum yield and excitation spectrum extending into the deep-UV (detailed excitation spectra of fluorescein can be found here [124]). It can be noted that fluorescein has poor photostability, but because short exposure

times were used and no long-term imaging was done, this did not cause issues. A 3D block of agarose dissolved in fluorescein was chosen as this allows the flexibility of choosing the thickness of the agarose block to allow for sufficient fluorescence signal based on the path length of the block. To produce the agarose block, 0.8% agarose (Sigma Aldrich 05066) was added to 100 μmol fluorescein (Sigma Aldrich F6377) in distilled water, microwaved until dissolved and pipetted into a 3D printed mould, 2 mm in depth, attached to a microscope slide. The specimen was placed in a slide holder (Thorlabs XF50) as close as possible to the LED (3.5 mm as limited by thickness of the bandpass filter).

A 10x/0.3 NA objective lens (Olympus UPLFLN10XP) with a working distance of 10 mm was chosen to collect the fluorescence emission from a relatively large field of view and the focal plane was set to the specimen. Two plano-convex lenses, 100 mm (Thorlabs LA1509-A) and 50 mm (Thorlabs LA1608-A) in focal length respectively, were used to focus the image of the fluorescent sample onto the CMOS camera (IDS UI-3060CP). This configuration resulted in a total magnification of 2.5x, pixel size of 2.3 μm and a field of view of 4.5 mm. An emission filter (562/40 nm, Semrock FF01-562/40-25) was placed in front of the camera for detection of fluorescein. To investigate any changes in LED emission pattern with varying drive currents, images were acquired at LED drive currents ranging from 50-350 mA. An image was also acquired with the LED turned on but no fluorescent specimen in place to measure the background intensity of any excitation light bleeding through to the detector. Finally, as this is an indirect technique which relies on the assumption that fluorophores are distributed evenly across the fluorescent sample, images were acquired with the fluorescent specimen having been rotated around different axes and flipped to ensure that any measured emission pattern was a property of the LED and not of the fluorescent specimen itself.

Images acquired in this way only show a small portion of the emission pattern due to restrictions of the microscope FOV, but give an indication of the distribution of light delivered across the specimen if the LED were used to directly illuminate the specimen. To analyse the intensity distribution, images were imported into Fiji [125] and background corrected by subtracting the image of the light bleedthrough to the camera. A false colour look-up table was applied to aid visualisation of the intensity

distribution. To measure the emission pattern across the field of view, an intensity line profile was taken horizontally across the image as this allowed measurement of a larger area due to the aspect ratio of the camera. A linewidth of 50 pixels was taken, corresponding to 116 μm, to reduce noise in the intensity profile.

To collect information on the angular emission pattern of the LED, the LED was rotated about the axis shown in figure 2.4. To do this, the LED was mounted on a rotating stage (Thorlabs RP01) 65 mm from the sample such that the chip lay on the axis of rotation parallel to the detector. The stage was rotated between 0° and 90° from the normal in both directions at a constant current of 350 mA and images were taken at each angle with a longer exposure time of 50 ms to compensate for the decrease in intensity due to increased LED-sample distance. The average intensity across the image was recorded and plotted as a function of angle. An average of 3 images was recorded per angle. The data was then fitted against a perfect Lambertian using equation 2.7.

To test the ability of the technique in distinguishing between types of LED packaging geometries, measurements were repeated with a second deep-UV LED specimen (Thorlabs M275D2) emitting at 275 nm which exhibits a non-Lambertian emission pattern. This was an LED emitting at 275 nm and exhibiting a batwing emission pattern (Thorlabs M275D2), which typically has two lobes each with its own point of maximum intensity. Batwing emission patterns can stem from specific patterning in the chip itself, for example, the LED used in this experiment had a chip which was split into 4 sections. Images were obtained at a higher exposure time of 50 ms for static measurements and 150 ms for rotational measurements to compensate for the lower radiant power of this LED. Image analysis was performed as described above.

2.3 Results

2.3.1 Electroluminescence Spectrum

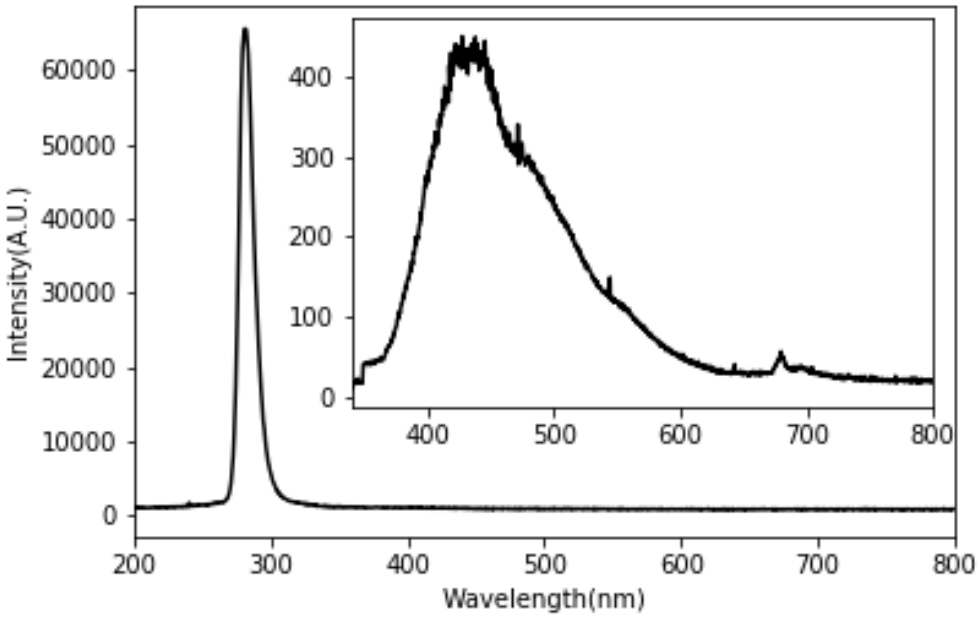

FIGURE 2.5: Emission spectrum of 280 nm LED using OceanOptics USB-2000+UV-VIS spectrometer. Inset Spectrum measured at wavelengths above 350 nm using OceanOptics USB-2000 spectrometer.

The electroluminescence spectrum of the LED is shown in figure 2.5, measured by the USB2000+UV-VIS spectrometer. The spectrum shows a peak at 281.5 $\pm$ 0.75 nm with a FWHM of 12 $\pm$ 0.75 nm. This spectrum agrees well with the spectral profile of a typical LED, exhibiting a narrow FWHM when compared to more traditional sources used for widefield microscopy such as arc lamps.

The spectrum acquired using the USB2000 spectrometer is shown in figure 2.5 (inset). With this visible-spectrum spectrometer, low-intensity broadband emission is visible between 350-800 nm, peaking at a wavelength of 425 nm and tailing off with increased wavelength. This can explain the visibly blue colour of the LED chip when switched on. As discussed in section 1.2.2, this is a common issue in deep-UV LEDs [72] [73] and is referred to as parasitic emission. This is thought to be due to electron overflow into the semiconductor layers neighbouring the bandgap region.

The bandgaps of these layers are often different to that of the active region, thus radiative recombination within these layers yields photons of different wavelengths.

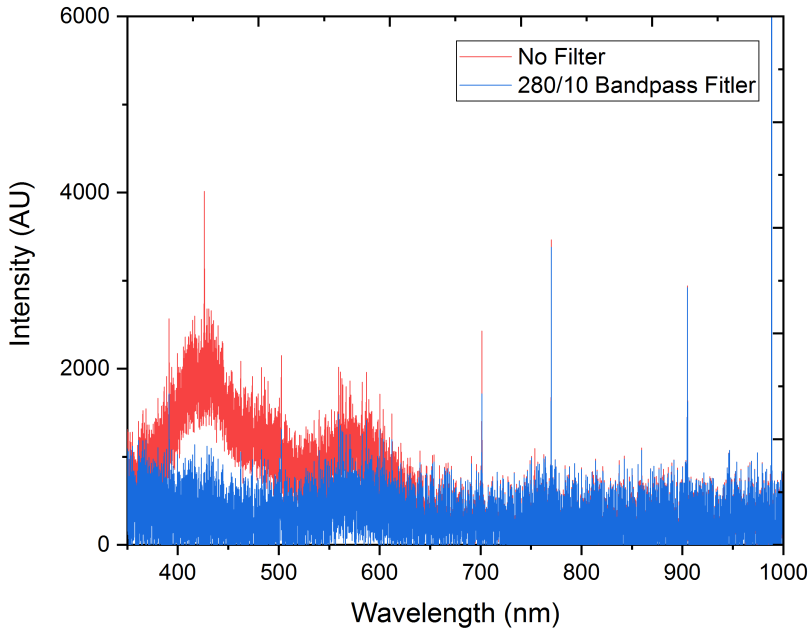

FIGURE 2.6: Spectrum of 280 nm LED obtained at wavelengths between 350 nm and 1000 nm using an OceanOptics USB2000 spectrometer, with and without the use of a 280/10 nm excitation filter

This feature was present in the first 280 nm LED and has been observed more recently by Liu *et. al.* in lower wavelength AlGaN LEDs [72].

Two bandpass filters were tested to reduce the parasitic emission of the LED and the spectrum of the parasitic LED emission whilst using these filters are shown in figures 2.6 and 2.7.

Figure 2.6 shows the reduction in spectral intensity in this region after addition of a 280/10 nm bandpass filter and figure 2.7 shows the reduction in spectral intensity in this region after the addition of a 300/50 nm bandpass filter. Both filters display relatively similar improvements in reducing unwanted emission in this region, with the 280/10 nm bandpass performing slightly better around 575 nm. However, the transmission spectral FWHM of this filter is narrower than that of the LED emission and because of this, this filter will also block some of the 280 nm light from the LED. In addition to this, the 280/10 nm bandpass filter reports only 68% transmission at 280 nm, further reducing already limited optical power of the LED. The 300/50 nm filter reports a similar transmission at $\sim$ 60%, however, the wider transmission spectral FWHM of this filter allows more light from the desired LED wavelengths to be

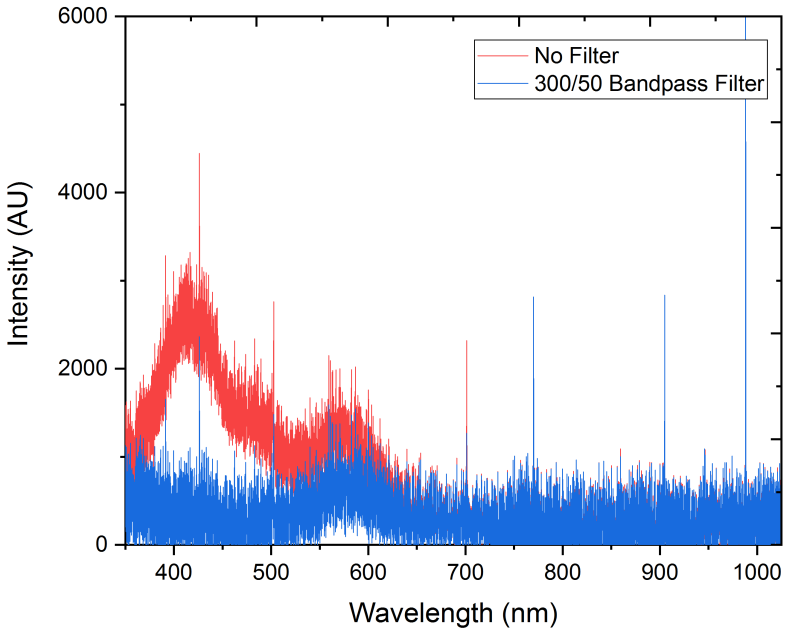

FIGURE 2.7: Spectrum of 280 nm LED obtained at wavelengths between 350 nm and 1000 nm using an OceanOptics USB2000 spectrometer, with and without the use of a 300/50 nm excitation filter.

transmitted. Therefore, where conservation of optical power at 280 nm is a priority, the 300/50 nm bandpass filter will instead be used to reduce the parasitic emission of the LED.

The relationship between LED drive current and electroluminescence spectrum was then investigated using the Ocean Optics USB2000+UV-Vis spectrometer. The peak emission wavelength as a function of current is shown in figure 2.8.

As mentioned in the introduction to this chapter, LEDs are sensitive to thermal change and any increases in peak wavelength towards high drive currents are likely to be due to an increase in temperature across the LED chip owing to improper thermal management. The mean peak wavelength was found to be 281.58 nm with a standard deviation of $\pm$ 0.97 nm occurring over varying drive currents. This standard deviation value is smaller than the resolution of the USB2000+UV-Vis spectrometer at 1.37 nm, hence the variation in peak wavelength with increasing current can be considered negligible. In this case the thermal state of the LED appears not to affect the emission wavelength due to appropriate thermal management and the LED spectrum appears to be highly stable over a wide range of drive currents. The peak wavelength of the

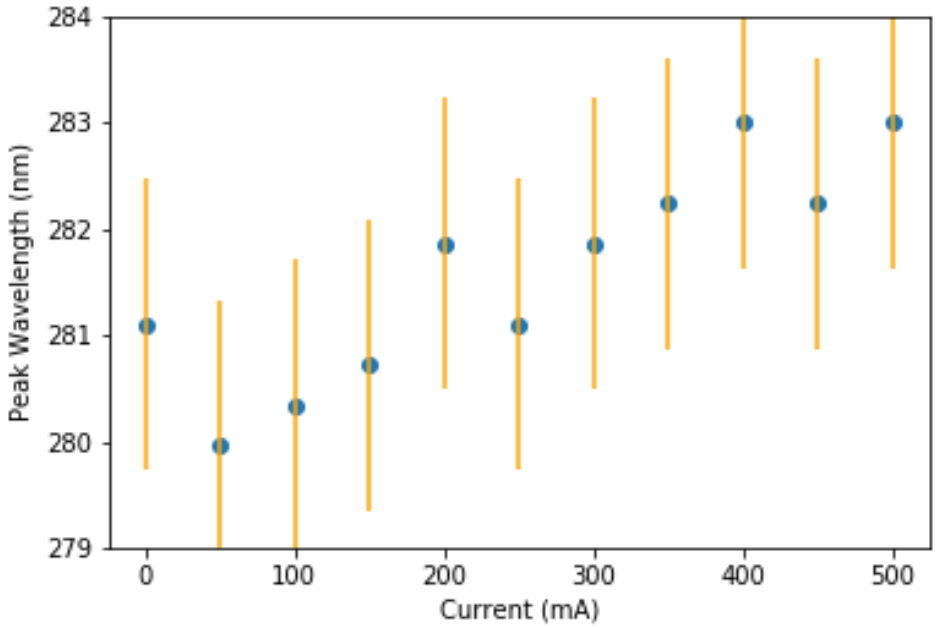

FIGURE 2.8: Peak emission wavelength of 280 nm LED using OceanOptics USB-2000+UV-VIS spectrometer as a function of LED drive currents between 1 and 500 mA. Error bars represent the resolution of the spectrometer.

LED over a period of 6 hours of continuous use was investigated using the same spectrometer to assess the suitability of the LED for time-lapse imaging experiments. The peak LED wavelength as a function of time is shown in figure 2.9.

The mean wavelength of the LED over a period of 6 hours was found to be 281.47 nm with a standard deviation of ± 0.26 nm. Since the standard deviation is smaller than the resolution of the spectrometer, the change in peak wavelength over time can also be considered negligible. As spectral shifting is largely caused by temperature changes, these negligible fluctuations in peak wavelength suggest that the LED unit is designed appropriately to manage temperature over time periods associated with time-lapse imaging.

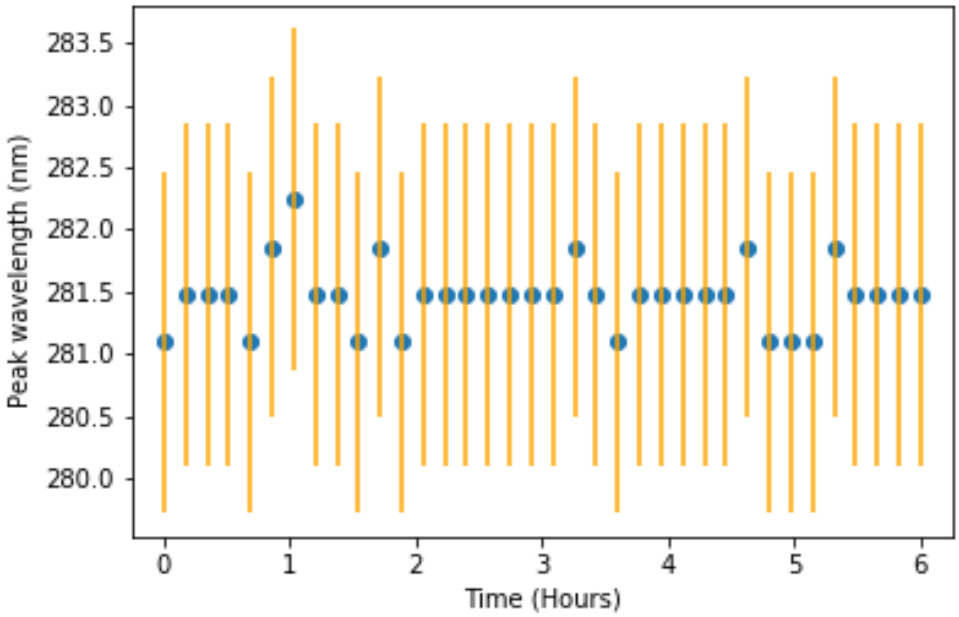

FIGURE 2.9: Peak emission wavelength of 280 nm LED measured using OceanOptics USB-2000+UV-VIS spectrometer as a function of time. Error bars represent the resolution of the spectrometer.

2.3.2 Optical Power

To assess the linear relationship between LED drive current and optical power, the power from the LED was measured as a function of drive current. This is shown in figure 2.10. As expected, there is a linear relationship between drive current and optical power, with an increase in current resulting in increased optical power. This trend confirms that the LED optical power can indeed be adjusted by changing the drive current applied to the LED, and that an increase in current translates linearly to an increase in power emitted from the LED.

At a current of ∼350 mA, the maximum drive current recommended by the manufacturer, the gradient begins to change slightly and there is no longer the same degree of increase. This is known as the "efficiency droop" in nitride-based semiconductors. A drive current of 350 mA is recommended by the manufacturer and increasing the current beyond this value results in "overdriving" of the LEDs. This will increase the optical power achievable by the LED, however, this may come at the cost of reduced LED lifespan.

The 6-hour optical power stability of the LED as measured using the thermopile

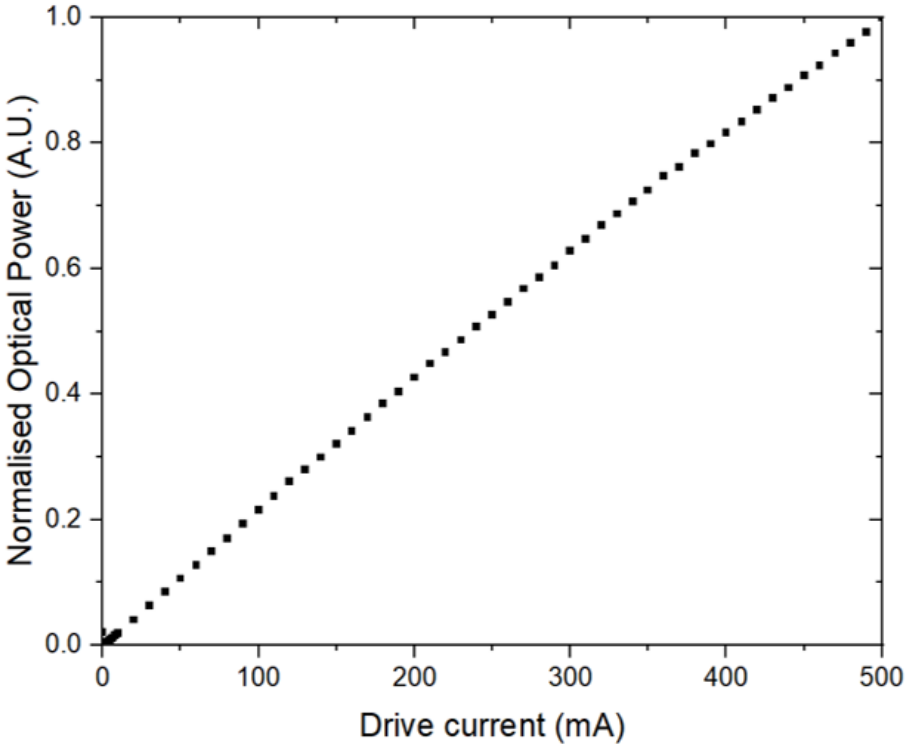

FIGURE 2.10: Normalised optical power as a function of LED drive current.

sensor is shown in figure 2.11. After initial switch-on, the LED appears to undergo a warm up period in which the power increases before reaching a stable value at around the 30 minute mark. This is uncharacteristic of an LED which should illuminate almost instantly at full power as soon as a current is applied. Including the warm up curve, the standard deviation from the mean is $\pm 1.6\%$. A similar effect had been noticed by previous investigation into the stability of commercially packaged visible spectrum LEDs, although on a much smaller scale [59]. This was thought to be due to high-brightness LEDs, similar to the 280 nm LED used here, with inferior thermal management taking longer to reach thermal stability.

Thermopile optical power sensors are based on thermocouples which convert incoming optical power to heat at the sensor surface [126]. For this reason, it was a concern that the thermopile sensor was also detecting heat emitted from the LED chip and reading this as a change in optical power.

To test this theory, a photodiode sensor was used to repeat this measurement. Photodiode sensors have a smaller detection range than a thermopile, 200-1100 nm in the

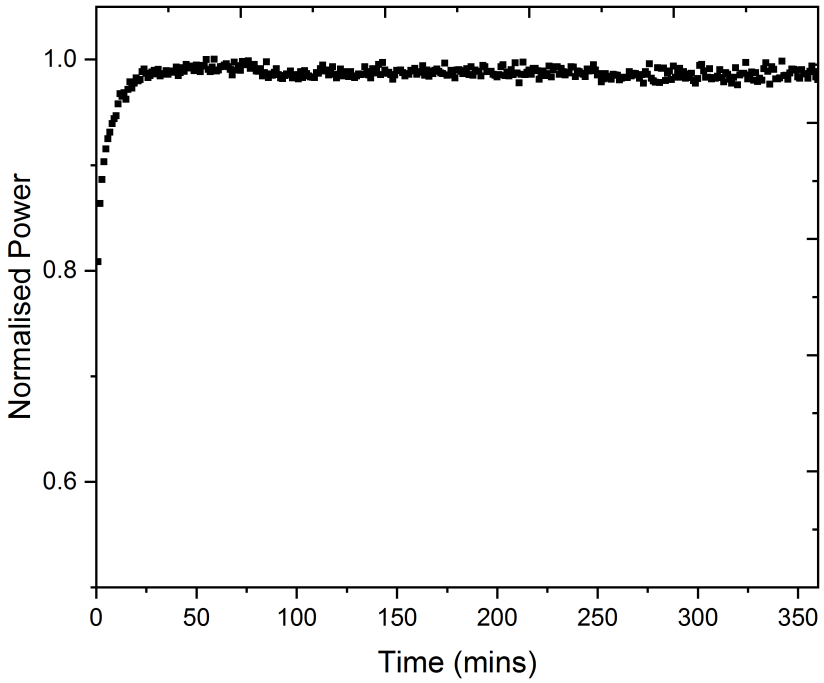

FIGURE 2.11: Normalised optical power of the LED over 6 hours as measured by a thermopile sensor.

case of a UV extended diode, but rather than using heat to generate signal, a photodiode is a semiconductor device in which incoming photons generate electrical signal based on the photoelectric effect.

The stability of the LED as measured using the photodiode sensor is shown in figure 2.12. The trend is much more stable than that measured by the thermopile sensor, with the warm up period disappearing completely. With this sensor, the standard deviation of the mean is reduced to $\pm$ 0.1%. This behaviour is characteristic of an LED and aligns very well with the stability of commercial LEDs measured previously [59]. In all future quantification of light dose in this work, the photodiode sensor will be used to avoid potential errors due to this effect.

2.3.3 Emission Pattern

The spatial emission pattern of the 280 nm LED across the field of view of the microscope is shown in figure 2.13, using fluorescence to indicate the spatial intensity of the LED.

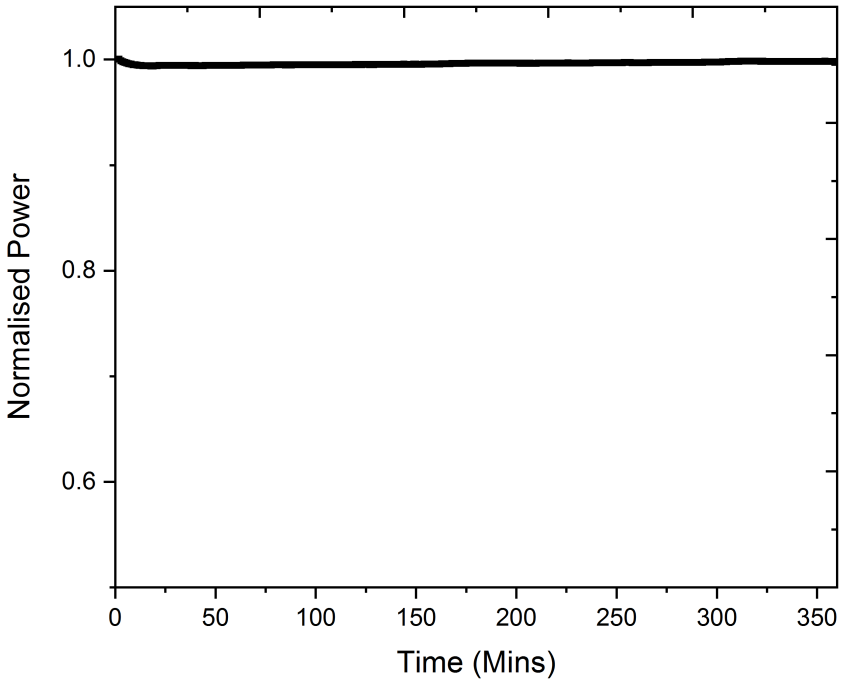

FIGURE 2.12: Normalised optical power of the LED over 6 hours as measured by a photodiode sensor.

Figure 2.13 (a) gives the intensity distribution across the field of view of the microscope and (b) gives the intensity profile taken horizontally through the centre of the field of view. The fluorescence intensity is at its highest in the centre of the field of view, reaching 60% of its maximum output at the edge. This is a substantial difference in illumination intensity across the field of view which would significantly impact the fluorescence excitation of any specimens imaged using the LED in direct illumination.

After adjusting the drive current between 50 and 350 mA and imaging the emission pattern at each current, it was found that changing the drive current had no effect on the intensity distribution profile, confirming that the result is a property of the LED itself and not the fluorescent specimen. Similarly, rotating and flipping the specimen had no effect on the obtained emission pattern.

By rotating the LED about its axis, the angular emission pattern of the LED can be measured and this is shown in figure **??** along with standard deviation error bars on the y-axis.

The incident angle has a tolerance of $\pm$ 1% as limited by the scale on the rotating

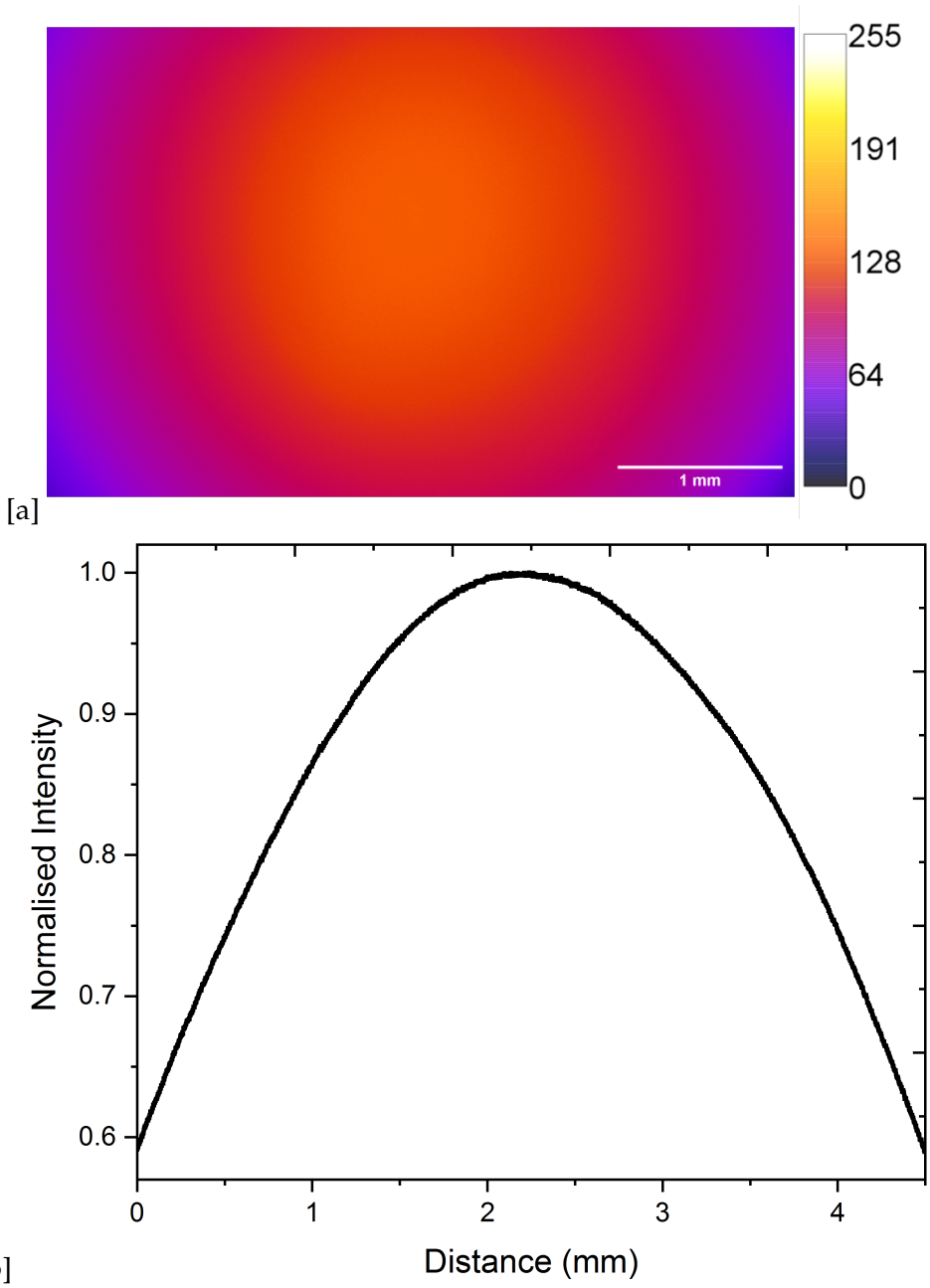

FIGURE 2.13: (a) Image of emission pattern of a Lambertian LED taken at a drive current of 350 mA and camera exposure time of 5 ms. A false colour look-up table has been applied to aid visualisation. (b) Plot profile of above image taken horizontally across the field of view at a width of 116 μm

stage. The intensity of the fluorescence emission is at its maximum at 0° and reaches approximately 50% of its maximum value at 60° from the normal which is consistent with the Lambertian trend so common in LED emitters [74]. To test the correlation between the data acquired using the LED and a Lambertian trend, the data was fitted using equation 2.7 (shown in dotted lines). The data fits the Lambertian trend with

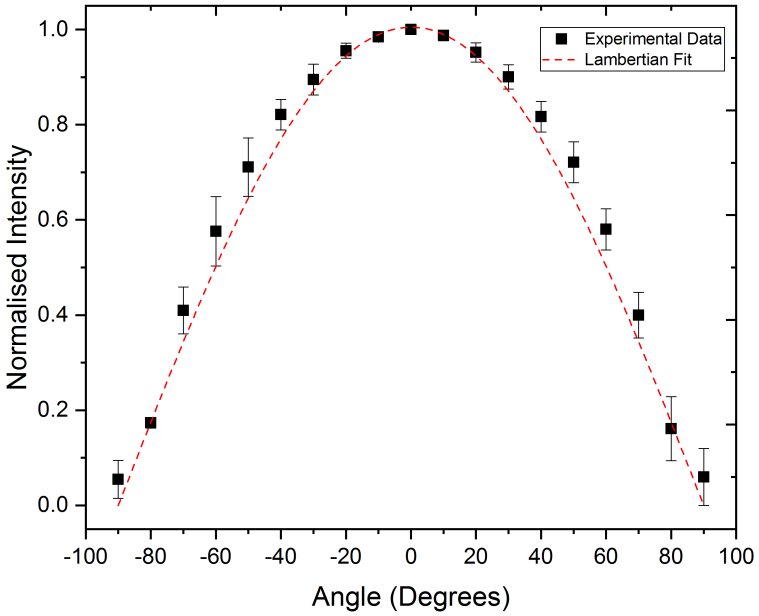

(A) Emission intensity as a function of angle.

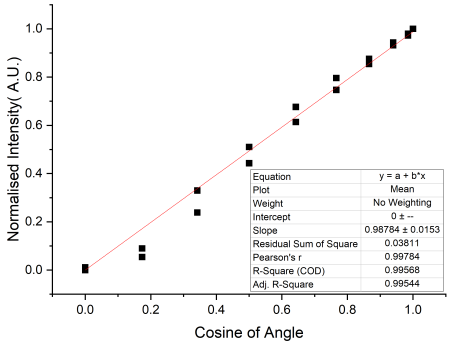

(B) Linearised version of 3.14 (A).

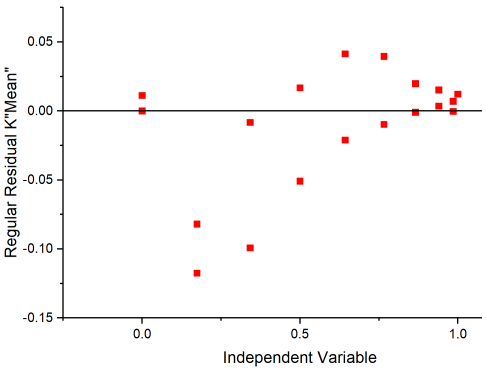

(C) Residual analysis of figure 3.14 (B).

FIGURE 2.14: (A) Emission intensity as a function of angle. The LED was rotated between 0° and 90° from the normal of the chip surface and each intensity value was recorded. Standard deviation error bars are shown on the y-axis and x-axis error bars correspond to the angular divisions on the rotating stage at ± 1°. Figures (B) and (C) show a linearised version of figure (A) with a line of best fit and corresponding fit analysis.

a coefficient of determination of 0.996, confirming that there is a strong correlation between the experimental data and a Lambertian trend. This is to be expected, as the 280 nm LED used in this work is a planar chip with no external ball lenses and hence fits the criteria for a Lambertian emitter.

To further support the finding that the LED did indeed exhibit a Lambertian emission pattern, figure 2.14a was linearised by plotting the cosine of the incident angle

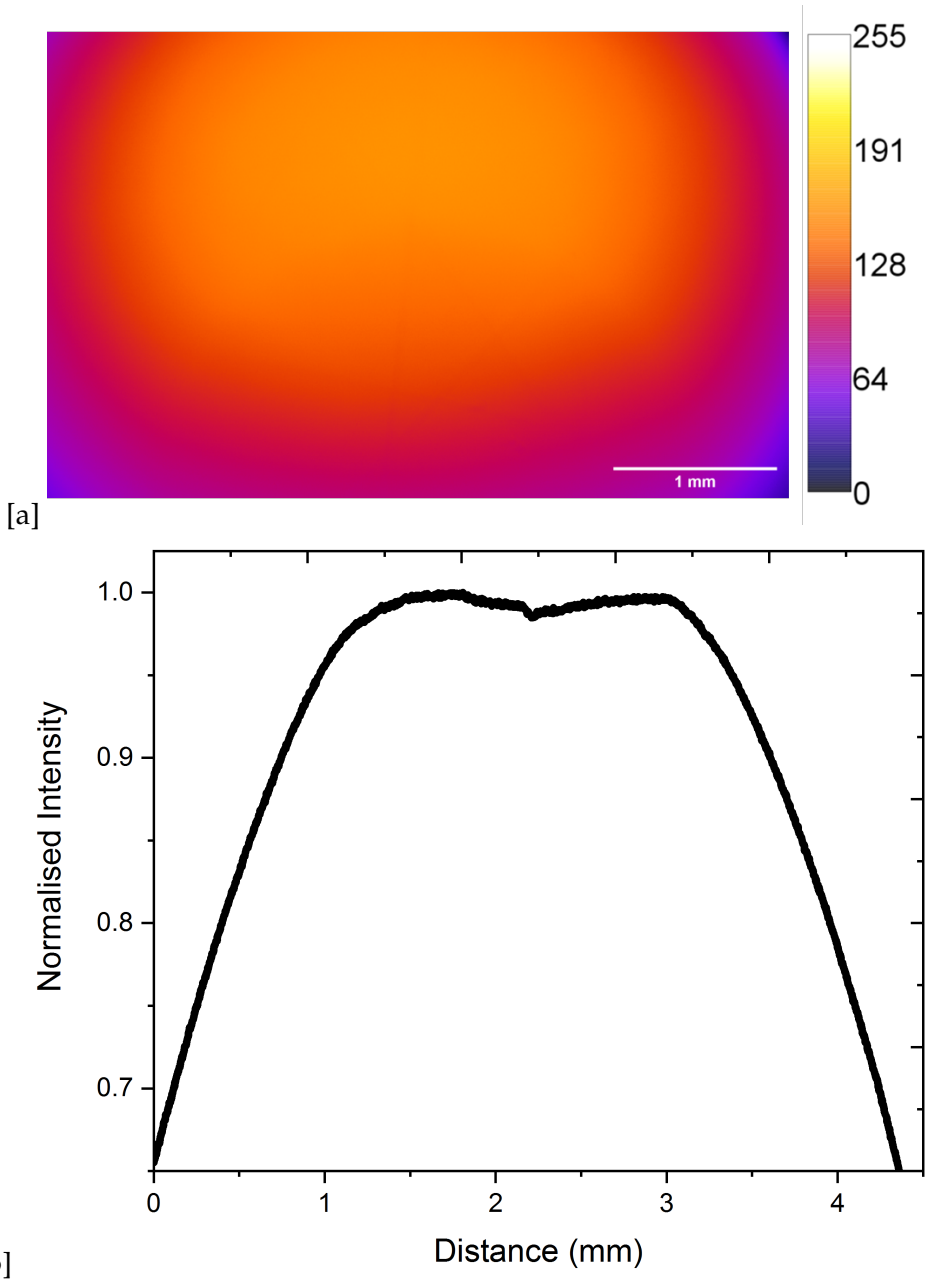

FIGURE 2.15: (a) Image of emission pattern of a Batwing LED taken at a drive current of 350 mA and camera exposure time of 5 ms. A false colour look-up table has been applied to aid visualisation. (b) Plot profile of above image taken horizontally across the field of view at a width of 116 μm

against intensity (figure 2.14b) and applying a linear fit. This again gave a coefficient of determination of 0.996 confirming that the data has a good correlation with the linear fit. The residuals analysis related to this linear fit is shown in figure 2.14c. The residuals appear to be smaller at angles close to 0°and 90°, and higher at other angles. This could be consistent with operator error in manually setting angles on the rotating stage as the stage presents with 20°angular increments.

To ensure that the measured results were in fact the emission pattern of the LED and not some other factor, a second LED was chosen to test the ability of the new technique to successfully identify different LED emission patterns. The spatial emission pattern of the batwing LED is shown in figures 2.15 and 2.16.

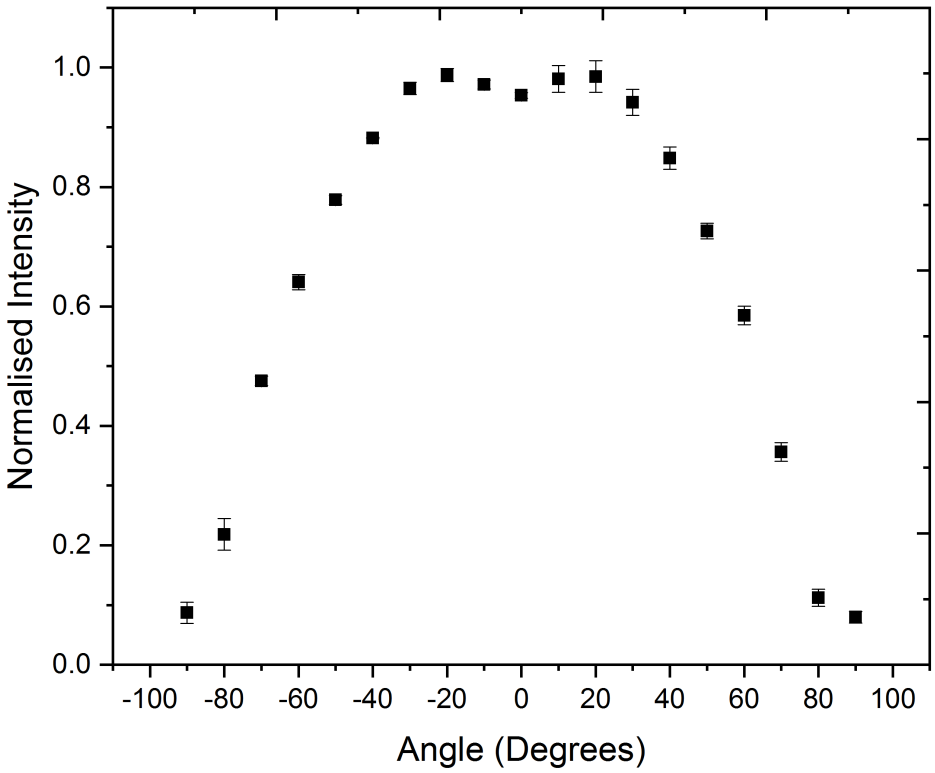

FIGURE 2.16: Emission intensity as a function of angle. The LED was rotated between 0° and 90° from the normal of the chip surface and each intensity value was recorded. Standard deviation error bars are shown on the y-axis and x-axis error bars correspond to the angular divisions on the rotating stage at $\pm$ 1°

These results are consistent with the data sheet supplied with the LED and show a significant difference from the measured emission pattern of the 280 nm LED, confirming that the technique can successfully distinguish between LEDs with different packaging geometries and characterise the emission patterns of different LEDs.

2.4 Discussion

Although the electroluminescence spectrum of the LED shows a sharp, narrow spectral band at 280 nm, the issue of parasitic emission can cause complications in fluorescence microscopy. As the spectral width of this parasitic emission is so broad, it will almost certainly overlap with fluorescence from labelled specimens and interfere with image contrast. This is particularly concerning in techniques such as MUSE [10] which choose not to use an excitation bandpass filter to spectrally separate excitation light from emission light, relying solely on the objective lens to act as a filter. As a result, using this LED necessitates the use of a bandpass filter to block this region of emission and ensure good quality images. Spectral filters in this region do exist, however, current technology limits transmission of 280 nm light through a bandpass filter in some cases to just 60% - meaning that 40% of 280 nm photons can be lost in the process. Thus, we often have a trade-off between preserving optical power and restricting LED spectral output to the desired wavelengths.

The LED stability is excellent when measured using the photodiode sensor, although the trends measured by the thermopile sensor differ significantly. This could potentially be because of the nature of detection of the thermopile sensor. Thermopiles measure power by converting a rise in temperature to a voltage [126]. As thermopiles have a spectral range high enough to absorb thermal radiation, this could potentially be absorbing excess heat emitted from the semiconductor and skewing measurements. To combat this, the photodiode sensor will be used for all future measurements of LED power in this thesis. Although the stability of the LED is much higher when measured with the photodiode sensor, there is still a small change in optical power within the first couple of minutes after LED switch on. Although this is uncharacteristic of an LED, which should illuminate at full power as soon as switched on and remain stable afterwards [59], this is a trend which has been observed in multiple LEDs in the study of Mubaid *et. al.* in 2019. This is thought to be a consequence of parameters including cooling and electronics [59]. For example, high-brightness LEDs can heat up very quickly and the heat-sink must work to propagate this heat away from the LED. Depending on the thermal properties of the heat sink, i.e. how quickly it can propagate heat, this could result in the LED temperature being unregulated for an initial period

after switch on, affecting the output for the reasons detailed in section 2.1.2. In addition to this, because the optical power of the LED is directly proportional to drive current, fluctuations in the power supply could also cause this initial change in optical power. For example, if the power supply takes a few minutes to reach a stable output, this could cause the trend shown in figure 2.12.

The new technique developed here to measure the emission pattern is not limited to LEDs emitting at 280 nm - it could be applied to measure any wavelength of deep-UV LED due to the ability of fluorescein to become excited by wavelengths as low as 200nm [127]. In addition, the technique can be used to measure the homogeneity of deep-UV illumination using methods such as critical and Köhler illumination by adding the appropriate optics in the illumination pathway between LED and fluorescent specimen, as previously demonstrated using visible wavelength LEDs [81].

Although this technique has been useful in measuring emission patterns of deep-UV LEDs, the emission patterns exhibited, particularly by the 280 nm LED intended for use throughout the project, are not ideal for direct illumination in fluorescence microscopy due to significant variation in illumination intensity across the field of view of the objective lens. Increasing the LED-specimen distance can reduce the variation in intensity as the angular distribution across the field of view becomes smaller. However, this is at the expense of the intensity of light reaching the specimen which is inversely proportional to the square of the LED-specimen distance (equation 2.7). For this reason, the LED should not be used to directly illuminate the specimen as there is a trade off between illumination homogeneity and optical power at the specimen plane, which are both critical in fluorescence microscopy. Using this information, optical designs with external quartz lenses to homogenise the light can be explored in chapter 3 which focusses on determining the optimum method of delivering 280 nm light to the specimen plane for fluorescence microscopy acquisition.

2.5 Conclusion

This chapter has outlined the development of a novel method to measure the emission pattern of a 280 nm LED using a standard camera and visible-wavelength fluorescence. This technique was validated by comparing the measured emission pattern

of the LED to its theoretical pattern, and also by using a second LED with differing emission pattern to ensure the technique could distinguish between LED types. This allowed accurate measurement of the emission pattern of the 280 nm LED in use within this thesis which will assist in developing a suitable optical set up to deliver homogeneous 280 nm illumination to the specimen plane in chapter 3. This chapter has also investigated two further optical properties to consider when developing an LED into a suitable microscope light source: the electroluminesence spectrum and LED stability, including any adjustments that have to be made in order to accurately measure in the deep-UV. Detailed measurements of the electroluminescence spectrum using two spectrometers revealed a strong, narrow peak at 280 nm but also unforeseen parasitic emission across the visible spectrum. With this information available, I was able to identify two suitable excitation filters which I will use in future experiments to narrow the LED spectrum to the desired wavelengths. The 280 nm LED was found to be highly stable, with a standard deviation from the mean of only $\pm 0.1\%$ over a period of 6 hours. It was also found that a thermopile sensor is not a reliable detector for high-brightness LEDs of this type and as a result I will use a photodiode detector for any further power measurements of this LED.

Chapter 3

Systematic comparison of microscopy illumination techniques compatible with 280 nm

Integrating a new LED system into a commercial microscope for fluorescence excitation is a relatively simple modification. Many LED systems for fluorescence microscopy are designed to attach to the epifluorescence port of the microscope, either by direct fit or by liquid light-guide. Once fitted to the microscope, the light then passes through a series of lenses and apertures to align for Köhler illumination, before being reflected by a dichroic mirror and passing through the objective lens to illuminate the specimen. Whilst epifluorescence is a simple method of illumination for visible wavelength light, due to the low transmission of 280 nm through glass optical elements (of which commercial microscopes contain many) it is almost impossible to illuminate in epifluorescence with this wavelength on a non-modified microscope. In this chapter, I systematically compare existing methods to overcome this transmission issue in fluorescence imaging, with the aim of identifying the optimum method used to study QD-labelled cells excited using 280 nm light in fluorescence microscopy in later chapters. I expore methods including the use of transmission fluorescence and epifluorescence with specialised UV-compatible objective lenses. I identify the quality of these methods with 280 nm excitation by taking into consideration parameters such as availability of light at the specimen plane, homogeneity of illumination and quality of the resulting images. I then compare these methods and identify the optimum method to implement fluorescence imaging with 280 nm excitation which will then be

used in chapter 4 for widefield imaging, and in chapter 5 for standing wave imaging, of QD-labelled cells.

3.1 Introduction

One of the most significant issues in integrating 280 nm light into a microscope is the transmission of deep-UV light through optical elements. A typical commercial microscope will have optics manufactured from a type of glass usually known as optical glass, capable of transmitting light of wavelengths ranging from the near-UV (350 nm) to the near-infrared. One of the most popular choices of optical glass is N-BK7, a type of borosilicate glass [128], and a typical transmission curve of 10 mm thick N-BK7 can be shown in figure 3.1 [129]. From this figure, we can expect just ∼1.6% transmission of 280 nm light through each glass optical element - a dramatic loss in light by the time light passes through the optical elements in a commercial microscope needed for Köhler illumination.

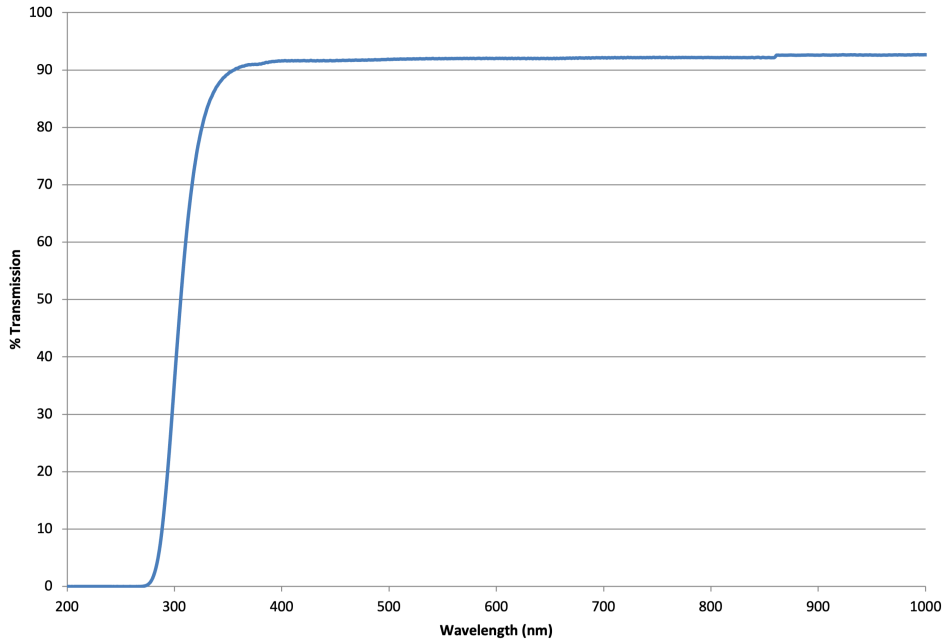

FIGURE 3.1: Transmission curve of a 10 mm thick NBK-7 type plano-convex lens. Reproduced with permission from Thorlabs [129].

The issue of transmission is not limited to internal microscope optics. A well-manufactured objective lens contains several lens elements, each contributing to a specific correction factor of the objective. Each of these lens elements contributes to

absorption of 280 nm light, making it almost impossible to deliver any light to the specimen plane, even if limited light were to make it through the Köhler illumination optics. Since the optical power of the 280 nm LED used here is already limited to just 100 mW, it is necessary to develop a higher throughput optical system to allow sufficient excitation light at the specimen plane to excite fluorescence from samples.

In contrast to glasses such as N-BK7, quartz (sometimes referred to as fused silica) is highly transmissive in the UV. A transmission curve of a 10 mm thick quartz lens is shown in figure 3.2 [130]. From this data, we can expect approximately 93% transmission at a wavelength of 280 nm - a stark contrast compared to conventional glass. Hence, quartz optics are a much better solution for guiding UV light to the specimen plane. However, it is not currently possible to purchase a commercial microscope whose optics are made from quartz. For this reason, the internal optics of a commercial epifluorescence microscope would have to be stripped and replaced with quartz to allow UV transmission.

Because of the limitations in imaging with 280 nm light on a commercial microscope, several techniques to overcome this issue have been established, including the use of specialised objective lenses such as quartz and reflective objectives, transmission fluorescence and oblique illumination.

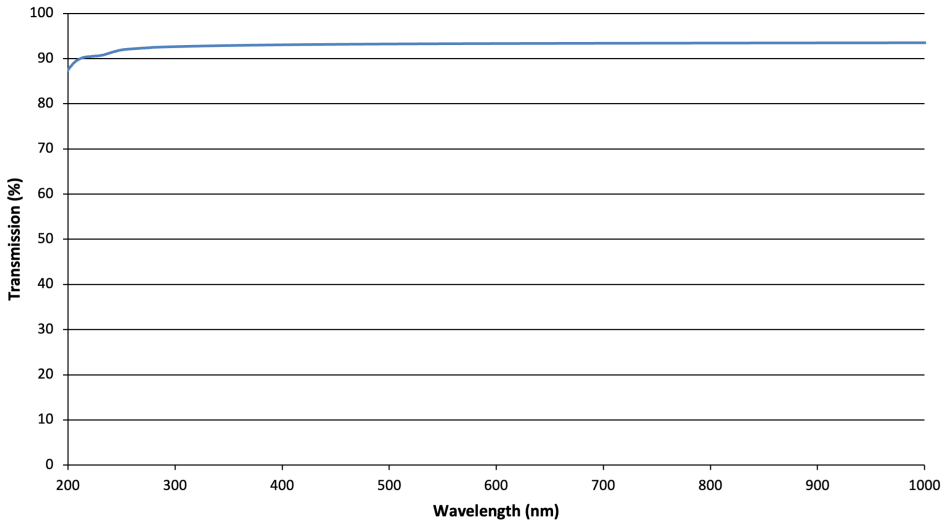

FIGURE 3.2: Transmission curve of a 10 mm thick quartz plano-convex lens. Reproduced with permission from Thorlabs [130]

.

The first of these techniques uses the quartz objective lens. These objectives are manufactured fully from quartz and as a result, lens elements have high transmission

and low autofluorescence in order to optimise image quality. Although excellent for autofluorescence imaging of biological specimens [39], quartz objectives have limited applications and as a result are not widely available commercially. One of the only microscope manufacturers to stock quartz objective lenses are Zeiss who have a limited range of Ultrafluar objective lenses. These lenses are available in only two magnifications - 10x/0.2NA and 40x/0.6NA glycerol immersion. These lenses have significantly lower NAs when compared to their glass counterparts of equal magnifications, limiting the lateral and axial resolution of the system as well as the amount of fluorescent light that can be collected from the specimen when compared to using glass objectives.

Owing to their excellent transmission of deep-UV light, quartz objectives have been used extensively in deep-UV epifluorescence imaging. This includes the first use of deep-UV microscopy by August Köhler in 1904. Some more recent examples of quartz lenses in deep-UV microscopy include investigation of native protein fluorescence using UV epifluorescence microscopy [36] and the work of Zeskind *et. al.* described in detail in chapter 1, which uses a quartz objective lens to carry out deep-UV autofluorescence microscopy of biological specimens [39].

The second type of specialised objective is a reflective objective. These objectives use reflective rather than refractive elements to focus and collimate light.

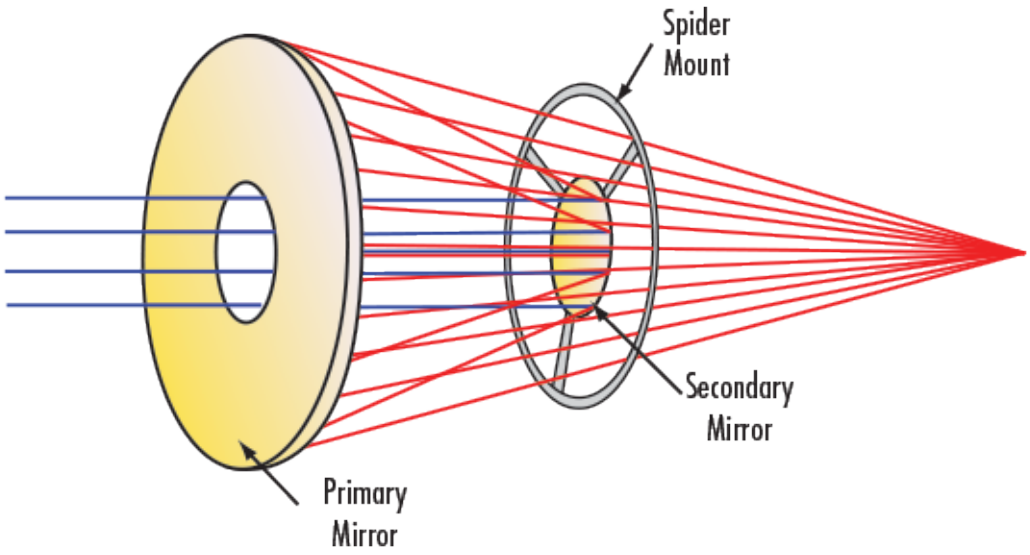

FIGURE 3.3: Schwarzschild reflective objective lens. Reproduced with permission from Edmund Optics [131].

The most common type of reflective objective is the Schwarzschild objective (figure

3.3) which uses two mirrors - a small "secondary" mirror at the bottom of the objective facing upwards (in the case of an upright microscope), suspended by two or three small pieces of metal commonly referred to as spider legs. The primary mirror is found at the top of the objective, facing downwards. Both mirrors are curved in order to focus light [132, 133].

Reflective objectives are particularly advantageous in deep-UV microscopy, or in imaging applications which use a wide range of wavelengths. This is because the reflective (rather than refractive) nature of the lens allows for the focusing of a broad range of wavelengths without chromatic abberation [132]. In addition to this, many metals reflect deep-UV light well, and lenses with enhanced reflective coatings specific to the deep-UV are readily available. However, reflective objectives also come with their own caveats. In these systems, a central area of the secondary mirror will reflect light straight upwards back through the cavity in the primary mirror instead of reflecting the light onto the primary mirror. This is known as obscuration, usually quoted in the objective specifications, [131] and can be anywhere between 15% and 25% [133]. Secondly, as the mirrors used in these objectives are curved, there is a discrepancy in the focal points of light rays across the mirrors, resulting in a lack of flatness of field. Therefore, images appear sharply in focus in the center of the image and out of focus around the edges of the image. Reflective objectives can only focus, and not collimate light, at the specimen plane. From figure 3.3, light passing through the objective must be focussed by the mirrors to avoid any obscuration by the secondary mirror. If the light were to be collimated by the primary mirror, the light reaching the specimen plane would have a large central portion missing due to obscuration from the secondary mirror, alongside the 3 spider mounts, which does not alleviate the problem of inhomogenous specimen illumination. As a result, it is possible only to have critical illumination of the specimen with this objective lens.

Reflective objectives, however, are free from chromatic aberration - their reflective, rather than refractive nature ensures that light of all wavelengths are focussed to the same point [132]. Reflective objectives are also efficiently corrected for astigmatism, spherical aberration and coma aberration [133].

Because of their wide range of transmission, reflective objective lenses are commonly used in applications using wavelengths on the far ends of the visible spectrum

[131]. In deep-UV microscopy specifically, reflective objectives have been used to provide UV excitation to specimens via the epifluorescence pathway since 1954, when Uretz *et. al.* developed a reflection based epifluroescence microscope to image chromosomes with UV light [134]. Since this time, reflective objectives have been used to efficiently provide excitation light at wavelengths down to 210 nm [135].

More recently, alternative approaches have been applied to deep-UV microscopy to avoid the use of modified epifluorescence designs. Most notable is the MUSE microscope design [10, 46, 136, 137, 138], described in chapter 1 which uses off-axis illumination to provide UV excitation light to the specimen [50]. This design, however, limits the available objective lenses to low magnifications such as 4x and 10x, due to the long working distances required for the excitation light to reach the specimen plane, and sacrifices illumination homogeneity due to the elongation of the off-axis light hitting the specimen. For this reason, an alternative method of specimen illumination was sought which can provide good illumination homogeneity and that is not limited by choice of objective lens.

One of the simplest forms of a fluorescence microscope is the transmission fluorescence microscope. This takes the general form of a brightfield microscope (such as that in figure 1.2, with light transmitted through the specimen and into the objective lens, but uses excitation and emission filters to prevent excitation light from reaching the detector. This has implications on image contrast as filters are not perfect and some excitation light can reach the detector, however this negates the need for expensive UV-compatible objectives and therefore makes the microscope much more accessible and versatile. Transmission fluorescence using 240-280 nm excitation light has previously shown a simple way to excite specimens in fluorescence microscopy for a number of applications including FLIM [37] and identifying protein crystals [36]. This method of fluorescence microscopy is advantageous compared to epifluorescence in the case of deep-UV microscopy as it allows for the use of standard objectives since only visible-wavelength fluorescence needs to be transmitted by the objective lens. However, a further limitation of this technique is the penetration depth of 280 nm light into tissue [10]. This limits excitation of fluorescence to only a few μm below the specimen surface, limiting this technique to thin, transparent specimens.

When searching for a suitable method of specimen illumination when using this

method, the following parameters were taken into consideration. The first was transmission of 280 nm light through the optical system, or more precisely the available optical power of light at a wavelength of 280 nm at the specimen plane. This is because the available excitation power is critical for excitation of fluorescence, particularly in weakly emitting specimens, and the 280 nm LED itself has already limited optical power of only 100 mW. The second was homogeneity of illumination light. As discussed in chapter 2, inhomogneity of illumination across the specimen is problematic in fluorescence microscopy as differences in excitation intensity across the specimen will lead to increases in fluorescence intensity, causing misleading results. The third parameter is quality of fluorescence images, particularly image contrast which is typically defined by [77, 139]:

$$\text{Image Contrast} = \frac{\text{Brightness of Specimen - Brightness of Background}}{\text{Brightness of Specimen + Brightness of Background}} \tag{3.1}$$

From this equation, contrast is measured in range between 0 and 1, with 1 being the maximum achievable image contrast associated with infinitely low background and infinitely high fluorescence intensity. These imaging parameters will be considered along with the practicality and versatility of use of the system being discussed.

3.2 Methods

3.2.1 Transmission of 280 nm light through a commercial microscope

In order to demonstrate the difficulties in using a commercial microscope with 280 nm light, the transmission of this wavelength through various commercial refracting objective lenses designed for visible wavelength operation and the internal lenses of a commercial microscope (Olympus BX50) were measured (at a drive current of 350 mA) using a Thorlabs power meter (PM100) coupled to a UV-enhanced photodiode (S120VC). The power of the 280 nm LED was measured before and after each lens element and the power loss attributed to each element was calculated. To ensure that the transmission measured was only at the peak of the 280 nm LED and not longer wavelength parasitic emission described in chapter 2, a 280/10 nm bandpass filter was placed in front of the LED for all measurements.

3.2.2 Additional 280 nm excited autofluorescence within the fluorescence microscope pathway

In addition to the transmission of 280 nm light through glass and quartz optics, the autofluorescence of some additional elements within the optical path were measured. This included coverslips and slides, which are used in all specimen preparations for imaging under the microscope, and specimen mounting media which is used to hold the specimen in place between the coverslip and slide. This is a particularly important consideration in sample preparation when using 280 nm excitation, as autofluorescence of coverslips, slides and mounting media can interfere with the fluorescence signal obtained from the specimen and cause low image contrast.

In order to compare the autofluorescence of typical glass coverslips and slides to those of quartz, borosilicate coverslips (VWR 631-0153) and slides (VWR 630-2012) were used, alongside quartz coverslips (Alfa Aesar 43211) and slides (Alfa Aesar 42296). These were each imaged using 280 nm light at a current of 350 mA and an exposure time of 350 ms and the mean fluorescence intensity of these images was recorded using Fiji.

Similarly, the autofluorescence of 3 available mounting media were measured to determine the optimum mountant to be used for 280 nm excitation. These were ProLong Glass (Thermo Fisher P36982), VECTASHIELD antifade mountant (Vector Laboratories H-1000-10) and gelvatol, which was made in the lab by a previous group member.

Each of these mounting media were placed between a coverslip and slide and imaged with 280 nm light at an LED current of 350 ms and an exposure time of 500 ms. The mean fluorescence intensity of these images were again recorded.

3.2.3 Quartz objective

The epifluorescence microscope constructed to allow UV transmission is shown in figure 3.4. This design is broadly similar to a commercial epifluorescence set up described in figure 1.5, but built from off-the-shelf quartz optical components.

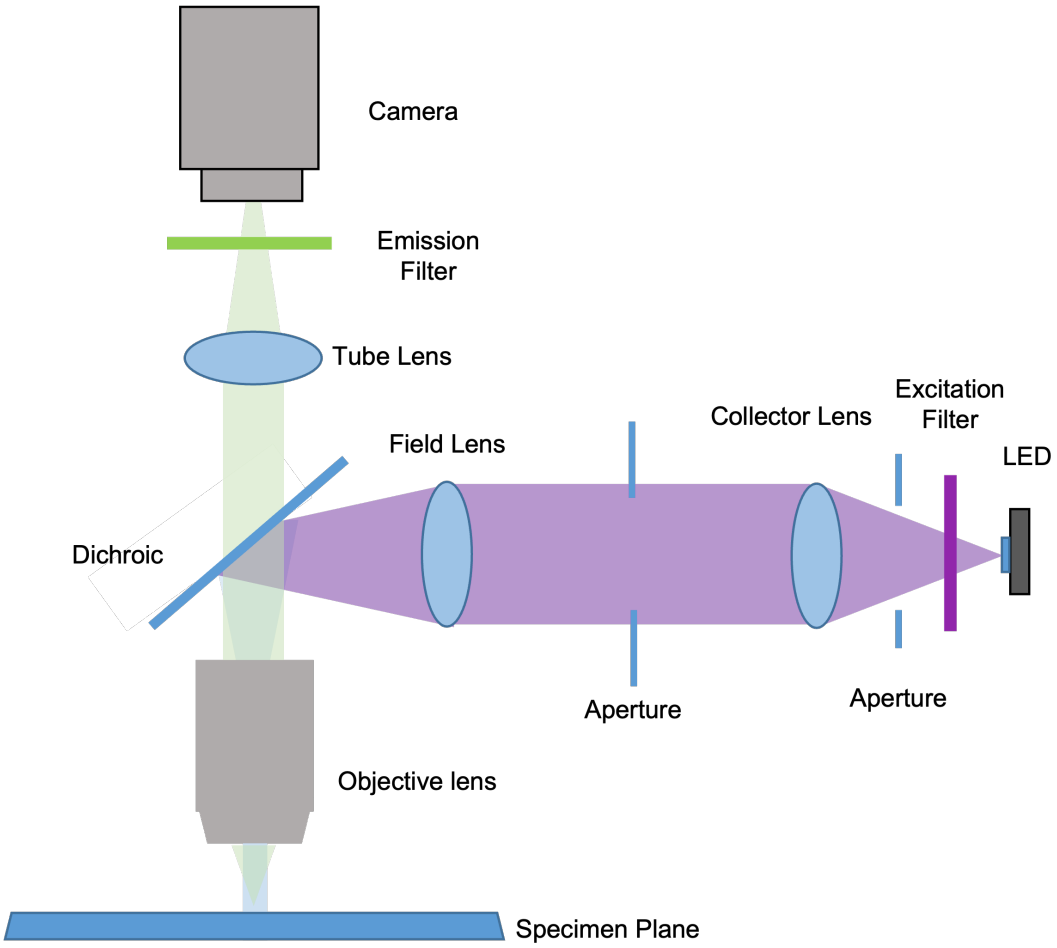

FIGURE 3.4: Custom-built quartz epifluorescence microscope for 280 nm transmission.

To construct this microscope, two apertures (Thorlabs ID25/M) were used to control the intensity and spot size of the illumination light. A quartz collector lens (Thorlabs LA4052-UV) with a 35 mm focal length was used to collect and collimate as much 280 nm light as possible. A second quartz lens (LA4380-UV, f = 100 mm) was used to focus the 280 nm light at the back focal plane of the objective. A dichroic mirror with high reflectance at 280 nm and transmission beyond 400 nm was purchased from Teledyne Acton Optics (266/V-FR45). This was placed at an angle of 45° above the objective lens to reflect 280 nm light to the objective and transmit any fluorescence. A tube lens was purchased from Edmund Optics at a focal length of 175 mm (49-363) which was as close as possible to the tube lens length used by Zeiss to ensure the correct magnification of the specimen was achieved. An x-y adjustable microscope stage was used to support the specimen and this was mounted on a translation stage (Thorlabs MT1) to control the stage position axially, allowing the specimen to be focussed. Finally, the IDS uEye camera described in chapter 2 was used as a detector and controlled using the uEye software. To compare the transmission of light through the quartz optical elements to that of the glass elements detailed in section 3.2.1, the same method was used.

The quartz objective used was a 10x/0.2NA objective lens and this was loaned by Zeiss as an ex-demo model. To test the ability of this objective lens to transmit light to the specimen plane, the power at the specimen plane was measured using the same Thorlabs power meter and sensor detailed above. To determine the homogeneity of illumination across the specimen plane, a Chromablock slide was used (Chroma 92001). The 280 nm LED was turned on at a drive current of 500 mA and allowed to excite fluorescence from the fluorescent slide and an image of this was acquired at a 500 ms exposure time. A line profile with a width of 20 pixels was taken horizontally across the field of view of the microscope using Fiji to average fluorescent signal. To analyse this, this was imported into Python and a standard deviation of the mean intensity was calculated to determine the variation in illumination homogeneity across the field of view.

To assess the ability of this objective to allow excitation of fluorescent specimen, eosin stained lens tissue paper was used as a sample. Eosin was chosen as a fluorescent dye as this has strong absorption below 300 nm as described in the work of MUSE [10].

To make this, 10 μM eosin was dissolved in water and a piece of lens cleaning tissue was submerged in this for 5 minutes. The tissue was then sandwiched between a quartz coverslip and slide. An image of this specimen was acquired using this set-up at the LED drive currents required to produce a fluorescent signal - in this case, 1 s exposure and 500 mA drive current. The image was imported into Fiji and thresholded to create ROIs containing the fluorescent tissue fibers. The mean fluorescence intensity of the fibers were measured, and then an ROI of the image background was obtained to measure the mean intensity of the background. The image contrast was then calculated by equation 3.1.

3.2.4 Reflective objective

To image in epifluorescence using a reflective objective, the same optical design described in figure 3.4 was used, switching the quartz objective lens used previously for a reflective objective. The reflective objective used here was an Ealing 25-0555 with 15x magnification and an NA of 0.5. This objective lens has a significantly higher NA when compared to the quartz objective at a similar magnification.

To measure the transmission of 280 nm light through this objective, the optical power at the specimen plane was measured using the method described above.

The uniformity of illumination of this objective was also measured due to its difference in illumination method compared to refractive lenses. To do this, the method described in section 3.2.2 was used. This was repeated with a quartz homogenising rod (Edmund Optics 65-838) in place to homogenise the light. Homogenising rods are hexagonal pieces of glass several cms long that use total internal reflection to homogenise light [140]. Light exiting the rod is homogenous at the rod surface and an image of this surface can then be re-imaged onto the specimen plane to create homogenous illumination. To do this, the set-up in figure 3.4 was used with the homogenising rod placed between the LED and collector lens. The 280 nm LED was placed as close as possible to the homogenising rod surface in order to collect as much light as possible.

To assess the image quality of the reflective objective, the eosin stained tissue was again used as a specimen (with exposure time of 500 ms) and image contrast was calculated by equation 3.1.

3.2.5 Transmission Fluorescence

To create a transmission fluorescence set-up, the stage, tube lens, emission filter and camera from the epifluorescence design were kept consistent. In place of the specialised UV objective, a standard Olympus objective (20x/0.5 NA) was used. Below the stage, a UV-compatible optical set-up was constructed as follows (figure 3.5):

The 280 nm LED was collimated by a doublet of two identical f = 30 mm, D = 20 mm quartz lenses (Edmund optics 49-965). Doubling up the lenses to collimate the 280 nm LED light was carried out thanks to the optical modelling of Alex Gramann at CoolLED. Due to the f-number of these lenses (focal length/diameter) being high, more rays of light from the LED can be collected meaning that the intensity at the specimen plane should be higher.

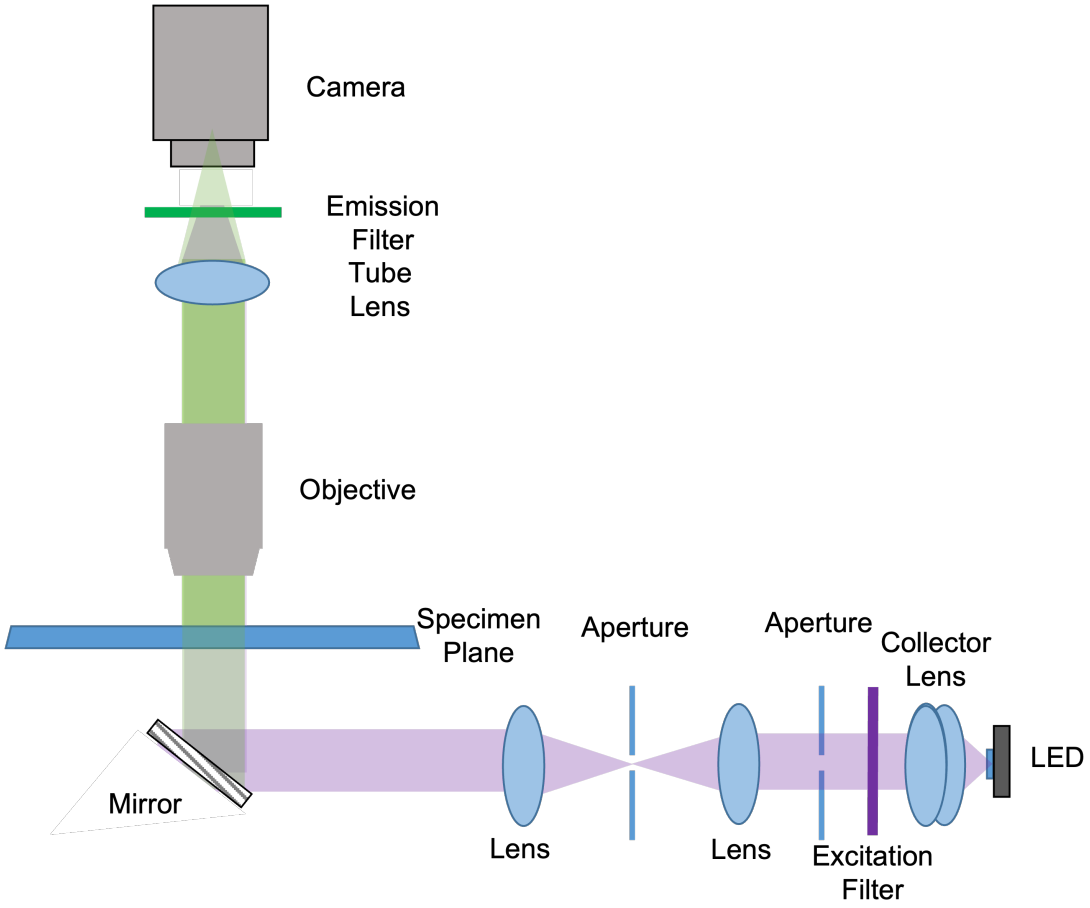

FIGURE 3.5: Transmission fluorescence microscope with UV excitation.

After collimating the 280 nm light, the 280/10 nm filter used in chapter 2 was put in place to narrow the emission of the LED. This is particularly important in transmission fluorescence microscopy as here we are relying solely on excitation and emission filters

to preserve image contrast. After the excitation filter, an aperture is used to adjust the light intensity, although to preserve optical power at the specimen plane, this was kept open. Next, a quartz lens (f = 50 mm) was used to focus 280 nm light onto a second aperture used to adjust the spot size of illumination light. After diverging, the 280 nm light is then re-collimated by a f = 100 mm quartz lens and reflected at 90° to the specimen plane by a UV-enhanced aluminium mirror (Thorlabs PFSQ10-03-F01).

Due to the excitation light illuminating the specimen from the opposite direction of the objective lens, this technique does not require any UV-compatible objective lenses, but also does not limit the objectives used to low-magnification, long working distance lenses such as in MUSE systems [10].

The optical power at the specimen plane available with this set-up was measured as above. To test the homogeneity of illumination across the specimen, the same Chromablock fluorescent slide was used as above. To compare the imaging quality of this setup with that of the specialised objectives, eosin stained tissue paper was again used and image contrast was calculated by equation 3.1.

3.3 Results

3.3.1 280 nm transmission through glass and quartz optical elements

The measured transmission of different make and models of objective are shown in table 3.1, alongside other microscope optics required for epifluorescence microscopy such as Köhler optics and dichroic mirrors.

Optical Element	Transmission through element at 280 nm
Internal Lenses for Köhler Illumination	0.01%
400 nm Dichroic Shortpass	10%
Olympus UPlanFl 10x/0.3 NA	0.009%
Leica Plan 25x/0.4 NA	0.01%
Olympus UplanSApo 40x/0.9 NA	0.002%
Nikon SFluor 60x/0.7 NA	0.001%

TABLE 3.1: Percentage transmission of 280 nm light through various optical elements found in commerical microscopes.

All lens elements reveal low transmission of 280 nm light, typically less than 0.01%. Low magnification and NA objective lenses perform better than high magnification, high NA lenses, presumably due to the higher number of lens elements present in the high magnification, high NA objectives. This limits the optical system to low resolution in the case of using 280 nm illumination in order to preserve optical power. Although a 400 nm dichroic longpass filter is designed to reflect light below 400 nm, this still has very low reflectance at 280 nm, at only 10%. This further supports the evidence that standard optics have low throughput at 280 nm and if high UV transmission is needed, specialised UV optics must be used.

The low transmission of 280 nm light through these lens elements has severe implications for an LED with an optical power of 100 mW. Based on these calculations, an LED of 100 mW after being transmitted through the internal lenses, reflected by a dichroic mirror and passing through the best performing objective, would produce 0.7 nW of optical power at the specimen plane. This is far from the typical optical power required to excite sufficient fluorescence from a specimen to generate a good quality image with a decent signal to background ratio (typically in the range of a few mW). Therefore, using a standard commercial epifluorescence microscope with this wavelength of illumination light is not feasible.

To demonstrate the increase in throughput of 280 nm light through quartz compared to other types of glass, table 3.3 shows the measured transmission through the optical system described in figure 3.4.

Optical Element	Transmission through element at 280 nm
280/10 nm bandpass filter	41.98%
Quartz plano-convex lens	96.94%
UV Dichroic	86.79%

TABLE 3.2: Percentage transmission of 280 nm light through optical elements in set up described in figure 3.4

Compared to using glass optical elements, we see a significant increase in transmission at 280 nm when using optics optimised for deep-UV performance. While the quartz plano-convex lenses and UV-enhanced dichroic mirror perform very well, there is surprisingly low performance in the 280 nm bandpass filter. This is likely because the narrow FWHM of the filter is cutting off some of the LED spectrum in combination with the limited percentage transmission associated with this filter. Throughput could be improved by using the 300/50 nm filter described in chapter 2 which has a larger transmission spectral FWHM.

3.3.2 Autofluorescence of coverslips, slides and mounting media

The necessity of using quartz coverslips and slides within the optical path when using 280 nm excitation was determined by comparing the autofluorescence intensities of those compared to standard glass coverslips and slides. The result of this is shown in figure 3.6. From this graph, it is clear that using a combination of a quartz coverslip and quartz slide significantly reduces autofluorescence intensity when compared to using a glass coverslip and slide, or a combination of glass coverslip quartz slide and vice versa. For this reason, for the best possible image contrast quartz coverslips and slides were identified for use in all future imaging of biological specimens with 280 nm excitation.

Similarly, the autofluorescence of a few different available mounting media were investigated to determine the best mounting medium for imaging with 280 nm light. The result of this is shown in figure 3.7. VECTASHIELD performs the worst, with a significantly higher autofluorescence intensity than ProLong glass and gelvatol. Gelvatol appears to have the lowest autofluorescence intensity under 280 nm excitation.

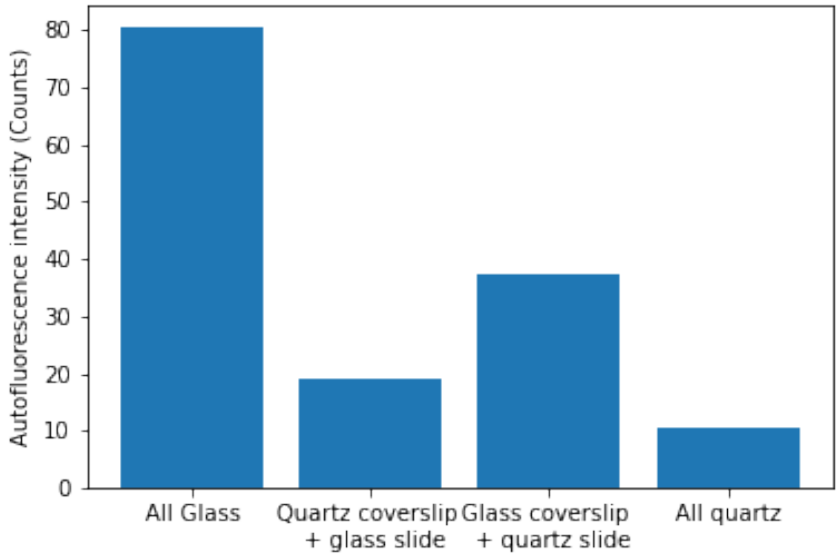

FIGURE 3.6: Autofluorescence intensities of combinations of glass and quartz coverslips and slides under 280 nm excitation.

As a result of this, gelvatol was identified as the mountant of choice for all future 280 nm imaging of fluorescent specimen.

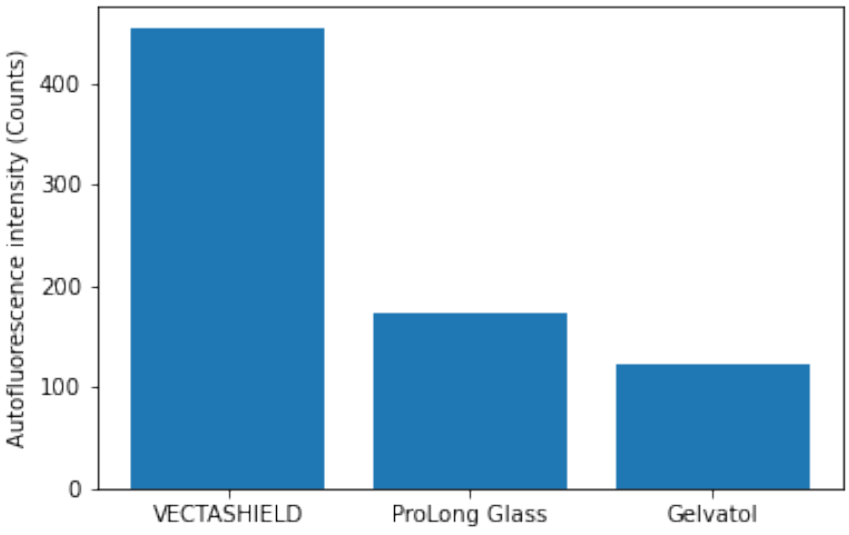

FIGURE 3.7: Autofluorescence of a selection of different mounting media under 280 nm excitation.

3.3.3 Quartz Objective

To determine the throughput of the quartz objective lens, the power at the specimen plane was measured and this was found to be 1.14 mW. In terms of the transmission of the objective lens, this is somewhat surprising as Zeiss quote 70% transmission at a wavelength of 300 nm. Whilst the optical power of ∼1 mW is still low compared to the powers achievable with visible wavelength LEDs, this is much improved over the performance of the glass microscope optics shown in table 3.1.

The epifluorescence pathway was set up in Köhler illumination to produce as homogeneous illumination at the specimen plane as possible. The illumination uniformity achieved here is shown in figure 3.8.

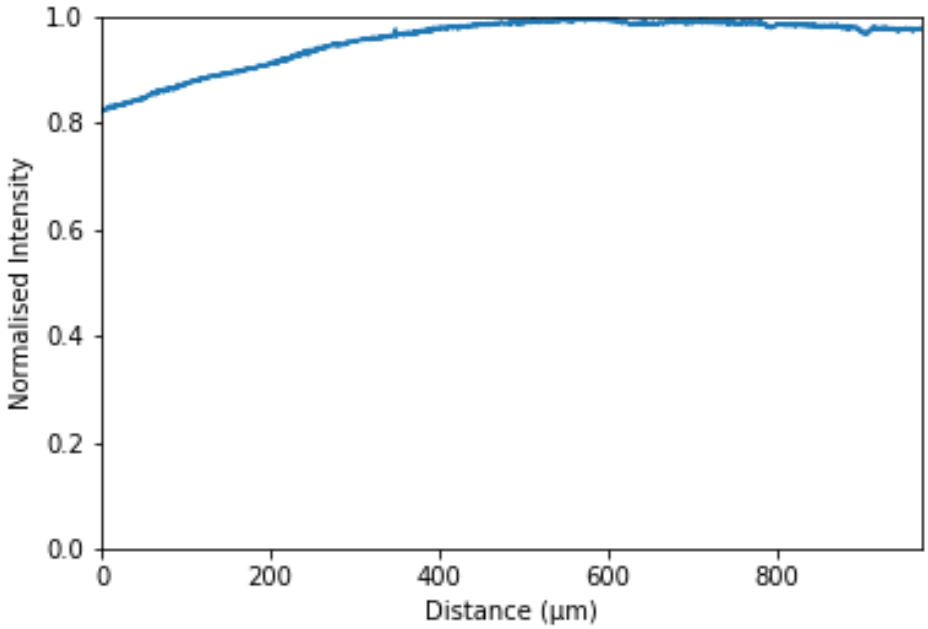

FIGURE 3.8: Illumination homogeneity of epifluorescence set up using a quartz objective lens.

This shows relatively good homogeneity with slight decrease towards the edge of the field of view. Overall, there is a standard deviation of only ±4.9% in illumination intensity across the nearly 1 mm field of view of the objective. Although the intensity does drop off towards one side of the field of view, this could potentially be improved with better optical alignment.

An image of eosin stained tissue paper was acquired to indicate the quality of images obtained using this set up and this is shown in figure 3.9.

FIGURE 3.9: Image of eosin stained tissue paper taken using an epifluorescence set-up with a quartz objective lens. Acquired with an exposure time of 1 s.

Although this image was acquired at a high drive current of 500 mA (driving the LED higher than the 350 mA recommended by the manufacturer) and an exposure time of 1 second, the image has a low contrast (0.16) and relatively low fluorescence counts. This is most likely due to the limited excitation power available at the specimen plane and results in having to use particularly high exposure times to obtain any fluorescent signal. Despite high drive current and high exposure time, the fluorescence image is relatively poor compared to typical images of fluorescent specimens obtained with commercial microscopes and visible wavelength light. This has implications in applications such as time-lapse imaging where the long exposure times required to obtain fluorescent signal will severely impact the temporal resolution of the system, preventing dynamic processes from being observed.

3.3.4 Reflective Objective

To test the reflective objective, the set-up in figure 3.4 was used with the quartz objective lens replaced with the reflective objective. It is worth noting that the reflective objective used here is extremely large in size, roughly 3x the thickness of a standard microscope objective and also significantly longer. For this reason, the microscope stage had to be moved in order to accommodate the size of this objective lens, along

with its long working distance - a typical trait of reflective objectives [133].

The power at the specimen plane was measured to be 3.5 mW, significantly greater than that of the quartz objective lens. This could be because of the reduced number of optical elements in the reflective objective or because the UV-enhanced aluminium mirrors provide greater reflectance at 280 nm than the quartz lenses provide transmission.

To demonstrate the illumination homogeneity of this lens, an image of the fluorescent slide illuminated using this objective is shown in figure 3.10.

FIGURE 3.10: Inhomogeneity of illumination across a fluorescent slide when using epifluorescence illumination with a reflective objective.

From this figure, it is clear that an image of the LED chip is being focussed onto the specimen plane due to the reasons described in section 3.1. This is apparent due to the shape of the chip being visible within the field of view of the microscope, highlighting the textured surface of the LED chip. This is less than ideal in fluorescence imaging as images of the specimen will be distorted by the presence of the LED chip image. Whilst the image of the LED chip could be magnified to fill the whole field of view of the microscope, this would still provide inhomogenous illumination to the specimen due to the heavily textured surface of the chip.

A quartz homogenising rod was implemented to rectify this. The effect of this can be seen in figure 3.11, with the illumination profiles across the specimen plane both

with and without the homogenising rod compared in figure 3.12.

FIGURE 3.11: Illumination pattern of 280 nm LED travelling through a homogenising rod before being focussed through the reflective objective.

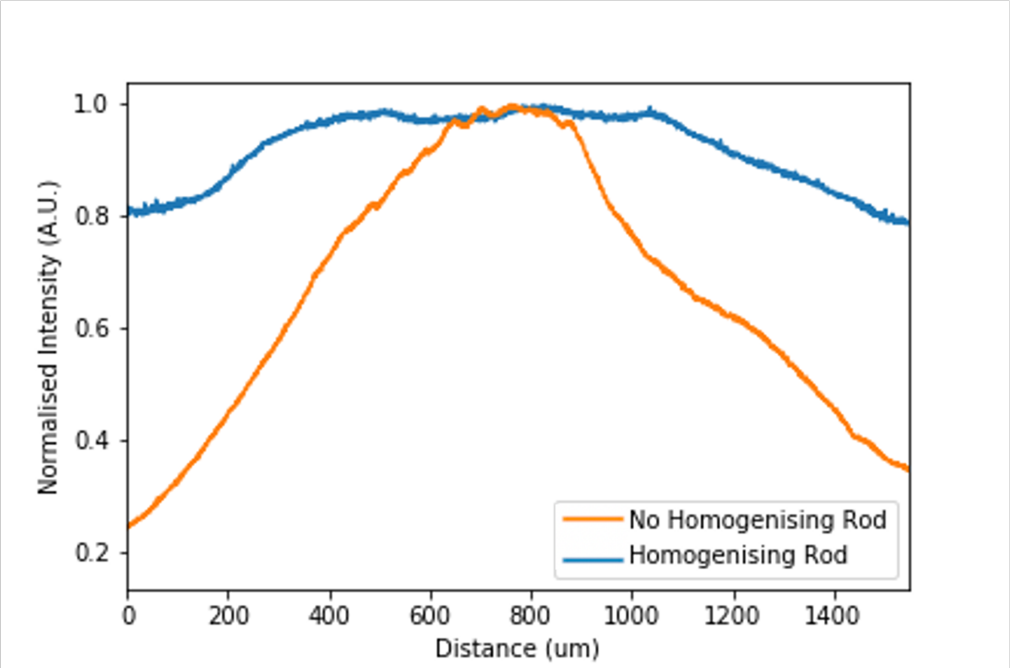

FIGURE 3.12: Intensity as a function of distance across the field of view measured from figures 3.10 and 3.11.

As shown in these figures, the illumination homogeneity is much improved with use of the homogenising rod compared to critical illumination, with a standard deviation of $\pm 15.3\%$ when using a homogenising rod compared to $\pm 34.8\%$ when critical

illumination is used - more than a twofold improvement in homogeneity of illumination.

To test the imaging quality of the reflective objective lens, eosin stained paper was again imaged using this objective with the homogenising rod in place to ensure as good illumination uniformity as possible. This was carried out using a drive current of 350 mA and an exposure time of 500 ms. The resulting image is shown in figure 3.13.

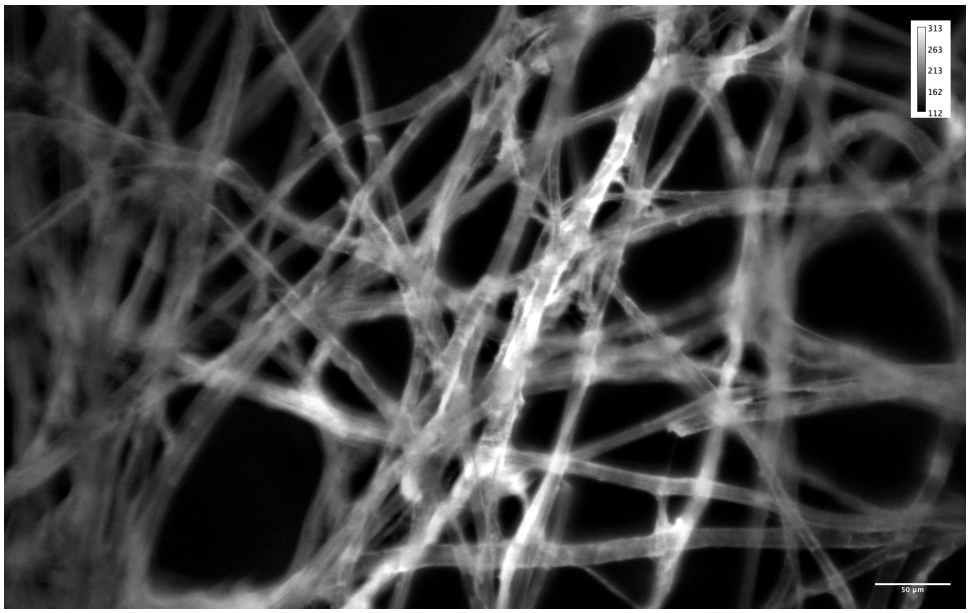

FIGURE 3.13: Eosin stained tissue paper imaged in epifluorescence with 280 nm excitation through a reflective objective lens.

This image show much improved fluorescence intensity compared to that of the image obtained using the quartz objective (figure 3.9). Using equation 3.1, in this technique we calculate an image contrast of 0.60, a 4-fold increase in that obtained using the quartz objective.

However, when observing the image quality of figure 3.13, it becomes apparent that there are some aspects where the reflective objective falls short. From this figure, it is clear that there is a lack of flat-field correction within this objective as the periphery of the image is out of focus whilst the center portion of the image is in focus. This renders a large portion of the field of view of the microscope unusable as the meaningful data occurs only within the center portion of the image. This is a common issue with reflective objectives because of their inherent design - reflective objectives use

curved mirrors to image specimens which can mean that the focal points of the image can change depending on the position within the mirror which they are reflected.

3.3.5 Transmission Fluorescence

The next method of illumination to be tested was transmission fluorescence. The transmission fluorescence microscope detailed in figure 3.5 was constructed fully from quartz plano-convex lenses and a UV-enhanced aluminium mirror and, as a result, transmission of 280 nm light is expected to be high for this set-up based on the measured transmission of 280 nm light through quartz lenses (table 3.3). An optical power of 4.9 mW was measured at the specimen plane - higher than both set-ups using UV compatible objective lenses - confirming the excellent transmission obtained by using only quartz plano-convex lenses to provide illumination to the specimen. It is worth noting that a much higher optical power at the specimen plane could be achieved by removing the excitation filter, which significantly attenuates the power of the 280 nm LED (or switching to the 300/50 nm filter). In transmission fluorescence, removing of the filter completely can negatively impact image quality as it increases the amount of excitation light reaching the detector. This is particularly impactful when using this LED which, as reported in chapter 2, has broad-wavelength parasitic emission overlapping with the emission wavelengths of the fluorescent samples used here. As a result, there is a trade off between optical power reaching the specimen plane and image contrast.

The homogeneity of illumination across the specimen plane when illuminating using transmission fluorescence is shown in figure 3.14. The illumination is much more homogeneous using this set up than that of the reflective objective and similar to that of the quartz objective. From this data, the intensity of illumination across the specimen plane has a standard deviation of only $\pm 3.3\%$.

To determine the imaging quality of this optical set-up, eosin stained paper was again imaged and this is shown in figure 3.15.

Immediately, this image has a much greater contrast than that acquired using the quartz objective lens and comparable to the reflective objective. This could be due to the high optical power at the specimen plane (close to 5 mW) which allows sufficient fluorescence intensity to be excited from the eosin stained paper. Using equation 3.1,

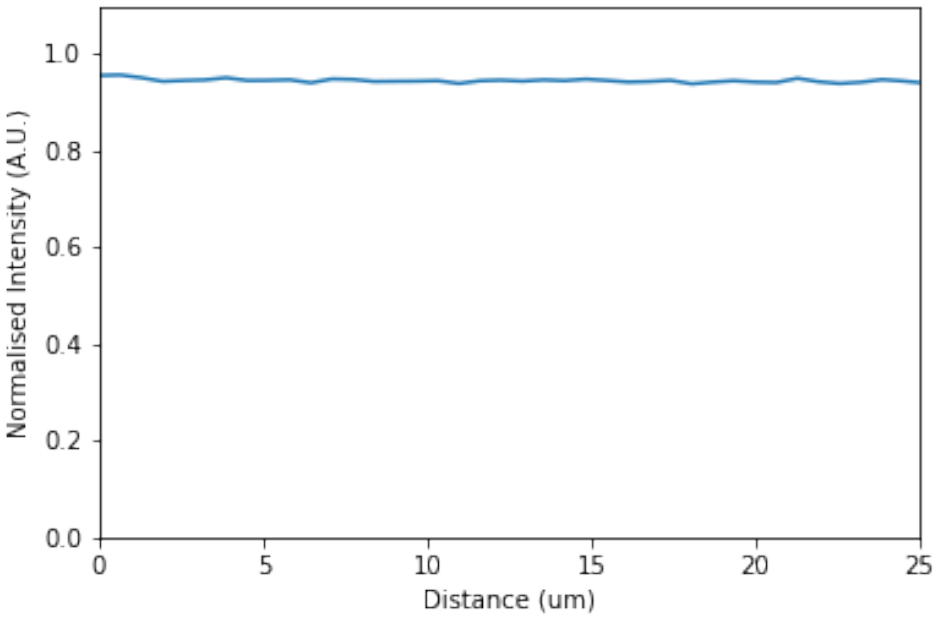

FIGURE 3.14: Intensity profile across the field of view of the transmission fluorescence set-up detailed in figure 3.14.

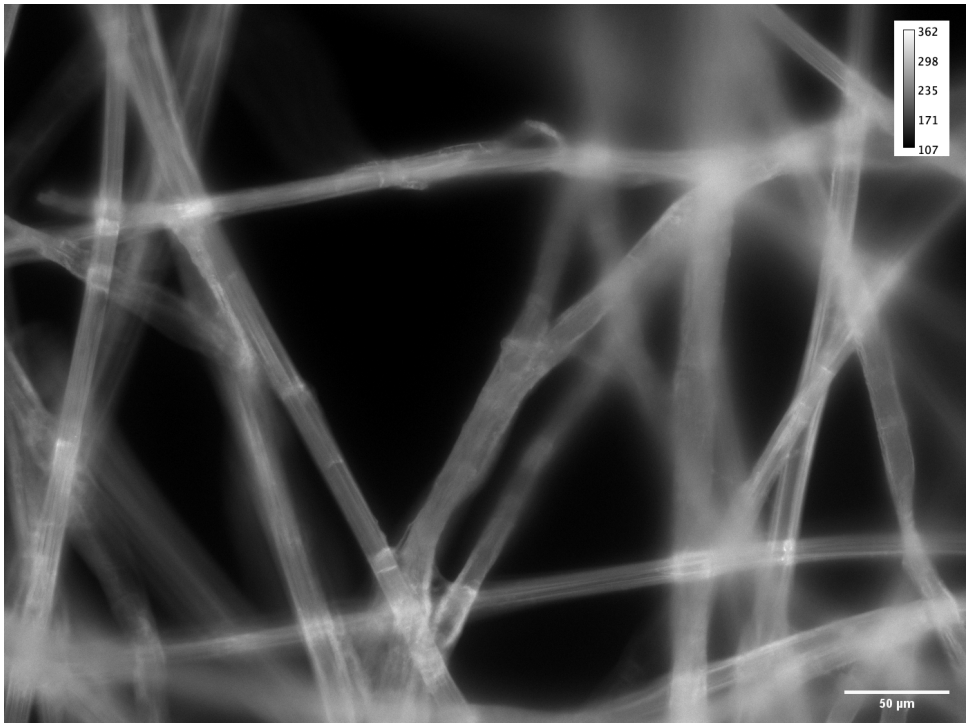

FIGURE 3.15: Eosin stained paper imaged using the transmission fluorescence set-up detailed in figure 3.5

Technique	Homogeneity	Contrast	Usability
Quartz objective	± 4.9%	0.16	Limited magnifications and NAs
Reflective objective	± 15.3%	0.60	Limited magnifications and NAs
Transmission fluorescence	± 3.3%	0.64	Versatile choice of objectives

TABLE 3.3: Summary of deep-UV microscopy techniques presented in chapter 3.

we calculate an image contrast of 0.64, the highest of the three techniques presented here. This is a promising result because in this technique, image contrast relies heavily on the ability of the excitation and emission filters in place to separate excitation from fluorescence and allow a high signal-to-background ratio. This image confirms the ability of these filters to produce a high-contrast fluorescence image akin to (or in cases better than) epifluorescence images. Alongside this, because this image was acquired with a commercial glass objective lens, the lens has been flat-field corrected which means that this image does not suffer from the same issues of field curvature that the image acquired using the reflective objective (figure 3.13). Although some out-of-focus fibers are observed in this image, this is only because these fibers lie outwith the focal plane of the objective lens rather than any optical aberrations.

3.4 Discussion

As presented in section 3.3.1, the issue of transmission through commercial glass microscope optics leads to the essential use of quartz or UV-enhanced optics in all microscope designs for 280 nm illumination. All three techniques for UV illumination presented here have advantages and disadvantages. Whilst a quartz objective would be the initial choice for deep-UV imaging as this provides the ability to image in epifluorescence mode, the most popular technique in fluorescence microscopy for generating high quality images, the performance is not as great as expected. The optical throughput of this objective is poor, resulting in low power at the specimen plane, and is insufficient for excitation of weakly-fluorescent specimens. This is demonstrated in figure 3.9 which has low image contrast. Although the homogeneity of the quartz epifluorescence configuration was not as good as that of transmission fluorescence, this has the potential to be further improved by more precise alignment. In the set up shown in figure 3.4, all optics were built on a vertical breadboard and aligned by hand. In a more refined optical set-up for more repeatable image acquisition, a cage system or fine translation control could be employed to align all optical elements to a high tolerance.

In addition to this, these objective lenses come in very limited magnifications and NAs - as mentioned previously, Zeiss manufacture only a 10x/0.2 objective and a 40x/0.6 glycerine immersion objective, limiting the NAs (and therefore fluorescence intensities collected by the objective) to a fraction of those available in commercial glass objectives.

Reflective objectives efficiently overcame the issue of transmission experienced by the quartz lens, however, proved to provide their own issues. As demonstrated in figure 3.13, reflective objectives suffer from field curvature which means that the periphery of the image and the center of the image are never in focus at the same time. This results in distortion of the edges of the image, meaning that the field of view must be dramatically cropped to view only the in-focus region. Reflective objectives also suffer from the same lack of availability as quartz objectives. Although reflective objectives are manufactured in a wider range of magnifications, these suffer from low NAs compared to traditional glass objectives. A 75x magnification reflective objective

has an NA of only 0.65, less than half of an Olympus oil immersion objective of similar magnification [132, 133]. Reflective objectives are incompatible with any type of immersion media except air due to their reflective elements which means that NAs can never be above unity and that refractive index matching in specimens cannot be carried out to reduce spherical aberration in imaging. Reflective objectives, however, are free from chromatic aberration - their reflective, rather than refractive nature ensures that light of all wavelengths are focussed to the same point [132].

In comparison to this, the use of a transmission fluorescence set-up bypasses the need for a UV-compatible objective lens, arguably the most troublesome component to obtain when designing a microscope compatible with 280 nm light. A transmission fluorescence set-up uses off the shelf optical components such as quartz plano-convex lenses, irises and a mirror which are easily obtainable and inexpensive. These can be used in combination with optical components already present in most microscope labs such as stages, glass objective lenses and cameras. Perhaps the most attractive property of using a transmission set-up compared to the two epifluorescence set-ups described here is the ability to use standard glass objective lenses. This allows much more versatility in imaging, ranging from low magnification (4x) to high magnification (100x) and spanning all immersion media including water and oil. This gives much more freedom in image magnifications and resolutions when compared to both quartz and reflective objectives which come only in a small variety of magnifications and offer limited NAs compared to their glass counterparts. Whilst transmission fluorescence relies heavily on excitation and emission filters to separate excitation light and fluorescence to preserve image contrast, the objective lens can also act as a filter itself because of its inability to transmit 280 nm light. This was demonstrated in MUSE [10] which did not require any excitation filter as the objective lens worked to block excitation light. Unfortunately, due to the parasitic emission observed in the 280 nm LED used in this work, the objective lens alone is not sufficient to spectrally separate excitation and emission light. As a result, an excitation filter is required which introduces a trade-off between optical power at the specimen plane and image contrast. However, as demonstrated in figure 3.15, this does not seem to cause an issue as an image with good contrast and fluorescent signal is achieved whilst using the excitation filter. Though the issue of parasitic emission is common in deep-UV LEDs,

technology in this area is advancing and it is hoped that with time, new LEDs will be developed which have narrow emission at 280 nm which will make it much easier to spectrally separate from fluorescence emission. Another benefit to using transmission fluorescence is that it can easily be applied to existing commercial microscopes with minimal disturbance. For example, the condenser unit of a commercial microscope can easily be removed and the optics described in figure 3.5 placed along the optical bench to reflect light up to the specimen plane. This results in the advantage of high-throughput transmission of 280 nm light to the specimen plane combined with the excellent usability of the commercial microscope, such as a stage with x/y/z control, an objective turret and a filter wheel.

Transmission illumination allows for much greater flexibility in objective lenses when compared to techniques such as MUSE, including high magnification, high numerical aperture lenses which allow for more detailed imaging of cell specimens with improved resolution. In addition to this, the limited penetration depth of 280 nm light within thick tissues has limited MUSE to illuminating and detecting on the same side of the specimen. However, with sufficiently thin specimens (i.e. less than a few μm in thickness), the limited penetration depth of 280 nm light becomes less of a concern and transmission fluorescence imaging is possible.

When comparing these three techniques, it is clear that the transmission fluorescence set-up is superior to both epifluorescence set-ups using quartz and reflective objectives. The transmission set-up provides high optical power at the specimen plane, excellent illumination homogeneity, high image contrast and flexibility regarding objective lenses. Furthermore, it can be constructed from off-the-shelf components and is therefore easy to implement and much more cost effective than purchasing a UV-compatible objective lens. For this reason, a transmission fluorescence set-up was chosen for the application of 280 nm LEDs to fluorescence imaging presented in the following chapters 4 and 5.

3.5 Conclusion

One of the most prevalent issues in integrating 280 nm light into optical microscopy is the low transmission of deep-UV wavelengths through glass - for this reason, using a commercial microscope is not possible. This chapter first quantified transmission of 280 nm light through commercial microscope optics, confirming that integration of the LED into a commercial microscope without modification of lens elements was not practicable. This chapter then presented three methods of illuminating the specimen to overcome this issue - a fully-quartz epifluorescence set-up using both a quartz objective and a reflective objective and a fully-quartz transmission fluorescence set-up. Properties such as optical power reaching the specimen plane, illumination homogeneity and image contrast were compared for each optical design to determine the most appropriate choice for future microscope applications. It was found that the quartz objective lens provided too little power at the specimen plane to generate sufficient fluorescence intensity from specimens, meaning that image contrast was low. The reflective objective overcame this problem due to its increased transmission of 280 nm light, however it was possible to illuminate only in critical illumination with this objective, meaning that an image of the LED chip was projected onto the specimen, providing poor illumination homogeneity. This was overcome by using a homogenising rod, but when imaging fluorescent specimens it became apparent that the objective suffered from field curvature, meaning that the center and periphery of images could never be in focus simultaneously. Finally, a transmission fluorescence set-up provided excellent throughput of optical power to the specimen plane, illumination homogeneity and image contrast. As a result, transmission fluorescence was chosen as the method to provide 280 nm excitation of fluorescent specimens in the following thesis chapters.

Chapter 4

280 nm Excitation of Quantum Dots

Semiconductor quantum dots (QDs) have significant advantages over more traditional fluorophores used in fluorescence microscopy. QDs are bright, photostable and emit in a wide spectral range spanning the entire visible spectrum. QDs have a unique, broad excitation spectrum with extinction coefficients increasing dramatically into the deep-UV. However, due to limited availability of suitable light sources, QDs are often excited far from their optimum excitation wavelengths in the deep-UV. Based on their excitation spectrum, it is expected that excitation at a wavelength of 280 nm would yield greater fluorescence intensity when compared to longer, more accessible wavelengths, and hence improve image quality. Now, the high-brightness 280 nm LED in use in this thesis, combined with the optical design for illumination described in chapter 3, provides the opportunity to carry out 280 nm excitation of QDs used as cellular labels.

In this chapter, I use an adaptation of the transmission fluorescence set-up developed in chapter 3 to image these with 280 nm excitation. I then go on to determine whether there is an improvement in fluorescence intensity when using 280 nm light to excite semiconductor QDs when compared to a longer, more commercially available wavelength of 365 nm, and the extent of this increase. I also investigate the limitations in applying 280 nm excitation of QDs to live cell imaging. Parts of this chapter have been reproduced, with permission, from the following work published by IOP Publishing: Mollie McFarlane, Nicholas Hall and Gail McConnell "Enhanced fluorescence from semiconductor quantum dot-labelled cells excited at 280 nm", Methods Applications in Fluorescence, 2022, 10, 025004.

4.1 Introduction

As covered in chapter 1, QDs have several significant advantages over traditional fluorophores commonly used in fluorescence microscopy which make them appealing for cell imaging applications [141][102][142]. QDs have optical properties which make them excellent for fluorescence imaging, including their narrow spectral bands which make them easy to separate from both each other and from excitation light [102]. QDs are known to be highly photostable which is appealing for long-term imaging of live cells [89]. However, one of their most interesting properties is their broad, continuous excitation spectrum which differs significantly from the organic fluorophores commonly used in fluorescence microscopy. The excitation spectrum of QDs spans from the wavelength corresponding to the semiconductor bandgap deep into the UV, allowing the excitation of QDs at essentially any wavelength below their semiconductor bandgap [86]. An example of this is shown in figure 4.1 which shows the excitation and emission spectra of two commercial QD products, QD525 and QD605.

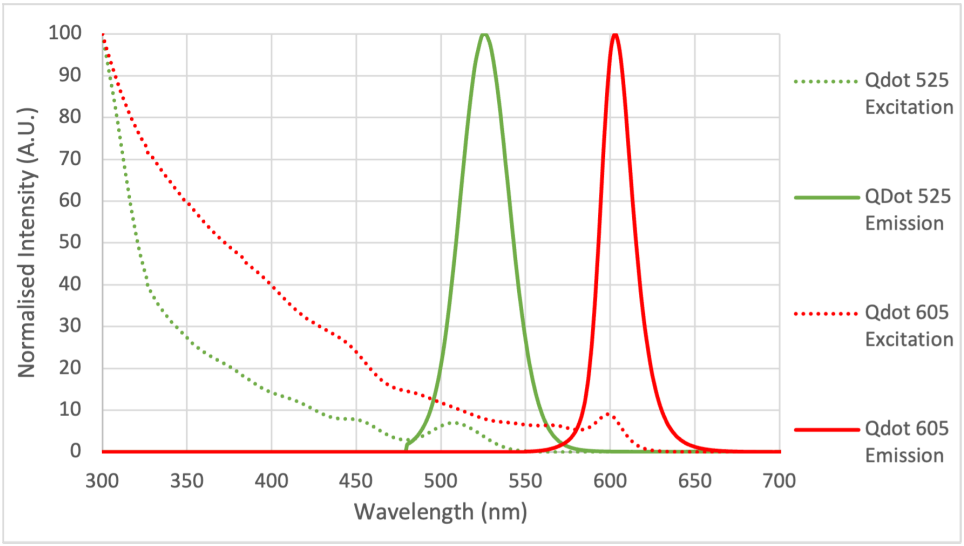

FIGURE 4.1: Excitation and emission spectra of commercial semiconductor QDs QD525 and QD605.

QDs are currently most often excited in the blue or near-UV region of the spectrum due to availability of suitable light sources. Before the widespread use of LEDs in widefield fluorescence microscopy, excitation of QDs was achieved using arc lamps with excitation filters centering around wavelengths such as 470 nm [89] [143]. Previous choices in confocal microscopy include the 488 nm laser line [105, 144, 145, 146]

and the 405 nm laser line [147].

Despite the common use of blue excitation wavelengths, the extinction coefficients of QDs increase dramatically with shorter wavelengths [49]. This makes the use of deep-UV light advantageous as short wavelengths yield greater probability of excitation, leading to increased fluorescence. Whilst a basic requirement of an excitation light source is that it overlaps generally with the excitation spectrum of the chosen fluorophore, wavelengths which closely match the peak of the excitation spectrum increase the fluorescent signal available in fluorescence imaging [54, 77].

Now, with the high-brightness 280 nm LEDs used in this thesis, there is the possibility of achieving the required power at the specimen plane to excite fluorescence from fluorescent specimens in microscopy. Based on the reasons described above, we would expect excitation at this wavelength to provide significantly greater fluorescence intensity when compared to longer, more commonly used wavelengths in the near-UV or blue. This enhanced fluorescence intensity combined with the already notable optical properties of QDs can provide great advantage in fluorescence microscopy. Alongside this, excitation at a wavelength of 280 nm creates a larger effective Stokes shift which is advantageous because not only does 280 nm light allow simultaneous excitation of multiple sizes of QD it also allows enhanced spectral separation in applications in which image contrast is of particularly high importance [49].

For these reasons, the work described in this chapter set out to compare the excitation efficiency of semiconductor QDs excited at 280 nm to a longer, more commercially available wavelength of 365 nm, already in possession of many microscopists for excitation of common fluorophores such as DAPI.

4.2 Methods

4.2.1 Optical set-up for 280 nm and 365 nm light delivery

The transmission fluorescence microscope set-up developed in chapter 3 (figure 3.5) was adapted to image QDs with both 280 nm and 365 nm light. To do this, the quartz optical path from figure 3.5 was moved onto the bottom of a commercial microscope, as shown in figure 4.2.

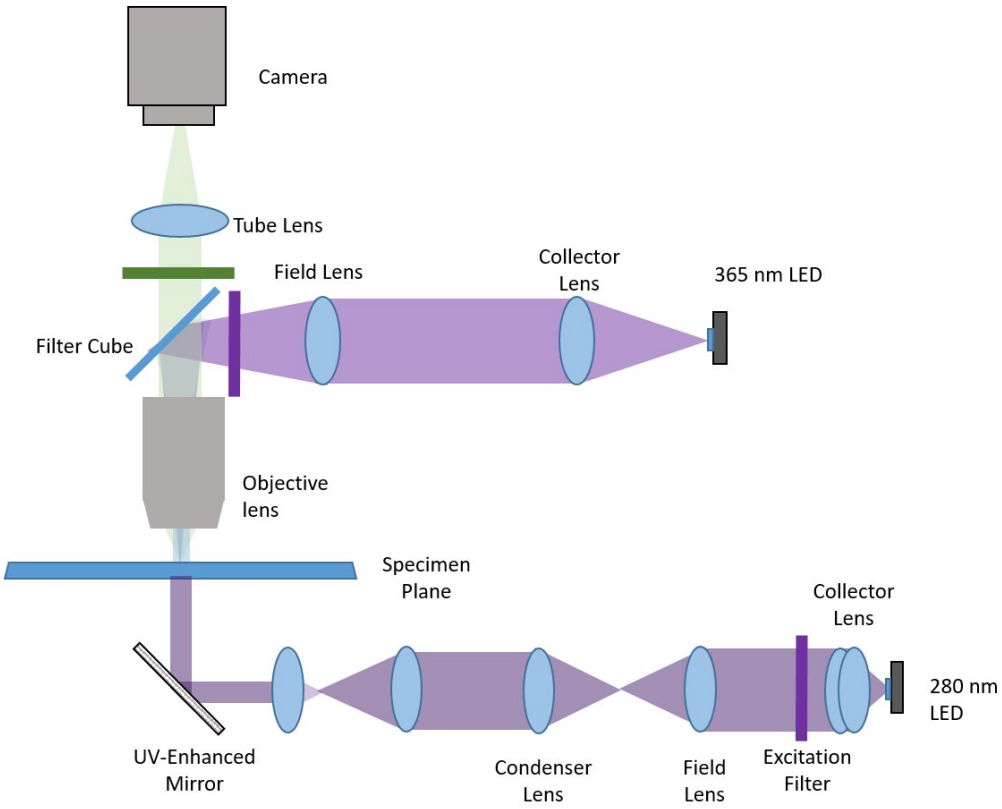

FIGURE 4.2: Modified Olympus BX50 microscope developed to deliver 365 nm light and 280 nm light to the specimen plane. 365 nm light was delivered to the specimen through the epifluorescence pathway of the commercial microscope and 280 nm light was delivered to the specimen in transmission fluorescence using quartz optics.

The microscope used was an Olympus BX50 upright widefield system. To add the transmission pathway, the condenser unit was completely removed from the microscope, leaving a gap between the microscope base and the stage for optics to be added.

As in the previous chapter, the 280 nm light was relayed to the specimen plane as follows: the 280 nm LED was collimated by the set of 2 plano convex lenses, placed together to increase the collection efficiency of 280 nm photons and through the 300/50

nm excitation filter to ensure that no parasitic emission is transmitted. The 300/50 nm filter was used in place of the 280/10 nm filter to allow as much 280 nm light as possible to reach the specimen plane. Light was then relayed through two quartz lenses (Thorlabs LA4380-UV, LA4148-UV) to achieve better illumination uniformity, as focusing the light onto the specimen plane creates areas of uneven illumination due to the heavily patterned surface of the LED chip (as previously shown in figure 3.10). In addition to the transmission fluorescence set up described previously, here the spot size of the illumination light was then reduced using an additional quartz lens pair (Thorlabs LA4148-UV, LA4052-UV) to roughly match the illumination spot size to the field of view of the microscope. This ensured that no light was being wasted on illuminating parts of the specimen outwith the area that could be imaged at any given time. Light was then reflected to the specimen plane at 90° using the UV-enhanced aluminium mirror.

The 365 nm excitation was achieved in epifluorescence mode by attaching a CoolLED pE-300white SB illuminator system to the epifluorescence port of the BX50 microscope. The illumination from the 365 nm LED was homogenized by aligning the microscope for Köhler illumination. A 400 nm dichroic mirror was used in the filter cube to reflect the 365 nm light to the specimen plane. In the emission filter port in the filter cube, a 525/20 filter was used for detection of 525 nm emitting QDs (Semrock FF03-525/50-25), and a 561 LP emission filter was used for detection of 605 nm emitting QDs (Semrock BLP02-561R-25). Finally, a Teledyne Photometrics CoolSnap HQ2 camera with 14-bit digitization was used as a detector.

4.2.2 Labelling of mammalian cells with commerical semiconductor QDs

As described in detail in chapter 1, labelling cells with QDs can take many forms and three methods of doing so were investigated to determine the optimum cell labelling method. These were using either streptavidin-conjugated QDs or QDs directly conjugated to an antibody, both purchased commercially. In the case of streptavidin conjugated QDs, these can either be used to label the endogenous biotin within the cell, or used with a biotinylated secondary antibody to create a versatile probe against the target protein of choice. In the case of QDs conjugated to an antibody, these can be used against any primary antibody provided it is raised in the correct species.

HeLa cells were used in this work. HeLa cells are the most widely used human cell line used in biological studies [148] and are a robust cell line. HeLa cells were cultured in Dulbecco's modified eagle medium (DMEM) supplemented with 10% Fetal Bovine Serum (FBS), 1% L-Glutamine and 1% penicillin-streptomycin and kept in a 37°C incubator with 5% CO_2. To prepare cells for imaging, cells were seeded onto quartz coverslips (Alfa Aesar 43211) coated in a 1:100 solution of fibronectin (Sigma Aldrich F1141-1MG) and allowed to grow in a 6 well plate until they were 60-80% confluent. The cell media was removed and the cells were subsequently fixed in 4% formaldehyde by adding 1 ml of formaldehyde to the well plate for 20 minutes in a 37°C incubator. After this time, cells were washed 3x with PBS.
The following protocol to label fixed cells with streptavidin-functionalised QDs was adapted from Thermo Fisher Scientific [149]. After fixation, the cell membrane was permeabilised to allow antibodies and QDs to enter the cell. Permeabilisaiton buffer was made using 0.25% Triton X-100 (Thermo Fisher A16046.0F) in PBS. 1 ml of this solution was added to the well for 20 minutes. The coverslips were then removed from the well plates and washed in a petri dish filled with PBS for 5 minutes, 3 times.

First, the endogenous biotin within the cells was labelled to assess the suitability of streptavidin-conjugated QDs as a non-specific cell label. Biotin occurs naturally within the cytoplasm and mitochondria in a wide variety of cell types and as a result the streptavidin-QD conjugates can be used to non-specifically label the cell. For labelling of endogenous biotin, streptavidin-conjuaged QDs emitting at 525 nm were prepared by diluting 2μl of stock QD525 streptavidin conjugate in 100 ml of blocking buffer (6% bovine serum albumin (BSA) in PBS). This was added to the cell-coated coverslip for 2 hours. After this time, the cells were washed with PBS and the coverslip was mounted onto a quartz microscope slide (Alfa Aesar 42296) using gelvatol mounting medium.

Next, a 3-step anibody labelling was tested which uses a biotinylated secondary antibody against a primary antibody for the target of interest. Using this antibody can provide flexible and versatile use, as any wavelength of streptavidin-conjugated QD can be used with a single biotinylated antibody. This is considerably less costly than purchasing a QD-conjugated antibody for each required QD emission wavelength. For antibody labelling of cells with a biotinylated secondary antibody, fixation and permeabilisation were performed as above and subsequent steps were performed in

a humidity chamber. This was constructed using a glass Petri dish with a small piece of wet tissue paper on the base. On top of this, parafilm was added to cover the tissue paper and the coverslip was put on top. This humidity chamber prevents further buffers added to the coverslip from drying out. First, blocking of endogeneous biotin was performed. As mentioned, biotin occurs naturally within the cell, therefore blocking is necessary as without this step, streptavidin conjugates will bind to existing biotin sites and interfere with the specificity of the antibody labelling. To achieve this, a commercial biotin blocking kit (Invitrogen E21390) was used. This kit contains two reagents designed to be used sequentially. Firstly, unlabelled streptavidin (component A) was added to the cell specimen to bind to the endogenous biotin sites for 45 minutes. Three 5-minute washes were performed in PBS. Secondly, unlabelled biotin was added (component B) for 45 minutes to bind to the streptavidin, effectively rendering the cell free of available biotin sites. Three 5-minute washes were subsequently performed in PBS.

Next, all other potential binding sites in the cell were blocked in order to prevent non-specific antibody binding. This was done using 6% BSA in PBS. 1ml of blocking buffer was added to the coverslip for 1 hour. Three 5-minute washes were subsequently performed in PBS.

A primary antibody was then chosen for a cellular target. The first cellular targets chosen to label using immunolabelling were focal adhesions using an antibody against Paxillin (ThermoFisher MA5-13356). Tubulin (ThermoFisher A11126) was also chosen as a target due to its occurrence throughout the cell cytoplasm, providing many binding sites for QDs. The primary antibody was diluted 1:200 in blocking buffer and added to the coverslip. The coverslip was then left overnight in the fridge to allow binding of the primary antibody to bind to the cell.

Next, the specimen was washed 3 times in PBS for 5 minutes each. Subsequently, an anti-mouse biotinylated antibody was added to the coverslip at a dilution of 1:200 in blocking buffer. This was left at room temperature for 2 hours to allow binding of the secondary antibody to the primary antibody. After this time, three, 5-minute washes were again performed in PBS.

Finally, the QD525 streptavidin conjugate was prepared by diluting the stock solution (ThermoFisher Q10151MP) in 200 μl of blocking buffer to obtain a concentration of between 10 nM and 40 nM. This was added to the coverslip and left at room temperature for 2 hours. After this time, 3, 5-minute washes were performed in PBS and the coverslip was mounted to a quartz microscope slide using gelvatol mounting medium.

Next, a 2-step method using a secondary antibody already conjugated to QD525 was investigated. Using an immunolabelling process with 2 components rather than 3 can reduce the probability of mistakes in the labelling process as there are less steps. To label cells using 2-step immunolabelling, anti-mouse secondary antibodies raised in donkey and conjugated to QD525 were purchased from Thermofisher Scientific (Q22073). The protocol to label using these antibodies is very similar to that of strepavidin-based labelling but with less steps. Cells were fixed and permeabilised as described previously. Cells were subsequently blocked with 6% BSA in PBS for one hour. The primary antibody against tubulin was added to the coverslip as described previously, and left overnight. The next morning, the secondary antibody-QD conjugate was added at a dilution of 1:50 for two hours. Coverslips were washed and mounted to a quartz microscope slide using gelvatol.

To identify the quality of the immunolabelling, cells were imaged using the epifluorescence pathway of the microscope in figure 4.2 under 365 nm excitation. Cells were imaged using a 40x/0.95 NA objective lens or 60x/1.4 NA oil immersion objective lens. All imaging acquisitions in this chapter were performed using μManager [150]. Cell images were analysed using Fiji and equation 3.1 was used to quantify the image contrast.

4.2.3 Comparison of excitation of QDs at 280 nm and 365 nm

The optical set-up described in figure 4.2 was used for all acquisitions with a 10X/0.4 NA objective lens.

The spectra of the 365 nm and 280 nm LEDs were measured at the specimen plane to ensure that the wavelengths of light reaching the QDs from the epifluorescence pathway was in fact 365 nm. This was done using the Ocean Optics USB2000+UV-Vis spectrometer described in chapter 2. These LED spectra were compared against each

other to ensure there was no spectral overlap in excitation that would convolute the comparison of 280 nm and 365 nm excitation.

The power of excitation light at the specimen plane was measured using a Thorlabs power meter with the UV-extended photodiode sensor described in chapter 2. When measuring each wavelength of light, the detection wavelength was programmed into the power meter to account for wavelength dependency in the detector. LED drive currents were adjusted to ensure the optical power at the specimen plane was equal for each wavelength of light.

The homogeneity of illumination for both excitation wavelengths were measured using a fluorescent microscope slide (Chroma 92001). The slide was placed at the focal plane of the 10X objective and sequentially illuminated with each wavelength of light. For each wavelength, an image was acquired with an exposure time of 150 ms. To determine the illumination uniformity of 365 nm and 280 nm light, images of the fluorescent slide were opened in Fiji. For each image, a line profile with a width of 50 pixels was taken horizontally across the field of view, and the intensity plotted as a function of distance. The standard deviation of the mean intensity was calculated for each illumination wavelength.

Images of a blank quartz coverslip-slide combination were obtained to measure the background of each image. This was done by placing a coverslip on top of a slide at the specimen plane and illuminating with each wavelength of light. The average background intensity value was later subtracted from each QD image pair.

The autofluorescence of unlabelled HeLa cells was also investigated to ensure any increase in fluorescence in QD labelled cells was due to increased QD excitation efficiency rather than increased autofluorescence. To do this, HeLa cells were cultured as above and seeded onto quartz coverslips for 24 h. After this time, cells were fixed with 4% formaldehyde and mounted onto a quartz microscope slide using gelvatol. Unlabelled HeLa cells were imaged with the same camera exposure and LED power as the QD image pair. The mean autofluorescence intensity across all cells in the field of view was measured at each excitation wavelength and these were later subtracted from fluorescence intensities of QD-labelled cells.

Two QD-labelled HeLa cell specimens were used to determine whether there was an increase in fluorescence intensity associated with 280 nm - the first was labelled

using 525 emitting QDs (QD525) and the second was labelled using QDs emitting at 605 nm (QD605), both against cellular target tubulin. These two sizes of QDs were chosen to confirm that any observed increase in fluorescence from QDs was applicable to multiple sizes of QDs and not just the ones in use. HeLa cells were labelled as described above, using an anti-tubulin antibody, a biotinylated secondary antibody and either QD525 or QD605 labels. QD-labelled cells were imaged first with 365 nm excitation light, then the same region was immediately imaged with 280 nm excitation of the same optical power. The power at the specimen plane and camera exposure were set to 3.8 mW and 500 ms, respectively, for QD525-labelled cells, and 4.8 mW and 100 ms for QD605-labelled cells. Optical powers and camera exposure times were chosen to avoid overexposure in images due to differing quantum yields between QD525 and QD605 samples.

Data analysis was performed using a Python code found in Appendix A [151]. This code was written by Nicholas Hall. To briefly describe how this works, images of QD-labelled HeLa cells excited at both wavelengths (referred to from now on as "image pairs") were imported into Python, alongside background images and autofluorescence images. Image pairs were background corrected by subtracting the average background intensity value from the acquired background images. Next, autofluorescence images were thresholded using an Otsu algorithm [152] to create regions of interest (ROIs) around cells. A mean intensity was then obtained from these cellular ROIs to calculate the mean autofluorescence intensity of cells excited with 280 nm and 365 nm. The QD image pairs were then thresholded using the same Otsu algorithm to isolate the regions of interest containing fluorescent signal from QDs in both images. 280 nm:365 nm intensity signal ratios were then calculated on a pixel-by pixel basis and mean autofluorescence values from cells excited at 280 nm and 365 nm were subtracted to ensure that increases in intensity reflect enhanced fluorescence from QDs and not higher autofluorescence from cells. By using the measured fluorescent signal and background intensity values, equation 3.1 could be used to calculate the image contrast. Finally, fluorescence intensity distributions from images excited with 280 nm and 365 nm were subjected to Welch's t-test [153] under the null hypothesis that the intensity distributions have identical mean values, implying that there is no significant difference in emission intensity between excitation wavelengths.

4.2.4 Photobleaching of QDs under 280 nm excitation

The rate of photobleaching of QDs irradiated with 280 nm and 365 nm was investigated over an 8 hour period to ensure that the higher energy associated with 280 nm light did not have a more profound effect on photobleaching of QD-labelled cells. To compare photobleaching of QDs illuminated with different excitation wavelengths, HeLa cells with QD605 labelled microtubules were prepared as above on quartz coverslips and slides.

Each QD605-labelled cell specimen was exposed to each wavelength of light for an 8 hour period. An optical power of 0.45 mW at the specimen plane was chosen for both wavelengths of light to avoid degradation of the gelvatol over long periods of irradiation with high-intensity 280 nm light. Cells were irradiated constantly with light and imaged once every 10 minutes at a camera exposure of 500 ms. Experiments were repeated in triplicate.

To analyse the photobleaching rate of QDs, a thresholding operation was performed using Fiji and using this, ROIs were created around each cell. This was applied to the corresponding time-lapse image stack and the mean intensity of the cellular ROIs were measured for each frame. Mean fluorescence intensity was then plotted as a function of time.

4.2.5 Cell Viability under 280 nm irradiation

To investigate the effect of 280 nm irradiation on live cells, and hence the possibility of applying 280 nm excitation of QDs to live cell imaging, the 280 nm light path was moved onto an inverted microscope (Olympus IX71) to facilitate live cell imaging. The adapted set-up can be found in figure 4.3.

One key difference in this set-up is in the LED illuminator. The 280 nm LED used in the study was developed into a prototype illuminator product, the pE-280, by CoolLED. This unit is much improved over the LAM design used previously as it can be connected to a PC to drive the LED electronically. This is particularly important for time-lapse imaging, where an image is acquired at regular intervals, as the LED can be triggered automatically by the PC to acquire an image. The LED unit also has a white LED for brightfield imaging. However, internal elements such as dichroic

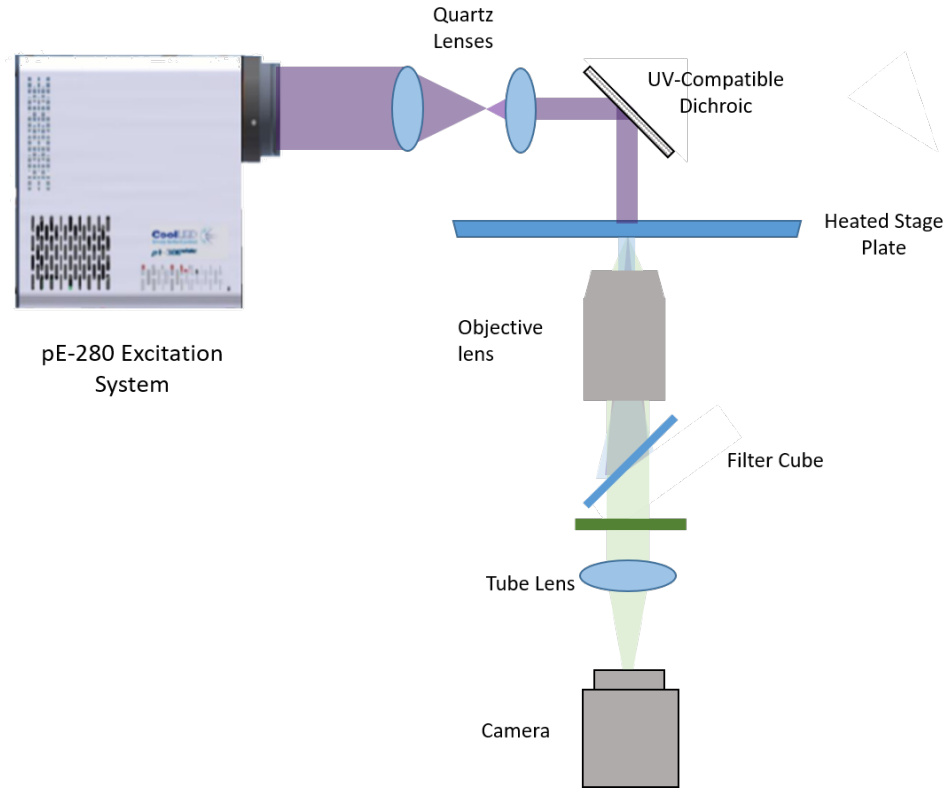

FIGURE 4.3: Amended version of the optical set-up described in figure 4.2 for an inverted system.

mirrors used to guide the LED light to the exit, mean that some optical power is lost compared to when using the LED chip-on-board. In this case, a maximum optical power at the specimen plane of 2.5 mW was achieved compared to the almost 4.8 mW optical power achieved when using the transmission fluorescence set-up shown in figure 4.2. Some optics were adjusted as follows to better match the output of the pE-280.

In the CoolLED illuminator design, light is collimated by a 2-inch diameter quartz lens, creating a wide, 2-inch beam diameter. For this reason, another 2-inch diameter quartz lens is required to re-focus the light as a standard 1-inch optic will result in a significant amount of light being lost. This lens was a f = 60 mm lens from Thorlabs (LA4464-UV). This light is allowed to diverge and is then re-collimated by a f = 100 mm quartz lens (Thorlabs LA4380-UV). It is then reflected at an angle of 90° to the specimen plane by the 280 nm dichroic mirror used previously in chapter 3. This mirror not only reflects the 280 nm light downwards to the specimen, but also helps to reduce the parasitic emission from the LED discussed in chapter 2. Finally, a heated stage plate (Linkam Scientific CO 102) was placed on the microscope stage to facilitate

a constant temperature of 37°C for live cell imaging.

When imaging live cells, they are most commonly kept in imaging chambers such as ibidi dishes (Ibidi 81156). These are designed specifically for live cell imaging with inverted microscopes and cells can be grown in these dishes and allowed to adhere to the bottom surface, through which they can be imaged. This allows cells to be imaged in culture media which will allow optimum conditions for the cells to remain alive whilst imaging. However, the top and bottom surfaces of ibidi dishes are made from glass or polymer, and, as is a recurring theme throughout this thesis, are incompatible with 280 nm light. As the optical set-up described here use transmission fluorescence to image cells, the top surface of the dish must be replaced with quartz such that illumination light can reach the cells, and the bottom surface must also be replaced with quartz such that the surface does not autofluoresce and cause poor image contrast (as discussed in chapter 3). The bottom surface of an ibidi dish is made from a polymer or glass coverslip which was then replaced with a quartz coverslip by gluing with a watertight, alcohol resistant adhesive (Techsil Momentive RTV157). This type of adhesive was found to be key in developing this quartz ibidi dish, as other glues such as superglue were not resistant to liquid or humidity and as a result dissolved in the incubator. A hole was cut into the lid of the dish and on top of this hole a second quartz coverslip was glued. This quartz dish allowed cells grown on the bottom quartz coverslip to be imaged using the inverted microscope and 280 nm light was able to penetrate the top surface to irradiate the cells.

To identify when cells were no longer viable, propidium iodide (PI) was used as a cell stain. PI is cell-impermeant to live cells, and as a result it is often used as a marker for determining if a cell is dead [154]. PI is a nuclear stain, attaching itself between the bases of DNA. To first identify a threshold which indicates a cell was no longer viable, HeLa cells were fixed and stained with PI to measure fluorescence intensity from PI within dead cells. HeLa cells were cultured on coverslips for 24 h, fixed with 4% formaldehyde for 20 min and stained with 1.5 μM PI for 5 min. Fixed cells were imaged with a 10x/0.3 NA lens at an excitation wavelength of 525 nm and collected through a 620/60 nm emission filter (Chroma ET620/60m) with a camera exposure of 500 ms.

Next, live HeLa cells were cultured for 24 h in the quartz Ibidi dishes with the

bottom surface coated in fibronectin. Before imaging, cell media was removed and replaced with Fluorobrite DMEM imaging media incubated with 1.5 M of PI. Cells were initially imaged in brightfield at an exposure time of 10 ms to identify the positions of cells within the field of view. Cells were then exposed to 2.5 mW of 280 nm light over a 500 ms period at 5 minute intervals to mimic a typical time-lapse experiment. At each 5-minute interval, following exposure to 280 nm light, fluorescence images of PI within cells were acquired at a camera exposure time of 500 ms, with excitation at 525 nm and emission measured using a 620/60 nm emission filter. Experiments were repeated in triplicate.

To analyse this data, a mean fluorescence intensity from the fixed, PI stained HeLa cells was obtained to give a benchmark against which the intensity of PI within live cells would be measured. This was done in Fiji by thresholding the image of fixed cells, creating ROIs around the cell nuclei and then obtaining a mean intensity value. In live cell images, a population of 50 cells from the initial brightfield frame was chosen and regions of interest were taken across the cell nuclei. In each timepoint, the intensity of the cell nucleus was measured and the cell was defined as dead when the intensity of the nucleus reached the threshold set by the fixed cells. The number of viable cells as a percentage was then plotted against time.

4.3 Results

4.3.1 Antibody labelling of mammalian cells

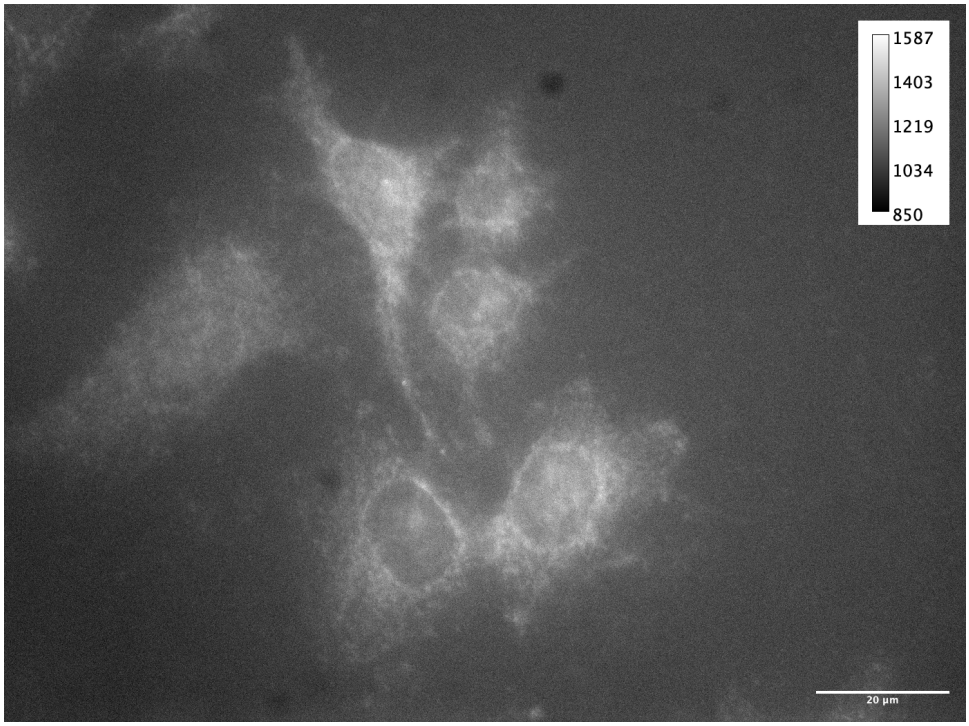

FIGURE 4.4: HeLa cells labelled with QD525 by allowing the streptavidin-conjugated QDs to bind to endogenous biotin within the cell. Excited at 365 nm and imaged using a commercial microscope.

Cells whose endogenous biotin has been labelled with QD525 is shown in figure 4.4.

Whilst it seems that the QDs have successfully attached to the biotin within the cell, the image contrast is very poor. When using equation 3.1 to calculate image contrast, this gives a value of only 0.07. This could potentially be due to low levels of endogenous biotin within the cell, meaning that limited streptavidin-conjuaged QDs are able to bind and resulting in low fluorescence signal. In general the image quality is poor with high levels of noise due to the low fluorescent signal.

The first cellular target used for immunolabelling with a biotinylated antibody was paxillin and images of the cell specimen is shown in figure 4.5.

Similarly to that of endogenous biotin labelling, these cells exhibit a very weak fluorescent signal from within the cell cytoplasm. When compared to other examples of focal adhesions labelled using an antibody against paxillin (e.g. [155]) it is clear that

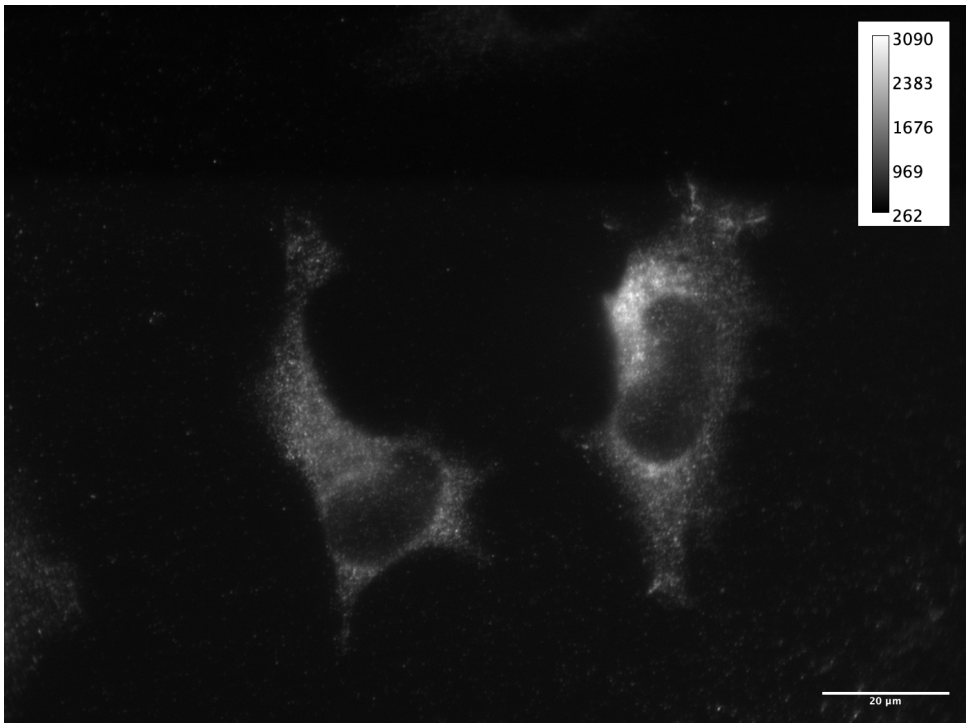

FIGURE 4.5: HeLa cells labelled with QD525 using indirect antibody labelling against Paxillin (focal adhesions). Excited at 365 nm and imaged using a commercial microscope.

the fluorescent signal from within the cell comes from non-specific binding within the cytoplasm rather than focal adhesions, which occur around the perimeter of the cell. In additon to this, image contrast is low, with a value of only 0.33. After several unsuccessful attempts at labelling focal adhesions within the cell, this target was abandoned.

Next, an antibody against tubulin was chosen for use with the biotinylated secondary antibody. HeLa cells with microtubules labelled with QDs are shown in figure 4.6. Cells within these images have a much greater image contrast with bright fluorescent signal when compared to paxillin, with a value of 0.57. This is likely due to more specific binding of the QDs to the intended target, possibly due to the use of a better quality antibody. When compared to previous examples of tubulin labelling, these samples agree well with the structure of tubulin, with microtubule networks visible within the cell cytoplasm.

For these reasons including the increased performance when compared to anti-paxillin antibodies, tubulin was chosen as the cellular target for imaging QD-labelled cells in following experiments.

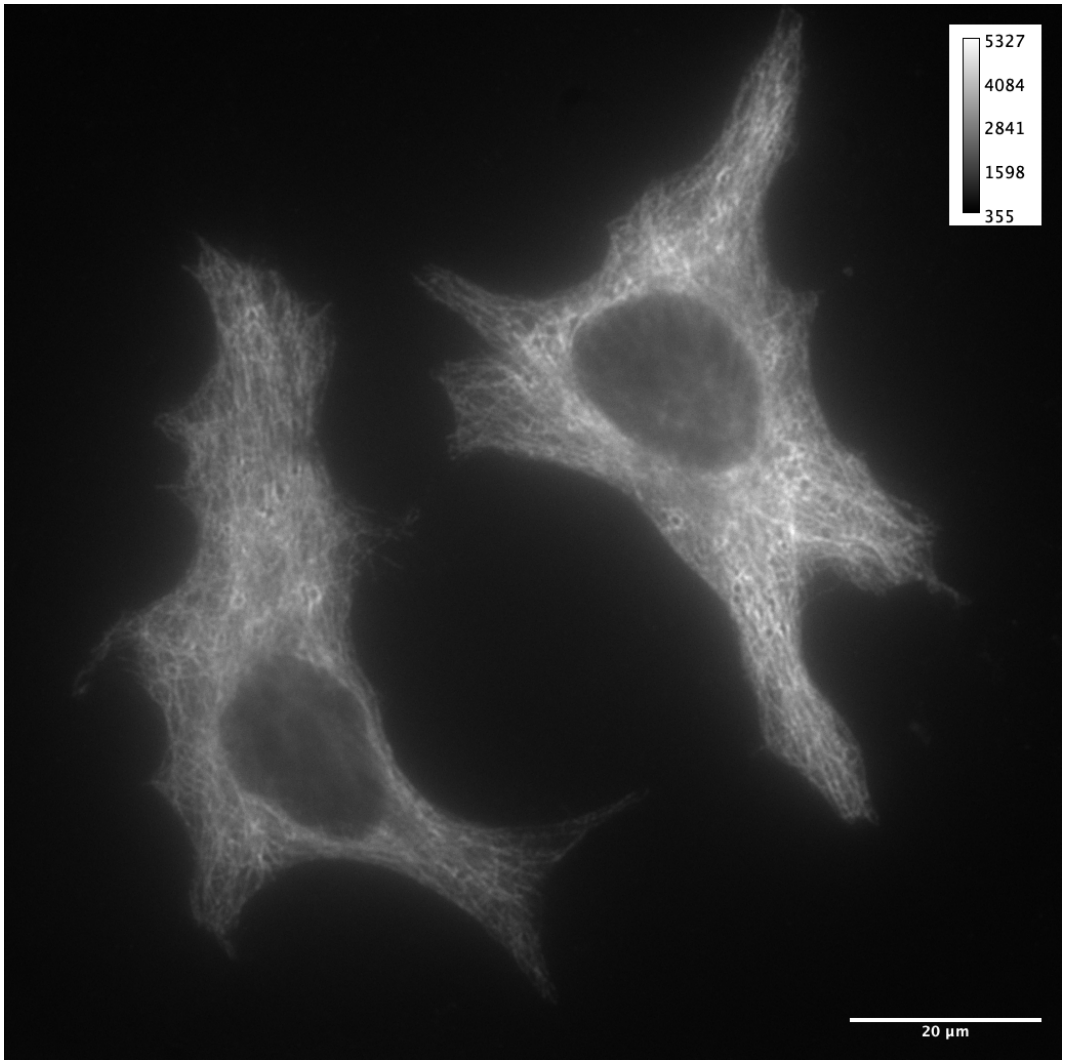

FIGURE 4.6: HeLa cells labelled with QD605 using streptavidin QDs and a biotinylated secondary antibody. The cellular target is tubulin. Excited at 365 nm and imaged using a commercial microscope.

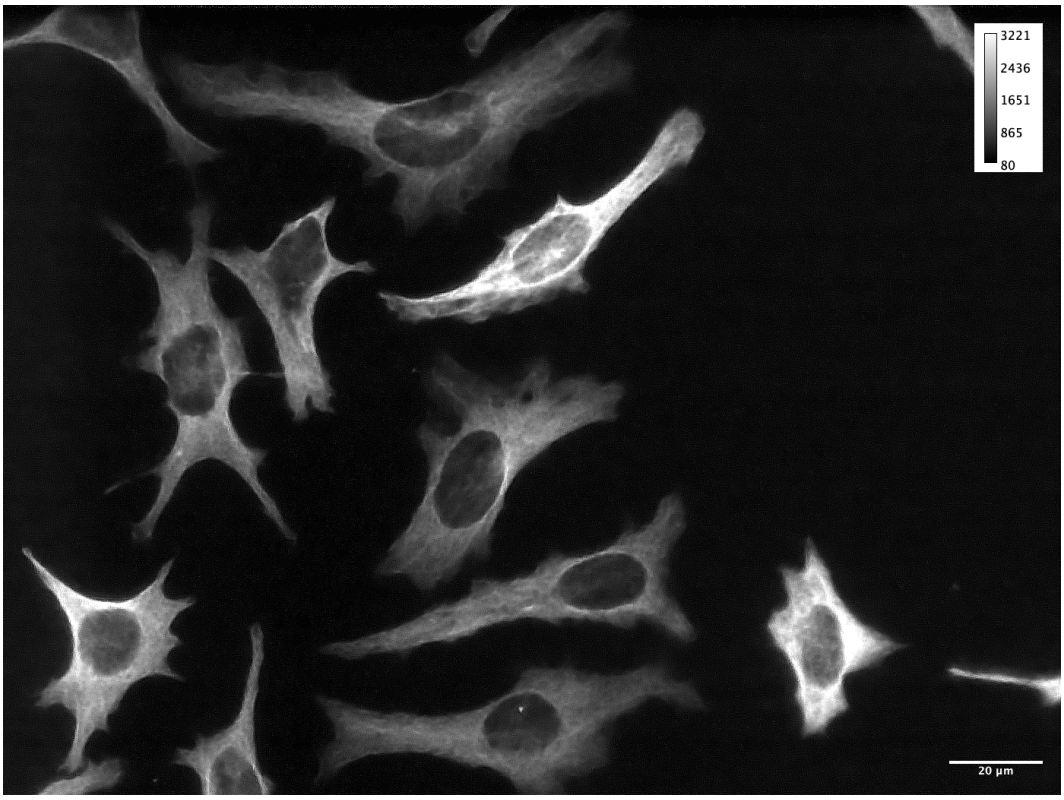

FIGURE 4.7: HeLa cells labelled with QD525 using indirect antibody labelling against tubulin. Excited at 365 nm and imaged using a commercial microscope.

Finally, labelling was repeated using a QD525-conjugated secondary antibody to test performance between this method and using a biotinylated antibody. The result of this is shown in figure 4.7.

These cells show good labelling, with visible microtubules within the cell confirming the antibody has good specificity. This image also has good contrast of 0.63. However, as this labelling method shows limited improvement compared to using a biotinylated antibody to label microtubules in figure 4.6, the versatility of the biotinylated antibody becomes more advantageous as this can be used to label cells with any QD streptavidin conjugate of choice. Therefore, the biotinylated antibody against a cellular target of tubulin was chosen for investigations into the excitation efficiency of 280 nm LEDs in QD imaging.

4.3.2 Excitation of QD-labelled cells at a wavelength of 280 nm compared to 365 nm

The spectrum of the 280 nm and 365 nm LEDs used in this study, as measured at the specimen plane, are shown in figure 4.8.

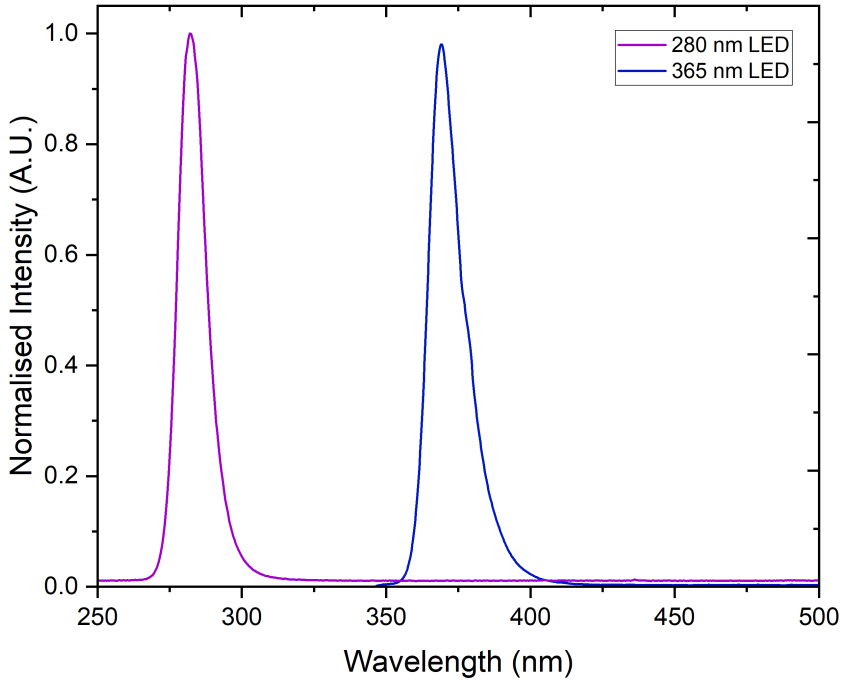

FIGURE 4.8: Spectra of the LEDs used to compare excitation of semiconductor QD–labelled cells.

This confirms that the intended excitation wavelengths, 365 nm and 280 nm, are reaching the specimen plane to excite fluorescence from the QD-labelled specimens and that there is no overlap in excitation wavelength that may convolute results.

In order to understand the extent of which any inhomogeneity in illumination may affect intensity ratios, the variation in illumination across the field of view of the microscope for each illumination wavelength is shown in figure 4.9.

The 280 nm LED exhibits a deviation of $\pm 3.4\%$ in intensity from the mean across the field of view of the microscope and the 365 nm LED exhibits a deviation of $\pm 4.6\%$ in intensity from the mean. Due to the differences in illumination intensity across the field of view for each LED, this could result in higher standard deviations when

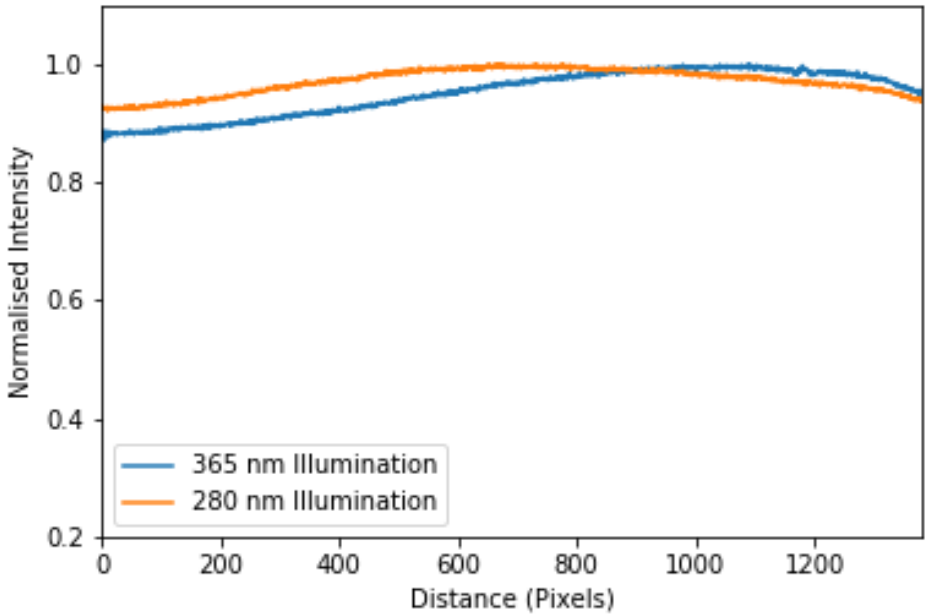

FIGURE 4.9: Variation in illumination intensity across the field of view of a 10x lens for 365 nm and 280 nm illumination.

considering the increase in fluorescence intensity when using 280 nm light compared to 365 nm light.

The autofluorescence images of unlabelled HeLa cells are shown in figure 4.10, along with the mean intensity values (in grey levels) associated with cell autofluorescence. The mean autofluorescence intensities for cells excited with 365 nm light and 280 nm light detected at a wavelength of 525 nm were 24 ± 20 and 71 ± 21, respectively. The autofluorescence intensity of cells excited at 280 nm is higher than of those excited with 365 nm. This is to be expected as 280 nm is known to be the peak excitation wavelength of several naturally occurring fluorophores within the cell, notably tryptophan and tyrosine [13]. The mean autofluorescence values were subtracted from mean QD intensity values to ensure that any increase in fluorescence occurring at an excitation wavelength of 280 nm was from increased excitation efficiency of QDs rather than increased autofluorescence.

Images of QD525-labelled HeLa cells excited with 280 nm and 365 nm light are shown in Figure 4.11. Figure 4.11a shows QD525-labelled cells excited with 365 nm light, and 4.11b shows cells excited with 280 nm light, with the same contrast adjustment. From the first glance, QD-labelled cells appear significantly brighter when

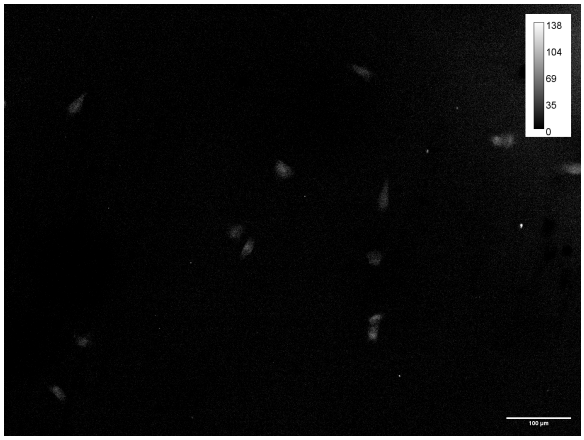

(A) 365 nm excitation

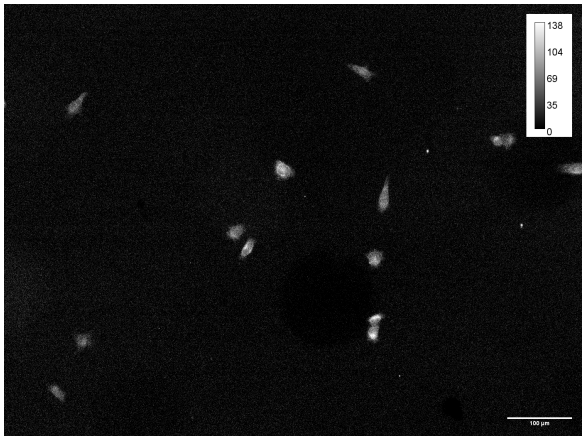

(B) 280 nm excitation

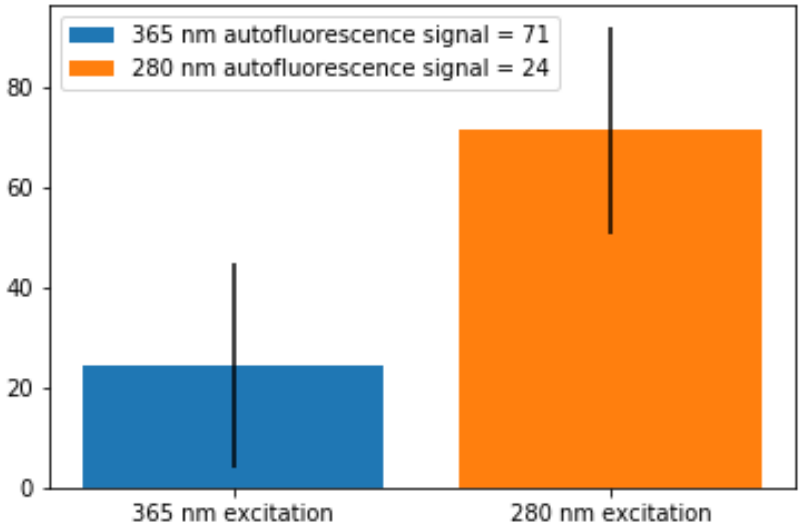

(C) Intensity bargraph

FIGURE 4.10: Comparison of cell autofluorescence of (a) and (b) as detected at 525 nm. Y-axis values correspond to grey levels. Error bars correspond to the standard deviation of the mean pixel intensity within cell regions of interest.

excited with 280 nm light, although minimal intensity contributions will come from the increased cellular autofluorescence shown in figure 4.10. However, this increase in fluorescence combined with minimal change in background intensity results in a much improved signal-to-background ratio and therefore image quality. To quantify the image contrast, equation 3.1 was used and yields a contrast of 0.69 with 280 nm excitation and 0.35 with 365 nm excitation.

To quantitatively describe the increase in fluorescence intensity from QDs excited

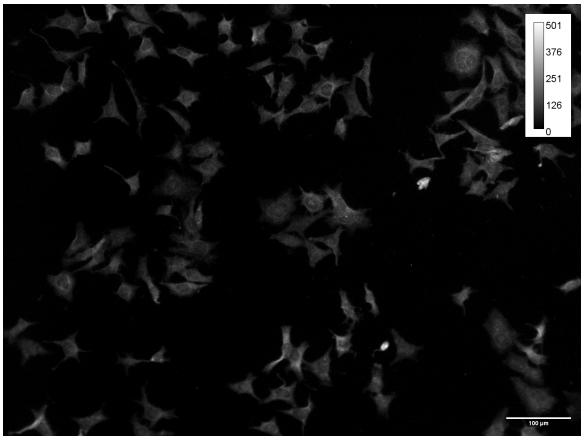

(A) 365 nm excitation

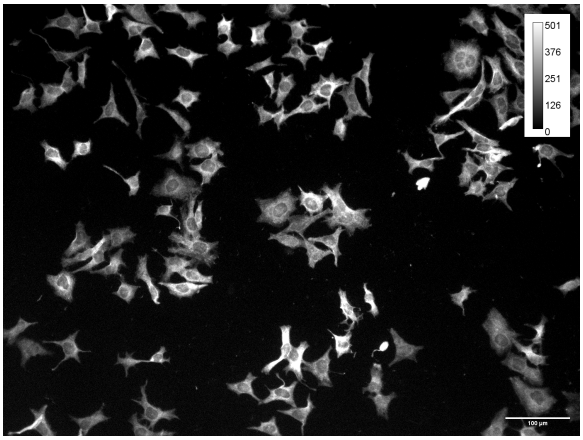

(B) 280 nm excitation

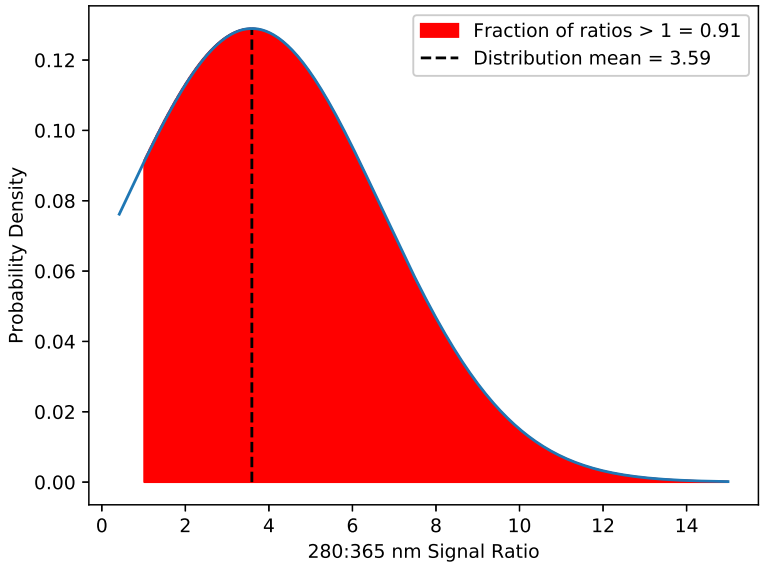

(C) Distribution of 280:365 nm fluorescent signal ratio

FIGURE 4.11: HeLa cells with QD525-labelled microtubules excited with (a) a wavelength of 365 nm and (b) a wavelength of 280 nm. (c) The probability distribution of the ratios of fluorescent signal from 280 nm and 365 nm excitation. The mean of the distribution is 3.59. The area shaded in red represents the the ratios > 1, which comprise 0.91 of the total cumulative probability density which is above 0.

with 280 nm, the distribution of 280 nm:365 nm intensity ratios is shown in figure 4.11c. This data yields a mean intensity ratio of 3.59, meaning that on average QD525-labelled cells excited with 280 nm are 3.59x brighter than those excited with 365 nm. Furthermore, a two-sided t-test of 280 nm and 365 nm intensity distributions was performed under the null hypothesis that the distributions have identical mean values. This test yields a t-statistic of 472.43 and a p value of ≤ 0.00001, confirming that the

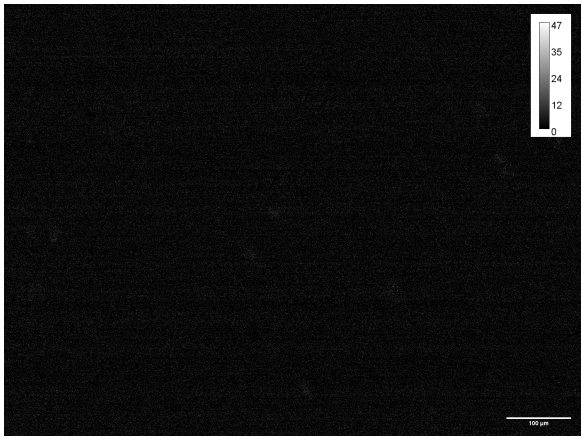

(A) 365 nm excitation

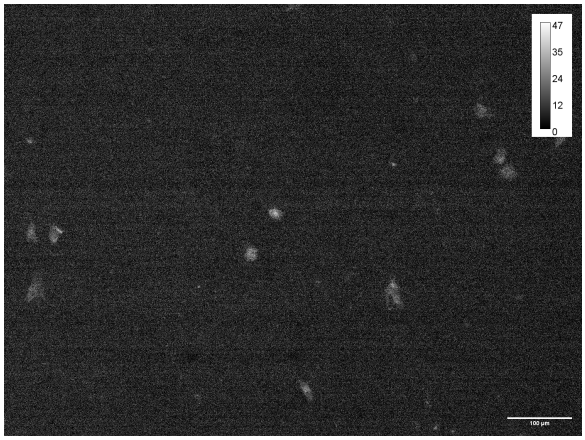

(B) 280 nm excitation

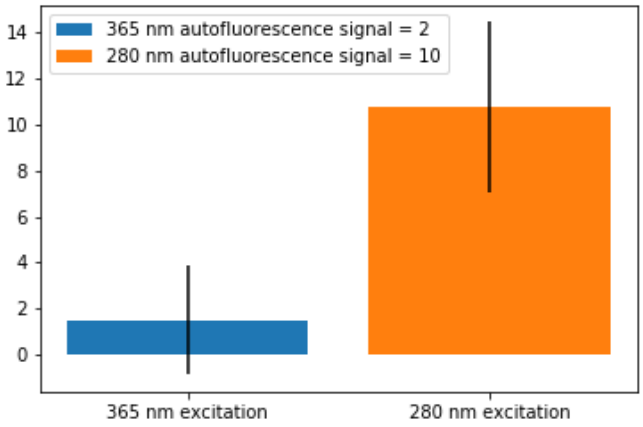

(C) Intensity bargraph

FIGURE 4.12: Comparison of cell autofluorescence of (a) and (b) as detected >561 nm. Y-axis values correspond to grey levels. Error bars correspond to the standard deviation of the mean pixel intensity within cell regions of interest.

difference in mean fluorescence intensities of QDs excited with each wavelength is statistically significant.

Imaging was then repeated with QD605 labelled cells. Autofluorescence images of unlabelled cells excited with 365 nm and 280 nm, detected at a wavelength >561 nm are shown in figure 4.12. Autofluorescence intensities from unlabelled cells excited with 365 nm and 280 nm were 2 ± 2 and 11 ± 4, respectively. The autofluorescence intensities are significantly lower within this detection range because of the reduced number of autofluorescent components within the cell that emit at wavelengths above 561 nm. As a result, where autofluorescence is a problem it would be advantageous to use QDs emitting at longer wavelengths at which autofluorescence intensity is lower.

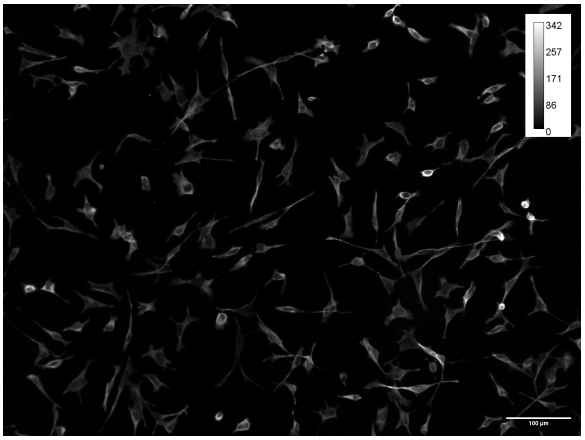

(A) 365 nm excitation

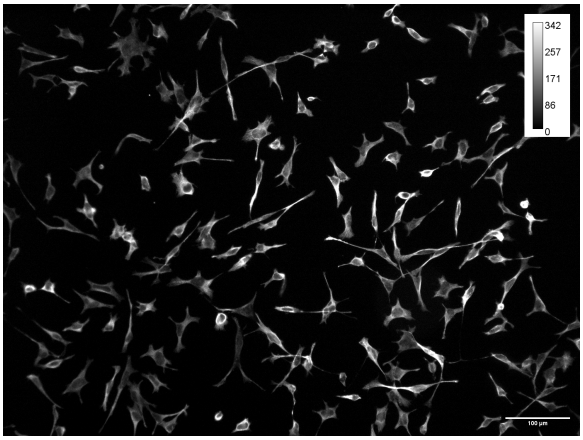

(B) 280 nm excitation

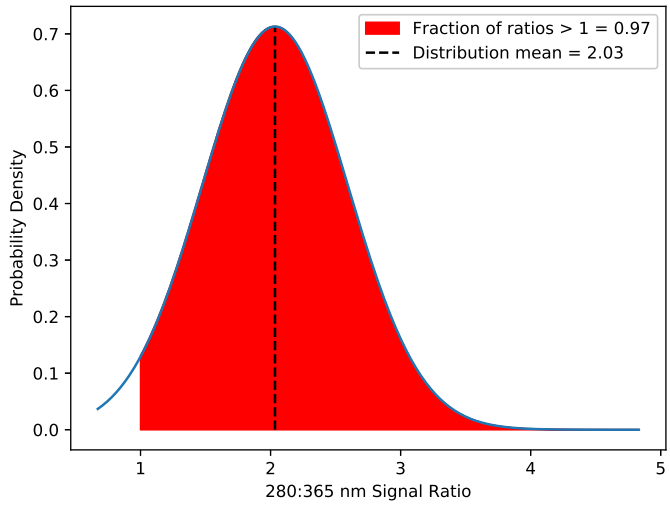

(C) Distribution of 280:365 nm fluorescent signal ratio

FIGURE 4.13: HeLa cells with QD605-labelled microtubules excited with (a) a wavelength of 365 nm and (b) a wavelength of 280 nm. (c) The probability distribution of the ratios of fluorescent signal from 280 nm and 365 nm excitation. The mean of the distribution is 2.03. The area shaded in red represents the the ratios > 1, which comprise 0.97 of the total cumulative probability density which is above 0.

Nevertheless, these autofluorescence intensities can be subtracted from below QD intensities.

HeLa cells with microtubules labelled using QD605 are shown in Figure 4.13, again excited with 365 nm light (4.13a) and 280 nm light (4.13b). Whilst there is a visually apparent increase in intensity, this does not appear to be as pronounced as in the case of QD525-labelled cells. Data analysis was performed as before and the resulting comparison of mean QD fluorescence intensities can be found in Figure 4.13. Again, we

see a significant increase in fluorescence when using 280 nm excitation, with a mean intensity increase of 2-fold compared 365 nm light. By using equation 3.1, we can calculate image contrasts of 0.81 associated with 280 nm excitation and 0.57 associated with 365 nm excitation. A two-sided t-test of 280 nm and 365 nm intensity distributions was again performed. This test yields a t-statistic of 269.961 and a p-value $\leq$ 0.00001, confirming that the difference in mean fluorescence intensities of QDs excited with each wavelength is statistically significant. This confirms that the increase in fluorescence intensity observed is applicable to multiple sizes of QD.

4.3.3 Photobleaching of QDs Excited at 280 nm

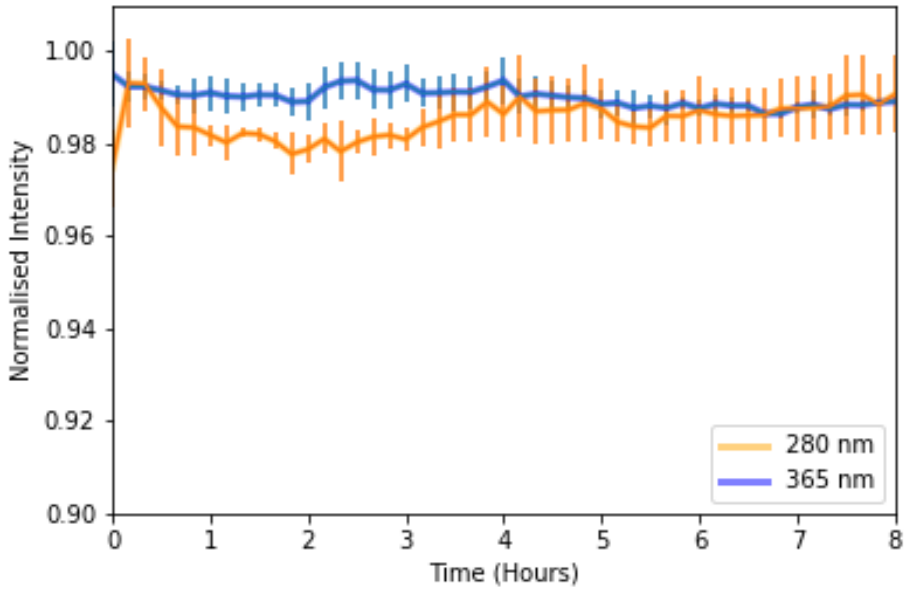

FIGURE 4.14: Mean intensity of QD605-labelled HeLa cells over an 8 hour period of constant irradiation with 365 nm (blue) and 280 nm (orange). Error bars represent the standard deviation of the mean.

The rate of photobleaching of QD605-labelled cells excited with 280 nm and 365 nm over an 8 hour period is shown in figure 4.14. After irradiating QD labelled cells each with 365 nm and 280 nm light for an 8-hour period, no evidence was found that 280 nm excitation causes increased photobleaching in commercial QDs when compared to 365 nm excitation. Fluorescence intensity from QDs was found to decrease by 0.59% over the 8-hour period when irradiated with 365 nm light, and increase by 1.64% when irradiated with 280 nm light.

4.3.4 280 nm illumination of live cells

As demonstrated above, 280 nm excitation can significantly improve the brightness from semiconductor QDs when compared to longer wavelengths, meaning that brighter fluorescence can be obtained without having to increase the power at the specimen plane. This is particularly useful in live cell imaging where the optical power at the specimen plane must be carefully controlled in order to preserve cell viability. However, as discussed, 280 nm light has specific cell damage mechanisms which make it significantly more dangerous than visible wavelength or even near-UV light.

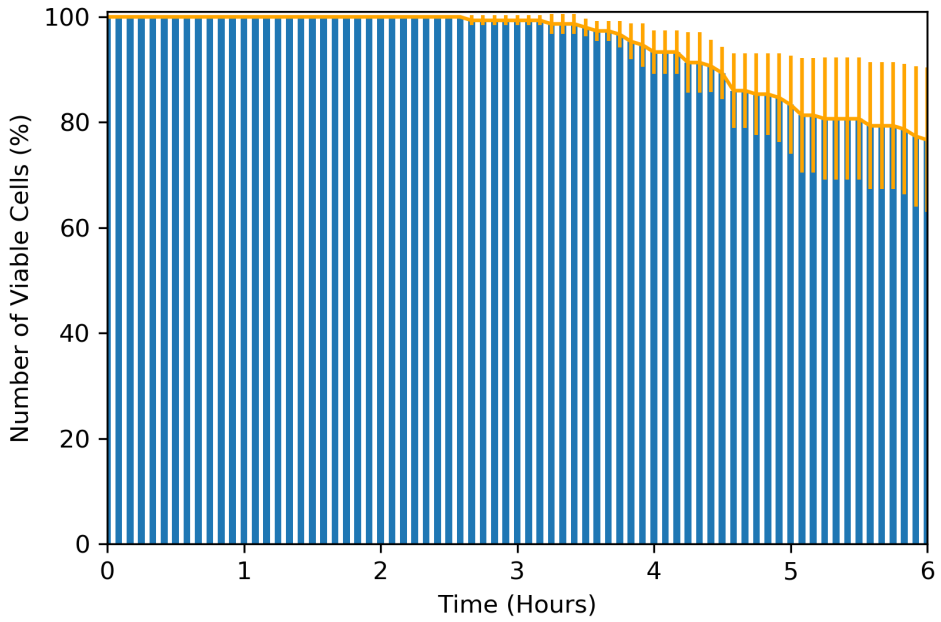

FIGURE 4.15: Percentage of viable cells over time after irradiation of 280 nm light. Cells were exposed to 2.5 mW of 280 nm light for 500 ms every 5 minutes.

Figure 4.15 shows the number of viable cells as a function of time. This data suggests that on average, after exposure to this light dose, around 80% of cells remain viable after 6 h. This result is similar to that reported by previous cell viability assays such as in the work of Benjamin Zeskind [39]. Whilst an exposure time of 500 ms and intervals of 5 minutes were used in this experiment, higher cell viability may be achieved by further optimisation of live cell imaging conditions such as shorter exposure times and longer gaps between imaging to allow cell recovery.

4.4 Discussion

Although an excitation wavelength of 365 nm was compared against 280 nm and resulted in an increase in fluorescence intensity of up to 3.59x, this increase in fluorescence intensity associated with 280 nm is expected to be even greater in comparison to those using longer excitation wavelengths such as 405 or 470 nm. The observed increase in fluorescence intensity of QD-labelled cells is expected to apply to all sizes of commercial semiconductor QDs since all sizes of QDs have absorption spectra with broadly similar distributions [49]. Therefore, all sizes of QDs are likely to have a higher absorption efficiency at 280 nm compared to longer wavelengths. However, although the absorption spectra distributions are similar, they are not identical for all QDs (as shown in figure 4.1) and the extent of the increase in fluorescence signal depends on the specific difference in absorption efficiency between 280 nm and longer wavelengths for different sizes of QD. Broad distributions in intensity ratios can partly be attributed to inhomogeneity of the illumination light. Whilst both illumination sources were aligned to achieve the best possible homogeneity of illumination across the field of view, it was not always possible to achieve this perfectly. As reported, some variations in intensity across the field of view occurred for both illumination wavelengths, affecting the mean increase in fluorescence intensity achieved using 280 nm excitation. In addition to this, while the size and absorption/emission properties of semiconductor QDs can be controlled via synthesis, not all synthesis methods result in QDs of one single size [96]. Therefore, within a sample of commercial QDs there will be a size tolerance leading to some variation in emission and absorption spectra [156, 157] which, as the increase in excitation efficiency is dependent on the shape of the absorption spectrum, can affect the mean increase in intensity between excitation wavelengths.

Despite the substantial overlap in standard deviations from the mean fluorescence intensity at 280 nm and 365 nm excitation for both the QD525 and QD605 datasets, this does not correspond to significant instances where 365 nm excitation yields equivalent or brighter emission intensity. Indeed, the percentage of pixels where the 280:365 intensity ratio is >1 (i.e. the percentage of pixels where the pixel in the 280 nm excitation image has a higher intensity then the same pixel in the 365 nm excitation image)

is 98.88% and 99.28% for QD525 labelled cells and QD605 labelled cells, respectively. This near universal increase in intensity in favour of 280 nm excitation, coupled with p-values close to zero, confirms that these standard deviations from the mean do not detract from the conclusion that excitation of QDs with 280 nm light yields an increased fluorescence intensity.

Some increase in fluorescence intensity can be noted over the 8-hour imaging period in figure 4.14. Although the fluorescence intensity of CdSe QDs does not show long-term degradation in when dispersed in an organic solution [158], increase in fluorescence intensity from QDs over time has been reported previously [89]. This has been attributed to carriers being transferred to surface traps present at the interface of the CdSe core and ZnS shell of the QDs or photo-assisted release of trapped carriers on the QD surface [158]. Further to this, there is also the possibility that the use of high-energy UV light could affect the thermal state of the specimen, e.g. heating of the gelvatol mounting medium, causing fluctuations in fluorescence intensity. This problem could be minimised by using aqueous mountant such as in live cell imaging experiments. Previous studies have shown that various steps in the labelling protocol can cause increased photobleaching in commercial QDs [141] but as the same sample was used in measurements of both excitation wavelengths, this should have no effect on the comparison of photobleaching between excitation wavelengths. Since minimal photobleaching of QDs occurs in the short term under either excitation wavelength, this makes it unlikely that the intensity difference observed in QDs excited by 280 nm vs 365 nm light is caused by photobleaching. In addition, the images with 365 nm excitation were acquired before the images with 280 nm excitation, further ruling out the possibility of photobleaching affecting intensity ratios as the second image acquired is always brighter than the first. In all, this confirms that long-term imaging of QDs using 280 nm excitation is possible without causing any photobleaching to the specimen.

Although irradiation with 280 nm light does have some more impact on cell viability compared to longer wavelengths, several steps can be taken in live cell studies to reduce the dosage of 280 nm light to the specimen. Although 2.5 mW of optical power was used in this study, this can be significantly reduced whilst taking measures to preserve fluorescence intensity, including using higher numerical aperture lenses and

utilising camera binning. As discussed, it has also been shown that increasing the camera exposure time and decreasing the optical power of the illumination source, effectively keeping the light dose the same, can reduce toxicity to cells [34]. Depending on the nature of the experiment, longer time periods between acquisitions can be introduced to further limit light exposure and allow for cell recovery. In fact, it has been shown that cells irradiated with 270 nm and 290 nm light showed recovery rates of 25% to 50%, whilst cells irradiated with a longer wavelength of light did not show any recovery ability [60]. Therefore, it is thought that although some longer wavelengths of light may induce less DNA damage than lower wavelengths, long-term exposure to these may result in severe and irreparable damage. In addition to prolonging cell viability by limiting UV exposure, installing further environmental controls on a microscope for live cell imaging can provide cells with optimum environmental conditions, such as humidity and $C0_2$ control [54]. It is hoped that by using these approaches, and very careful optimisation of imaging parameters, we could exploit the high fluorescence intensity associated with 280 nm excitation of QDs to study cell dynamics with minimal UV-induced toxicity.

However, the issue of labelling live cells with QDs poses another issue in addition to UV-induced cell damage. Whilst the development of fluorescent proteins dramatically changed live cell imaging, allowing targeting of subcellular structures whilst preserving cell viability, QDs do not have this benefit. To apply QDs as cellular labels, there are only a few established techniques and few of these provide specificity. Endocytic uptake can provide non-specific labelling of the cell cytoplasm, however, due to the aggregative nature of nanoparticles, QDs within the cytoplasm tend to form clumps and do not provide homogenous labelling of the cell [89, 105, 110]. This can provide sufficient information for applications such as cell tracking [105], but only when used in correlation with a second technique such as brightfield imaging to identify the position of the cell. Other labelling methods can include labelling of the cell surface as this does not require the QD label to pass through the membrane of the cell. This can be done using biotinylation of the cell membrane or antibody labelling of the membrane [92]. However, labelling cell surface receptors on the cell can interfere with cell adhesion, making it more difficult to image dynamics such as cell migration. In all, for the application of 280 nm excitation of QDs in live cell imaging to be useful,

there must first be a labelling method developed to allow QDs to bind to the cell in a way that does not interfere with normal cell function and also provides either specific labelling to a cellular target or provides homogenous labelling across the cell for more general cell studies. Given more time and opportunity, the application of 280 nm excitation of QD-labelled live cells would be an interesting and rewarding study, however, it still stands that the use of 280 nm excitation of QDs in fixed cells provides an excellent advantage compared to excitation with longer wavelengths.

4.5 Conclusion

In this chapter, I have explored the application of 280 nm LEDs as an excitation source for QDs. I first optimised a labelling technique for labelling fixed HeLa cells with QDs and then went on to use 280 nm light to excite these on the 280 nm compatible microscope adapted from my work in chapter 3. Using this, I compared excitation of QDs at a wavelength of 280 nm with an excitation wavelength of 365 nm. By doing this, I showed up to a 3.59-fold increase in fluorescence intensity from semiconductor QDs excited at 280 nm compared to 365 nm, which significantly improves image contrast. I showed that this increase applies to multiple QD sizes and is expected to apply to all emission varieties of commercial semiconductor QDs due to their similarly distributed absorption spectra. In addition to this, I found no significant increase in photobleaching of QDs when illuminated with 280 nm light over an 8-hour period when compared to 365 nm light, confirming that long-term imaging at 280 nm can be achieved without causing photobleaching to the specimen.

I also investigated the possibility of imaging live cells at this wavelength. By irradiating cells with 280 nm light for moderate exposure times (500 ms) and leaving long periods between acquisitions (5 mins) I was able to image cells for 6 hours with 20% loss in viability. It is hoped that by carefully optimising imaging conditions such as exposure time, LED power and imaging period, it would be possible to apply the benefit of increased QD fluorescence at 280 nm to live cell imaging without distressing cells, however there are some adjacent issues in the labelling of live cells with semiconductor QDs which may provide a further barrier to this.

Chapter 5

Standing wave microscopy with 280 nm excitation

Standing wave microscopy is a technique for achieving axial super-resolution. In this technique, two counter-propogating waves interfere with each other and generate regions of destructive interference (nodes) and constructive interference (antinodes), with only the antinodes able to excite fluorescence from the specimen. For this reason, in standing wave microscopy, the antinodal FWHM is typically quoted as the axial resolution as this is the uncertainty within which a fluorophore can be located. The antinodal planes have a typical FWHM of a quarter of the wavelength of excitation light used (or less with high refractive index media), restricting the excited fluorescence to several tens of nanometers, allowing far greater axial precision in the localisation of fluorescently labelled structures. As the axial resolution in this technique is proportional to the excitation wavelength, a wavelength of 280 nm is desirable as this theoretically offers an axial resolution of up to $\sim$47 nm - a near twofold increase in previous resolutions achieved with visible wavelength standing wave. For this reason, this chapter explores the possibility of using standing wave microscopy with 280 nm excitation. It first describes and models the theoretical standing wave produced using 280 nm excitation, including the expected antinodal spacing and antinodal FWHM. It then describes a method used to generate a standing wave using 280 nm excitation which does not require the use of an epifluorescence set-up. Finally, it goes on to apply this new method of 280 nm standing wave microscopy to image QD-labelled fixed mammalian cells.

5.1 Introduction

A standing wave is an interference phenomenon resulting from the interference of two counterpropagating waves [159]. As shown in figure 5.1, interference between the light propagating in one direction (red) and the light propagating in the opposite direction (blue) gives rise to a standing wave (black). Areas of constructive interference give rise to antinodes, and destructive interference to nodes. Standing waves are called such because they appear to be stationary, with nodes and antinodes having fixed positions along the optical axis.

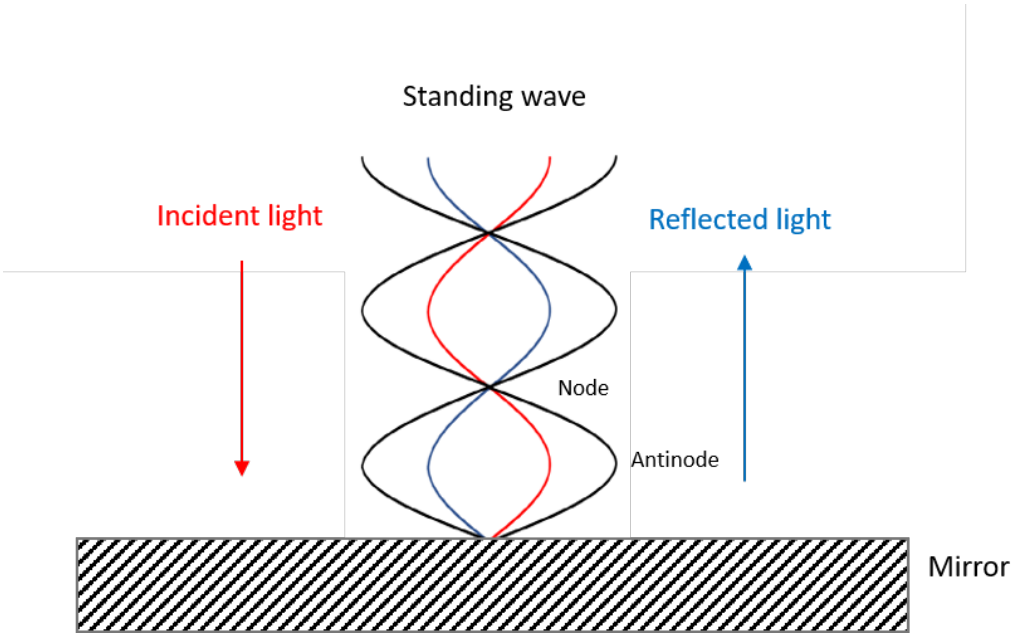

FIGURE 5.1: A standing wave formed by the interference of two counterpropagating waves of light at 0°. A wave propagating in one direction (red) interferes with a wave propagating in the opposite direction (blue) and creates a standing wave (black).

Standing waves were discovered by Otto Wiener in 1890 [160][161]. Wiener used a thin layer of photographic film on a glass slide which he placed very close to a silver mirrored surface at a slight angle. When the mirror was illuminated and the photographic film was developed, Wiener found that the film appeared black in areas which corresponded to the antinodes of the standing wave. These experiments were shortly after confirmed by Drude and Nernst in 1892, but using a layer of fluorescent material in place of a photographic film [162].

The application of standing waves in microscopy was described first by Frederick

Lanni in 1986 [163]. In his initial design, two sources of coherent light were propagated in opposite directions and overlapped across the field of view of the microscope (figure 5.2). Standing waves were formed in the volume of overlap of the two beams and the antinodal spacing δ_s was determined by:

$$\delta_s = \frac{\lambda}{2ncos\theta} \tag{5.1}$$

where λ is the wavelength of incident light, n is the refractive index of the surrounding medium and θ is the angle of incidence of the excitation light. This technique resulted in fluorescence only being excited in antinodal planes, which was then detected using an air immersion objective lens. A second, similar design used total internal reflection at the slide-specimen interface to create the standing wave, requiring only one light source illuminating the specimen at an angle. These designs allowed control over the antinodal spacing of the standing wave by adjusting the incident angle, however the antinodal spacing can never be at its minimum due to the geometry of the set up. Nevertheless, Lanni showed that it was possible to use this standing wave system to image 3T3 cells stained with rhodamine phalloidin, with nodal and antinodal planes clearly visible within the cell.

Some years later, Lanni and coworkers developed a further two designs for generating a standing wave using a microscope [164, 165, 166]. The first was a 4Pi type configuration [167, 168], with two opposing objective lenses facing onto the specimen plane. Laser excitation light would propagate through these objectives and interfere with each other, generating a standing wave at the specimen plane. This way, the authors were able to achieve the minimum antinodal spacing possible since the angle of intersection between the two counterpropagating waves was now 0°. These standing waves create an excitation field with closely spaced nodes and antinodes which allows optical sectioning of a specimen with high axial resolution, reported to be better than 95 nm [164] when using blue light and high refractive index materials. This is compared to the axial resolution of 300 nm measured with a confocal microscope [169]. However, this configuration is very difficult to achieve as it involves alignment of both objectives to a high precision. A second design in this paper utilised a mirror to reflect incident light from the epifluorescence pathway to create a standing wave.

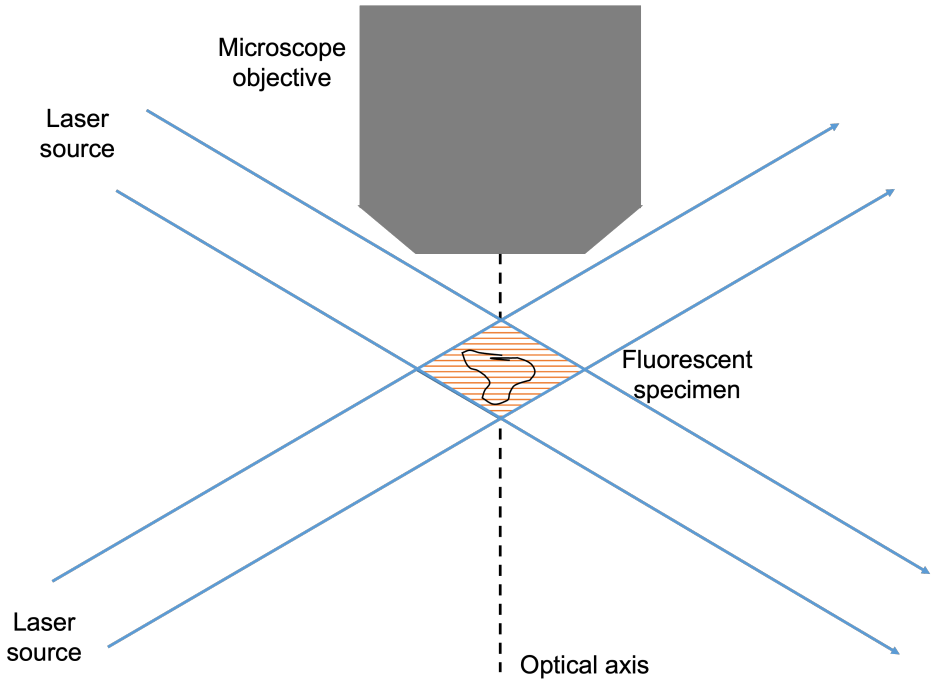

FIGURE 5.2: Lanni's first design for a standing wave microscope, making use of two overlapping coherent light sources [163]. Standing waves are formed in the volume of overlap and the properties of the wave are determined by the angle of incidence, wavelength of excitation and the refractive index of the medium. In this design, the antinodal spacing can never be at a minimum as the angle of incidence is non-zero.

In this method, interference occurs between the direct and reflected components of the excitation beam which again creates a standing wave pattern that excites fluorescence only at the antinodal planes with minimum spacing. This design paved the way for future work on standing wave microscopy due its simplicity and low-cost nature.

Due to the normal incidence of light in these designs, the angular dependence variable in equation 5.1 becomes 1. Hence, antinodal spacing δs and FWHM are then defined by:

$$\delta s = \frac{\lambda}{2n} \tag{5.2}$$

and

$$FWHM = \frac{\lambda}{4n} \tag{5.3}$$

i.e. the antinodal spacings are at their minimum value. Around the same time, Freimenn *et. al.* developed their own standing wave configuration using confocal

laser scanning and a beamsplitter, designed to have high nodal plane flatness and be accessible and easy to use [170]. Using this standing wave microscope, the authors were able to image actin filaments within cells whilst shifting the standing wave axially using a piezoelectric shift of the beamsplitter.

In more recent years, Elsayad recognised the potential of standing wave microscopy to identify the distances between molecules and surfaces, deemed "nanosectioning" [171]. In this work, a reflective surface was generated by coating a quartz substrate with a metal layer and a dielectric layer. Fluorescently-labelled specimens were cultured directly onto these custom-designed substrates and an axial-distance-dependent emission spectrum was obtained. By using the first antinode of the standing wave only, the authors were able to estimate the axial positions of fluorophores with a precision of 5-10 nm [171].

A potential disadvantage of standing wave microscopy is that if the specimen is thicker than the anti-nodal spacing, several planes may be excited at once and their contributions may be difficult to separate from each other. With a suitable specimen (varies in x/y with axial distance), distinct excitation fringes can be recognised and used as contour lines for 3D mapping. The depth of field of the microscope objective lens can also be a limiting factor as only a few antinodal planes can be in focus at the same time. However, this can be used to an advantage as with a curved specimen, the standing wave technique can be used as a contour map to provide information on specimen shape.

This work was pioneered by Amor *et. al.* who used a confocal laser scanning microscope to excite multiple antinodal planes at once and produce 3D contour maps [161] of model and cell specimens. By choosing specimens that were much thicker than the antinodal separation, multiple antinodal planes were imaged simultaneously with encoded axial information provided that the fluorescently-labelled structure within the specimen varies in x/y with axial distance such that the antinodal planes can be separated laterally. To demonstrate this, the authors coated the curved side of a plano-convex lens with a monolayer of fluorescent dye and obtained a standing wave image. This comprised of concentric rings of fluorescence emission, located within antinodal planes, and dark rings at positions of nodal planes. By using the geometry of the lens, the authors were able to extract axial information such as antinodal spacing from the

images and compare these measured values against the theoretical standing wave PSF. Cellular specimens make excellent candidates for standing wave microscopy due to their biconcave structure, and the authors went on to study red blood cells with an axial resolution of 90 nm [161]. However, due to the use of a confocal laser scanning microscope in this work, acquisition times were around 40 s which significantly limits temporal resolution, resulting in the loss of dynamic processes [161].

Whilst standing wave microscopy has traditionally been carried out using coherent laser light sources, standing wave microscopy has recently been extended to include LED sources [172]. Tinning and coworkers reported the first use of widefield standing wave microscopy using LED illumination. The authors found no significant difference in antinodal spacings or antinodal FWHM compared to using laser illumination, despite the significantly larger spectral FWHM of LEDs compared to laser excitation sources. While previous work by Amor *et. al.* on the imaging of red blood cells with a confocal laser scanning microscope meant that the temporal resolution was limited to 40 s per frame and fast membrane movements could not be captured [161] [172], Tinning's experiments using a widefield system gave high temporal resolution at a speed of 30.3 Hz as well as an axial resolution better than 100 nm [172].

One of the significant drawbacks of using standing wave microscopy with thick specimens is the information gap produced as a result of the nodal gaps between fluorescence excitation. This results in an incomplete picture of the specimen, with approximately 50% of the specimen lost to nodal regions [173]. Recent work by Schniete et al in 2021 [173] theorised that, based on equations 5.2 and 5.3, the information lost in single-wavelength standing wave could be recovered by using multiple excitation wavelengths. This technique, coined Tartan standing wave, uses 3 excitation wavelengths, 488 nm, 514 nm and 543 nm to increase the sampling density from 50% with a single excitation wavelength, to 98%.

As the aforementioned experiments utilise multiple antinodal planes to image fluorescent specimen, the full axial PSF for standing wave microscopy is described using a convolution of the excitation standing wave pattern and the widefield axial emission PSF.

The intensity field of a standing wave can be described by [163, 174]:

$$I = I_0[1 - cos(Kz + \psi)] \tag{5.4}$$

where $K = \frac{4\pi n cos(\theta)}{\lambda_{exc}}$, z is axial height and ψ is the relative phase of the two counter-propagating waves.

The axial PSF of a widefield microscope can be described by [175]:

$$PSF_{epi} = [sinc(\frac{NA^2}{2n\lambda_{em}}z)] \tag{5.5}$$

where NA is the numerical aperture of the objective lens, λ_{em} is the wavelength of fluorescence emission and n is the refractive index of the immersion medium.

As the resulting PSF is a convolution of the axial PSF of the microscope and the intensity of a standing wave field [174], the theoretical standing wave microscopy PSF can be given as [163]:

$$PSF_{SW} = [1 - cos(Kz)][sinc(\frac{NA^2}{2n\lambda_{em}}z)]^2 \tag{5.6}$$

Based on equations 5.3 and 5.2, it is clear that a shorter excitation wavelength results in narrower antinodal FWHM and antinodal spacing, effectively improving axial resolution and sampling density compared to previous standing wave work. For this reason, this work focussed on the implementation of standing wave microscopy at an excitation wavelength of 280 nm.

Whilst in theory it should be simple to achieve high axial resolution by changing the excitation wavelength in well-established standing wave techniques, the issue of transmission of 280 nm through microscope optics becomes a barrier more than ever. This issue, a running theme throughout the work in this thesis, almost completely rules out the popular, cost effective standing wave technique of placing a mirror below the specimen in an epifluorescence microscope. This issue could be overcome by using a specialised UV objective lens, such as those made of quartz or reflective components, but these are not without their own limitations. As discussed in detail in chapter 3, quartz lenses are limited in variety, with only 10x and 40x lenses presently available at low NAs, and they also suffer from limited transmission of deep-UV light. While the attenuation of quartz lenses is not to the extent of that of glass objective lenses, this still

poses an issue with 280 nm LEDs with already limited optical powers. This makes the detection of a standing wave using a lens specimen particularly challenging where the fluorescence intensity from a monolayer of dye is low. Secondly, reflective objectives offer much higher transmission at 280 nm but suffer from a lack of flat-field correction due to the curved nature of the mirrors within the lens, resulting in the centre of the image being in focus and the outer portions being out-of-focus. This is a particular issue in standing wave microscopy when measuring antinodal thickness and spacing as the out-of-focus areas in the image will cause inconsistent antinodal thicknesses, preventing accurate measurements of the standing wave.

For these reasons, it became necessary to devise a new method of generating a standing wave using 280 nm light that bypasses the need for a standard epifluorescence microscope configuration. In the work carried out in this chapter, I developed such a technique to successfully generate a standing wave with 280 nm light, and I compared the experimentally measured standing wave properties with those expected from theory. I then applied this new technique to image fixed mammalian cells prepared with quantum dot labels with 280 nm standing wave microscopy.

5.2 Methods

5.2.1 Theoretical Standing Wave PSF

To plot the theoretical standing wave PSF, equation 5.6 was used. The Python code written which plots the theoretical PSF and calculates the peak positions and peak widths can be found in Appendix B. To calculate the theoretical PSF for the variables used here, the excitation wavelength was set to 280 nm, the emission wavelength to 655 nm, the refractive index to 1 for measurements in air, or 1.341 for measurements in 4% BSA, and the NA to 0.4. These values were chosen to match the intended experimental parameters to later be used to measure the standing wave. The theoretical PSF produced using this code could then be directly compared to the experimental values.

5.2.2 Methods used to Generate and Measure 280 nm Standing Waves

Due to the limitations in mirror-based standing wave described in the introduction, a new method of generating a 280 nm standing wave was investigated which bypasses the need to use any commercial microscope optics. This method involved use of an inverted microscope and a 400 nm longpass filter - in principle, it should be possible to form a standing wave using a semi-reflective surface (such as a filter) provided that the surface has excellent reflection at the excitation wavelength - in this case, 280 nm. The filter is then used to generate a standing wave with the excitation light, whilst being able to transmit longer wavelength light (fluorescence from the sample) to be collected by the microscope objective. The set up developed to accommodate this is shown in figure 5.3.

This optical set-up was adapted from that of figure 4.3, with the only addition being the optical filter at the specimen plane. Although in principle a reflecting filter should be able to produce a standing wave, many longpass filters absorb rejection wavelengths rather than reflecting them [176]. Many manufacturers also do not provide information on whether filters reject wavelengths by reflection or absorption - for this reason, a range of optical filter manufacturers were contacted for information on reflection data in order to select an appropriate filter for generating a standing wave.

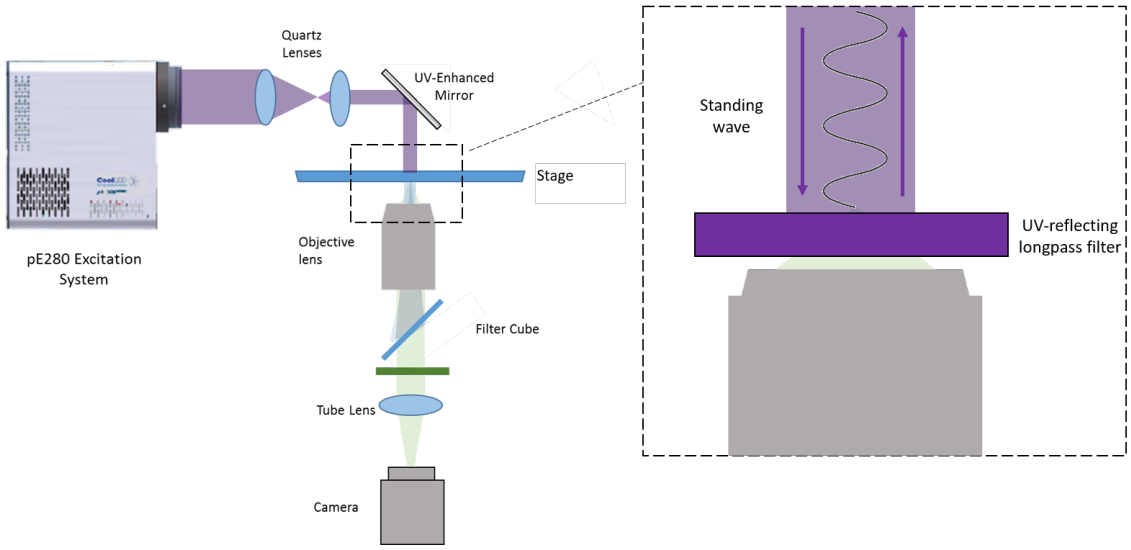

FIGURE 5.3: Inverted microscope set-up to produce a standing wave using 280 nm light. An Olympus IX71 was used as the main microscope body for imaging specimen. Around this, a fully quartz transmission fluorescence set-up was built in order to deliver 280 nm light to the specimen from above. The 280 nm light was reflected to the specimen plane by a dichroic mirror. In order to generate a standing wave, a 400 nm longpass filter was placed at the specimen plane to reflect the excitation light at an angle of 180° and transmit longer wavelength fluorescence from specimens to the objective lens.

One manufacturer, Chroma (supplied by Cairn research), was able to supply both reflection (red) and transmission (blue) data for their 400 nm longpass filter (ET400LP) which is shown in figure 5.4.

This data suggests that the filter would provide excellent reflection at 280 nm (∼85%) and as such the filter was purchased for standing wave experiments.

In order to determine whether a standing wave was successfully formed, the technique previously used by [161] [172] and [173] was used. This method involves placing a fluorescently-coated plano-convex lens (curved side down) on the reflective surface used to generate the standing wave. When a standing wave is formed by the incident and reflected light, the antinodes of the standing wave will intersect the surface of the lens specimen in different lateral positions due to the curvature of the lens (figure 5.5). As fluorescence is only excited in antinodal planes, the resulting image of the curved surface of the lens specimen will be a series of concentric rings.

By taking a line profile through the radius of the rings and converting distance in μm to axial height, the antinodal spacing and antinodal thickness in nm can be measured. This was done by using the known geometry of the lens (figure 5.5).

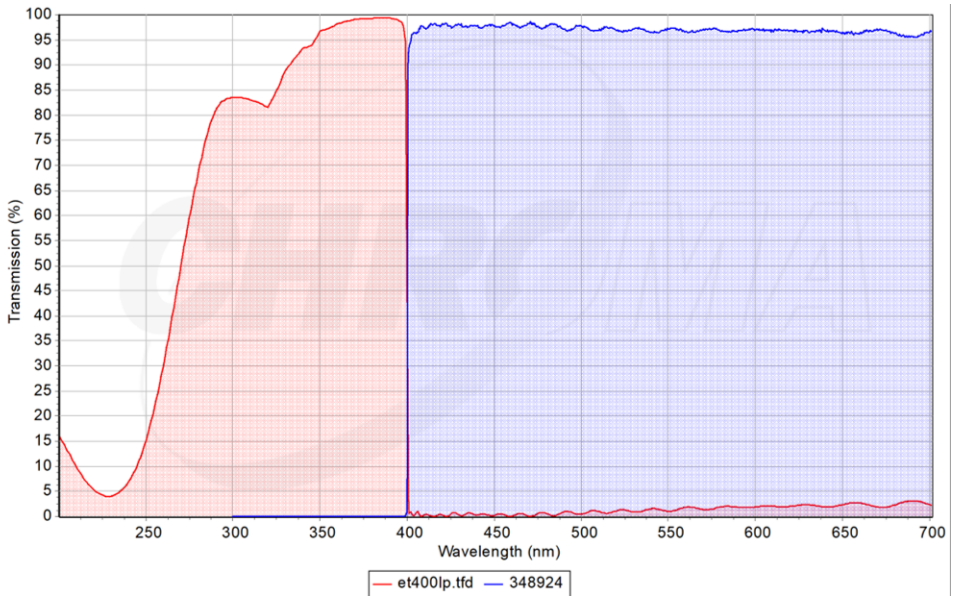

FIGURE 5.4: Reflection (red) and transmission (blue) data for Chroma ET400LP filter provided by Cairn Research.

The axial height L is given by:

$$L = R - \sqrt{R^2 - r^2} \tag{5.7}$$

where R is the radius of curvature of the lens and r is the radial distance from the centre of the lens. By plotting L against intensity, a trace of the standing wave can be obtained, from which the antinodal spacing and FWHM can be measured. These values can then be compared to the theoretical antinodal spacing and FWHM calculated using equations 5.2 and 5.3.

Quartz plano-convex lenses were purchased from Thorlabs, with 6 mm diameters and in focal lengths of either 15 (LA4917) or 20 (LA4194) mm (depending on availability). To fluorescently label these, QDs were used due to their excellent fluorescence intensity when excited with 280 nm light, as described in detail in chapter 4.

A monolayer of QDs was bound to these lenses using an adaptation of the protocol described previously [161] [172] [173] to accommodate for streptavidin-biotin based binding. The lenses were first rinsed 3 times in dry acetone and subsequently placed in a solution consisting of 0.2 ml of 3-amino-propyltrimethoxysilane (APTMS, Sigma Aldrich 281778) and 9.8 ml of dry acetone for 6 hours. After this time, the lens was washed with dry acetone a further 3 times and dried with compressed air. Next, biotin-N-hydroxysuccinimide-ester (Sigma Aldrich H1759-25MG) was prepared

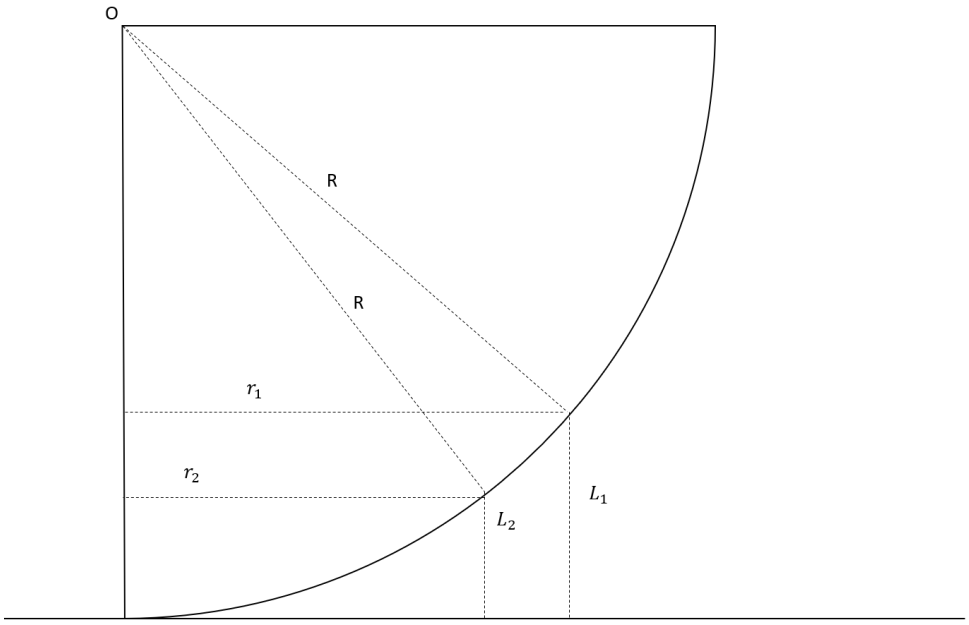

FIGURE 5.5: Geometry of a fluorescently-coated lens placed curved-side down on a mirrored surface. When a standing wave is formed, the antinodal planes intersect the lens at different positions axially and laterally. By using the radius of curvature of the lens R, 3D information can be extracted from standing wave images of the lens.

by adding 5 mg of biotin-NHS-ester to 500 μL of DMSO and 5 ml of PBS. The lens was placed in this convex-side-up and left on a plate rocker for 1 hour. A solution of 50 nM QD-streptavidin conjuages emitting at 655 nm (Q10123MP) was made in PBS and sonicated for 20 seconds to break up QD aggregates. This wavelength of QD was chosen due to its high quantum yield compared to other QD conjugates, but also because of its long wavelength. As demonstrated in chapter 2, the 280 nm LED exhibits parasitic emission in the visible wavelength, however, this tails off towards the red portion of the spectrum. As a result, using fluorescent specimens which are less likely to overlap with this parasitic emission will help to preserve image contrast, particularly in weakly-emitting specimens such as a monolayer of dye. After washing the lens with PBS, the QD solution was added to a dish with the lens placed convex-side-up and placed back on the plate rocker overnight. The next morning, the lens was washed with PBS and dried with compressed air.

In order to measure standing waves, the lens specimen was placed convex-side-down on the filter in the set-up shown in figure 5.3. The 280 nm LED was turned on at 100% power and the camera exposure set to 500 ms. The lens specimens were imaged using the Olympus 10x/0.4 NA objective lens detailed in the previous chapters.

Using the visible edges of the lens as a guide, the field of view of the microscope was navigated to the centre of the lens specimen at the point of contact between the lens and the filter. The visibility of the characteristic concentric rings of nodes and antinodes was used as confirmation that a standing wave was indeed generated by the proposed optical set-up. To image the lens specimen, the specimen was moved such that the concentric rings were in the centre of the field of view. Images were acquired using either 500 ms or 1 s exposure times and 100% LED power to achieve sufficient signal-to-background ratios in order to best analyse images.

In order to more accurately match the cellular environment, a standing wave was also generated with 4% BSA used as an immersion medium. 4% BSA was made by diluting 2 g of BSA in 50 ml of PBS. To measure the refractive index of this, an Abbe 60 refractometer (Bellington and Stanley Ltd) was used after being calibrated using water and methanol. This gave the refractive index of 4% BSA as 1.341. Using a pipette, a drop of 4% BSA was placed onto the filter in the optical set-up before placing the lens specimen on top. Imaging was then repeated as before.

To analyse the standing wave images, a MATLAB code developed by Ross Scrimgeour, shown in Appendix C was used. Briefly, this code finds the centre of the standing wave image and uses radial averaging to take a line profile through the centre to the edges of the images. The code then uses equation 5.7 to convert radial distance into axial height and a peak finding function was used to find the positions and FWHM of antinodal peaks. The mean antinodal spacing and FWHM were calculated alongside the standard deviations. Antinodal FWHM and spacing were then compared to the theoretical values determined by equations 5.3 and 5.2. To compare the statistical significance of the theoretical vs experimentally obtained value, a single sample t-test was perfomed using GraphPad Prism [177].

5.2.3 Optimisation of cell labelling for standing wave microscopy

When choosing a target cellular structure for visualising using standing wave microscopy, it is important to choose a structure that varies suitably laterally with height so that standing wave fringes are clearly visible. For this reason, the cell surface is often used as a target as standing wave can be used to visualise surface topography. Previous examples of standing wave imaging of cellular specimen have used

membrane stains such as DiI, DiO [161, 172, 173] or lipilight [173]. In addition to the cell membrane, the actin cytoskeleton has been a popular structure for imaging using standing wave microscopy since Lanni's 1986 experiments [163, 164, 170, 173]. Many of these imaging experiments have used phalloidin-based dyes for labelling the actin cytoskeleton [163, 164, 173].

Whilst both membrane stains and actin stains have shown good results in standing wave imaging, the challenge here was in finding a suitable fluorophore that can be excited at 280 nm. Luckily, as described in detail in chapter 4, QDs have excellent excitation at this wavelength and are very versatile for cellular labelling using immunofluorescence. In order to label the cell with QDs for standing wave imaging, an antibody against β actin was chosen (ThermoFisher MA1-140).

To test the labelling method and observe cells labelled with QDs under typical standing wave microscopy using visible wavelengths, cells were first grown on mirrors and imaged under an epifluorescence microscope. MCF-7 breast cancer cells were chosen due to their large axial height when adherent to a surface, which make them good candidates for observing fringes in standing wave microscopy [173]. Mirrors were coated in fibronectin for 30 minutes and MCF-7 cells were seeded onto the mirrors and allowed to adhere overnight. The next morning, cells were fixed in 4% formaldehyde.

The antibody labelling process for Streptavidin QD conjugates described in detail in chapter 3 was used to label cells. As the primary antibody was raised in mouse, the anti-mouse biotinylated secondary antibody was used to allow binding of the QD655 streptavidin conjugates (ThermoFisher Q10121MP).

To visualise the effect of standing wave imaging on these cellular targets, these specimens on the mirror were imaged in standing wave using a conventional upright system. This was done on an Olympus BX50 widefield microscope with a CoolLED pE-300 illuminator as the excitation source and a IDS camera as the detector. A wavelength of 365 nm was used to excite the QD-labelled cells and these were detected using a 430 nm longpass filter.

By obtaining standing wave images of MCF-7 cells using standard standing wave techniques, this can both ensure that the labelling method can provide good-quality

standing wave images of cells and also provide a point of reference for 280 nm standing wave imaging.

5.2.4 280 nm standing wave imaging of mammalian cells

The protocol to label cells adherent to a mirror was followed for cells on the filter, however it was more difficult to get cells to adhere to the surface of the filter. For this reason, a solution of 0.01% poly-L-lysine (Sigma Aldrich P4832) was used instead which creates an electrostatic interaction between the cells and the filter [178]. This was much more successful at getting the cells to adhere and spread out across the filter surface. MCF-7 cells were seeded onto the filter surface and allowed to adhere in DMEM for 24 h. After this time, the cells were fixed in 4% formaldehyde and labelling of the actin filaments was performed as described in the previous section.

To image these cells with standing wave microscopy with 280 nm excitation, the cell-coated filter was placed on the microscope set-up shown in figure 5.3 with the cell covered surface facing up. Cells were imaged using 280 nm excitation at 100% power (corresponding to 2.5 mW at the specimen plane) and an exposure time of 500 ms. Cells were imaged through the filter using a 20x/0.5 NA objective lens for better visualisation of standing wave fringes within cells compared to a 10x lens.

5.3 Results

5.3.1 Theoretical Standing Wave

The theoretical PSF of a standing wave with 280 nm excitation, 655 nm emission and imaged in air is shown in figure 5.6.

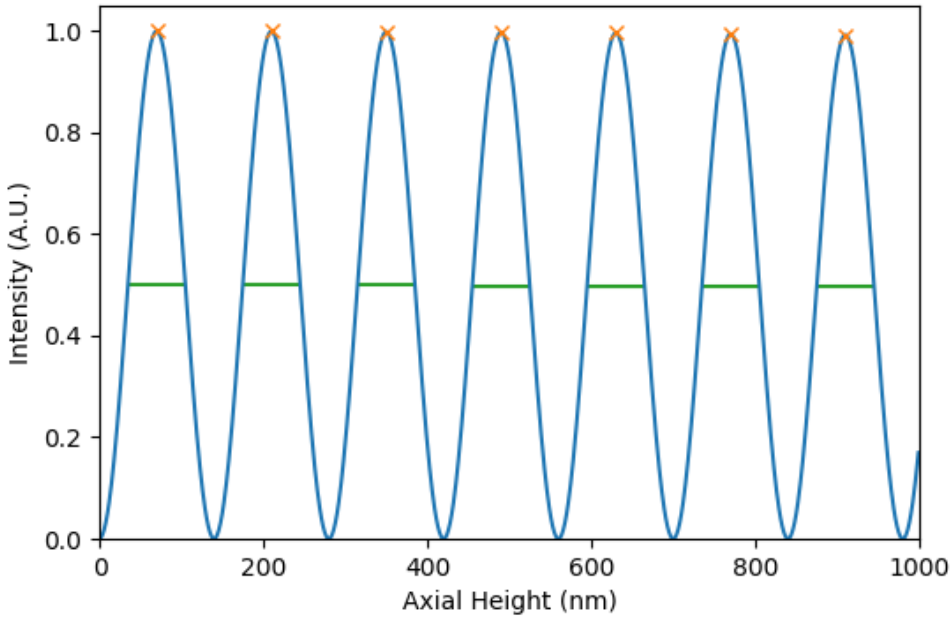

FIGURE 5.6: Theoretical PSF based on equation 5.6 with 280 nm excitation in air. Positions of antinodal peaks are shown in orange. The positions at which the width of the antinodal peaks were calculated are shown in green.

This figure shows a typical standing wave pattern, with equally spaced nodes and antinodes. From this plot and equations 5.3 and 5.2, theoretical antinodal spacing was calculated to be 140 nm and the theoretical antinodal FWHM was measured to be 70 nm. When compared to the antinodal FWHM achieved using previous standing wave techniques with longer wavelengths [161, 172], the theoretical axial resolution is improved by a minimum of 20 nm. This is expected to improved even further by using an immersion medium with higher refractive index as the antinodal thickness is directly dependent on refractive index (equation 5.3).

The theoretical standing wave pattern was also generated using 4% BSA which has a measured refractive index of 1.341 and this is shown in figure 5.7. Due to the

standing wave's dependence on refractive index, this reduces the antinodal spacing and thickness by a factor of 1.341.

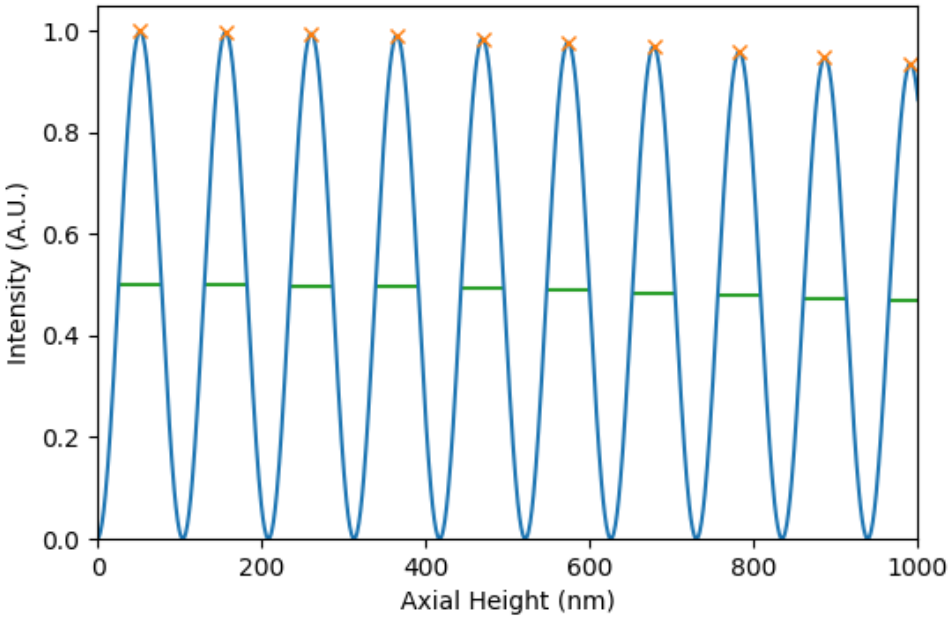

FIGURE 5.7: Theoretical PSF based on equation 5.6 with 280 nm excitation in 4% BSA. Positions of antinodal peaks are shown in orange. The positions at which the width of the antinodal peaks were calculated are shown in green.

From this plot and equations 5.3 and 5.2, this gives a theoretical antinodal spacing of 104.4 nm and a theoretical FWHM of 52.2 nm. Hence, when using 280 nm standing wave microscopy with cellular specimens, we would expect an axial resolution of closer to 50 nm. This is a near two-fold improvement on previous work which achived an axial resolution of around 90 nm [161].

5.3.2 Generation and measurement of a 280 nm standing wave

Figure 5.8 shows the image of a QD655 coated lens specimen placed curved-side down on the 400 nm LP filter.

From this figure, we can identify a limitation in the coating of the lens specimen from the inhomogeneity of fluorescence across the lens. This is a common issue when using QD nanoparticles as these have a tendency to aggregate in solution [88, 179, 180]. For this reason, the fluorescence across the lens surface is inhomogenous with

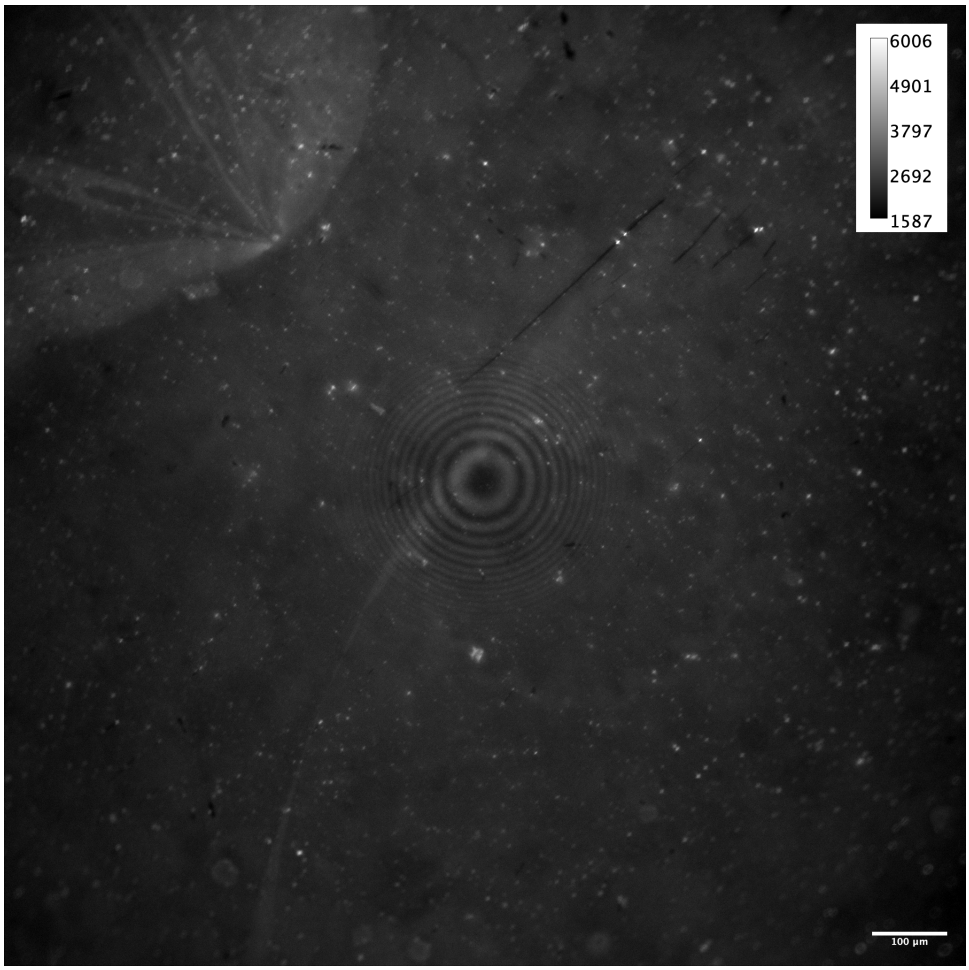

FIGURE 5.8: Standing wave image of a QD655 coated plano-convex lens specimen placed on the optical filter in the set-up detailed in figure 5.3, with no immersion media placed between the lens and filter surface. At the centre of the lens, within the field of view in this figure, concentric light and dark rings are visible which point to the formation of standing wave nodes and antinodes.

some bright clumps of aggregated QDs, despite the sonication of the QD sample. Nevertheless, it was possible to acquire images of the fluorescently coated lens.

When navigating the microscope field of view to the point of contact between the lens specimen and filter, i.e. the centre of the lens specimen, it was possible to see the bright and dark concentric rings characteristic of a SW image of a lens specimen, and these are clearly visible within figure 5.8. By converting radial distance to axial height, fluorescence intensity as a function of axial height from the surface of the filter was plotted and is shown in figure 5.9.

This plot agrees well with the theoretical trace in figure 5.6, with the same number of fringes within a 1000 nm axial distance. From this figure and the data analysis described in the methodology section, the antinodal spacing and antinodal FWHM

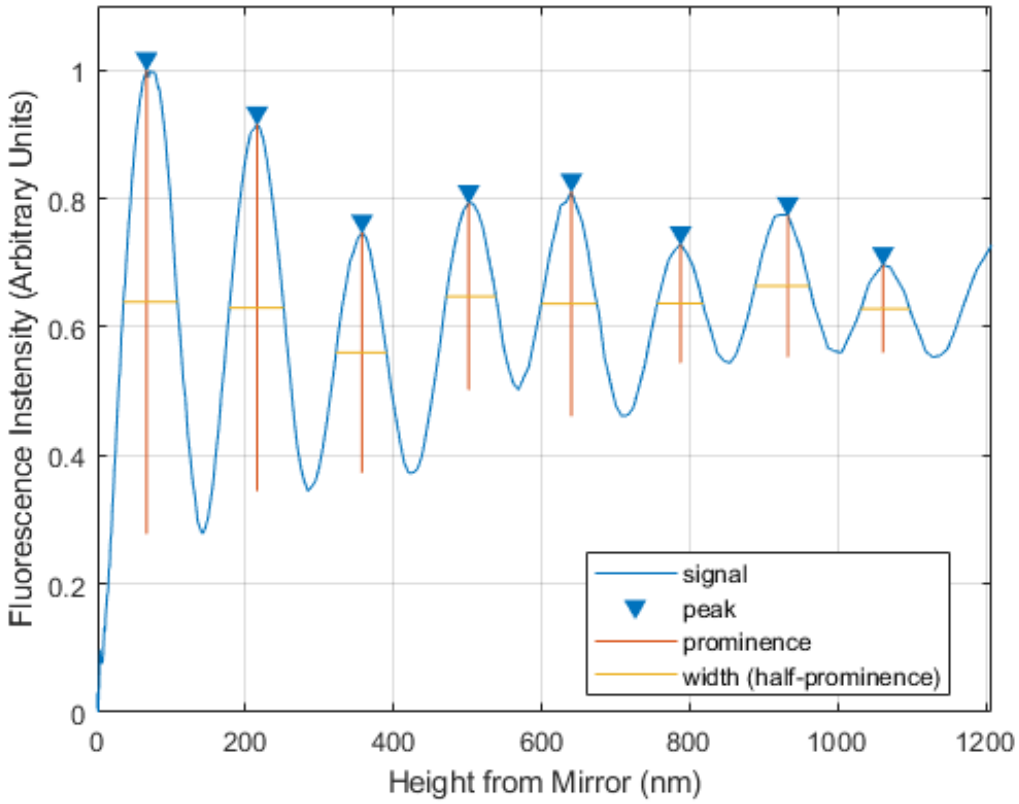

FIGURE 5.9: Intensity as a function of axial height from the mirror surface of the standing wave observed in figure 5.8. Blue arrows correspond to peak positions of antinodes and the width of the antinode is given in orange, measured at half of the height (prominence) of the antinodal peak.

of the standing wave were extracted. These values, along with the corresponding theoretical values, can be found in table 5.1.

	Antinodal Spacing (nm)	Antinodal FWHM (nm)
Theoretical	140	70
Experimental	142.1 ± 4.7	69.7 ± 7.0
Statistical Significance	$P > 0.05$	$P > 0.05$

TABLE 5.1: A comparison of the theoretical values for standing wave antinodal spacing and antinodal FWHM and the corresponding experimental results using a lens specimen in air.

These data give an antinodal thickness of 69.7 ± 7.0 nm and FWHM of 142.1 ± 4.7 which agree well with the theoretical antinodal thickness of 70 nm as the theoretical values are within the standard deviation of the measured values. Furthermore, a one sample t-test was performed in order to compare the measured values of antinodal FWHM and spacing, which yielded P values of greater than 0.05, confirming that

there is no significant statistical difference between the measured and theoretical mean values for either antinodal thickness or spacing.

Whilst 69.7 nm axial resolution is a much improved result over previous work which reported up to 90 nm resolution [161], this is only the worst-case-scenario when using 280 nm light - as the resolution of 69.7 nm measured here was in air. With a refractive index of 1, there can only be an improvement in resolution when using immersion media with higher refractive indices.

The measurement of the standing wave was repeated with the lens specimen immersed in 4% BSA, more accurately representing a cellular environment. The image acquired of the lens specimen in BSA is shown in figure 5.10.

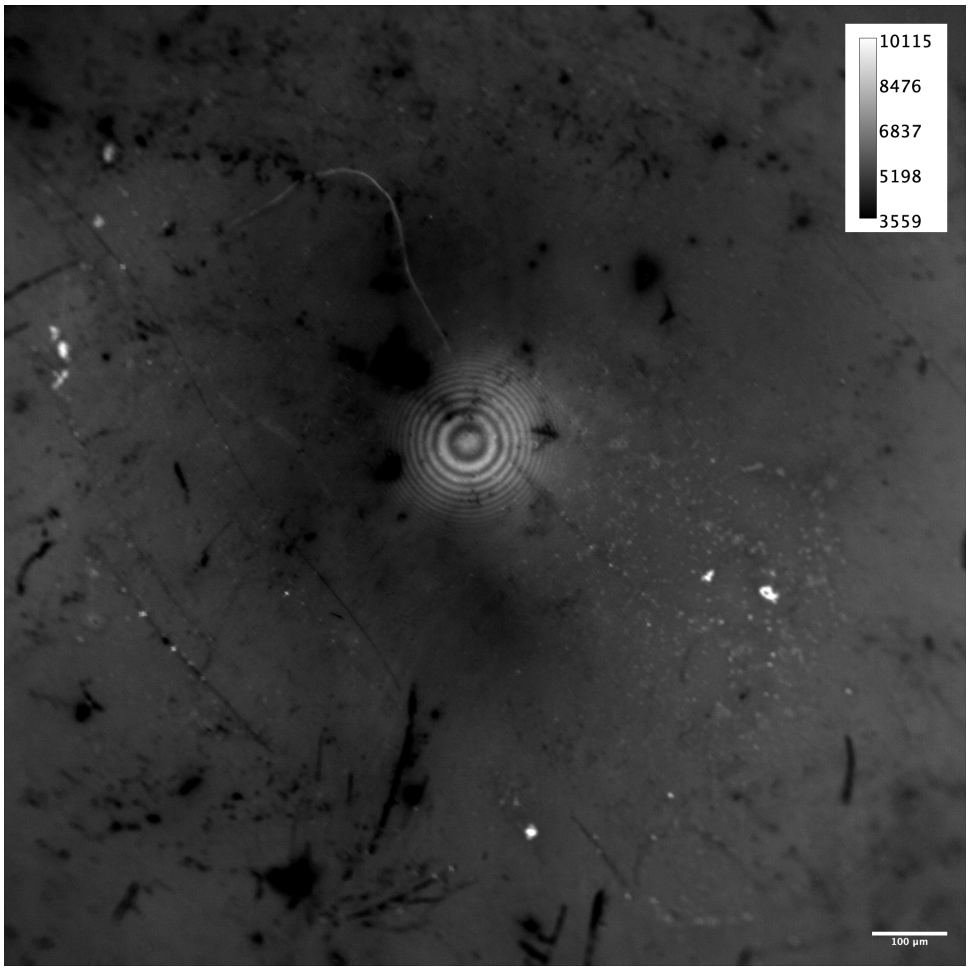

FIGURE 5.10: Standing wave image of a QD605 coated plano-convex lens specimen placed on the optical filter in the set-up detailed in figure 5.3, with 4% BSA (n=1.341) placed between the lens and filter surface.

When comparing the lens specimen profile when immersed in 4% BSA compared

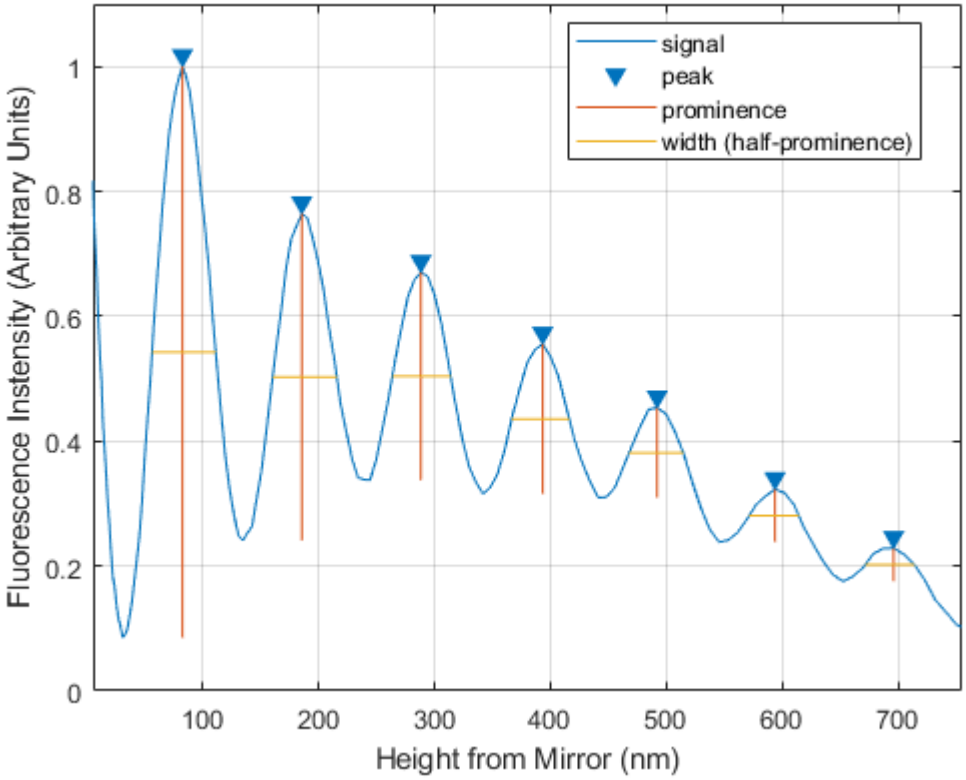

FIGURE 5.11: Intensity as a function of axial height from the mirror surface of the standing wave observed in figure 5.10. Blue arrows correspond to peak positions of antinodes and the width of the antinode is given in orange, measured at half of the height (prominence) of the antinodal peak.

to that of air in figure 5.8, it is immediately clear that the antinodal spacing and thickness are much reduced due to the addition of the higher refractive index medium. The radially averaged line profile and resulting measured antinodal spacing and antinodal FWHM can be found in figure 5.11 and table 5.2.

	Antinodal Spacing (nm)	Antinodal FWHM (nm)
Theoretical	104.4	52.2
Experimental	102.3 ± 2.1	48.9 ± 5.1
Statistical Significance	$P > 0.05$	$P > 0.05$

TABLE 5.2: A comparison of the theoretical values for standing wave antinodal spacing and antinodal FWHM and the corresponding experimental results using a lens specimen immersed in 4% BSA with a refractive index of 1.341.

In this aqueous environment, which more closely resembles that of the cellular environment, we measure an antinodal spacing of 102.3 ± 2.1 nm compared to the theoretical value of 104.4 nm and an antinodal thickness of 48.9 ± 5.1 compared to

a theoretical value of 52.2 nm. Again, both of these theoretical values are within the window of error of the measured standing wave values. When a one sample t-test was performed on both spacing and thickness, a P value of $P > 0.05$ was obtained which confirms that there is no statistically significant difference between the theoretical and measured values.

5.3.3 Standing wave images of mammalian cells obtained using standard methods

A standing wave image of fixed MCF-7 cells plated onto a mirror and labelled using QD655 against cellular target actin is shown in figure 5.12.

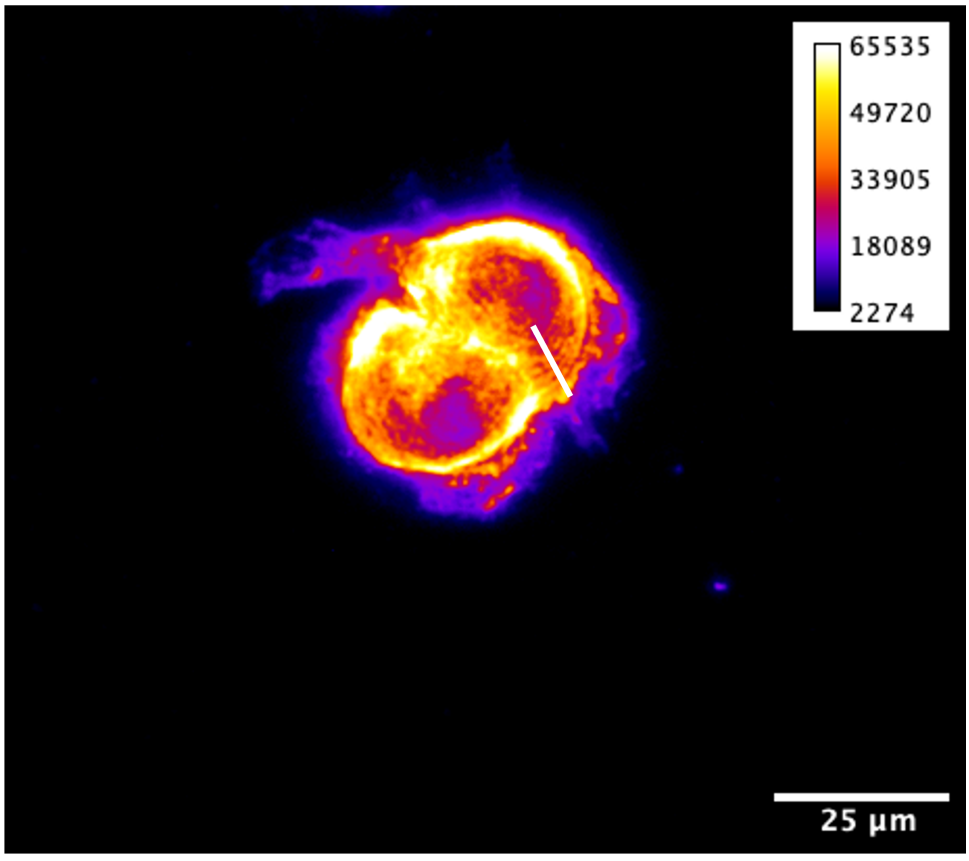

FIGURE 5.12: Standing wave image of MCF-7 cells with actin filaments labelled using QD655. This image was taken using a conventional standing wave set up with a mirror and upright microscope at an excitation wavelength of 365 nm. A look up table has been applied to aid visualisation of standing wave fringes and the white line indicates where the line profile has been taken to produce figure 5.13.

In this figure, fringes in the actin filaments are clearly visible throughout the cell. This is in agreement with the effect of standing wave microscopy on actin filaments

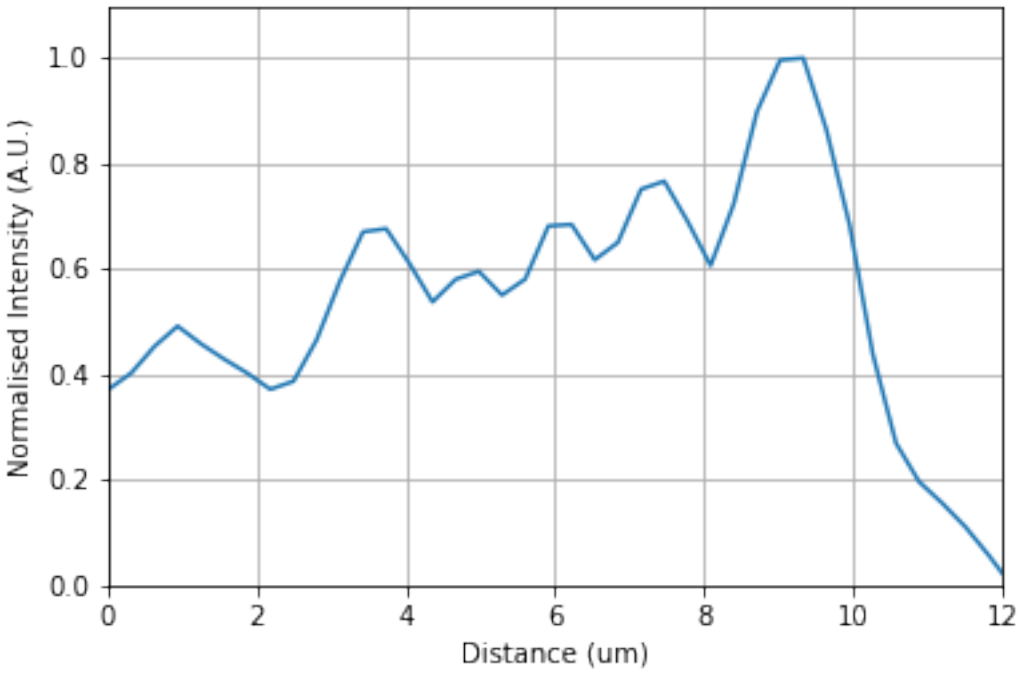

FIGURE 5.13: Line profile through the edge of the cell shown in figure 5.12 demonstrating the presence of standing wave fringes.

seen in previous work [163, 170, 173]. Although the fringes are visible by eye in the image, these are very close together laterally (due to the high degree of curvature of the cell) and are only just resolved by the microscope. This is at an excitation wavelength of 365 nm and, with 280 nm excitation, the fringes will be significantly closer together. This may make resolving the fringes difficult with a low magnification lens such as 20x at this excitation wavelength, depending on the curvature of the cell.

To demonstrate the presence of fringes, a line profile through the edge of the cell is shown in figure 5.13. Nevertheless, it is possible to observe standing wave fringes within this cellular structure and because of this, standing wave imaging with 280 nm excitation was performed using cells labelled against actin. These standing wave images of MCF-7 cells using standard methods can also act as a basis to which 280 nm standing wave images of cells are compared to ensure the accuracy of the new method.

5.3.4 280 nm standing wave imaging of mammalian cells

Standing wave images of QD655-labelled MCF-7 cells with 280 nm excitation are shown in figure 5.14. In this figure of cells excited with the 280 nm standing wave field, there are fringes within the cell characteristic of standing wave excitation. The observed effect on the cell actin network caused by standing wave excitation is in good agreement with the images taken by Frederick Lanni of the actin network observed within 3T3 cells [163].

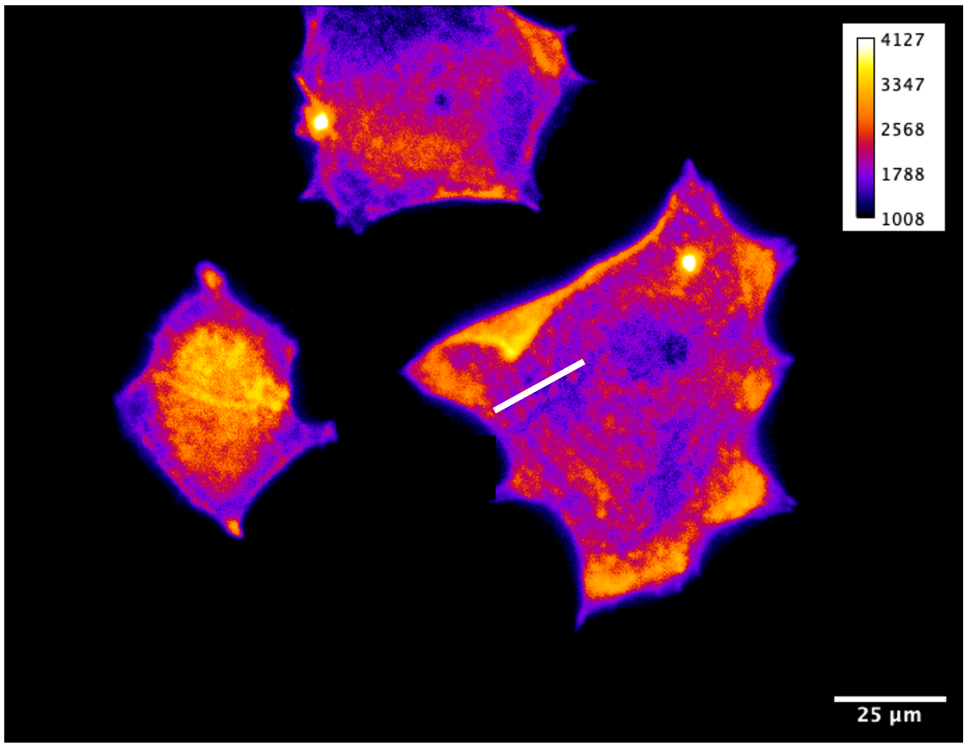

FIGURE 5.14: 280 nm standing wave images of MCF-7 cells whose actin filaments have been stained with QD655. A look up table has been applied to aid visualisation of standing wave fringes and the white line indicates where the line profile has been taken to produce figure 5.15.

To demonstrate the presence of fringes, a line profile through the edge of the cell is shown in figure 5.15.

With this comparison in mind, and the comparison to the effect observed with traditional standing wave microscopy shown in figure 5.12, it is highly likely that this effect is indeed caused by standing wave excitation with 280 nm light and that the optical design in figure 5.3 is capable of imaging both lens specimens and mammalian cells with standing wave excitation. Unfortunately, as the geometry of the cell is unknown, it is not possible to measure the thickness or spacing of the fringes as carried

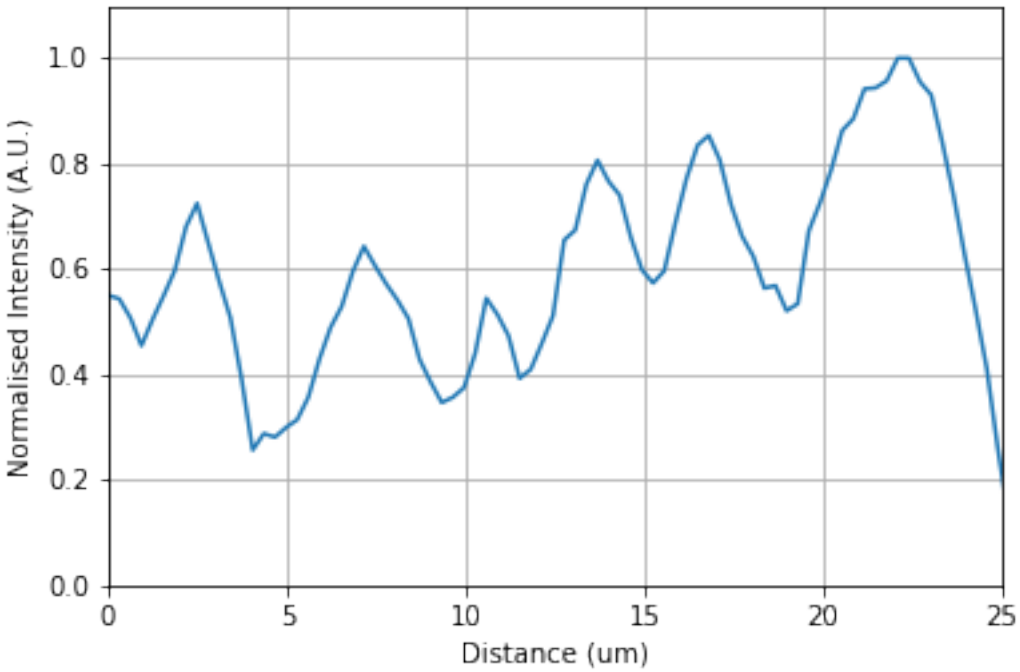

FIGURE 5.15: Line profile through the edge of the cell shown in figure 5.14 demonstrating the presence of standing wave fringes.

out in section 5.3.2. However, the visible presence of fringes is still a promising result which points to successful standing wave imaging of cellular specimens with 280 nm excitation.

5.4 Discussion

Although we have successfully identified fringes within QD-labelled cells imaged using 280 nm standing wave microscopy, the fringes are not quite as sharp as those seen in in figure 5.12. This could be for a number of reasons. The first potential reason is that, due to the radius of curvature of the cell, some fringes are too close together to be able to resolve. As measured from the lens specimen shown in figure 5.10, we expect only a ∼100 nm axial distance between antinodes, which could be too close together to resolve if the specimen is not varying significantly in x/y with axial distance. This problem was faced when imaging actin filaments in standing wave microscopy by Schniete *et. al.* [173] who were unable to resolve fringes within the actin network in thin areas of the cell. Secondly, in the technique used here to image with 280 nm excitation (shown in figure 5.3), instead of imaging through a 170 μm thick coverslip, we are forced to image through an optical filter which has a significantly greater thickness of a few mm. As objective lenses are corrected for much thinner coverslip thicknesses, imaging through this filter causes significant spherical aberration. The issues in imaging cellular specimen through a filter manifest in difficulty in focusing onto the specimen, and a "halo" effect around the cell caused by aberrations which affect the axial performance. Nevertheless, fringes in the cell are visible using 280 nm standing wave excitation with this inverted set-up even in the presence of spherical aberration, with expected axial resolutions of around 50 nm.

At present, the most significant barrier to high-quality standing wave images using this technique with 280 nm excitation is the thickness of the long-pass filter used in place of the first surface reflector. Many objective lenses are engineered to image through a specific coverslip thickness. This is most typically 170 μm in thickness, whilst the filter used to generate the standing wave was over 1 mm thick. Imaging through such a thick optical element can generate multiple axial aberrations - notably astigmatism and spherical aberration. Astigmatism is visible whilst attempting to image specimen as when the stage is moved up and down through focus, the lens specimen profile can be observed to move from left to right. In addition to this, spherical

aberration can have the effect of elongating the axial PSF which will affect the measured antinodal spacing and thicknesses in experimental data. This can in part account for the errors in mean antinodal thicknesses in these data sets being larger than those previously reported [161, 172]. Despite this, the standard errors in the means are still less than 10% and statistical analysis confirmed no significant differences between theoretical and measured antinodal thicknesses.

Not only does the thickness of the filter cause increased axial aberration, but it also restricts the lenses that can be used to image specimens due to the long working distance required. In this work, a 20x lens was used to image cells and this had to be so close to the bottom of the filter in order to focus on the cells that it was almost touching. As a result, any higher magnification lens (offering increased lateral resolution) with a shorter working distance cannot be used with this particular set up. With some more time and research, it may be possible to come up with a solution to this by developing a thinner reflective surface. This could, for example, be a quartz coverslip which is coated in a material that reflects 280 nm light and transmits visible light. This would then generate a standing wave in the same way as an optical filter, but remove increased optical aberrations and the restriction of imaging objectives. Similarly, the implementation of a high-transmission quartz objective lens would negate the need for the inverted system used here and allow standing waves to be generated using the tried and tested mirror method.

Whilst when using a mirrored surface, the point of contact between the lens and curved surface is always a node, but in figure 5.10 we see an antinode at this point of contact. This could potentially be because the layer of BSA between the lens and filter is causing a slight axial shift of the lens with respect to the filter surface, or because the reflective nature of the filter means that either a node or antinode may occur at the point of contact. It is also worth noting that the standing wave generated by either a mirrored surface or a reflective surface such as the filter depend also on coatings. Where a mirror is a first-surface reflector, we see a node at the mirror surface [162, 181]. However, some reflectors have a coating, meaning that the reflection of the incident wave may take place slightly below the surface of the reflector - causing an antinode at the point of contact between the lens and reflector. The particular 400 nm filter used in this work happens to have a Nb2O5-SiO2 sputter coating as well as a Ta2O5/SiO2

anti-reflection coating, and as a result it is difficult to determine at which axial position the reflection of the incident light is taking place. If the specimen is significantly far from the reflective surface, this could also affect the contrast of fringes visible within the images as the intensity of antinodes decreases with distance from the point of reflection. Nevertheless, we do see successful generation of a standing wave excitation field which accurately resembles the theoretical wave.

One much-discussed limitation in standing wave microscopy is the information gap caused by the generation of nodal planes. By using 280 nm light, we see a decrease in the spacing between antinodes which can provide much more information about the specimen than the use of longer wavelengths. For example, in previously published work by Tinning *et. al.* using 550 nm excitation, the authors were able to generate only 5 antinodal planes within a 1000 nm axial height [172]. By using 280 nm light, we can generate 7 fringes within the same height and therefore recover more axial information about the specimen. Furthermore, as discussed in the introduction, the development of Tartan standing wave [173] which uses multiple excitation wavelengths to image the specimen has greatly improved the sampling density of standing wave imaging. Tartan standing wave could be applied to UV wavelengths using this technique. As demonstrated in figure 5.4, the 400 nm longpass filter used to generate the standing wave has the capability of reflecting wavelengths from 400 nm down to 250 nm. Therefore, Tartan standing wave could be used with multiple UV excitation wavelengths which would combine the improved axial resolution associated with short wavelengths with the improved sampling density achieved in Tartan standing wave imaging. QDs would be an excellent candidate for Tartan standing wave with UV excitation because of their notable broad excitation wavelength capable of being excited at any wavelength below their semiconductor bandgap.

As this is a widefield technique, it is possible to carry out imaging of live cell specimens with both high temporal and high axial resolution, as demonstrated by Tinning *et. al.* [172]. This could be carried out with 280 nm standing wave microscopy, achieving around 2x better axial resolution whilst doing so. However, the issue of UV-induced cell toxicity, described in detail in chapter 4, remains an issue. Whilst it would be possible to image short, dynamic processes in the cell with minimal UV induced toxicity (e.g. membrane fluctuations), exposure would have to be carefully

controlled to ensure cell viability throughout the experiment. Whilst previous studies by Tinning *et. al.* [172] showed that standing wave excitation does not cause any further toxicity to cells than standard widefield imaging, the use of 280 nm light causes cellular damage via much different mechanisms. As a result, it would be interesting to, in future, compare cell viability with 280 nm standing wave imaging to that of standard widefield imaging.

5.5 Conclusion

Whilst standing wave microscopy is an already well established technique, there is a clear benefit in using 280 nm excitation - because of the resolution dependence on excitation wavelength (rather than emission wavelength in most cases in fluorescence microscopy), the use of shorter wavelengths such as 280 nm shows a dramatic increase in axial resolution.

This chapter has shown the development of a technique to generate a standing wave using 280 nm light which is not practicable using the more common approach combining a mirror and an upright epifluorescence microscope due to the transmission issues covered in detail in chapter 3. Instead, a technique was designed using transmission fluorescence on an inverted microscope with an optical filter at the specimen plane to reflect 280 nm light to generate the standing wave. This technique has proven to be successful, with standing waves visible when using the lens specimen. It was shown that the measured standing waves using this technique are not statistically different from the theoretical values ($P>0.05$) despite spherical aberrations in the system caused by imaging through a thick filter.

It was demonstrated that using this technique, we can achieve an axial resolutions of 48.9 nm in an aqueous, cell-like environment - a near two-fold increase of that achieved in previous work [161]. It was also demonstrated that, using this technique, it is possible to visualise standing wave fringes within the actin network of QD-labelled cells.

One particular limitation of this technique is imaging through a thick optical filter. Although the standing wave fringes are still visible, imaging in this way creates a significant amount of spherical aberration, which makes focusing on and resolving fine elements, such as actin filaments, difficult. This also restricts imaging lenses to long working distance objectives such as 4, 10 or 20x magnifications. In future, it may be possible to overcome this issue by designing and implementing a thinner partially-reflective surface to generate the 280 nm standing wave, such as a quartz coverslip with a layer of reflective material.

Chapter 6

Conclusion

The contents of this thesis have presented the work carried out over the 4 years of my PhD in characterising, integrating and applying a 280 nm LED in biomedical optical imaging.

In chapter 2, I characterised some of the optical properties of the 280 nm LED in use which then went on to direct my optical design in the following chapters. Alongside characterisation of the optical properties of the 280 nm LED in chapter 2, I also developed a novel technique to characterise the emission pattern of the LED by converting 280 nm light to visible light using fluorescence such that a UV-enhanced camera was not required. I determined that this technique could accurately identify this LED as a Lambertian emitter and verified the ability of the technique to successfully distinguish between two LED types. I hope that this technique will be useful for researchers in deep-UV LEDs in measuring emission patterns without the necessity of purchasing expensive, UV-enhanced detectors.

I then investigated methods of delivering 280 nm light to the specimen. I chose 3 designs, namely a fully-quartz epifluorescence set-up with which I used both a quartz objective and a reflective objective and a fully-quartz transmission fluorescence set-up. With all 3 techniques, I investigated properties such as the optical power available at the specimen plane, the homogeneity of illumination and the quality of resulting fluorescence images. Although all techniques had their advantages and disadvantages, it was the transmission fluorescence set-up that provided the highest optical power at the specimen plane, together with excellent illumination homogeneity and good image contrast. For this reason, I chose this method for the application of 280 nm excitation to fluorescence imaging detailed in chapters 4 and 5.

I also presented a quantitative analysis of the excitation of semiconductor QDs compared this to a longer, more commonly used excitation wavelength of 365 nm. I found that QDs are up to 3.56x brighter in fluorescence intensity when excited with a wavelength of 280 nm compared to 365 nm and found no evidence of increased photobleaching associated with the higher-energy excitation of 280 nm. It is hoped that this demonstrated enhancement in fluorescence intensity associated with this wavelength will provide researchers with a way to achieve higher-quality fluorescence images by simply changing the excitation wavelength. I also found that live cells can be exposed to triggered 280 nm illumination for extended periods ($\sim$ 6 h) with minimal cell death, although further optimisation of imaging methods using this wavelength are needed to ensure cells remain as healthy as possible.

Finally I presented a new method of standing wave microscopy with 280 nm excitation. I first developed a new optical design for generating a standing wave which was compatible with 280 nm light. This involved an inverted microscope and a long-pass filter which selectively reflected incident 280 nm light, creating a standing wave, whilst transmitting visible wavelength fluorescence. By using an established technique to measure the standing wave using a fluorescently-coated lens, I was able to measure antinodal FWHM, akin to axial resolution, of up to 48.9 nm - a near two-fold improvement on the axial resolution achieved by previous standing wave imaging. Finally, I labelled fixed mammalian cells with QDs and used standing wave microscopy to image these, showing that it is possible to measure standing wave fringes within 280 nm standing wave images of cells.

Whilst only two applications of 280 nm light in biomedical optical imaging were ultimately investigated in detail, there are many more opportunities which could be explored given more time.

280 nm light has many more potential applications in biomedical imaging, for example, excitation of carbon dots which exhibit excitation-dependent fluorescence emission, meaning that 280 nm excitation yields emission at shorter wavelengths, improving optical resolution. 280 nm light itself, due to its short wavelength, yields high-resolution images when used in brightfield and this is another opportunity to be explored. MUSE, whilst widely used in histological samples, has thus far not been applied to cultured cell specimens and the effects of limited penetration depth on cells

would be an interesting study. Although some indication of cell viability can be given by the study in chapter 4, further optimisation of cell imaging conditions under 280 nm irradiation could be carried out to ensure the best possible outcome for cell viability. This, alongside optimisation of live-cell labelling methods using semiconductor QDs could lead to the advantage in increased fluorescence associated with 280 nm light to be applied to live-cell imaging, which could benefit from reduced light exposure whilst preserving image contrast.

Further to this, I have shown a near two-fold improvement in the axial resolution achievable using standing wave microscopy by using 280 nm excitation. Whilst this is a notable result in itself, there is still much more that can be done using this wavelength of light in standing wave microscopy. Firstly, only one biological specimen - the mammalian cell line MCF-7 - was imaged using this method. There are many more, interesting, biological specimens which can be imaged with standing wave microscopy in order to greater understand their topology. This example includes red blood cells, which have been used in previous standing wave work, and the greater axial resolution observed using 280 nm standing wave microscopy could provide even more information about this specimen. In addition to this, 3D reconstructions of standing wave data have been done previously and it would be of benefit to apply this to 280 nm excitation to investigate the potential improvement that this increased axial resolution has in constructing 3D models of specimens. In addition to this, the optical filter used to generate the standing wave has the potential to generate standing waves of any excitation wavelength below 400 nm. Given more time, the opportunity to test Tartan standing wave using several UV wavelengths would have been invaluable.

These are only some examples of the potential applications of 280 nm LEDs in microscopy, most of which have not yet been conceived. It is my hope that over the next years, 280 nm LEDs will become more widely used in microscopy and that many more exciting applications will be found. To conclude this thesis, it is my hope that the new discoveries I have presented here will be able to inform future researchers and the new methods I have developed will be beneficial to those working within the field.

Okay, so you're a rocket scientist?

- Shania Twain

Appendix A

Code for analysing QD image pairs

```
mport skimage.filters
import time
import scipy.stats as stats
import pandas as pd
from sklearn import preprocessing
import math
import scipy.optimize
from scipy import interpolate

save_figures = True
timestamps = False
 @@ -33,6 +38,8 @@
auto_365_bg_p1 = np.asarray(Image.open('data\\365 auto bg p1.tif'),
    dtype=np.int16)
auto_365_bg_p2 = np.asarray(Image.open('data\\365 auto bg p2.tif'),
    dtype=np.int16)

print("~~~~~~~~~~~ Image pair analysis results ~~~~~~~~~~~")

# Do background correction
background_280_mean_p1 = np.mean(background_280_p1)
background_280_mean_p2 = np.mean(background_280_p2)
background_365_mean_p1 = np.mean(background_365_p1)
background_365_mean_p2 = np.mean(background_365_p2)
```

```
background_280_auto_mean_p1 = np.mean(auto_280_bg_p1)
background_280_auto_mean_p2 = np.mean(auto_280_bg_p2)
background_365_auto_mean_p1 = np.mean(auto_365_bg_p1)
background_365_auto_mean_p2 = np.mean(auto_365_bg_p2)
bg_280_corrected_p1 = raw_280_p1 - background_280_mean_p1
bg_280_corrected_p2 = raw_280_p2 - background_280_mean_p2
bg_365_corrected_p1 = raw_365_p1 - background_365_mean_p1
bg_365_corrected_p2 = raw_365_p2 - background_365_mean_p2
# Analyse autoflouresent signal distributions at 280nm and 365nm excitation
corrected_280_auto_p1 = auto_280_p1 - background_280_auto_mean_p1
corrected_280_auto_p2 = auto_280_p2 - background_280_auto_mean_p2
corrected_365_auto_p1 = auto_365_p1 - background_365_auto_mean_p1
corrected_365_auto_p2 = auto_365_p2 - background_365_auto_mean_p2
auto_280_triangle_thresh_p1 =
    skimage.filters.threshold_triangle(corrected_280_auto_p1)
auto_280_triangle_thresh_p2 =
    skimage.filters.threshold_triangle(corrected_280_auto_p2)
auto_365_triangle_thresh_p1 =
    skimage.filters.threshold_triangle(corrected_365_auto_p1)
auto_365_triangle_thresh_p2 =
    skimage.filters.threshold_triangle(corrected_365_auto_p2)
auto_280_triangle_p1 = corrected_280_auto_p1 > auto_280_triangle_thresh_p1
auto_280_triangle_p2 = corrected_280_auto_p2 > auto_280_triangle_thresh_p2
auto_365_triangle_p1 = corrected_365_auto_p1 > auto_365_triangle_thresh_p1
auto_365_triangle_p2 = corrected_365_auto_p2 > auto_365_triangle_thresh_p2
auto_280_signal_p1 = corrected_280_auto_p1[auto_280_triangle_p1]
auto_280_signal_p1[np.where(auto_280_signal_p1 < 0)[0]] = 0
auto_280_signal_p2 = corrected_280_auto_p2[auto_280_triangle_p2]
auto_280_signal_p2[np.where(auto_280_signal_p2 < 0)[0]] = 0
auto_365_signal_p1 = corrected_365_auto_p1[auto_280_triangle_p1]
auto_365_signal_p1[np.where(auto_365_signal_p1 < 0)[0]] = 0
auto_365_signal_p2 = corrected_365_auto_p2[auto_280_triangle_p2]
auto_365_signal_p2[np.where(auto_365_signal_p2 < 0)[0]] = 0
mean_auto_280_p1 = np.mean(auto_280_signal_p1)
mean_auto_280_p2 = np.mean(auto_280_signal_p2)
mean_auto_365_p1 = np.mean(auto_365_signal_p1)
```

```
mean_auto_365_p2 = np.mean(auto_365_signal_p2)
# t_stat_signal_p1, p_value_signal_p1 = stats.ttest_ind(auto_280_signal_p1,
    auto_365_signal_p1, equal_var=False)
# print("T-statistic of two-tailed t-test for the 280nm and 365nm 1st
    autofluorescent image pair signal distributions is",
#       " %.5f with a p-value %.5f" % (t_stat_signal_p1, p_value_signal_p1))
#
# t_stat_signal_p2, p_value_signal_p2 = stats.ttest_ind(auto_280_signal_p2,
    auto_365_signal_p2, equal_var=False)
# print("T-statistic of two-tailed t-test for the 280nm and 365nm 2nd
    autofluorescent image pair signal distributions is",
#       " %.5f with a p-value %.5f" % (t_stat_signal_p2, p_value_signal_p2))
# Generate the binary masks for selecting the cell regions of interest
bg_280_otsu_thresh_p1 = skimage.filters.threshold_otsu(bg_280_corrected_p1)
bg_280_otsu_thresh_p2 = skimage.filters.threshold_otsu(bg_280_corrected_p2)
bg_365_otsu_thresh_p1 = skimage.filters.threshold_otsu(bg_365_corrected_p1)
bg_365_otsu_thresh_p2 = skimage.filters.threshold_otsu(bg_365_corrected_p2)
bg_280_otsu_p1 = bg_280_corrected_p1 > bg_280_otsu_thresh_p1
bg_280_otsu_p2 = bg_280_corrected_p2 > bg_280_otsu_thresh_p2
bg_365_otsu_p1 = bg_365_corrected_p1 > bg_365_otsu_thresh_p1
bg_365_otsu_p2 = bg_365_corrected_p2 > bg_365_otsu_thresh_p2
# Mask out the regions of interest in the imaging data
bg_280_masked_p1 = bg_280_corrected_p1 * bg_280_otsu_p1
bg_280_masked_p2 = bg_280_corrected_p2 * bg_280_otsu_p2
bg_365_masked_p1 = bg_365_corrected_p1 * bg_280_otsu_p1
bg_365_masked_p2 = bg_365_corrected_p2 * bg_280_otsu_p2
# Analyse background corrected signal distributions at 280nm and 365nm
    excitation
bg_280_signal_p1 = bg_280_corrected_p1[bg_280_otsu_p1] - mean_auto_280_p1
bg_280_signal_p2 = bg_280_corrected_p2[bg_280_otsu_p2] - mean_auto_280_p2
bg_365_signal_p1 = bg_365_corrected_p1[bg_280_otsu_p1] - mean_auto_365_p1
bg_365_signal_p2 = bg_365_corrected_p2[bg_280_otsu_p2] - mean_auto_365_p2
# Assuming the 280nm and 365nm signals are normally distributed, acquire the
    relevant parameters to reconstruct the
# intensity distributions
bg_280_signal_mean_p1 = np.mean(bg_280_signal_p1)
```

```
bg_280_signal_std_dev_p1 = np.sqrt(np.var(bg_280_signal_p1))
print("Mean of 1st 280nm signal is %.5f with a standard deviation of %.5f" %
    (bg_280_signal_mean_p1, bg_280_signal_std_dev_p1))
bg_280_signal_mean_p2 = np.mean(bg_280_signal_p2)
bg_280_signal_std_dev_p2 = np.sqrt(np.var(bg_280_signal_p2))
print("Mean of 2nd 280nm signal is %.5f with a standard deviation of %.5f" %
    (bg_280_signal_mean_p2, bg_280_signal_std_dev_p2))
x_280_p1 = np.linspace(np.max([0,
    (bg_280_signal_mean_p1-(5*bg_280_signal_std_dev_p1))]),
                (bg_280_signal_mean_p1+(5*bg_280_signal_std_dev_p1)),
                    bg_280_signal_p1.shape[0])
x_280_p2 = np.linspace(np.max([0,
    (bg_280_signal_mean_p2-(5*bg_280_signal_std_dev_p2))]),
                (bg_280_signal_mean_p2+(5*bg_280_signal_std_dev_p2)),
                    bg_280_signal_p2.shape[0])
y_280_p1 = np.exp((-(x_280_p1 - bg_280_signal_mean_p1) ** 2) / (2 *
    bg_280_signal_std_dev_p1 ** 2))
y_280_p2 = np.exp((-(x_280_p2 - bg_280_signal_mean_p2) ** 2) / (2 *
    bg_280_signal_std_dev_p2 ** 2))
bg_365_signal_mean_p1 = np.mean(bg_365_signal_p1)
bg_365_signal_std_dev_p1 = np.sqrt(np.var(bg_365_signal_p1))
print("Mean of 1st 365nm signal is %.5f with a standard deviation of %.5f" %
    (bg_365_signal_mean_p1, bg_365_signal_std_dev_p1))
bg_365_signal_mean_p2 = np.mean(bg_365_signal_p2)
bg_365_signal_std_dev_p2 = np.sqrt(np.var(bg_365_signal_p2))
print("Mean of 2st 365nm signal is %.5f with a standard deviation of %.5f" %
    (bg_365_signal_mean_p2, bg_365_signal_std_dev_p2))
x_365_p1 = np.linspace(np.max([0,
    (bg_365_signal_mean_p1-(5*bg_365_signal_std_dev_p1))]),
                (bg_365_signal_mean_p1 + (5*bg_365_signal_std_dev_p1)),
                    bg_280_signal_p1.shape[0])
x_365_p2 = np.linspace(np.max([0, (bg_365_signal_mean_p2 -
    (5*bg_365_signal_std_dev_p2))]),
                (bg_365_signal_mean_p2 + (5*bg_365_signal_std_dev_p2)),
                    bg_280_signal_p2.shape[0])
```

```
y_365_p1 = np.exp((-(x_365_p1 - bg_365_signal_mean_p1) ** 2) / (2 *
    bg_365_signal_std_dev_p1 ** 2))
y_365_p2 = np.exp((-(x_365_p2 - bg_365_signal_mean_p2) ** 2) / (2 *
    bg_365_signal_std_dev_p2 ** 2))
t_stat_signal_p1, p_value_signal_p1 = stats.ttest_ind(bg_280_signal_p1,
    bg_365_signal_p1, equal_var=False)
print("T-statistic of two-tailed t-test for the 1st 280nm and 365nm image
    pair is %.5f with a p-value %.5f"
      % (t_stat_signal_p1, p_value_signal_p1))
t_stat_signal_p2, p_value_signal_p2 = stats.ttest_ind(bg_280_signal_p2,
    bg_365_signal_p2, equal_var=False)
print("T-statistic of two-tailed t-test for the 2nd 280nm and 365nm image
    pair is %.5f with a p-value %.5f"
      % (t_stat_signal_p2, p_value_signal_p2))
# Analyse the ratio of 280nm:365nm signal intensities
#
    ~~~~~~~~~~~~~~~~~~~~~~~~~~~~~~~~~~~~~~~~~~~~~~~~~~~~~~~~~~~~~~~~~~~~~~~~~~~~~~~~~~~~~~~~~~~~~~~~
# Remove the pixels with 0 value in the 365nm signal data to ensure no divide
    by 0 errors in subsequent calculations
#
    ~~~~~~~~~~~~~~~~~~~~~~~~~~~~~~~~~~~~~~~~~~~~~~~~~~~~~~~~~~~~~~~~~~~~~~~~~~~~~~~~~~~~~~~~~~~~~~~~
bg_280_signal_no_zero_p1 = bg_280_signal_p1[np.where(bg_365_signal_p1 > 0)[0]]
bg_280_signal_no_zero_p2 = bg_280_signal_p2[np.where(bg_365_signal_p2 > 0)[0]]
bg_365_signal_no_zero_p1 = bg_365_signal_p1[np.where(bg_365_signal_p1 > 0)[0]]
bg_365_signal_no_zero_p2 = bg_365_signal_p2[np.where(bg_365_signal_p2 > 0)[0]]
bg_signal_ratio_p1 = bg_280_signal_no_zero_p1/bg_365_signal_no_zero_p1
bg_signal_ratio_p2 = bg_280_signal_no_zero_p2/bg_365_signal_no_zero_p2
print("Minimum 280nm:365nm signal ratio of the 1st image pair = %.5f" %
    np.min(bg_signal_ratio_p1))
print("Minimum 280nm:365nm signal ratio of the 2st image pair = %.5f" %
    np.min(bg_signal_ratio_p2))
# Assuming the 280nm:365nm signal ratio is normally distributed, acquire the
    relevant parameters to reconstruct the
# intensity ratio distribution
bg_signal_ratio_mean_p1 = np.mean(bg_signal_ratio_p1)
bg_signal_ratio_mean_p2 = np.mean(bg_signal_ratio_p2)
```

```
bg_signal_ratio_std_dev_p1 = np.sqrt(np.var(bg_signal_ratio_p1))
bg_signal_ratio_std_dev_p2 = np.sqrt(np.var(bg_signal_ratio_p2))
print("Mean 280nm:365nm ratio of the 1st image pair is %.5f with a standard
    deviation of %.5f"
     %(bg_signal_ratio_mean_p1, bg_signal_ratio_std_dev_p1))
print("Mean 280nm:365nm ratio of the 2nd image pair is %.5f with a standard
    deviation of %.5f"
     %(bg_signal_ratio_mean_p2, bg_signal_ratio_std_dev_p2))
x_p1 = np.linspace(np.max([np.min(bg_signal_ratio_p1),
    (bg_signal_ratio_mean_p1-(5*bg_signal_ratio_std_dev_p1))]),
               (bg_signal_ratio_mean_p1+(5*bg_signal_ratio_std_dev_p1)), 1000)
y_p1 = np.exp((-(x_p1 - bg_signal_ratio_mean_p1) ** 2) / (2 *
    bg_signal_ratio_std_dev_p1 ** 2))
x_p2 = np.linspace(np.max([np.min(bg_signal_ratio_p2),
    (bg_signal_ratio_mean_p2-(5*bg_signal_ratio_std_dev_p2))]),
               (bg_signal_ratio_mean_p2+(5*bg_signal_ratio_std_dev_p2)), 1000)
y_p2 = np.exp((-(x_p2 - bg_signal_ratio_mean_p2) ** 2) / (2 *
    bg_signal_ratio_std_dev_p2 ** 2))
# Repeat the analysis the ratio of 280nm:365nm signal intensities, this time
    with the 'outlier' data points removed.
#
    ~~~~~~~~~~~~~~~~~~~~~~~~~~~~~~~~~~~~~~~~~~~~~~~~~~~~~~~~~~~~~~~~~~~~~~~~~~~~~~~~~~~~~~~~~~~~~
# Since the 280nm Otsu threshold mask will capture some pixels in the 365nm
    data which are basically noise, it is
# possible to get ratios which are extremely large (i.e. 200+) but these are
    not representative of signal-to-signal
# ratios between the two excitation wavelengths. Therefore, we seek to
    perform the previous statistical analysis while
# excluding these outliers. An 'outlier' intensity ratio is determined to be
    any ratio which is 5 standard deviations
# from the mean intensity ratio, since this is likely to be due to these
    noise divisions. Other methods of determining
# outliers are, of course, equally valid and should be specified here.
#
    ~~~~~~~~~~~~~~~~~~~~~~~~~~~~~~~~~~~~~~~~~~~~~~~~~~~~~~~~~~~~~~~~~~~~~~~~~~~~~~~~~~~~~~~~~~~~~
outlier_thresh_p1 = bg_signal_ratio_mean_p1 + (5*bg_signal_ratio_std_dev_p1)
```

```
outliers_p1 = np.where(bg_signal_ratio_p1 > outlier_thresh_p1)
perc_outliers_p1 =
    (np.shape(outliers_p1[0])[0]/bg_signal_ratio_p1.shape[0])*100
print("Percentage of ratios in the 1st image pair which are outliers =
    %.5f%%" % perc_outliers_p1)
outlier_thresh_p2 = bg_signal_ratio_mean_p2 + (5*bg_signal_ratio_std_dev_p2)
outliers_p2 = np.where(bg_signal_ratio_p2 > outlier_thresh_p2)
perc_outliers_p2 =
    (np.shape(outliers_p2[0])[0]/bg_signal_ratio_p2.shape[0])*100
print("Percentage of ratios in the 2nd image pair which are outliers =
    %.5f%%" % perc_outliers_p2)
bg_signal_ratio_no_out_p1 = bg_signal_ratio_p1[np.where(bg_signal_ratio_p1 <=
    outlier_thresh_p1)]
bg_signal_ratio_no_out_p2 = bg_signal_ratio_p2[np.where(bg_signal_ratio_p2 <=
    outlier_thresh_p2)]
bg_signal_ratio_no_out_mean_p1 = np.mean(bg_signal_ratio_no_out_p1)
bg_signal_ratio_no_out_std_dev_p1 = np.sqrt(np.var(bg_signal_ratio_no_out_p1))
 @@ -235,7 +242,156 @@
y_out_p2 = np.exp((-(x_out_p2 - bg_signal_ratio_no_out_mean_p2) ** 2) / (2 *
    bg_signal_ratio_no_out_std_dev_p2 ** 2))
```

Appendix B

Code for plotting theoretical standing wave PSF

```
\left
# In[78]:


import numpy as np \\
import scipy \\
import matplotlib.pyplot as plt\\
import math
from scipy.signal import find_peaks
from scipy.signal import peak_widths
from scipy.optimize import curve_fit
from scipy import asarray as ar,exp

# Theoretical SW Pattern
# Excitation Wavelength
exc_wavelength = 280

#Em Wavelength
em_wavelength = 655
# Refractive index
n = 1
```

```
#Numerical Aperture
NA = 0.4


#Theoretical Antinodal Thickness
antinodal_FWHM = exc_wavelength/(4*n)
print(antinodal_FWHM)


#Theoretical Antinodal Spacing
antinodal_spacing = exc_wavelength/(2*n)
print(antinodal_spacing)


#Theoretical PSF

axial_distance = np.arange(0,1500,1)

K = (4*3.14159*n*1)/exc_wavelength
A = K*axial_distance
B = ((NA*NA)/(2*n*em_wavelength))

intensity1 = np.array([1-(np.cos(A))])
intensity2 = np.array([np.sinc(B*axial_distance)])
intensity3 = intensity2*intensity2
intensity4 = intensity1*intensity3*0.5

intensity4.shape = (1500,1)
intensity = intensity4.flatten()


#Antinodal Spacing Analysis
peaks = scipy.signal.find_peaks(intensity)
peaks_array = peaks[0]
antinodal_spacing = peaks_array[1]-peaks_array[0]
```

```
print(antinodal_spacing)
# print(peaks)
#Antinodal FWHM Analysis
width_analysis = scipy.signal.peak_widths(intensity, peaks_array,
    rel_height=0.5)
FWHM = width_analysis[0]
print(FWHM)

#Plots
plt.plot(axial_distance,intensity4)
plt.ylim([0,1.05])
plt.xlim([0,1000])
plt.plot(peaks_array, intensity[peaks_array], "x")
plt.hlines(*width_analysis[1:],color="C2")

plt.xlabel("Axial Height (nm)")
plt.ylabel("Intensity (A.U.)")
plt.savefig("theoretical_wave_air", dpi = 100)
plt.show()
```

Appendix C

Code for analysing standing wave images

```
close all;\\
clc;\\
clearvars;\\

#Calculates the Radius of curvature of a lens from the lens makers equation
    using the thin lens approximation \\
Focal_length = 63e-3; \\
n_air = 1; \\
n_lens = 1.458; \\
R_lens = (n_lens-n_air)*Focal_length;\\
R_lens = 9.2e-3;\\

#Calibration factor for the pixels to distance \\
calib = 1.610;   \\

#Opens file explorer to load image file\\
[filename, pathname, filterindex] = uigetfile({'*.jpg;*.tif;*.png;*.gif','All
    Image Files'});\\
Filename = strcat(pathname,filename)\\
SWImage = imread (Filename); \\
```

```
#Reads in the image size
[h,w] = size(SWImage);\\

#checks if the image is square. \\
if w==h\\

   z = SWImage;\\

else\\
    if h > w\\
       h = w \\
    else if w > h\\
            w = h \\
         end\\
    end    \\
       z = SWImage(1:h,1:w);\\
end\\

    #Checks if the width and height are even or odd. If they are odd
    # one is minus from the width and height values
    if mod(w,2)==1;
        w2 = w-1;
    else
        w2 = w;
    end

    if mod(h,2)==1;
        h2 = h-1;
    else
        h2 = h;
    end

z = SWImage(1:h2,1:w2);
figure(4);imshow(z)
half_height = h2/2;
half_width = w2/2;
```

```
m = half_height;

[Zr,R] = radialavg(z,m);
R_average = R*half_height;
radial_average = (R_average*1e-6/calib);
z_max = max(Zr);
z_min = min(Zr);
z_min2 = min(z_min);
z_max2 = max(z_max);
Zr_norm = (Zr- z_min2)/(z_max2-z_min2);

#Plots the Fluorescence Intensity vs Radial Distance
figure(1);plot(radial_average,Zr_norm)
xlabel('Radial Distance (\mum)')
ylabel('Fluorescence Instensity (Arbitrary Units)')

L = (R_lens-sqrt(R_lens^2-radial_average.^2))*1e9;
%L_mod = find(L(1,:)<750);

#Plots Fluorescence Intensity vs Height from mirror
figure(2);plot(L,Zr_norm)
xlabel('Height from Mirror surface (nm)')
ylabel('Fluorescence intensity (Arbitrary Units)')

# Finds the peaks and FWHM of for each standing wave.
%L_modified = L<165;
[pks,locs,widths] =
    findpeaks(Zr_norm,L,'MinPeakWidth',30,'Annotate','extents');

#Determines the average FWHM of the standing wave planes
Average_FWHM = mean(widths)
std_dev_FWHM = std(widths)

#Finds the size of the locs matrix
[x,num_pks] = size(locs);
```

```
#Calculates the anti-nodal-spacing for each peak
Anti_nodal_spacing = (locs(1,2:num_pks)-locs(1,1:num_pks-1))';
Avg_anti_nodal_spacing = mean(Anti_nodal_spacing)
std_dev_spacing = std(Anti_nodal_spacing)
m
# Plots Fluorescence Intensity vs Height from mirror with FWHM
figure(3);findpeaks(Zr_norm,L,'MinPeakWidth',30,'Annotate','extents')
xlabel('Height from Mirror (nm)')
ylabel('Fluorescence Instensity (Arbitrary Units)')
ylim([0 1.1])
xlim([0,750])
```

Bibliography

[1] L. Woodruff. “Microscopy before the nineteenth century”. In: *The American Naturalist* 73.749 (1939), pp. 485516. DOI: 10.1086/280861.

[2] A. J. M. Wollman et al. “From Animaculum to single molecules: 300 years of the light microscope”. In: *Open Biology* 5.4 (Apr. 2015), p. 150019. DOI: 10.1098/rsob.150019. URL: https://doi.org/10.1098/rsob.150019.

[3] R. Hooke. *Micrographia*. The Royal Society, 1665.

[4] B. J. Ford. “The van Leeuwenhoek Specimens”. In: *Records of the Royal Society* 36.1 (1981), pp. 3759.

[5] “Observations, communicated to the publisher by Mr. Antony van Leewenhoeck, in a dutch letter of the 9th Octob. 1676. here English'd: concerning little animals by him observed in rain-well-sea- and snow water as also in water wherein pepper had lain infused”. In: *Philosophical Transactions of the Royal Society of London* 12.133 (Mar. 1677), pp. 821–831. DOI: 10.1098/rstl.1677.0003. URL: https://doi.org/10.1098/rstl.1677.0003.

[6] S. Inoue. “Foundations of Confocal Scanned Imaging in Light Microscopy”. In: *Handbook of Biological Confocal Microscopy*. Ed. by James B. Pawley. 3rd ed. New York: Springer Science+Business Media, 2006. Chap. 17.

[7] H. Volkmann. “Ernst Abbe and his work”. In: *Applied Optics* 5.11 (1966).

[8] M. Born and E. Wolf. “Geometrical theory of aberrations”. In: *Principles of Optics*. Cambridge University Press, 2019.

[9] R. Chippendale et al. “Microscope Project for Undergraduate Laboratories”. In: (2016), pp. 1–27. arXiv: 1606.03052. URL: http://arxiv.org/abs/1606.03052.

[10] F. Fereidouni et al. "Microscopy with ultraviolet surface excitation for rapid slide-free histology". In: *Nature Biomedical Engineering* 1.12 (2017), pp. 957–966. ISSN: 2157846X. DOI: 10.1038/s41551-017-0165-y. URL: http://dx.doi.org/10.1038/s41551-017-0165-y.

[11] G. Stokes. "On the change of refrangibility of light". In: *Philosophical Transactions of the Royal Society of London* 142 (1852), pp. 463–562. DOI: 10.1098/rstl.1852.0022. URL: https://doi.org/10.1098/rstl.1852.0022.

[12] J. R. Lacowicz. "Introduction to Fluorescence". In: *Principles of Fluorescence Spectroscopy*. 2nd ed. New York: Springer Science + Business Media, 2004. Chap. 1-24.

[13] J. R. Lakowicz. *Principles of fluorescence spectroscopy*. Kluwer Academic/Plenum, 1999.

[14] L. Song et al. "Photobleaching kinetics of fluorescein in quantitative fluorescence microscopy". In: *Biophysical Journal* 68.6 (June 1995), pp. 2588–2600. DOI: 10.1016/s0006-3495(95)80442-x. URL: https://doi.org/10.1016/s0006-3495(95)80442-x.

[15] J. R. Lacowicz. "Protein Fluorescence". In: *Principles of Fluorescence Spectroscopy*. New York: Springer Science+Business Media, 2004. Chap. 16, pp. 445–486.

[16] T. Robertson, F. Bunel, and M. Roberts. "Fluorescein Derivatives in Intravital Fluorescence Imaging". In: *Cells* 2.3 (2013), pp. 591–606. ISSN: 2073-4409. DOI: 10.3390/cells2030591.

[17] S. Sivakumar, J. R. Daum, and G. J. Gorbsky. "Live-Cell Fluorescence Imaging for Phenotypic Analysis of Mitosis". In: *Methods in Molecular Biology*. Springer New York, 2014, pp. 549–562. DOI: 10.1007/978-1-4939-0888-2_31. URL: https://doi.org/10.1007/978-1-4939-0888-2_31.

[18] O. Shimomura, F. H. Johnson, and Y. Saiga. "Extraction, purification and properties of aequorin, a bioluminescent". In: *Journal of Cellular and Comparative Physiology* 59.165 (1962), pp. 223–239. ISSN: 00959898. DOI: 10.1002/jcp.1030590302.

[19] D. C. Prasher et al. "Primary structure of the Aequorea victoria green-fluorescent protein". In: *Gene* 111.2 (Feb. 1992), pp. 229–233. DOI: 10.1016/0378-1119(92)90691-h. URL: https://doi.org/10.1016/0378-1119(92)90691-h.

[20] "Fluorescent Proteins - From the Beginnings to the Nobel Prize". In: *Leica Microsystems* (2012). URL: https://www.leica-microsystems.com/science-lab/fluorescent-proteins-from-the-beginnings-to-the-nobel-prize/.

[21] R. Wayne. "Methods of Generating Contrast". In: *Light and Video Microscopy*. 2nd ed. Elsevier, 2014. Chap. 6, pp. 111–125.

[22] M. Renz. "Fluorescence microscopy-A historical and technical perspective". In: *Cytometry Part A* 83.9 (2013), pp. 767–779. ISSN: 15524922. DOI: 10.1002/cyto.a.22295.

[23] A. Stemmer, M. Beck, and R. Fiolka. "Widefield fluorescence microscopy with extended resolution". In: *Histochemistry and Cell Biology* 130.5 (2008), pp. 807–817. ISSN: 09486143. DOI: 10.1007/s00418-008-0506-8.

[24] J. G. White, W. B. Amos, and M. Fordham. "An evaluation of confocal versus conventional imaging of biological structures by fluorescence light microscopy." In: *The Journal of Cell Biology* 105.1 (1987), pp. 41–48. ISSN: 00219525. DOI: 10.1083/jcb.105.1.41.

[25] P. Mahmudi-Azer S.and Lacy and R. Moqbel. "Tracing Intracellular Mediator Storage and Mobilization in Eosinophils". In: *Methods in molecular medicine* 56 (Jan. 2001), pp. 367–81. DOI: 10.1385/1-59259-151-5:367.

[26] G. J. Brakenhoff, P. Blom, and P. Barends. "Confocal scanning light microscopy with high aperture immersion lenses". In: *Journal of Microscopy* 117.2 (1979), pp. 219–230.

[27] C. J. R. Sheppard et al. "Signal-to-Noise Ratio in Confocal Microscopes". In: *Handbook of Biological Confocal Microscopy*. New York: Springer Science + Business Media, 2006. Chap. 22, pp. 442–451.

[28] J. Jonkman and C. M. Brown. "Any Way You Slice It - A Comparison of Confocal Microscopy Techniques". In: *Journal of Biomolecular Techniques* 26 (2015), pp. 54–65.

[29] S. Munck et al. "Challenges and advances in optical 3D mesoscale imaging". In: *Journal of Microscopy* 286.3 (May 2022), pp. 201–219. DOI: 10.1111/jmi.13109. URL: https://doi.org/10.1111/jmi.13109.

[30] M. Petran et al. "Tandem-Scanning Reflected-Light Microscope". In: *Journal of the Optical Society of America* 58.5 (1968), p. 661.

[31] A. R. Halpern et al. "Versatile, do-it-yourself, low-cost spinning disk confocal microscope". In: *Biomedical Optics Express* 13.2 (Feb. 2022), p. 1102. DOI: 10.1364/boe.442087. URL: https://doi.org/10.1364/boe.442087.

[32] S. Inoue and T. Inoue. "Direct-view high-speed confocal scanner: The CSU-10". In: *Methods in Cell Biology* 2002.70 (2002), pp. 87–127. ISSN: 0091679X. DOI: 10.1016/s0091-679x(02)70003-4.

[33] Y. Kumamoto. "Deep-Ultraviolet Microscopy and Microspectroscopy". In: *Far- and Deep-Ultraviolet Spectroscopy*. Ed. by Yukihiro Ozaki and Satoshi Kawata. Tokyo: Springer Japan, 2015, pp. 123–144. ISBN: 978-4-431-55549-0. DOI: 10.1007/978-4-431-55549-0_7. URL: https://doi.org/10.1007/978-4-431-55549-0_7.

[34] A. Köhler. "Mikrophotographische Untersuchungen mit ultraviolettem Licht". In: Zeitschrift für wissenschaftliche Mikroskopie und für mikroskopische Technik: Sonderabdruck. Zeitschrift für wissenschaftliche Mikroskopie und für mikroskopische Technik, 1904. URL: https://books.google.co.uk/books?id=i3K3AAAAIAAJ.

[35] H.C. Ernst and S.B. Wolbach. "Ultra-Violet photomicrography: (A Preliminary Communication.)" In: *The Journal of Medical Research* 14.3 (1906), pp. 463470.

[36] R. A. Judge, K. Swift, and C. González. "An ultraviolet fluorescence-based method for identifying and distinguishing protein crystals". In: *Acta Crystallographica Section D Biological Crystallography* 61.1 (Dec. 2004), pp. 60–66. DOI: 10.1107/s0907444904026538. URL: https://doi.org/10.1107/s0907444904026538.

[37] C. J. de Jong et al. "Deep-UV fluorescence lifetime imaging microscopy". In: *Photonics Research* 3.5 (Sept. 2015), p. 283. DOI: 10.1364/prj.3.000283. URL: https://doi.org/10.1364/prj.3.000283.

[38] B. J Zeskind. "Quantitative imaging of living cells by deep ultraviolet microscopy". PhD thesis. 2006. URL: http://dspace.mit.edu/handle/1721.1/38693.

[39] B. J. Zeskind et al. "Nucleic acid and protein mass mapping by live-cell deep-ultraviolet microscopy". In: *Nature Methods* 4.7 (2007), pp. 567–569. ISSN: 15487091. DOI: 10.1038/nmeth1053.

[40] G. Lucena-Aguilar et al. "DNA Source Selection for Downstream Applications Based on DNA Quality Indicators Analysis". In: *Biopreservation and Biobanking* 14.4 (Aug. 2016), pp. 264–270. DOI: 10.1089/bio.2015.0064. URL: https://doi.org/10.1089/bio.2015.0064.

[41] F. Jamme et al. "Synchrotron UV fluorescence microscopy uncovers new probes in cells and tissues". In: *Microscopy and Microanalysis* 16.5 (2010), pp. 507–514. ISSN: 14319276. DOI: 10.1017/S1431927610093852.

[42] F. Jamme et al. "Deep UV autofluorescence microscopy for cell biology and tissue histology". In: *Biology of the Cell* 105.7 (2013), pp. 277–288. ISSN: 02484900. DOI: 10.1111/boc.201200075.

[43] E. Estève et al. "Detection and localization of calcium oxalate in kidney using synchrotron deep ultraviolet fluorescence microscopy". In: *Journal of Synchrotron Radiation* 29.1 (2022), pp. 214–223. DOI: 10.1107/S1600577521011371. URL: https://doi.org/10.1107/S1600577521011371.

[44] Q. Li, T. Ruckstuhl, and S. Seeger. "Deep-UV Laser-Based Fluorescence Lifetime Imaging Microscopy of Single Molecules". In: *The Journal of Physical Chemistry B* 108.24 (May 2004), pp. 8324–8329. DOI: 10.1021/jp0375160. URL: https://doi.org/10.1021/jp0375160.

[45] Trevor A. Smith et al. "Deep-UV confocal fluorescence imaging and super-resolution optical microscopy of biological samples". In: *Journal of Innovative Optical Health Sciences* 5.4 (2012), pp. 1–9. ISSN: 17935458. DOI: 10.1142/S1793545812500253.

[46] A. Qorbani et al. "Microscopy with ultraviolet surface excitation (MUSE): A novel approach to real-time inexpensive slide-free dermatopathology". In: *Journal of Cutaneous Pathology* 45.7 (2018), pp. 498–503. ISSN: 16000560. DOI: 10.1111/cup.13255.

[47] T. Yoshitake et al. “Rapid histopathological imaging of skin and breast cancer surgical specimens using immersion microscopy with ultraviolet surface excitation”. In: *Scientific Reports* 8.1 (2018), pp. 1–12. ISSN: 20452322. DOI: 10.1038/s41598-018-22264-2. URL: http://dx.doi.org/10.1038/s41598-018-22264-2.

[48] J. Guo et al. “Three-Dimensional Microscopy by Milling with Ultraviolet Excitation”. In: *Scientific Reports* 9.1 (2019), pp. 1–9. ISSN: 20452322. DOI: 10.1038/s41598-019-50870-1. arXiv: 1905.04358.

[49] J. Guo et al. “Multiplex protein-specific microscopy with ultraviolet surface excitation”. In: *Biomedical Optics Express* 11.1 (2020), p. 99. ISSN: 2156-7085. DOI: 10.1364/boe.11.000099.

[50] C. Wong, M. E. Pawlowski, and T. S. Tkaczyk. “Simple ultraviolet microscope using off-the-shelf components for point-of-care diagnostics”. In: *PLoS ONE* 14.4 (2019), pp. 1–11. ISSN: 19326203. DOI: 10.1371/journal.pone.0214090.

[51] A. Ojaghi et al. “Label-free hematology analysis using deep-ultraviolet microscopy”. In: *Proceedings of the National Academy of Sciences of the United States of America* 117.26 (2020), pp. 14779–14789. ISSN: 10916490. DOI: 10.1073/pnas.2001404117.

[52] N. Kaza, A. Ojaghi, and F. E Robles. “Hemoglobin quantification in red blood cells via dry mass mapping based on UV absorption”. In: 26 (August 2021), pp. 1–10. DOI: 10.1117/1.JBO.26.8.086501.

[53] D. J. Stephens and V. J. Allan. “Light microscopy techniques for live cell imaging”. In: *Science* 300.5616 (2003), pp. 82–86. ISSN: 00368075. DOI: 10.1126/science.1082160.

[54] A. Ettinger and T. Wittmann. *Fluorescence live cell imaging*. 1st ed. Vol. 123. Elsevier Inc., 2014, pp. 77–94. ISBN: 9780124201385. DOI: 10.1016/B978-0-12-420138-5.00005-7. URL: http://dx.doi.org/10.1016/B978-0-12-420138-5.00005-7.

[55] A. Kiepas et al. "Optimizing live-cell fluorescence imaging conditions to minimize phototoxicity". In: *Journal of Cell Science* 133.4 (2020). ISSN: 14779137. DOI: 10.1242/JCS.242834.

[56] R. A. Hoebe et al. "Controlled light-exposure microscopy reduces photobleaching and phototoxicity in fluorescence live-cell imaging". In: *Nature Biotechnology* 25.2 (2007), pp. 249–253. ISSN: 10870156. DOI: 10.1038/nbt1278.

[57] C. Boudreau et al. "Excitation light dose engineering to reduce photo-bleaching and photo-toxicity". In: *Scientific Reports* 6 (2016), pp. 1–12. ISSN: 20452322. DOI: 10.1038/srep30892. URL: http://dx.doi.org/10.1038/srep30892.

[58] P. P. Laissue et al. "Assessing phototoxicity in live fluorescence imaging". In: *Nature Methods* 14.7 (2017), pp. 657–661. ISSN: 15487105. DOI: 10.1038/nmeth.4344. URL: http://dx.doi.org/10.1038/nmeth.4344.

[59] F. Mubaid et al. "Fluorescence microscope light source stability". In: *Histochemistry and Cell Biology* 151.4 (2019), pp. 357–366. ISSN: 1432119X. DOI: 10.1007/s00418-019-01776-6. URL: http://dx.doi.org/10.1007/s00418-019-01776-6.

[60] R. Masuma et al. "Effects of UV wavelength on cell damages caused by UV irradiation in PC12 cells". In: *Journal of Photochemistry and Photobiology B: Biology* 125 (2013), pp. 202–208. ISSN: 18732682. DOI: 10.1016/j.jphotobiol.2013.06.003. URL: http://dx.doi.org/10.1016/j.jphotobiol.2013.06.003.

[61] R. P. Sinha and D. P. Häder. "UV-induced DNA damage and repair: A review". In: *Photochemical and Photobiological Sciences* 1 (4 Apr. 2002), pp. 225–236. ISSN: 14749092. DOI: 10.1039/b201230h.

[62] R. P. Rastogi et al. "Molecular mechanisms of ultraviolet radiation-induced DNA damage and repair". In: *Journal of Nucleic Acids* 2010 (2010). ISSN: 20900201. DOI: 10.4061/2010/592980.

[63] T. R. Dunkern and B. Kaina. "Cell Proliferation and DNA Breaks Are Involved in Ultraviolet Light-induced Apoptosis in Nucleotide Excision Repair-deficient Chinese Hamster Cells". In: *Molecular biology of the cell* 13.6 (2002), pp. 2170–2179. ISSN: 1059-1524. DOI: 10.1091/mbc.01.

[64] K. Hung et al. "The 6-4 photoproduct is the trigger of UV-induced replication blockage and ATR activation". In: *Proceedings of the National Academy of Sciences* 117.23 (2020), pp. 12806–12816. DOI: 10.1073/pnas.1917196117. eprint: https://www.pnas.org/doi/pdf/10.1073/pnas.1917196117. URL: https://www.pnas.org/doi/abs/10.1073/pnas.1917196117.

[65] "Ultra-violet microspectro- graphy of living tissue culture cells." In: *Discussions of the Faraday Society* 9 (1950), pp. 461–470.

[66] D. F. Albeanu et al. "LED arrays as cost effective and efficient light sources for widefield microscopy". In: *PLoS ONE* 3.5 (2008), pp. 1–8. ISSN: 19326203. DOI: 10.1371/journal.pone.0002146.

[67] E. F. Schubert. "History of LEDs". In: *Light-Emitting Diodes*. New York: Cambridge University Press, 2006.

[68] R. Nave. *P-n junction*. URL: http://hyperphysics.phy-astr.gsu.edu/hbase/Solids/pnjun.html.

[69] E. F. Schubert. "The AlGaInN Material System and Ultraviolet Emitters". In: *Light-Emitting Diodes*. New York: Cambridge University Press, 2006.

[70] M. Kneissl et al. "The emergence and prospects of deep-ultraviolet light-emitting diode technologies". In: *Nature Photonics* 13.4 (2019), pp. 233–244. ISSN: 17494893. DOI: 10.1038/s41566-019-0359-9. URL: http://dx.doi.org/10.1038/s41566-019-0359-9.

[71] W. Sun et al. "Continuous wave milliwatt power AlGaN light emitting diodes at 280 nm". In: *Japanese Journal of Applied Physics, Part 2: Letters* 43.11 A (2004). ISSN: 00214922. DOI: 10.1143/JJAP.43.L1419.

[72] D. Liu et al. "226 nm AlGaN/AlN UV LEDs using p-type Si for hole injection and UV reflection". In: *Applied Physics Letters* 113.1 (2018). ISSN: 00036951. DOI: 10.1063/1.5038044.

[73] D. Liu et al. "226nm AlGaN/AlN UV LEDs using p-type Si for hole injection and UV reflection". In: *Applied Physics Letters* 113.011111 (2018).

[74] E. F. Schubert. "LED Basics: Optical Properties". In: *Light-Emitting Diodes*. New York: Cambridge University Press, 2006.

[75] M.A. Würtele et al. "Application of GaN-based ultraviolet light emitting diodes UV LEDsfor water disinfection." In: *Water Research* (2011). DOI: 10.1016/j.watres.2010.11.015.

[76] J. Li et al. "A compact breath acetone analyser based on an ultraviolet light emitting diode". In: *Sensors and Actuators, B: Chemical* 273.May (2018), pp. 76–82. ISSN: 09254005. DOI: 10.1016/j.snb.2018.05.114. URL: https://doi.org/10.1016/j.snb.2018.05.114.

[77] B. Hohman. "LED light source advances fluorescence microscopy". In: *Advanced Imaging* 22.10 (2007), pp. 22–27. ISSN: 10420711.

[78] R. Wegerhoff, O. Weidlich, and M. Kässens. "Basics of Light Microscopy and Imaging". In: *Imaging and Microscopy* 1 (2006), pp. 1–56.

[79] F. Mubaid and C. M. Brown. "Less is More: Longer Exposure Times with Low Light Intensity is Less Photo-Toxic". In: *Microscopy Today* 25.6 (2017), pp. 26–35. ISSN: 1551-9295. DOI: 10.1017/s1551929517000980.

[80] E. F. Schubert. "LED Basics: Electrical Properties". In: *Light-Emitting Diodes*. New York: Cambridge University Press, 2006.

[81] J. B. Bosse et al. "Open LED illuminator: A simple and inexpensive LED illuminator for fast multicolor particle tracking in neurons". In: *PLoS ONE* 10.11 (2015), pp. 1–21. ISSN: 19326203. DOI: 10.1371/journal.pone.0143547.

[82] W. C.W. Chan and S. Nie. "Quantum dot bioconjugates for ultrasensitive nonisotopic detection". In: *Science* 281.5385 (1998), pp. 2016–2018. ISSN: 00368075. DOI: 10.1126/science.281.5385.2016.

[83] G. D. Scholes and G. Rumbles. "Excitons in nanoscale systems". In: *Nature Materials* 5.9 (Sept. 2006), pp. 683–696. DOI: 10.1038/nmat1710. URL: https://doi.org/10.1038/nmat1710.

[84] D. Vasudevan et al. "Core-shell quantum dots: Properties and applications". In: *Journal of Alloys and Compounds* 636 (2015), pp. 395–404. ISSN: 09258388. DOI: 10.1016/j.jallcom.2015.02.102. URL: http://dx.doi.org/10.1016/j.jallcom.2015.02.102.

[85] Ute Resch-Genger et al. "Quantum dots versus organic dyes as fluorescent labels". In: *Nature Methods* 5.9 (Aug. 2008), pp. 763–775. DOI: 10.1038/nmeth.1248. URL: https://doi.org/10.1038/nmeth.1248.

[86] M. Bruchez et al. "Semiconductor nanocrystals as fluorescent biological labels". In: *Science* 281.5385 (1998), pp. 2013–2016. ISSN: 00368075. DOI: 10.1126/science.281.5385.2013.

[87] V. Stsiapura et al. "Functionalized nanocrystal-tagged fluorescent polymer beads: Synthesis, physicochemical characterization, and immunolabeling application". In: *Analytical Biochemistry* 334.2 (2004), pp. 257–265. ISSN: 00032697. DOI: 10.1016/j.ab.2004.07.006.

[88] A. P. Alivisatos, W. Gu, and C. Larabell. "Quantum Dots as Cellular Probes". In: *Annual Review of Biomedical Engineering* 7.1 (2005), pp. 55–76. ISSN: 1523-9829. DOI: 10.1146/annurev.bioeng.7.060804.100432.

[89] J. K. Jaiswal et al. "Long-term multiple color imaging of live cells using quantum dot bioconjugates". In: *Nature Biotechnology* 21.1 (2003), pp. 47–51. ISSN: 10870156. DOI: 10.1038/nbt767.

[90] A. Sukhanova et al. "Biocompatible fluorescent nanocrystals for immunolabeling of membrane proteins and cells". In: *Analytical Biochemistry* 324 (2003), pp. 60–67.

[91] M. Nasilowski et al. "Gradient CdSe/CdS Quantum Dots with Room Temperature Biexciton Unity Quantum Yield". In: *Nano Letters* 15.6 (2015), pp. 3953–3958. ISSN: 15306992. DOI: 10.1021/acs.nanolett.5b00838.

[92] J. K. Jaiswal and S. M. Simon. "Potentials and pitfalls of fluorescent quantum dots for biological imaging". In: *Trends in Cell Biology* 14.9 (2004), pp. 497–504. ISSN: 09628924. DOI: 10.1016/j.tcb.2004.07.012.

[93] A. L. Efros and D. J. Nesbitt. "Origin and control of blinking in quantum dots". In: *Nature Nanotechnology* 11.8 (2016), pp. 661–671. ISSN: 17483395. DOI: 10.1038/nnano.2016.140. URL: http://dx.doi.org/10.1038/nnano.2016.140.

[94] A. Valizadeh et al. "Quantum dots: synthesis, bioapplications, and toxicity". In: *Nanoscale Research Letters* 7.1 (Aug. 2012). DOI: 10.1186/1556-276x-7-480. URL: https://doi.org/10.1186/1556-276x-7-480.

[95] M. L. Steigerwald et al. "Surface Derivatization and Isolation of Semiconductor Cluster Molecules". In: *Journal of the American Chemical Society* 110 (1987), pp. 3046–3050.

[96] C. B. Murray, D. J. Norris, and M. G. Bawendi. "Synthesis and Characterization of Nearly Monodisperse CdE (E = S, Se, Te) Semiconductor Nanocrystallites". In: *Journal of the American Chemical Society* 115.19 (1993), pp. 8706–8715. ISSN: 15205126. DOI: 10.1021/ja00072a025.

[97] M. L. Landry et al. "Simple syntheses of CdSe quantum dots". In: *Journal of Chemical Education* 91.2 (2014), pp. 274–279. ISSN: 00219584. DOI: 10.1021/ed300568e.

[98] E. M. Boatman, G. C. Lisensky, and K. J. Nordell. "A safer, easier, faster synthesis for CdSe quantum dot nanocrystals". In: *Journal of Chemical Education* 82.11 (2005), pp. 1697–1699. ISSN: 00219584. DOI: 10.1021/ed082p1697.

[99] A. Foubert et al. "Bioconjugation of quantum dots: Review & impact on future application". In: *TrAC - Trends in Analytical Chemistry* 83 (2016), pp. 31–48. ISSN: 18793142. DOI: 10.1016/j.trac.2016.07.008. URL: http://dx.doi.org/10.1016/j.trac.2016.07.008.

[100] T. Pellegrino et al. "Hydrophobic Nanocrystals Coated with an Amphiphilic Polymer Shell: A General Route to Water Soluble Nanocrystals". In: *Nano Letters* 4.4 (2004), pp. 703–707.

[101] F. Patolsky et al. "Lighting-Up the Dynamics of Telomerization and DNA Replication by CdSe-ZnS Quantum Dots". In: *Journal of the American Chemical Society* 125.46 (2003), pp. 13918–13919. ISSN: 00027863. DOI: 10.1021/ja035848c.

[102] L.A. Bentolila et al. "Quantum dots for live cells, in vivo imaging, and diagnostics". In: *Science* 307.5709 (2005), pp. 538–544.

[103] W. C.W. Chan et al. "Luminescent quantum dots for multiplexed biological detection and imaging". In: *Current Opinion in Biotechnology* 13.1 (2002), pp. 40–46. ISSN: 09581669. DOI: 10.1016/S0958-1669(02)00282-3.

[104] E. R. Goldman et al. "Conjugation of luminescent quantum dots with antibodies using an engineered adaptor protein to provide new reagents for fluoroimmunoassays". In: *Analytical Chemistry* 74.4 (2002), pp. 841–847. ISSN: 00032700. DOI: 10.1021/ac010662m.

[105] E. B. Voura et al. "Tracking metastatic tumor cell extravasation with quantum dot nanocrystals and fluorescence emission-scanning microscopy". In: *Nature Medicine* 10.9 (2004), pp. 993–998. ISSN: 10788956. DOI: 10.1038/nm1096.

[106] B. Dubertret et al. "In vivo imaging of quantum dots encapsulated in phospholipid micelles". In: *Science* 298.5599 (2002), pp. 1759–1762. ISSN: 00368075. DOI: 10.1126/science.1077194.

[107] I. L. Medintz et al. "Self-assembled nanoscale biosensors based on quantum dot FRET donors". In: *Nature Materials* 2.9 (2003), pp. 630–638. ISSN: 14761122. DOI: 10.1038/nmat961.

[108] M. Dahan et al. "Diffusion Dynamics of Glycine Receptors Revealed by Single-Quantum Dot Tracking". In: *Science* 302.5644 (2003), pp. 442–445. ISSN: 00368075. DOI: 10.1126/science.1088525.

[109] T. Jamieson et al. "Biological applications of quantum dots". In: *Biomaterials* 28.31 (2007), pp. 4717–4732. ISSN: 01429612. DOI: 10.1016/j.biomaterials.2007.07.014.

[110] S. Skorupska and I. Grabowska-Jadach. "Cytotoxicity studies of quantum dots with the electroporation method". In: *Bioelectrochemistry* 126 (2019), pp. 86–91. ISSN: 1878562X. DOI: 10.1016/j.bioelechem.2018.11.011. URL: https://doi.org/10.1016/j.bioelechem.2018.11.011.

[111] A. M. Derfus, W. C.W. Chan, and S. N. Bhatia. "Probing the Cytotoxicity of Semiconductor Quantum Dots". In: *Nano Letters* 4.1 (2004), pp. 11–18. ISSN: 15306984. DOI: 10.1021/nl0347334.

[112] E. F. Schubert. "Radiative and Non-radiative Recombination". In: *Light-Emitting Diodes*. New York: Cambridge University Press, 2006.

[113] R. N. Hall. "Electron-Hole Recombination in Germanium". In: *Phys. Rev.* 87 (2 1952), pp. 387–387. DOI: 10.1103/PhysRev.87.387. URL: https://link.aps.org/doi/10.1103/PhysRev.87.387.

[114] W. Shockley and W. T. Read. "Statistics of the Recombinations of Holes and Electrons". In: *Phys. Rev.* 87 (5 1952), pp. 835–842. DOI: 10.1103/PhysRev.87.835. URL: https://link.aps.org/doi/10.1103/PhysRev.87.835.

[115] E. F. Schubert. "Packaging". In: *Light-Emitting Diodes*. New York: Cambridge University Press, 2006.

[116] G. Leschhorn and R. Young. "Handbook of LED and SSL Metrology". In: *Instrument Systems GmbH* (2017), p. 48. URL: http://www.instrumentsystems.com/fileadmin/editors/downloads/Products/LED_Handbook_e.pdf%5Cnhttp://scholar.google.com/scholar?hl=en\&btnG=Search\&q=intitle:Handbook+of+LED+Metrology#0.

[117] E. F. Schubert. "Human eye sensitivity and photometric quantities". In: *Light-Emitting Diodes*. New York: Cambridge University Press, 2006.

[118] I. Moreno and C. Sun. "Modeling the radiation pattern of LEDs". In: *Optics Express* 16.3 (2008), p. 1808. ISSN: 1094-4087. DOI: 10.1364/oe.16.001808.

[119] X. Sheng et al. "Design and fabrication of high-index-contrast self-assembled texture for light extraction enhancement in LEDs". In: *Optics Express* 19.S4 (2011), A701. ISSN: 1094-4087. DOI: 10.1364/oe.19.00a701.

[120] M. Keshavarzfathy and F. Taghipour. "Radiation modeling of ultraviolet light-emitting diode (UV-LED) for water treatment". In: *Journal of Photochemistry and Photobiology A: Chemistry* 377.March (2019), pp. 58–66. ISSN: 10106030. DOI: 10.1016/j.jphotochem.2019.03.030. URL: https://doi.org/10.1016/j.jphotochem.2019.03.030.

[121] M. Lapeyrade et al. "Design considerations for AlGaN-based UV LEDs emitting near 235 nm with uniform emission pattern". In: *Semiconductor Science and Technology* 32.4 (2017). ISSN: 13616641. DOI: 10.1088/1361-6641/aa5a7a.

[122] P. Manninen et al. "Method for analysing luminous intensity of light-emitting diodes". In: *Measurement Science and Technology* 18.1 (2007), pp. 223–229. ISSN: 13616501. DOI: 10.1088/0957-0233/18/1/028.

[123] OSRAM Opto Semiconductors. *General Lighting LED portfolio*. URL: https://www.osram.com/os/products/illumination-applications/product_portfolio_for_general_lighting.jsp.

[124] K. Schauenstein, E. Schauenstein, and G. Wick. "Fluorescence properties of free and protein bound fluorescein dyes". In: *The Journal of Histochemistry and Cytochemistry* 26 (4 1978), pp. 277–283.

[125] J. Schindelin et al. "Fiji: an open-source platform for biological-image analysis". In: *Nature Methods* 9.7 (2012), pp. 676682. DOI: 10.1038/nmeth.2019.

[126] Newport Corporation. *Thermopile Sensor Physics*. URL: https://www.newport.com/n/thermopile-physics.

[127] D. Gutierrez, J. Álvarez, and F. Racedo. "Development of a Steady-State Fluorescence Spectroscopy System and a Time-Resolved Fluorescence Spectroscopy System". In: *Journal of Physics: Conference Series* 1247.1 (2019). ISSN: 17426596. DOI: 10.1088/1742-6596/1247/1/012017.

[128] Schott Advanced Optics. *Transmittance of Optical Glass*. 2005. URL: https://www.schott.com/shop/medias/schott-tie-35-transmittance-of-optical-glass-eng.pdf.

[129] *N-BK7 Plano-Convex Lenses (Uncoated)*. https://www.thorlabs.com/newgrouppage9.cfm?objectgroup_id=112. Accessed: 2022-08-05.

[130] *UV Fused Silica Plano-Convex Lenses, Uncoated*. https://www.thorlabs.com/newgrouppage9.cfm?objectgroup_id=123. Accessed: 2022-08-05.

[131] *Introduction to Reflective Objectives*. https://www.edmundoptics.co.uk/knowledge-center/application-notes/microscopy/introduction-to-reflective-objectives. Accessed: 2022-08-05.

[132] Ealing. *Laboratory microscope objectives*. URL: https://www.mavin.com/pdf/Microscope_Components.pdf.

[133] Beck Optronic Solutions. *Reflecting Objective Lens Data Sheet*. URL: https://www.beckoptronic.com/uploads/cms/products/1/beck-ds-rog-lens-v13-pdf.pdf.

[134] R. B. Uretz, W. Bloom, and R. E. Zirkle. "Irradiation of parts of individual cells II. Effects of an ultraviolet microbeam focused on parts of chromosomes". In: *Science* 120.3110 (1954), pp. 197–199.

[135] R. Ishii, M. Funato, and Y. Kawakami. "Pushing the limits of deep-ultraviolet scanning near-field optical microscopy". In: *APL Photonics* 4.7 (2019). ISSN: 23780967. DOI: 10.1063/1.5097865. URL: https://doi.org/10.1063/1.5097865.

[136] F. Fereidouni et al. "Microscopy with UV Surface Excitation (MUSE) for slide-free histology and pathology imaging". In: *Optical Biopsy XIII: Toward Real-Time Spectroscopic Imaging and Diagnosis* 9318 (2015), 93180F. ISSN: 16057422. DOI: 10.1117/12.2080408.

[137] R. Levenson. "MUSE nearly instant slide-free microscopyplus bonus: getting special-stain results from H&E-stained slides". In: *Journal of Histotechnology* 41.4 (2018), p. 139. ISSN: 20460236. DOI: 10.1080/01478885.2018.1525983. URL: https://doi.org/10.1080/01478885.2018.1525983.

[138] R. Levenson et al. "Slide-Free Microscopy via UV Surface Excitation". In: *Microscopy and Microanalysis* 22.S3 (2016), pp. 1002–1003. ISSN: 1431-9276. DOI: 10.1017/s1431927616005857.

[139] E. Peli. "Contrast in complex images". In: *Journal of the Optical Society of America A* 7 (10 1990).

[140] *How to Select the Right Light Pipe Homogenizing Rod*. https://www.edmundoptics.co.uk/knowledge-center/application-notes/optics/how-to-select-the-right-light-pipe-homogenizing-rod/. Accessed: 2022-08-05.

[141] S. Prost et al. "Working with commercially available quantum dots for immunofluorescence on tissue sections". In: *PLoS ONE* 11.9 (2016), pp. 1–23. ISSN: 19326203. DOI: 10.1371/journal.pone.0163856.

[142] A. P. Alivisatos. "Semiconductor Clusters, Nanocrystals, and Quantum Dots". In: *Science* 271 (1996), pp. 933–937. URL: http://www.sciencemag.org/content/271/5251/933.abstract?ijkey=f42f30cb86e463a3da384f31ed31a2ddb255ea20\&keytype2=tf_ipsecsha.

[143] X. Gao et al. "In vivo cancer targeting and imaging with semiconductor quantum dots". In: *Nature Biotechnology* 22.8 (2004), pp. 969–976. ISSN: 10870156. DOI: 10.1038/nbt994.

[144] L. Helmick et al. "Spatiotemporal response of living cell structures in Dictyostelium discoideum with semiconductor quantum dots". In: *Nano Letters* 8.5 (2008), pp. 1303–1308. ISSN: 15306984. DOI: 10.1021/nl0731441.

[145] H. Zeng et al. "Simultaneous multicolour imaging using quantum dot structured illumination microscopy". In: *Journal of Microscopy* 277.1 (2020), pp. 32–41. ISSN: 13652818. DOI: 10.1111/jmi.12862.

[146] J. Xu, K. F. Tehrani, and P. Kner. "Multicolor 3D super-resolution imaging by quantum dot stochastic optical reconstruction microscopy". In: *ACS Nano* 9.3 (2015), pp. 2917–2925. ISSN: 1936086X. DOI: 10.1021/nn506952g.

[147] A. Watson, X. Wu, and M. Bruchez. "Lighting Up Cells with Quantum Dots". In: *BioTechniques* 34.2 (Feb. 2003), pp. 296–303. DOI: 10.2144/03342bi01. URL: https://doi.org/10.2144/03342bi01.

[148] *Hela cells (1951)*. URL: https://www.immunology.org/hela-cells-1951.

[149] Invitrogen. *Qdotő Streptavidin Conjugates*. URL: https://www.thermofisher.com/document-connect/document-connect.html?url=https\%3A\%2F\%2Fassets.thermofisher.com\%2FTFS-Assets\%2FLSG\%2Fmanuals\%2Fmp19000.pdf.

[150] A. Edelstein et al. "Computer control of microscopes using manager". In: *Current Protocols in Molecular Biology* SUPPL. 92 (2010), pp. 1–22. ISSN: 19343639. DOI: 10.1002/0471142727.mb1420s92.

[151] N. Hall. *Data for: Enhanced Fluorescence from Semiconductor Quantum Dot-Labelled Cells Excited at 280nm*. URL: https://github.com/NickHallPhysics/Quantum_dot_image_analysis.

[152] N. Otsu. "A threshold selection method from gray level histograms". In: *IEEE Transactions on Systems, Man, and Cybernetics* 9 (1979), pp. 62–66.

[153] B. L. Welch. "The generalization of student's problem when several different population varlances are involved". In: *Biometrika* 34.1-2 (1947), pp. 2835. DOI: 10.1093/biomet/34.1-2.28.

[154] K. W. Teng et al. "Labeling proteins inside living cells using external fluorophores for microscopy". In: *eLife* 5 (2016), pp. 1–13. ISSN: 2050084X. DOI: 10.7554/eLife.20378.

[155] L. S. Kölln et al. "Label2label: training a neural network to selectively restore cellular structures in fluorescence microscopy". In: *Journal of Cell Science* 135.3 (Feb. 2022). jcs258994. ISSN: 0021-9533. DOI: 10.1242/jcs.258994. eprint: https://journals.biologists.com/jcs/article-pdf/135/3/jcs258994/2130156/jcs258994.pdf. URL: https://doi.org/10.1242/jcs.258994.

[156] D. Mutavdi et al. "Determination of the size of quantum dots by fluorescence spectroscopy". In: *Analyst* 136 (11 2011), pp. 2391–2396. DOI: 10.1039/C0AN00802H. URL: http://dx.doi.org/10.1039/C0AN00802H.

[157] B. M. Hutchins et al. "Optical properties of fluorescent mixtures: Comparing quantum dots to organic dyes". In: *Journal of Chemical Education* 84.8 (2007), pp. 1301–1303. ISSN: 00219584. DOI: 10.1021/ed084p1301.

[158] J. Rodríguez-Viejo et al. "Evidence of photo- and electrodarkening of (CdSe)ZnS quantum dot composites". In: *Journal of Applied Physics* 87.12 (2000), pp. 8526–8534. ISSN: 00218979. DOI: 10.1063/1.373573.

[159] E. Hecht. *Optics*. Boston: Addison-Wesley, 1988.

[160] O. Wiener. "Stehende lichtwellen und die schwingungsrichtung polarisirten lichtes". In: *Annalen der Physik* 276.6 (1890), pp. 203–243.

[161] R. Amor et al. "Standing-wave-excited multiplanar fluorescence in a laser scanning microscope reveals 3D information on red blood cells". In: *Scientific Reports* 4 (2014). ISSN: 20452322. DOI: 10.1038/srep07359.

[162] P. Drude and W. Nernst. "Ueber die Fluorescenzwirkungen stehender Lichtwellen". In: *Annalen der Physik* 281.3 (1892), pp. 460–474. DOI: https://doi.org/10.1002/andp.18922810305. eprint: https://onlinelibrary.wiley.com/doi/pdf/10.1002/andp.18922810305. URL: https://onlinelibrary.wiley.com/doi/abs/10.1002/andp.18922810305.

[163] F. Lanni. "Standing Wave Fluorescence Microscopy". In: *Applications of Fluorescence Microscopy*. 1986, pp. 505–521. DOI: 10.1007/springerreference_25502.

[164] B. Bailey et al. "Enhancement of axial resolution in fluorescence microscopy by standing-wave excitation". In: *Nature* 366.6450 (1993), pp. 44–48. ISSN: 00280836. DOI: 10.1038/366044a0.

[165] F. Lanni, D. L. Taylor, and A. S. Waggoner. *US Patent No. 4,621,911*. 1986.

[166] F. Lanni et al. "Excitation field synthesis as a means for obtaining enhanced axial resolution in fluorescence microscopes". In: *Bioimaging* 1.4 (1993), pp. 187–196. DOI: https://doi.org/10.1002/1361-6374(199312)1:4<187::AID-BIO1>3.0.CO;2-P. eprint: https://onlinelibrary.wiley.com/doi/pdf/10.1002/1361-6374. URL: https://onlinelibrary.wiley.com/doi/abs/10.1002/1361-6374%28199312%291%3A4%3C187%3A%3AAID-BIO1%3E3.0.CO%3B2-P.

[167] S. Hell and E. H. K. Stelzer. "Properties of a 4Pi confocal fluorescence microscope". In: *Journal of the Optical Society of America A* 9.12 (1992), p. 2159. ISSN: 1084-7529. DOI: 10.1364/josaa.9.002159.

[168] Stefan Hell and Ernst H.K. Stelzer. "Fundamental improvement of resolution with a 4Pi-confocal fluorescence microscope using two-photon excitation". In: *Optics Communications* 93.5 (1992), pp. 277–282. ISSN: 0030-4018. DOI: https://doi.org/10.1016/0030-4018(92)90185-T. URL: https://www.sciencedirect.com/science/article/pii/003040189290185T.

[169] W. B. Amos and G. McConnell. "Confocal microscopy". In: *Handbook of Comprehensive Biophysics*. Elsevier, 2012.

[170] R. Freimann, S. Pentz, and H. Hörler. "Development of a standingwave fluorescence microscope with high nodal plane flatness". In: *Journal of Microscopy* 187.3 (1997), pp. 193200. DOI: 10.1046/j.1365-2818.1997.2290789.x.

[171] K. Elsayad et al. "Spectrally coded optical nanosectioning (SpecON) with biocompatible metal-dielectric-coated substrates". In: *Proceedings of the National Academy of Sciences of the United States of America* 110.50 (2013), pp. 20069–20074. ISSN: 00278424. DOI: 10.1073/pnas.1307222110.

[172] P. W. Tinning, R. Scrimgeour, and G. McConnell. "Widefield standing wave microscopy of red blood cell membrane morphology with high temporal resolution". In: *Biomedical Optics Express* 9.4 (2018), p. 1745. ISSN: 2156-7085. DOI: 10.1364/boe.9.001745.

[173] J. K. Schniete et al. "An evaluation of multi-excitation-wavelength standing-wave fluorescence microscopy (TartanSW) to improve sampling density in studies of the cell membrane and cytoskeleton". In: *Scientific Reports* 11.1 (2021), pp. 1–10. ISSN: 20452322. DOI: 10.1038/s41598-020-78282-6. URL: https://doi.org/10.1038/s41598-020-78282-6.

[174] V. Krishnamurthi, B. Bailey, and F. Lanni. "Image processing in 3D standing-wave fluorescence microscopy". In: vol. 2655. SPIE, Apr. 1996, pp. 18–25. DOI: 10.1117/12.237480.

[175] P. W. Tinning. "New optical techniques and hardware for studying live cell dynamics". PhD thesis. University of Strathclyde, 2018.

[176] Edmund Optics. *Optical filters*. URL: https://www.edmundoptics.co.uk/knowledge-center/application-notes/optics/optical-filters/.

[177] H. Motulsky. *Graphpad prism*. 1995.

[178] Sigma Aldrich. *Poly-L-lysine cell attachment protocol*. URL: https://www.sigmaaldrich.com/GB/en/technical-documents/protocol/cell-culture-and-cell-culture-analysis/3d-cell-culture/poly-lysine-product.

[179] M. M. Barroso. "Quantum dots in cell biology". In: *Journal of Histochemistry and Cytochemistry* 59.3 (2011), pp. 237–251. ISSN: 00221554. DOI: 10.1369/0022155411398487.

[180] A. Banerjee et al. *Quantum dots-DNA bioconjugates: Synthesis to applications*. 2016. DOI: 10.1098/rsfs.2016.0064.

[181] H. Hertz. "Ueber die Ausbreitungsgeschwindigkeit der electrodynamischen Wirkungen". In: *Annalen der Physik* 270 (), pp. 551–569.